Understanding the Chemistry of Atmospheric Particles Using Single Particle Mass Spectrometry

by

Maria Anna Zawadowicz

B.S., Lake Forest College (2012)

Submitted to the Department of Earth, Atmospheric and Planetary Sciences
in partial fulfillment of the requirements for the degree of

Doctor of Philosophy in Atmospheric Chemistry

at the

MASSACHUSETTS INSTITUTE OF TECHNOLOGY

September 2017

Author ..... Signature redacted .....
Department of Earth, Atmospheric and Planetary Sciences
September 8, 2017

Certified by .. Signature redacted .....
Daniel J. Cziczo
Associate Professor
Thesis Supervisor

Signature redacted

Accepted by ....
Robert D. van der Hilst
Schlumberger Professor of Earth and Planetary Sciences
Head, Department of Earth, Atmospheric and Planetary Sciences

Understanding the Chemistry of Atmospheric Particles Using Single Particle Mass Spectrometry

by

Maria Anna Zawadowicz

Submitted to the Department of Earth, Atmospheric and Planetary Sciences
on September 8, 2017, in partial fulfillment of the
requirements for the degree of
Doctor of Philosophy in Atmospheric Chemistry

Abstract

This thesis explores ways in which single particle mass spectrometry can be extended, whether through hardware improvements, or through the use of advanced data processing techniques to provide new kinds of aerosol chemistry measurements. Most of this work has been carried out using the Particle Analysis by Laser Mass Spectrometry (PALMS) instrument, an aircraft deployable mass spectrometer that uses intense ($\sim 10^9$ Wcm^{-2}) UV laser pulses to vaporize and ionize single particles and measures their mass spectra using a time-of-flight mass spectrometer. Near-term and long-term hardware improvements as well as advanced data analysis techniques are explored in order to extract new chemical information from the thus obtained single particle mass spectra. Hardware improvements to PALMS are explored, such as the use of a high-powered femtosecond laser to obtain single particle mass spectra and a new high resolution compact mass analyzer. Also, a new commercial mass spectrometer LAAPToF is characterized and compared to PALMS. In addition to hardware improvements, novel data analysis techniques for analysis of single particle mass spectra were developed as a part of this work. In particular, a new method to identify biologically-derived particles is presented and used to derive vertical profiles of bioaerosol from near-surface to the upper troposphere.

Thesis Supervisor: Daniel J. Cziczo
Title: Associate Professor

Acknowledgments

I would like to acknowledge my advisor, Prof. Dan Cziczo, for his guidance over the last five years. Dan's mentoring and scientific expertise really helped me to become a better researcher and a scientist. Additionally, the other members of my committee, Prof. Jesse Kroll, Prof. Kerri Cahoy and Dr. Karl Froyd provided invaluable advice on writing and revising this thesis. I would like to thank numerous collaborators without whom none of this research would be possible. Dr. Dan Murphy at NOAA provided us with the first prototype of the sTOF analyzer, as well as unmatched expertise in design of single particle mass spectrometers and the interpretation of their data output. At Karlsruhe Institute of Technology, I have had the opportunity to work with Prof. Thomas Leisner, Dr. Ottmar Möhler, Dr. Ahmed Abdelmonem, Dr. Harald Saathoff, Dr. Claudia Mohr, other AIDA scientists and support staff, as well as the participants of the Fifth Ice Nucleation (FIN-1) workshop. I would also like to thank my collaborators at Aerodyne Research, Inc., Dr. Phil Croteau, Dr. John Jayne and Dr. Douglas Worsnop. Additionally, I would like to acknowledge the participants of the FIN-3 workshop and the Storm Peak Laboratory staff. I am also very grateful to Dr. Anne Perring, Prof. Colette Heald, Prof. Dominick Spracklen and Prof. Peter Buseck for their collaboration on the bioaerosols work.

I have spent wonderful five years with the Cziczo group at MIT and would like to acknowledge both the present and past members of the group with whom I worked: Martin Wolf, Tajana Erjavec, Dr. Sarvesh Garimella, Fabian Mahrt, Shaena Berlin, Costa Christopoulos, Libby Koolik, Dr. Alexandria Johnson, Dr. Michael Roesch, Dr. Carolin Roesch, Dr. Sara Lance, Dr. Karin Ardon Dryer and Dr. Simon Proud.

Additionally, I thank the Lake Forest College professors thanks to whom I went to graduate school: Prof. Lori Del Negro, Prof. Michael Kash, Prof. Elizabeth Fischer and Prof. Dawn Wiser.

I would also like to thank my close friends: Nadia Vinogradova, Jen Kurtz, Tom Pospiech and Derek Chang.

Finally, I would like to thank my family: Barbara Zawadowicz, Maria Skrzeczkowska

and Stanislaw Wroblewski for moral support throughout my PhD.

Contents

List of Figures

List of Tables

Chapter 1

Introduction

1.1 Aerosols, chemistry and climate change

Climate change is often discussed in the context of greenhouse gases that are emitted into the atmosphere and subsequently change the Earth's radiative balance (Boucher et al., 2013). However, the effects of small particulates (aerosols) and clouds that they produce are a far less well understood influence on climate (Boucher et al., 2013). The 2013 report of the Intergovernmental Panel on Climate Change (IPCC) estimates that the total effective radiative forcing due to aerosols and clouds is between -1.9 and -0.1 Wm^{-2} (Boucher et al., 2013). This estimate includes two effects: (1) the direct effect, where aerosol particles in the upper atmosphere scatter the incoming solar radiation and (2) the indirect effect, where aerosols influence the formation and persistence of clouds, which then in turn modify the radiative properties of the upper atmosphere.

The effective radiative forcing due to the direct effect is currently estimated to be -0.45 $\pm$ 0.5 Wm^{-2} by the 2013 IPCC report, based on earlier estimates by Lohmann and Ferrachat (2010) and Ghan et al. (2012) (Boucher et al., 2013). Direct scattering by aerosol particles is related to their optical properties, which in turn are determined by their size, shape and composition. Figure C-1 shows the IPCC estimates of direct forcing by aerosol composition for some common aerosol species. Sulfate particles scatter radiation very effectively, while black carbon aerosols absorb it. However, the total effect of those aerosols depends on their altitude: black carbon in the troposphere

warms the planet, but cools it in the stratosphere (Ban-Weiss et al., 2012; Yu et al., 2016).

The 2013 IPCC report adopts a 90% uncertainty range of 1.2 to 0 Wm^{-2} for the indirect effect, noting that the indirect effect is very difficult to estimate (Boucher et al., 2013). Aerosols contribute to cloud formation in the atmosphere. For example, cirrus clouds, which are especially relevant to radiative budgets due to their high altitude of formation and wide spatial coverage, are composed solely of ice crystals, which often heterogeneously nucleate on pre-existing aerosol particles (Lynch, 2002; Cziczo et al., 2013; Hoose and Möhler, 2012). Those particles, known as ice nucleating particles (INPs), have been shown to often be chemically distinct from background aerosol and very low in number concentration (Cziczo et al., 2013; DeMott et al., 2003; Ebert et al., 2011). Ice nucleation is a very active area of research and many kinds of efficient INPs have been identified in field and laboratory studies over the past two decades (Hoose and Möhler, 2012). In field studies, the composition of evaporated ice crystals (ice residuals) can be analyzed both on- and off-line (Cziczo and Froyd, 2014). For cirrus clouds, those studies usually point to mineral dust or anthropogenic metallic composition, although sea salts, organics and other aerosols have also been reported (Cziczo et al., 2013; DeMott et al., 2003; Froyd et al., 2010). However, sub-visible cirrus cloud residuals at the tropopause were found to be primarily composed of sulfate and organic particles and not necessarily distinct from background aerosol (Froyd et al., 2010). Efficiencies of individual INPs vary with temperature and relative humidity and while mineral dusts are good INPs for high altitude ice clouds, lower altitude mixed phase clouds are thought to nucleate on INPs that are more efficient at lower temperatures. Biological aerosols have been hypothesized to play that role, but reliable field-based observations are scarce (Hoose et al., 2010; Möhler et al., 2007). One study of mixed phase cloud residuals conducted at a high altitude research station (Jungfraujoch, Switzerland) reported no biological particles (Ebert et al., 2011), while another, conducted from a research aircraft flying over Wyoming, reported over 30% biological ice residuals for one cloud (Pratt et al., 2009). The formation of lower altitude liquid clouds can also be influenced by aerosol

particles, in particular their hygroscopicity. Hygroscopic particles, such as salts that promote the formation of cloud droplets are referred to as cloud condensation nuclei (CCN) (Petters and Kreidenweis, 2007). Populations of both INPs and CCNs can be influenced by anthropogenic particle emissions. In a polluted atmosphere, larger concentrations of INPs and CCNs are available, which results in thinner clouds with longer lifetimes (Lohmann and Feichter, 2005). Additionally, chemical composition of anthropogenic particles can have an effect on the ability of those particles to act as INPs—it has been shown that many ice cloud residuals observed in field studies had lead inclusions directly attributable to industrial lead use (Cziczo et al., 2009; Ebert et al., 2011).

In order to better describe the direct and indirect aerosol effects on climate, observations of particle compositions are of utmost importance. While satellites provide some insight into bulk particle compositions, many climate-relevant microphysical processes, such as cloud formation, occur at a single-particle level and are therefore best studied *in situ*. In addition to climate, heterogeneous aerosol chemistry plays an important role in the fate of certain gaseous species, like halogen radicals (Solomon et al., 2016).

1.2 Measuring aerosol chemistry: experimental challenges

Atmospheric aerosols demonstrate significant chemical diversity: their diameters can span nanometers to tens of microns, they can be solid or liquid or exist as a solid/liquid mixture and their chemical composition can be completely inorganic, completely organic or anything in between (Seinfeld and Pandis, 2006). The initial composition of an aerosol particle is constrained by the emission source and sometimes the emission mechanism. There are various natural particulate sources. For example, dust productive regions, such as deserts, emit mineral dust aerosols via a process known as saltation (wind-driven dispersal) (Kok et al., 2012), wildfires are a source of both

completely combusted elemental carbon (soot or black carbon aerosols) as well as incompletely combusted aerosols collectively known as biomass burning aerosol (Capes et al., 2008; Cubison et al., 2011; Adler et al., 2011; Hudson et al., 2004), and forests emit volatile organic compounds, such as isoprene, which oxidize in the atmosphere upon contact with UV radiation and condense into liquid particles known as secondary organic aerosol (Kroll and Seinfeld, 2008). Oceans produce large quantities of sea salt particles during wave breaking, which can be often enriched in marine organics (Cochran et al., 2017). In addition to the natural sources, many aerosols emitted into the atmosphere are anthropogenic: vehicular emissions and industrial activities such as fossil fuel burning can be a source of sulfate aerosols (Nabat et al., 2014), elemental carbon (Ramanathan and Carmichael, 2008), as well as ash enriched in heavy metals (Reff et al., 2009). In addition, human activity modulates some of the natural aerosol sources: for example, land use changes and deforestation contribute to mineral dust budgets in the atmosphere (Tegen and Fung, 1995). Once emitted into the atmosphere, aerosols can undergo a wealth of chemical transformations including reactions with atmospheric gases to form surface coatings (Usher et al., 2003), coagulation with other aerosols, and aqueous processing by condensed water phase (McNeill, 2015). Those changes are referred to as aging or atmospheric processing and they can drastically impact the properties of the initial aerosol particle. For example, there is evidence that sulfate and organic coatings decrease the ability of mineral dust to act as efficient INPs (Cziczo et al., 2009).

Because of their diversity, there are many analytical challenges in characterizing aerosol chemical composition. Some unique attributes of aerosol-specific analytical techniques include:

(1) Single or near-single particle resolution to differentiate between internal and external particle mixtures. As illustrated schematically in Figure C-2, internally mixed particles contain multiple components mixed together in a single particle, while externally mixed particles consist of different types of pure particles. An analytical technique that does not sample single particles cannot resolve those two types of mixtures. Particles that are internally mixed can have different atmospheric properties

than their pure counterparts. Mentioned previously, organic and sulfate coatings can alter properties of INPs such as dust (Cziczo et al., 2009). As an additional example, illustrated in Figure C-1, soot particles are very good absorbers of radiation, while sulfate particles tend to reflect radiation well. However, their optical properties are not additive: a mixed soot-sulfate particle can become an even better absorber due to the so-called lensing effect (Liu et al., 2017).

(2) Ability to characterize both volatile and refractory components. Due to their chemical complexity, atmospheric aerosols often contain both volatile (organics, sulfates, nitrates) and refractory components (soot, mineral dust) (Seinfeld and Pandis, 2006). Sensitivity to one but not the other can leave an incomplete picture of aerosol to be characterized.

(3) Sensitivity to a range of different particle diameters. It is challenging to use a single optical detection technique for aerosols from fine (<100 nm) to coarse (>1 μm) mode because particles of different diameters can interact with light very differently, i.e. the differential scattering cross-sections are proportional to the sixth power of particle diameter in the Mie theory of light scattering. Therefore, it can be very challenging to detect particles smaller than 100 nm optically and if they cannot be detected, analysis becomes impossible. In addition, for single particle characterization, sensitivity to very small analyte masses is required: mass of a 200 nm aerosol particle is on the order of femtograms.

(4) Ability to measure aerosol particles *in situ* from a wide variety of platforms. Because of volatile sample losses in storage and transport it is not advantageous to analyze aerosol samples off-line (Chow, 1995). Most modern aerosol instrumentation is rugged and portable enough to be deployable on aircraft, ships, mobile vans and high altitude research stations.

The earliest aerosol analysis methods involved collection of ambient atmospheric aerosols on filters and off-line analysis to extract the filters and measure the chemical composition with a variety of standard analytical techniques (GC-MS, LC-MS, ICP-MS and others) (Chow, 1995). While a thorough characterization of the chemistry of large particle ensembles can be achieved, those techniques cannot provide single

particle resolution. In such an analysis, rapid temporal changes of aerosol populations cannot be resolved and low number concentration components fall below the detection limit. Some off-line methods, such as electron microscopy, can provide single-particle resolution. Those are still successfully used for characterization of ambient aerosol and for ice residual studies (Ebert et al., 2011; Pósfai et al., 2003, 2013; Pósfai and Buseck, 2010). Ambient aerosol particles are collected on an EM grid and their morphology can be examined on a single-particle basis using an electron microscope (scanning or transmission) (Ebert et al., 2011; Pósfai et al., 2003, 2013; Pósfai and Buseck, 2010). EM can be coupled with precise chemical speciation techniques, such as EDX (Ault et al., 2012). Those methods have provided very valuable insights into atmospheric aerosol composition, but the analysis can be very time consuming as each particle needs to be examined separately.

In the last two decades, several rugged sensors for specific particle types have been developed to provide rapid detection a subset of aerosols in-situ and on a single-particle basis. Those methods take advantage of physical properties unique to a subset of aerosols that they target. One example of such technique is Single Particle Soot Photometer (SP2, Droplet Measurement Technologies, Longmont, CO), an in-situ, single particle instrument that uses laser incandescence to measure soot particle concentrations (Schwarz et al., 2006; Gao et al., 2007; Slowik et al., 2007). Particles to be analyzed cross an open cavity CW Nd:YAG laser beam (1064 nm wavelength). Because soot particles are excellent absorbers, they are heated by the laser beam until incandescence (Schwarz et al., 2006). The incandescent emission is measured and compared to laboratory standards. Other atmospheric particles that are not nearly as absorbent pass through the laser without incandescence, but their presence and size can be sensed by measuring scattered radiation. Therefore, the SP2 can provide absolute concentrations and fractions of soot particles in 200 nm - 700 nm, but it cannot determine the chemical composition of non-soot particles. Another recent example of an aerosol-specific technique is the Wideband Integrated Bioaerosol Sensor (WIBS, Droplet Measurement Technologies, Longmont, CO) (Kaye et al., 2005; Gabey et al., 2010; Toprak and Schnaiter, 2013; Perring et al., 2015). The

WIBS technique takes advantage of particle fluorescence when excited with pulses of UV radiation, which can be specific to particles containing complex organics with aromatic ring systems, which include bioaerosols (Kaye et al., 2005). Laboratory work to characterize the interferences and optimize the WIBS for bioaerosol sensitivity is currently underway (Perring et al., 2015; Hernandez et al., 2016). While those specific sensors can provide detailed information about particles that they target, they must be used in tandem with other techniques in order to achieve complete characterization of atmospheric aerosol populations.

1.3 *In situ* aerosol mass spectrometry

Since the late 1990s, various mass spectrometry techniques specifically for aerosol research have been introduced. The most widely used techniques described in the following sections, flash vaporization/electron impact ionization mass spectrometry (Jayne et al., 2000; DeCarlo et al., 2006; Drewnick et al., 2005; Canagaratna et al., 2007) and laser desorption/ionization mass spectrometry (Thomson et al., 2000; Gard et al., 1997; Murphy, 2007), differ in their ionization methods and the kind of chemical components that they target. However, they all share excellent sensitivity to small aerosol masses and portability that allows them to be used on research aircraft and a variety of other mobile platforms. Figure C-3 illustrates the number of recent publications by year obtained by searching aerosol mass spectrometry-related keywords in the Web of Science database. The increase in the number of publications since the year 2000 illustrates the growing interest in those techniques over the last 17 years.

There are, of course, other ways to leverage mass spectrometry for analysis of atmospheric aerosols. For example, Filter Inlet for Gases and Aerosols (FIGAERO) is a device that enables in-situ collection of aerosols on a filter followed by automated thermal desorption of volatile components and subsequent analysis with a chemical ionization mass spectrometer (Lopez-Hilfiker et al., 2014). Similarly, thermal desorption aerosol gas chromatograph (TAG) combines thermal desorption of collected aerosol with traditional gas chromatography techniques (Kreisberg et al.,

2009). Those techniques can be very useful for detailed organic speciation of volatile aerosol components, but they are not aerosol-specific methods and therefore they are not discussed in detail here.

1.3.1 Flash vaporization/electron impact ionization mass spectrometry

The most widely used member of this instrument class is the Aerosol Mass Spectrometer (AMS). First described by Jayne et al. (2000), AMS is a commercial mass spectrometer for aerosol in situ studies manufactured by Aerodyne Research, Inc (Billerica, MA). The modern version of the instrument uses an aerodynamic lens, a type of inlet that concentrates aerosol particles into a narrow beam, to introduce aerosols into the high vacuum (10^{-5} Torr) region of the instrument (Zhang et al., 2002, 2004). Particles enter the vacuum via mild supersonic expansion, which also accelerates them according to their inertia: large particles acquire lower velocities than small particles. The particle beam then passes through an opening of a rotating mechanical chopper, which modulates the beam into single particles or small particle groups (Jayne et al., 2000; DeCarlo et al., 2006; Drewnick et al., 2005). The particles move through a vacuum chamber and impact onto a resistively heated (~600°C) surface (Jayne et al., 2000; DeCarlo et al., 2006; Drewnick et al., 2005). The volatile chemical components of the particles are flash vaporized and the vapor molecules are ionized with 70 eV electrons emitted with a filament mounted orthogonally to the particle beam (Jayne et al., 2000; DeCarlo et al., 2006; Drewnick et al., 2005). Ions are extracted and accelerated into a time-of-flight mass spectrometer (DeCarlo et al., 2006; Drewnick et al., 2005). Because the mass spectrometer is synchronized with the chopper, it is possible to measure the particle transit time through the vacuum flight tube where the beginning is defined by particle entering the chopper opening and the end is defined as production of the ion signal. This transit time is proportional to the particle vacuum aerodynamic diameter.

AMS can characterize the vacuum diameter and the chemical composition of single

aerosol particles or an average chemical composition of a particle ensemble depending on whether the mechanical chopper is used (DeCarlo et al., 2006; Drewnick et al., 2005). Because vaporization of chemical components is a necessary step before the ionization, refractory components, such as mineral dust or soot cannot be detected. Electron impact ionization of the resulting vapor is widely used in mass spectrometric techniques and fairly well characterized. AMS spectra can be calibrated to provide quantitative loadings for volatile particle components (Canagaratna et al., 2007, 2015; Zhang et al., 2011; Jimenez et al., 2003). AMS is predominantly used for characterization of organic, sulfate and nitrate or chloride ions. It is field deployable and has been used all over the world to provide insights into atmospheric aerosol composition and transformations (Jimenez et al., 2009).

1.3.2 Laser desorption/ionization mass spectrometry

Aerosol particles can also be ionized using intense laser pulses. There are several established laser desorption/ionization mass spectrometers in use today, both custom and commercial (Thomson et al., 2000; Gard et al., 1997; Brands et al., 2011; Zelenyuk and Imre, 2005; Gemayel et al., 2016). In this instrument class, just like in the AMS, the particles are introduced into a vacuum region (10^{-5} Torr) using an aerodynamic lens inlet (Zhang et al., 2002, 2004). The particle transit time is also measured in order to derive their aerodynamic diameter, but the start and end is now defined by scattering events as particles cross two continuous wave (CW) lasers mounted a fixed distance away from each other. The second of those scattering events also provides a trigger for a pulsed laser, which vaporizes and ionizes the particles. A time-of-flight mass spectrometer is synchronized with the pulsed laser to provide spectra of single particles.

Wide variety of pulsed lasers can be used for desorption and ionization of atmospheric particles. Infrared pulsed CO_2 laser at 10.6 μm has been used, although the resulting ionization was reported to be difficult to control because of low threshold of plasma formation (Thomson and Murphy, 1993). Infrared lasers have, however, found their application as a component of a two-step desorption/ionization scheme,

in which one laser (infrared) is used for vaporization of particle components and another (UV) is used for ionization (Morrical et al., 1998; Zelenyuk et al., 1999). There is evidence that this scheme can increase the shot-to-shot reproducibility of the mass spectra significantly (Zelenyuk et al., 1999). Visible pulsed lasers at high fluence ($\sim 10^{10}$ Wcm^{-2} Q-switched Nd:YAG at 523 nm) have also been used for aerosol desorption/ionization (Reents and Schabel, 2001). However, UV lasers have found the most widespread use for aerosol ionization because they have been found to consistently ionize nearly all atmospherically-relevant chemical components at lower power densities than their visible counterparts (Thomson and Murphy, 1993; Thomson et al., 1997).

Because of the size of commercially available UV lasers, realistic choices (i.e. lasers that have commercial versions small enough to be flown on aircraft) include excimer lasers and frequency-quadrupled Nd:YAG lasers. The wavelength of the latter choice is 266 nm. The former laser can operate at different wavelengths depending on the gas lasing medium used (157 nm, 193 nm, 248 nm, 282 nm, 308 nm and 351 nm are common). Out of these wavelengths, it is advantageous to select the shortest wavelength because it allows ionization of all atmospherically-relevant substances (Thomson and Murphy, 1993; Thomson et al., 1997). However, the shortest wavelength is difficult to work with because it is strongly absorbed by air and tends to degrade optics rapidly. A subset of laser desorption/ionization mass spectrometers uses the 193 nm excimer laser as a simpler alternative. It can also ionize all atmospherically-relevant chemical constituents with the exception of very pure sulfuric acid and silicon dioxide (Thomson et al., 1997; Middlebrook et al., 1997). The 266 nm Nd:YAG does not easily ionize sulfuric acid (Thomson et al., 1997); however, it is simpler to deploy, as it does not require a gas lasing medium. Additionally, an Nd:YAG laser has a near-Gaussian beam spot, while the excimer can produce highly irregular beam profiles. The irregularity of the beam spot leads to less reproducibility of single particle spectra.

The choice of the ionization laser has an important consequence for design of laser desorption/ionization instruments. A particle scattering event at the CW sizing laser beam triggers the UV laser to fire a pulse. However, the delay between the trigger

event and the resulting UV pulse is different for the two commonly-used lasers: near-instantaneous for the excimer lasers and on the order of ms for the Nd:YAG lasers. Because of the rapid particle speeds in vacuum, the long delay of Nd:YAG lasers forces implementation of a timing circuit to anticipate the particle position at the laser firing time (Gard et al., 1997). In excimer-based instruments, this is not a limitation, as the laser can fire promptly. This affects the ionization efficiency of the two designs with the excimer design generally achieving a higher ionization rate (Cziczo et al., 2006).

In a laser desorption/ionization instrument, a particle beam with small divergence is essential because the beam spot of the ionization laser is much smaller than the vaporizer used in an AMS (Cziczo et al., 2006; Zelenyuk and Imre, 2005). Particle beams produced by aerodynamic lenses diverge, especially for non-spherical particles (Zhang et al., 2002, 2004). It is advantageous to make the instrument spacing as compact as possible for high particle detection efficiency and to avoid shape biases in particle detection.

A laser pulse extracts both positive and negative ions from particles. Because those contain different chemical information, it is advantageous to produce both positive and negative particle spectra, especially for the same particle. Unlike AMS, laser desorption/ionization instruments can identify both volatile and refractory components; however, quantification is complicated by the complexity of the laser desorption/ionization method. Ion signals are proportional not only to the amount of the analyte in the particle, but also to its ionization potential (Gross et al., 2000). The ionization potential for individual species can, in turn, depend on the chemical matrix, which can be variable for atmospheric particles. Semi-quantitative results are possible with careful laboratory calibration (Murphy et al., 2007; Cziczo et al., 2001; Froyd et al., 2010).

Particle Analysis by Laser Mass Spectrometry

Particle Analysis by Laser Mass Spectrometry (PALMS) is a very specific example of a laser desorption/ionization mass spectrometer for aerosol particles, especially rele-

vant to this work. Its schematic is shown in Figure C-4. It is an aircraft-deployable instrument initially described by Thomson et al. (2000) and subsequently by Cziczo et al. (2006). Currently, there are two copies of the PALMS instrument, one aircraft-deployable and the other laboratory-only. The flight copy uses a Schreiner-type isobaric inlet (Schreiner et al., 1998) and the laboratory copy uses a Liu-type aerodynamic lens (Zhang et al., 2002, 2004). The flight instrument uses a 405 nm violet laser for particle scattering and the laboratory instrument uses 532 nm Nd:YAG laser, but the inter-beam distance is the same at ~33 mm and the details of optical region construction are very similar. The ionization region is very compact: the excimer laser focus is only ~100 μm away from the triggering laser (Cziczo et al., 2006). The compact spacing of components allows ionization of over 90% of optically detected particles, but because of space constraints, it allows acquisition of only positive or negative spectrum at one time (Cziczo et al., 2006).

Because PALMS is designed for autonomous aircraft operation, it maintains optical alignment automatically, using a knife-edge profiler and motorized mirror mounts. The profiler measures the positions and widths of both the triggering and ionizing lasers at the source region with ~1 μm precision and the beams can be re-aligned automatically using motorized mirror mounts.

In the PALMS ionization region, an elliptical mirror collects light scattered by the particles from the CW triggering laser and reflects it onto a PMT surface (angles of about 20° to 160°) (Murphy and Thomson, 1995). Mass spectrometer backing plate with a central grid (to allow light transmission) is placed in front of the PMT (Murphy and Thomson, 1995). To acquire a single particle mass spectrum, voltages are applied to this backing plate as well as the elliptical mirror, which also acts as the ion extraction plate (Murphy and Thomson, 1995; Thomson et al., 2000). This provides a very compact design for the source region, but allows ion movement in only one direction (the other is blocked by the PMT) and therefore unipolar operation (Murphy and Thomson, 1995). After the ion source, there is an Einzel lens and a low voltage steering lens (Thomson et al., 2000; Murphy et al., 1998). The total drift tube length is 135 cm and it includes a reflectron (17 cm long, 14° angle between entrance and

exit beams) (Murphy et al., 1998). The flight instrument includes an additional 90° turn when ions come out of the source region for a more compact design. The ion detector is a multichannel plate (MCP).

PALMS can be deployed on the WB-57 and DC-8 aircraft. In addition, it can also be deployed at fields sites, such as Storm Peak Lab (DeMott et al., 2003). It has participated in a numerous field campaigns since the late 1990s. Among the most salient science results are measurements of meteoric material in the stratosphere (Cziczo et al., 2001; Murphy et al., 1998), in-situ characterization of ice residuals for anvil and sub-visible cirrus clouds (Cziczo et al., 2013; Froyd et al., 2010; Cziczo and Froyd, 2014; Cziczo et al., 2004), laboratory characterization of ice residuals in conjunction with cloud chambers (Cziczo et al., 2003; DeMott et al., 2003; Gallavardin et al., 2008), characterization of stratospheric aerosol (Murphy et al., 2014; Yu et al., 2016), measurements of atmospheric organosulfates (Froyd et al., 2010; Liao et al., 2015) and measurements of atmospheric lead (Murphy et al., 2007; Cziczo et al., 2009).

Current technology challenges

Laser desorption/ionization produces difficult to interpret mass spectra that contain both atomic ions and molecular clusters. The interpretation relies on comparisons to laboratory standards, but this can become very complicated for complex atmospheric particles that often do not have good laboratory analogues (biomass burning or complex marine particles). The degree of spectral fragmentation is dependent on the laser power and wavelength used (Silva and Prather, 2000; Reents and Schabel, 2001) and specific patterns are difficult to predict because of the poorly understood nature of laser ionization. This also complicates comparison of Nd:YAG and excimer-based instruments. As discussed above, laser desorption/ionization mass spectra are only semi-quantitative even with laboratory calibration (Murphy et al., 2007; Cziczo et al., 2001; Froyd et al., 2010) due to matrix effects that are also poorly understood.

Some hardware improvements can be unertaken to increase spectral reproducibility of laser ionization, which helps with spectral interpretation. For example, two-step laser desorption/ionization has been demonstrated to increase shot-to-shot re-

producibility of the mass spectra (Zelenyuk et al., 1999). However, addition of an extra laser increases the total size, weight and power consumption of instruments that are already challenging to deploy. Currently, only one custom instrument uses an integrated IR/UV laser for this purpose (Zelenyuk et al., 2015). Short of using an additional laser, achieving a top-hat laser profile by optical homogenization also helps with spectral reproducibility (Wenzel and Prather, 2004). Homogenizers have not been implemented on excimer lasers yet, as short wavelength of those lasers complicates the technology, but such solutions exist (Nikolajeff et al., 1997). Novel data analysis techniques and laboratory characterization of atmospherically-relevant aerosols can also help with interpretation of mass spectra, independently of hardware difficulties.

Additionally, size and weight of most laser desorption/ionization mass spectrometers in existence today limits deployment platform options. PALMS is the only laser desorption/ionization instrument capable of autonomous aircraft deployment (Thomson et al., 2000) and it has the longest airborne deployment history. It is however, limited to two aircraft, WB-57 and DC-8. Other instruments of this type have been deployed on C-130 (Pratt et al., 2009) and Gulfstream-1 (Creamean et al., 2013) aircraft. The instruments can also be deployed on mountaintop observatories (DeMott et al., 2003). With increased use of smaller manned and unmanned platforms, miniaturization of these instruments would be highly advantageous.

1.4 This study

This study is an exploration of aspects of laser desorption/ionization mass spectrometry aimed at characterizing some recent lab-based hardware advances and improving mass spectral interpretation. The first two chapters discuss two distinct hardware improvements to the PALMS instrument: an experiment intended to extend the capabilities of current laser desorption/ionization schemes and integration of a new mass analyzer and first attempts at measuring isotopic ratios using single particle mass spectra. The following chapter discusses a commercial single particle mass

spectrometer, LAAPToF, and compares its performance to PALMS. Finally, the last two chapters explore data processing and new information that can be extracted from SPMS mass spectra independently of hardware.

Chapter "Single Particle Time-of-Flight Mass Spectrometry Utilizing a Femtosecond Desorption and Ionization Laser" describes an experiment carried out at the Karlsruhe Institute of Technology (KIT), where the PALMS instrument was coupled to an ultrafast laser to experimentally demonstrate a possibility of using femtosecond pulses for single particle one-step desorption and ionization. A surprising conclusion of this experiment was that the mass spectra were not fundamentally different and that more powerful laser pulses did not allow for quantitative analysis of particle components.

Chapter "Measuring isotopic ratios using single particle mass spectrometry" describes laboratory results of integration of next generation time-of-flight mass spectrometer (the sTOF) into the PALMS. An appreciable improvement in resolution over the conventional PALMS relfectron-TOF is found and the feasibility of using these data to derive isotopic ratios is explored. This represents an important step towards further improvement and miniaturization of the PALMS instrument.

In keeping with discussion of hardware improvements, chapter "Quantifying and improving the performance of the Laser Ablation Aerosol Particle Time of Flight Mass Spectrometer (LAAPToF) instrument" focuses on performance assessment and improvements of the first commercial single particle laser desorption/ionization design, Aerodyne/AeroMegt Laser Ablation Aerosol Particle Time-of-Flight Mass Spectrometer (LAAPToF). The instrument was initially found to have insufficient optical particle detection efficiency for ambient measurements. A solution for improvement of the optical detection efficiency was implemented, resulting in an improvement of two orders of magnitude. Further advantages and limitations of the instrument and comparison to existing technology are discussed.

Chapter "Improved identification of primary biological aerosol particles using single particle mass spectrometry" presents a new method of differentiating bioaerosol from mineral dust using mass spectra collected by PALMS. A spectral library includ-

ing exemplary spectra of bioaerosol, phosphate-rich mineral dust, natural dust samples, fly ash and agricultural dust is used to derive a binary classifier for bioaerosol. The method is then validated with some previous PALMS field deployments. This represents an important advance in using single particle mass spectra.

The last chapter, "Measurement and modeling of the vertical and seasonal abundance of bioaerosol" extends the previous chapter into quantification of bioaerosol concentrations from previous PALMS airborne field deployments to report comprehensive vertical profiles of bioaerosol. The PALMS bioaerosol concentrations are also compared with results obtained with a particle fluorescence monitor and concentrations predicted from an aerosol microphysics model.

Chapter 2

Single Particle Time-of-Flight Mass Spectrometry Utilizing a Femtosecond Desorption and Ionization Laser

Single particle time of flight mass spectrometry has now been used since the 1990's to determine particle-to-particle variability and internal mixing state. Instruments commonly use 193 nm excimer or 266 nm frequency quadrupled Nd:YAG lasers to ablate and ionize particles in a single step. We describe the use of a femtosecond laser system (800 nm wavelength, 100 fs pulse duration) in combination with an existing single particle time-of-flight mass spectrometer. The goal of this project was to determine the suitability of a femtosecond laser for single particle studies via direct comparison to the excimer laser (193 nm wavelength, 10 ns pulse duration) usually used with the instrument. Laser power, frequency and polarization were varied to determine the effect on mass spectra. Atmospherically relevant materials that are often used in laboratory studies, ammonium nitrate and sodium chloride, were used for the aerosol. The detection of trace amounts of a heavy metal, lead, in an ammonium nitrate matrix was also investigated. The femtosecond ionization

had a large air background not present with the 193 nm excimer and produced more multiply charged ions. Overall, we find that femtosecond laser ablation and ionization of aerosol particles is not radically different than that provided by a 193 nm excimer.

2.1 Introduction

Aerosol particles are important in the fields of atmospheric science, industrial manufacturing, human health and nanoparticle engineering. In atmospheric chemistry, they represent sites on which chemical reactions can take place, thus altering the chemical composition of the atmosphere (George and Abbatt, 2010). In climate science they, and the clouds they spawn, are potential surfaces from which radiation can be scattered or on which it can be absorbed (Ramanathan et al., 2001). In industrial applications, particulates can represent unwanted sources of contamination that limit productivity, for example in pharmaceuticals and electronics (Cooper, 1986). In medicine, aerosol particles have been found to correlate with shorter life expectancy and ailments such as respiratory illnesses and cardiovascular disease (Dockery et al., 1993; Miller et al., 2007). In the field of nanoparticle engineering, submicron particles are fabricated for use in applications such as gas sensors or drug delivery (Panchapakesan et al., 2001; Hu et al., 2004). In all of these areas, despite the diversity of topic, the efficacy of an aerosol particle—in chemistry, in radiative transfer, as a contaminant, and in terms of health effects—depends critically on its chemical composition.

During the 1990's, the field of aerosol science underwent a significant change when single particle mass spectrometers (SPMSs) were developed by several groups almost simultaneously. These instruments have been the subject of several previous review papers (Johnston, 2000; Noble and Prather, 2000; Coe and Allan, 2006; Murphy, 2007). Among the salient advances, SPMSs allowed for analysis of small aerosol masses ($\sim 10^{-15}$ g), differentiation of internally mixed component properties from refractory (e.g. mineral dust) to volatile (e.g. sulfuric and nitric acid, organic compounds) on a particle by particle basis both in situ and in real time (Cziczo et al.,

2006).

There are several almost universal components among the few dozen SPMSs that have been custom and commercially produced (Murphy, 2007): (1) an inlet system to draw the sample into the instrument and drop pressure for subsequent analysis, most often via differential pumping, (2) a detection system, typically using photons scattered as particles pass through a continuous laser beam, (3) particle ablation and ionization, accomplished in "one step" (i.e., a single, pulsed, laser) or "two step" (i.e., separate ablation and ionization lasers) and (4) determination of chemical composition, typically via time-of-flight mass spectrometry.

The "one step" approach, where a single laser pulse both ablates the aerosol and ionizes the vaporized components (Noble and Prather, 2000; Coe and Allan, 2006; Murphy, 2007), is the most commonly used method in contemporary single particle mass spectrometry. For most field SPMS instruments, two laser wavelengths are typically used, 193 or 266 nm. UV wavelengths are preferred because they can ionize most atmospherically-relevant species (Thomson and Murphy, 1993; Thomson et al., 1997) and the lasers of both wavelengths are commercially available with low volume ($\sim$.1 m^3), mass ($\sim$10 kg) and power ($\sim$100 W). Typically, those lasers are operated at $\sim$10 ns pulse duration and 1-10 mJ pulse energy. With commonly used UV ionization lasers, the exact mechanisms of desorption and ionization of particles remain unresolved (Murphy, 2007; Carson et al., 1997a; Reinard and Johnston, 2008). Higher pulse energies can be used (10-100 mJ), even with visible wavelengths, leading to ionization via plasma formation.

Peak power density was found to be important for the degree of fragmentation observed in the mass spectra. Silva and Prather (2000) obtained organic spectra of pure PAH particles with very slight fragmentation, including the parent ion, using a 266 nm Nd:YAG laser at 10^8 W/cm^2. The 193 nm excimer laser creates significant fragmentation and some atomic high-energy ions (e.g. Na^-, Na_2^+) at a peak power density of $\sim 10^9$ W/cm^2. With reduced excimer power, there is less fragmentation and some parent ions for organic species. Reents and Schabel (2001) obtained spectra with only atomic ions and no fragments or clusters at a peak power density of 10^{10}

W/cm^2 using a 532 nm Nd:YAG laser. Similarly, Wang and Johnston (2006) use a 532 nm Nd:YAG laser with 169 mJ pulse energy and 10^{10} W/cm^2 peak power density to ionize small particles by plasma production, resulting in spectra consisting of only atomic ions, both singly and multiply charged.

Peak power density can be varied by changing the pulse energy, as in the examples provided above, or by changing the pulse duration. The effect of pulse duration on SPMS mass spectra has not been studied previously. Here we describe the use of a femtosecond laser (800 nm fundamental wavelength, 100 fs pulse duration) coupled to an existing SPMS, the Particle Analysis by Laser Mass Spectrometry (PALMS) instrument (Cziczo et al., 2006).

In addition to providing insight into the effect of pulse duration on single particle ionization, using femtosecond pulses can provide additional analytical advantages for SPMS. When femtosecond laser pulses interact with matter, nonlinear optical effects can arise. These effects have been used in many fields including, but not limited to, atomic scale resolution in tunneling microscopy (Tersoff and Hamann, 1985), high harmonic generation (Schafer and Kulander, 1997), chemical dynamics studies using fast spectroscopic techniques (Shim and Mathies, 2008) and surface probing using second harmonic generation (Petersen and Saykally, 2006; Abdelmonem et al., 2015).

Femtosecond lasers have been successfully used in laser ablation mass spectrometry of solid samples (Margetic et al., 2003; Hergenröder et al., 2006). It has been shown that using low-fluence femtosecond pulses to ablate solid samples in vacuum allows evaporation from very localized sites, as little as a few nanometers across, thereby enabling high-resolution depth profiling of layered samples (Margetic et al., 2003). Femtosecond ablation and ionization of dried organic solutions on substrates has been found to lead to a complete fragmentation of the sample, producing only atomic ions, in contrast to nanosecond ablation and ionization, which produces fragment ions and clusters (Kurata-Nishimura et al., 2002; Kato et al., 2007). This complete ionization occurs because of plasma formation as a result of the intense laser pulse (Kurata-Nishimura et al., 2002).

In organic vapors, in contrast to solid targets, femtosecond ionization can reduce

fragmentation, thus making the identification of mass spectral peaks simpler (Nakashima and Yatsuhashi, 2007; Liu et al., 2010). In contrast to nano- and pico-second pulses, a femtosecond pulse is able to bypass dissociation channels during the excitation processes (Nakashima and Yatsuhashi, 2007). Saturation ionization, a condition when all molecules present in the laser focus have been ionized, can occur for organic molecules irradiated with femtosecond laser pulses, which makes the technique highly sensitive and quantitative (Liu et al., 2010; Hankin et al., 2000). Laser intensity, wavelength and polarization have all been found to influence the fragmentation of organic molecules (Nakashima and Yatsuhashi, 2007; Itakura et al., 2001). Studies of ionization of vapors and gases are likely not directly applicable to ionization of bulk samples or small particles *in vacuo* because of different physics involved in the processes.

The experiment described here aims to demonstrate feasibility of combining a femtosecond laser with existing SPMS technology and investigate the amount of fragmentation resulting from ionization with shorter pulses. Answering these questions will provide insight into feasibility of using a femtosecond laser as a depth profiling tool for atmospheric aerosol.

We describe experiments on the effect of laser power, wavelength, pulse length and polarization variation on mass spectra. Atmospherically relevant materials, ammonium nitrate (NH_4NO_3) and sodium chloride (NaCl), the former with and without a trace metal, lead, were used for the aerosol and compared to spectra obtained using the traditional PALMS with an excimer laser (193 nm wavelength, $\sim$10 ns pulse duration).

2.2 Experimental Methods

The PALMS instrument focuses incoming particles using an aerodynamic inlet (Schreiner et al., 1998, 1999; Wang et al., 2005) and a set of differential pumping stages. A full description of PALMS is provided in Cziczo et al. (2006) In brief, particle detection and aerodynamic sizing occurs as particles pass through two 532 nm frequency dou-

bled Nd:YAG laser beams (PALMS sizing laser in Figure C-5) and scatter light. The beams are set a known distance apart, 34 mm, which allows for accurate aerodynamic sizing, as the aerodynamic lens accelerates particles to a size-dependent velocity. This velocity is measured as the transit time between the laser beams and compared to calibrated values for polystyrene latex (PSL) spheres of unit density and a specific size. The 193 nm excimer laser is triggered by a scattering event detected on the second Nd:YAG laser beam and timed to strike the particle in the "one step" method that ablates and ionizes the components. The laser, a PSX-100 excimer laser (MPB Technologies) nominally delivers 5 mJ per pulse with a ~3 ns width and can operate up to 100 Hz. In practice, spectral data recording limits acquisition to ~8 Hz and the measured pulse energy delivered to the source region is 2 mJ. Depending on the polarity of extraction plates, either positive or negative ions are accelerated into a reflectron time of flight mass spectrometer where they are detected with a microchannel plate (MCP). Particle vacuum aerodynamic diameter and chemical composition are measured in situ and in real time at the single particle level. Due to highly variable ionization efficiencies and matrix effects of common atmospheric materials and mixtures, SPMSs such as PALMS are not normally considered quantitative without calibration (Cziczo et al., 2001) although trends in ion signal have been used as an indication of relative abundance (Murphy, 2007; Spencer and Prather, 2006).

For this study, PALMS was modified by decoupling the excimer laser and replacing it with a Ti:Sapphire femtosecond laser system (Spectra Physics Solstice-100F Ultrafast Laser), hereafter termed "the femtosecond laser". The femtosecond laser has a fundamental wavelength of 800 nm, 3.5 mJ pulse energy, ~100 fs pulse width and 1 kHz repetition rate. The beam profile is close to Gaussian with beam quality factor, $M^2 < 1.3$ ($M^2 = 1$ for an ideal Gaussian beam).

Hereafter, we term the combined femtosecond laser and PALMS as "femto-PALMS". Several changes were made to the existing hardware in order to use the femtosecond laser as the PALMS ionization and ablation laser. During normal operation, the PALMS excimer laser is triggered to fire by pulses detected at a photomultiplier tube (PMT), which are produced by particles focused into the instrument by the

aerodynamic inlet which scatter light from a 532 nm sizing laser beam (PMT 1 in Figure C-5). The excimer trigger also begins the acquisition of the mass spectrum as ions are created in the PALMS ion source region. In the femto-PALMS experiment, an external triggering pulse from the femtosecond laser, coinciding with its firing, was provided to the PALMS trigger hardware to begin spectrum acquisition. This results in a significantly different mode of operation from that traditionally used for PALMS mass spectrum acquisition. Instead of a particle light scattering event starting the data acquisition process, femto-PALMS was run in a "free fire" mode where the fortuitous presence of a particle in the ionization and ablation region at the time the femtosecond laser fired resulted in mass spectral acquisition. While the trigger pulse frequency was 1 kHz in sync with the laser, the maximum PALMS data acquisition rate is limited at ~8 Hz by writing mass spectral data to the instrument computer, and this set the data acquisition rate. Concentrations in front of the PALMS inlet used in this experiment ranged from 1 to 3 $\times$ 10^4 particles/cm^3 and, with optimized optical alignment, 0.2% to 1% of acquired spectra have a signal consistent with a particle in the beam (see next sections for additional information). The hit rate is comparable to that of traditional PALMS run with the excimer laser under similar particle loading conditions.

A custom optical pathway was constructed between the femtosecond laser and PALMS. Two mirrors (M1 and M2) were mounted on the optical table, which supported the laser to redirect the beam. Two clamps were bolted between the femtosecond laser table and PALMS so that the optical path remained fixed. Lens L1, with 20 cm focal length, was used to focus the femtosecond laser beam into the PALMS ion source region at the same diameter (~250 μm) at the location of the particle beam from the aerodynamic lens as the traditional PALMS excimer laser. With the nominal pulse energy of 3.5 mJ and pulse duration of 100 fs, the peak power density of the femtosecond laser at the focus is 7 $\times$ 10^{13} W/cm^2. This is five orders of magnitude more than the peak power density produced by the excimer laser at the same focus (~9$\times$10^8 W/cm^2) although the energy densities were similar (~6 J/cm^2). The lens was mounted on an x-y-z micrometer stage to enable positioning of the

focus. This position was realigned for each experiment by optimizing particle ionization frequency. The experiments described here were carried out over the course of eight days at the Karlsruhe Institute of Technology in Karlsruhe, Germany with experiments conducted after daily realignment of the laser to maximize hit rate.

The optical path also allowed for experiments that varied the femtosecond laser wavelength, pulse stretching, polarization and power: (1) 800 and 400 nm experiments were conducted by placing a second harmonic generator (SHG) between M1 and M2, (2) three plates of glass were inserted between M1 and M2 for experiments involving spatial pulse stretching, (3) a three-mirror polarization rotator was inserted between M1 and M2 to change the femtosecond laser beam polarization by 90° and (4) M2 was replaced by beam splitters to produce pulses at 70%, 50%, and 30% of full power.

Test particles for femto-PALMS were produced by nebulizing solutions of NaCl ($\geq$ 99.5%, Merck), NH_4NO_3 ($\geq$ 99.5%, Fluka), or $Pb(NO_3)_2$ ($\geq$ 99.5%, Merck) mixed at known concentration with NH_4NO_3. Ultrapure water (18 MΩ·cm, Barnstead Nanopure Infinity, Werner Reinstwassersysteme) was used as the solvent. Particles were produced with a custom Collison atomizer and dried by passing the flow through a diffusion drier filled with silica gel (Merck). All femto-PALMS experiments were performed with 240 nm electrical mobility diameter particles (peak in number size distribution produced by atomizer) selected by a differential mobility analyzer (DMA 3081, TSI). The particles were size-selected to limit number concentrations produced by the atomizer. The number concentrations were kept at $\sim 10^4$ particles/cm^3 in order to avoid clogging the PALMS skimmers and minimize clogging of the PALMS critical orifice. Traditional PALMS spectra shown for comparison were polydisperse, produced by nebulizing solutions of NaCl ($\geq$ 99.0%, Macron) or NH_4NO_3 ($\geq$ 99.0%, Sigma-Aldrich) in Milli-Q water (18.2 MΩ·cm, Millipore, Bedford, MA). Due to the sensitivity of traditional PALMS, a medical nebulizer (Briggs Healthcare, Waukegan, IL), which produced a lower concentration of particles, was used.

2.3 Results and Discussion

2.3.1 Instrument Background

Positive and negative polarity spectra were acquired for NH_4NO_3 and NaCl particles with both traditional PALMS and femto-PALMS. Results are detailed in the following sections. For both particle types, positive femto-PALMS spectra, such as those shown in Figure C-6 for NH_4NO_3, exhibit a background larger than that observed for PALMS (note that the background is marked with a hatch pattern in Figure C-6). In cases where the ionization region does not contain an aerosol particle, both the excimer and femtosecond lasers still created ions, which constitute this background.

The abundance of air background ions was maximized by moving the laser focus inside the ionization region, which is also consistent with air beam ionization. An example of a femto-PALMS air beam background (i.e., a spectrum devoid of features attributable to a particle) is shown in Figure C-7. It contains both singly and multiply charged ions. The presence of singly (N^+, O^+) and multiply charged (O^{++}, N^{++}) ions in the background could suggest plasma formation at the focus. Note that a laser focus alignment that maximized the production of background ions did not coincide with high particle hit rates. In traditional PALMS excimer ionization a background is also present, but it is primarily organic in nature. In both cases, the mass scales of background spectra match the mass scales of particle spectra, suggesting that the background ions are created at the usual ion extraction point and do not result from surface reflections inside the ionization region. In traditional PALMS, the organic background accounts for 0.3 - 1% of the total positive ion current, measured as mA at the MCP.

For femto-PALMS the air background accounts for 30 - 60% of the positive ion current, on average. Background ions were not observed with either laser in negative polarity. The background signal was found to be a secondary indication of the quality of laser alignment and the experiments reported here are only those with minimized background and maximized particle hit rate. With this restriction, 221 particle spectra for NaCl, 413 for NH_4NO_3 and 190 for NH_4NO_3 doped with Pb form the basis of

this discussion.

2.3.2 NH_4NO_3 Aerosol Particles

NH_4NO_3 mass spectra obtained with femto-PALMS at two wavelengths–the 800 nm fundamental and 400 nm second harmonic–are shown in Figure C-6. Mass assignment in femto-PALMS spectra required refitting the mass scale because the position of the femtosecond laser focus was not exactly matched to the position of the excimer beam focus. An initial observation is that the spectra generated are similar, despite the different laser pulse durations, powers and wavelengths. The most obvious differences are a lack of a strong NO_2^+ peak in femto-PALMS spectra, which is present in PALMS, and the presence of N^+ and $NO_3HNO_3^-$ in the femto-PALMS spectra, but not PALMS. As a whole, these are minimal differences and imply similar ionization processes despite the different lasers.

As noted in the previous section, the interpretation of positive femto-PALMS spectra is complicated by the presence of the air background. A typical background spectrum for both laser wavelengths is plotted over the positive femto-PALMS spectra and highlighted with a hatch pattern. The ions that are not found in the background or enhanced by the presence of NH_4NO_3 particles, are +14, +15, +16, +17, +23, +35 and +30, corresponding to N^+, NH^+, O^+, OH^+, Na^+, Cl^+ and NO^+ (labeled in bold type in Figure C-6). Sodium and chlorine ions are present due to trace amounts, which remained in the aerosol generation system between experiments.

Femto-PALMS spectra of NH_4NO_3 tend to be lower in total signal than those taken with the excimer laser. Total ion currents for positive and negative spectra were measured and are discussed in the following section.

Peak shapes in femto-PALMS and PALMS are alike and this, with the similarity in ions generated, further suggests comparable ionization processes. Typical peak shapes of PALMS and femto-PALMS are shown in Figure C-8. Note the similarity in Na^+ peak shapes in the top panel. One exception is that some of the peaks in femto-PALMS spectra have a low mass "shoulder" (e.g., NO_2^- and NO_3^- in Figure C-6 and $^{35}Cl^+$ and $^{37}Cl^+$ in the bottom panel of Figure C-8), an effect infrequent for PALMS.

The shoulders could be due to either a very energetic ion formation mechanism, space charge effects in the ion source, or unimolecular decomposition of ions within the ion source or possibly the reflectron. We do not believe there is enough information to determine the exact mechanism at this time.

Laser Power Variation

Spectra of NH_4NO_3 were taken at four average laser powers and the generated ion current for each experiment is summarized in Figure C-9. The average power of the femtosecond laser was reduced to 70%, 50% and 30% of full by attenuating the beam with three beam splitters. The average laser power at each attenuation was measured after propagation through the focusing lens (L1 in Figure C-5) with a power meter. Values between 2.99 W (for no attenuation) and 0.53 W (for 70% attenuation) were measured. Pulse energies, shown on the x-axis of Figure C-9, were obtained by dividing the measured average laser power by the laser repetition rate of 1 kHz. Using a pulse duration of 100 fs, those pulse energies corresponded roughly to peak power densities between 1 and 6 $\times$ 10^{13} W/cm^2 at the laser focus in the source region. The ion currents recorded at the MCP for the different pulse energies are given for positive and negative spectra on the left and right y-axes in Figure C-9, respectively. At reduced pulse energies ions remained the same as those given in Figure C-6 but with reduced signal.

Negative ion current was, on average, an order of magnitude lower than positive ion current. Partially, this is accounted for by the background generated in positive spectra. For most points shown in Figure C-9 (with the exception of those at 2.83 mJ), the background ion current was 60% of the total positive ion current. This is significant but does not fully explain the difference of an order of magnitude between positive and negative, implying a higher average signal, regardless of background, in positive mode. For comparison, Figure C-9 provides ion current for NH_4NO_3 from traditional PALMS. The total positive ion current in PALMS is 2.4 times larger than negative, which is accounted for by the electrons extracted during the ionization process that are not measured by PALMS.

Excimer laser ionization has a power density threshold for ion production, which varies for particle composition and laser wavelength (Thomson and Murphy, 1993). Thresholds for ion production have previously been studied for the PALMS 193 nm excimer laser by Thomson and Murphy (1993) and Thomson et al. (1997). At power densities higher than the threshold, the ion yield is not typically linear with increasing power density (Thomson et al., 1997). Thomson et al. (1997) measured the ion production threshold for NH_4NO_3 ionized with the 193 nm excimer laser to be 5.6×10^6 W/cm^2 for positive ions and 5.3×10^6 W/cm^2 for negative ions. In the femto-PALMS dataset presented in Figure C-9, no clear threshold is present. This indicates that the threshold, if present, is lower than 1×10^{13} W/cm^2 since both positive and negative ions are still produced at 0.5 mJ. Because the ion production as a function of power density is expected to be nonlinear, the threshold cannot be deduced by a simple linear fit through the data.

In Figure C-9, error bars in femto-PALMS and PALMS data represent the range of ion currents generated by different particles and are of the same order. Differences in the PALMS data can be attributed to excimer shot-to-shot energy variability and to the non-constant position of particles within the profile of the laser beam. The latter is a particular challenge for the excimer laser because the beam is not Gaussian and local "hot spots" are possible (Murphy, 2007). The femtosecond laser beam is closer to Gaussian and there should be less spatial variability. Improvement in the beam quality of the femtosecond laser is apparently offset by alignment fluctuations and/or the particle position within the Gaussian profile of the beam. As an example, the data taken at 2.83 and 2.99 mJ were taken on different days and highlight this variability. For the point at 2.83 mJ, the background accounted for 30% of the total ion current in positive polarity whereas it represented 60% during the 2.99 mJ experiments. We suggest future experiments need to consider the reproducibility of the femtosecond laser alignment to minimize day-to-day variability.

The femtosecond pulses were dispersively broadened by 4% in one experiment. The ion current is reported in Figure C-9 and no differences in the kinds of ions produced were found.

Laser Wavelength Variation

Wavelength has been found to be an important consideration for the ion production threshold when considering traditional SPMSs. For atmospherically-relevant species, 193 nm excimer ionization thresholds are lower than those for longer wavelengths, such as a 266 nm Nd:YAG laser (Murphy, 2007; Thomson et al., 1997).

Spectra of NH_4NO_3 were obtained with the femtosecond laser frequency-doubled to 400 nm (Figure C-9). Examples of spectra generated are also shown in FigureC-6. Changes in the spectra with wavelength were small. The air background at 400 nm is lower in intensity although this may correlate with the lower power inherent in second harmonic generation (the average power of the 400nm beam used for these experiments was 0.79 W). Differences in the relative intensities of peaks such as NO^+ compared to NO_2^+ were smaller on average between 400 and 800 nm than the shot-to-shot variability at either wavelength.

2.3.3 NaCl Aerosol Particles

Femto-PALMS and PALMS spectra of NaCl aerosol particles are compared in Figure C-10. The femto-PALMS spectra in Figure C-10 were taken at 2.86 W average power and 800 nm wavelength. The significant difference between PALMS and femto-PALMS spectra is the presence of Cl^+ ions at +35 and +37. Those ions do not appear in any positive PALMS NaCl spectrum taken for this work or previously. Cl^+ ions require high energies to produce since the first ionization potential of chlorine is 13 eV (whereas the first ionization potential of sodium is 5.1 eV). In femto-PALMS, Cl^+ ions are present in 50% of the spectra. When present, the Cl^+ peaks are large (on the order of 10-20% of the total positive ion current). Additionally, the Cl+ features are associated with the presence of wide and/or split peaks (Figure C-8), similarly to NO_2^- and NO_3^- for NH_4NO_3 in Figure C-6. These observations may be indicative of a different ionization mechanism for chlorine, or possibly two distinct mechanisms. The power density is highest at the focus of the femtosecond laser beam although particles hit when outside the focus should still experience suitable power density to

ionize most species. Less common ions may be associated with particles ablated and ionized at or nearer the beam focus (i.e., peak power). Another noteworthy difference is that femto-PALMS spectra do not exhibit high mass ions at the same frequency as PALMS spectra. For example, the $Na_4Cl_3^+$ and $Na_3Cl_4^-$ ions are generated in 40% of the PALMS spectra, but only 1% of femto-PALMS spectra. This is also consistent with harder ionization in femto-PALMS.

As in the case of NH_4NO_3, femto-PALMS fragmentation patterns for NaCl are similar to fragmentation patterns of traditional PALMS with an excimer laser. Femto-PALMS spectra are, however, unlike spectra acquired with higher energy nanosecond pulses reported previously in literature. For example, Reents and Ge (2000) obtained positive NaCl spectra with a Nd:YAG laser operated simultaneously at 532 and 1064 nm and 300 mJ pulse energy. The Reents and Ge spectra consisted only of atomic ions (Na^+, C^+) and their doubly charged equivalents. Reents and Schabel (2001), using a 532 nm Nd:YAG at 93 mJ pulse energy, obtained similar spectra to Reents and Ge (2000). Peak power densities in those experiments were 1×10^{10} W/cm^2, between that of PALMS and femto-PALMS. The pulse energy used by Reents and Ge (2000) was larger, by two orders of magnitude, than that of PALMS or femto-PALMS. At this time, the degree of fragmentation appears related to the pulse energy, not the peak power density. The reason is unclear, although it may be indicative of the criticality of alignment of the laser focus with the particle beam (i.e., the actual power density experienced by the particle).

Average total ion currents for NaCl were the same (within uncertainty) for both positive and negative spectra for PALMS and femto-PALMS. For femto-PALMS, the total positive and negative ion currents at 2.86 mJ pulse energy were $4.4 (\pm 3.4) \times 10^{12}$ and $1.2 (\pm 1.1) \times 10^{12}$ mA, respectively. For PALMS, total positive and negative ion currents were $5.8 (\pm 2.0) \times 10^{12}$ and $8.6 (\pm 6.7) \times 10^{11}$ mA, respectively. Fewer than 10 spectra were acquired at 30% power at each polarity with femto-PALMS. Allowing for the variability in alignment and particle-to-particle differences, the exact trend in ion current signal versus power remains uncertain.

The polarization of the femtosecond laser was rotated by 90°, without a change

in average power, for some NaCl experiments. No effect on the spectral appearance or the total ion current was observed. These experiments were conducted because a change in pulse polarization will change the direction of the initial kinetic energy of the ions. This does not appear to have an effect on the mass spectra.

2.3.4 Sensitivity of femto-PALMS to lead in NH_4NO_3 particles

PALMS is sensitive to trace metallic species, with one atmospherically-relevant example being lead. Murphy et al. (2007) showed that a lead concentration calibration (i.e., a PALMS sensitivity to lead) could be obtained from laboratory data in order to infer concentrations in field data. The laboratory calibration data determined by Murphy et al. (2007) are shown in Figure C-11 (open diamonds). The calibration data were repeated for this work using femto-PALMS where lead was added in known quantities to an NH_4NO_3 matrix. Solutions of lead at a range of concentrations (0.09% - 1.20% by weight) were prepared in aqueous solutions of NH_4NO_3, and then atomized, dried and analyzed with femto-PALMS. The elemental lead peaks in the mass spectra were integrated and the resulting areas were compared to the total ion current after background subtraction, the same methodology used by Murphy et al. (2007).

Both PALMS and femto-PALMS are more sensitive to lead than to NH_4NO_3, which can be inferred from the positive slopes in Figure C-11. PALMS exhibits 27 times higher sensitivity than femto-PALMS. We note that the femto-PALMS signal appears to vary significantly with laser alignment and that the point with the highest lead content (1.2%) was taken during a period of high relatively background (50%, compared to 35% for other points). Overall, the data suggest that the limit of detection of lead in femto-PALMS is between 0.09% and 0.17% dry particle lead content.

2.4 Conclusions and Future Work

A femtosecond laser was coupled to an existing SPMS and compared to traditional excimer laser 1-step ablation and ionization. The lasers considered in this work, a

193 nm excimer laser and a 800nm/400nm femtosecond laser, have similar pulse energies, 2-4 mJ. They differ significantly, however, in wavelength, pulse duration and peak power. The femtosecond laser experiments had five order of magnitude greater power density and yet produced similar fragmentation patterns. Mass spectra of NH_4NO_3 and NaCl were similar for PALMS and femto-PALMS with the exception of N^+, O_2^+ and Cl^+ ions, which are not normally produced with a 193 nm excimer, and the NO_2^+ ion which is present only in PALMS spectra. The production of the high energy atomic ions suggests that there are some differences in ionization mechanisms, especially noteworthy in the case of Cl^+ production. Having considered only two relatively simple particle types here, we note that future work may find more significant differences if more complex particles (e.g. mixed organics and inorganics) are considered.

The high energy ions (Cl^+, N^+) evident in femto-PALMS are similar to spectra obtained with higher pulse energy (100 mJ) ionization lasers that produce ions through plasma formation, such as that used by Wang and Johnston (2006). At this time it is unclear why the pulse energy, and not the peak power density, appears to correlate with the fragmentation. Simulations Zhou et al. (2007) show that in plasma-formation regime, ablation and ionization is complete before the ionizing pulse reaches its peak intensity, which suggests that pulse length plays a limited role in the ionization process. However, ion clusters (e.g. NO^+, Na_2Cl^+) present in femto-PALMS spectra point to a more complex ionization mechanism than only plasma formation and the Zhou et al. (2007) results should be applied with caution. In order to experimentally investigate this correlation, pulse energy should be varied over a large range (1-100 mJ) under the same pulse duration and wavelength conditions.

Femto-PALMS was found to produce background ions consistent with ionization of the air beam. The air background consisted of atomic ions, both singly and multiply charged, which is similar to the background described by Wang and Johnston (2006) for a plasma ionization technique. Wang and Johnston (2006) found that the background signal was higher when a particle was present in the beam than in the absence of a particle, suggesting that plasma electrons play a role in background ion-

ization. No such effect was found here. Characterizing this air beam background with a closed and/or filtered inlet (i.e., when no particles are present) is suggested as an area of future interest.

Ionization laser wavelength has been shown to be an important consideration related to the ionization onset when considering UV lasers (Thomson and Murphy, 1993). Power densities used in this experiment were, in all cases, above the ionization threshold for NaCl and NH_4NO_3 despite the longer femtosecond laser wavelength. Dispersive broadening of the pulses and polarization of the femtosecond laser did not produce a significant change in the mass spectra or ion current. We suggest the effect of pulse broadening and circular and elliptical polarization as areas for future study. Additionally, using lower laser power densities or aerosols that are harder to ionize (e.g. sulfates) would enable determination of ionization threshold and comparison across ionization wavelengths.

Quantification of the femto-PALMS sensitivity to lead in a NH_4NO_3 matrix showed a lower sensitivity when compared to PALMS. Sensitivity to other heavy metals in other matrixes represents an area of interest in future experiments.

Femtosecond laser ablation has been successfully used for depth profiling of layered samples because it ablates small quantities of material from localized spots (Margetic et al., 2003; Hergenröder et al., 2006). Surface sensitivity and the potential for depth profiling of aerosol particles was not studied in this experiment. If this could be translated to depth-profiling of single aerosol particles it would represent a useful tool. For example, it could represent a means to study the morphology of phase-separated aerosols which are known to occur in many mixed organic-inorganic aerosols (Zawadowicz et al., 2015). In order to investigate this, a method to reproducibly align the femtosecond laser focus relative to the particle beam must first be developed.

2.5 Acknowledgements

This research was supported by NSF Grant 023693-001, MIT and KIT internal funding. D. J. C. acknowledges the support of the Victor P. Starr Career Development

Chair at MIT. M. A. Z. acknowledges the support of a NASA Earth and Space Science Fellowship.

This chapter has been previously published: Zawadowicz, M. A., Abdelmonem, A., Mohr, C., Saathoff, H., Froyd, K. D., Murphy, D. M., Leisner, T., Cziczo, D. J.: Single Particle Time of Flight Mass Spectrometry Utilizing a Femtosecond Desorption and Ionization Laser, Anal. Chem., 87, 12221-12229, 2015.
doi: 10.1021/acs.analchem.5b03158.

Chapter 3

Measuring isotopic ratios using single particle mass spectrometry

3.1 Introduction

Single particle mass spectrometers (SPMSs) are instruments that characterize chemical composition of single atmospheric aerosol particles in situ and in real time. There is a considerable interest in the chemistry of aerosol particles because they have been shown to affect climate both directly by scattering incoming radiation in the stratosphere and indirectly by providing nucleation sites for clouds to form (Boucher et al., 2013). Aerosol chemical composition, which also determines both optical and surface properties, is important to fully describe the effect of aerosol particles on climate in models (Boucher et al., 2013). Beyond climate, aerosols are also important in atmospheric chemistry, as they can provide sites for heterogenous chemistry (George and Abbatt, 2010; Solomon et al., 2016), and in particulate matter epidemiology studies, as aerosol particles can be hazardous to human health (Miller et al., 2007). SPMS can provide accurate aerosol particle chemistry in all those applications (Cziczo et al., 2013).

One distinct type of SPMS techniques uses short pulses of intense laser radiation to desorb and ionize particles in a single step. Particle Analysis by Laser Mass Spectrometery (PALMS), the instrument used in this study, uses ~10 ns pulses of

193 nm excimer laser to vaporize and ionize aerosol particles, which are then analyzed with a time of flight (TOF) mass spectrometer. The UV laser ionization produces atomic ions and ionized molecular fragments with a wide initial energy distribution. Differences in the initial kinetic energy of the ions affect their TOF flight times, producing broad peaks at the detector and decreasing the spectral resolution. A solution to this problem that has been widely used in single particle mass spectrometry is the reflectron-TOF (Figure C-12), which introduces an "ion mirror" that curves the ion paths. More energetic ions penetrate the reflectron further before they can be turned and thus experience longer total flight path. This compensates for the broad initial energy distribution.

Versions of the reflectron-TOF design are implemented on all SPMS designs in use today (Cziczo et al., 2006; Pratt et al., 2009; Zelenyuk and Imre, 2005; Gemayel et al., 2016; Brands et al., 2011). However, there now exists an alternative to this geometry recently described and prototyped by Murphy (2017). The sTOF geometry shown in Figure C-12 consists of two electrical sectors arranged in an s-shape. The sectors perform a similar function to the reflectron: ions with higher kinetic energies take a longer path though the sectors for improved resolution. A pair of sectors provides more compensation for an increased resolution over the standard reflectron design and the sectors do not require grids, which minimizes ion losses inside sectors. Using electrical sectors has additional advantages of making the mass analyzer less sensitive to varying initial ion positions and angles and making the design fit into a more compact space (Murphy, 2017). The prototype sTOF design provides a significant resolution improvement over the existing PALMS reflectron-TOF (Murphy, 2017).

This work aims at characterizing the performance of the sTOF analyzer on the laboratory PALMS set-up. In particular, a variety of laboratory-generated aerosol is analyzed under different instrumental conditions. Because of better mass resolution, it might be possible to use the sTOF analyzer to measure isotopic ratios for single aerosol particles or particle ensembles. Such measurements are useful for characterization of geological particle sources. Moreover, isotopic ratios provide a performance metric for the instrument as they are easily referenced to known values. This work discusses

the feasibility of measuring isotopic ratios with PALMS and explores some factors that limit the precision with which they can be reported.

3.2 Experimental

3.2.1 Particle Analysis by Laser Mass Spectrometry (PALMS)

The laboratory version of PALMS was used in this study. PALMS has been described previously (Thomson et al., 2000; Cziczo et al., 2006). Briefly, the instrument uses a Liu-type aerodynamic lens to introduce the particles into the vacuum region ($\sim 10^{-5}$ Torr), collimate them into a narrow ($\sim$1 mm) beam and impart them with a size-dependent velocity distribution. Two 532 nm Nd:YAG laser beams measure particle transit times that can then be correlated with vacuum aerodynamic diameter. Particle transit through the second 532 nm laser beam triggers a 193 nm excimer to fire a pulse that vaporizes and ionizes the particle. Simultaneously with the excimer laser firing, voltages are applied to the source region ion optics and to the mass analyzer in order to acquire mass spectra. One difference between the previously described versions of the instrument and one used in this work is a new excimer laser: the PSX-100 (MPB Technologies, Pointe-Claire, Quebec) laser was replaced with Ximer-300 (MPB Technologies, Pointe-Claire, Quebec), a new laser by the same manufacturer with the same wavelength and pulse length, but a higher maximum power, frequency and better shot-to-shot reproducibility.

3.2.2 sTOF, the new PALMS mass analyzer

The PALMS reflectron was designed in the early 1990s and has not improved radically since (Thomson et al., 2000; Murphy et al., 1998). The mass analyzer was replaced completely by the prototype sTOF described by Murphy (2017), which has two coupled (22 mm apart) cylindrical 255° sectors (Figure C-12) with 165 mm radius. There are straight drift tubes at the input and output of the sectors, whose total length is equal to $\pi r\sqrt{2}$ (r = sector radius) and grounded plates above and below the sectors

(17.2 mm separation on top and bottom) (Murphy, 2017). Different sector voltages between 500 V and 700 V were tested in the laboratory set-up, but not much difference in transmission or resolution was found. For majority of the experiments, the sectors were operated with unbalanced voltages 570 V/-670 V in positive ion mode and -570 V/670 V in the negative ion mode. As discussed by Murphy (2017), this allows for additional y-direction focusing of the ions. The voltages in the source were 4 kV (backing) and 1 kV (mirror) and the voltage on the Einzel lens at the source exit was -3 kV. As shown in Figure C-12, the sTOF also has an Einzel lens at the entrance; this lens was operated at -2 kV.

The laboratory PALMS is built around an optical breadboard and its spatial layout does not have a lot of flexibility. While the total weight and size of the sTOF is lower than the original reflectron-TOF, it was mounted inside a large stainless steel can for prototyping purposes, which could not be accommodated easily. As a result, the sTOF was installed far away (>25 cm) from the ion source region. This allows the ion beam to diverge before it enters the sTOF and therefore limits the resolution that could be achieved with this prototype set-up. Some compensation was provided by mounting the MCP detector on stand-offs, closer to the sTOF exit slit.

3.2.3 Lab test aerosol

Various atmospherically-relevant aerosol particles were generated for analysis with the sTOF, along with some more exotic particle types that were of interest for isotopic analysis. Table B.1 provides an overview of the test aerosol. Dry generated aerosol samples were either mechanically generated with a shaker used at low speed or manual shaking of a small test vial. Wet-generated samples were either atomized using disposable medical nebulizers (Briggs Healthcare, Waukegan, IL) to prevent cross-contamination or generated with a bubbler (these experiments were aimed specifically at reproducing marine sea spray aerosol). Dry-generated aerosols were not size-selected. The synthetic sea water aerosols produced with the bubbler were size-selected at 200 nm and 600 nm.

Elemental sulfur aerosol was generated as a part of a study on photooxidation

of carbonyl sulfide (COS). A mixture of N_2 and COS containing 5000 ppm COS was flown through a glass photochemical cell at 100 mL/min. A UV lamp provided the light source. The product of COS photooxidation is S_8, elemental sulfur, which nucleates into an aerosol phase. PALMS was used to sample from the photochemical cell, but the flow was first passed through a DMA (Brechtel, Hayward, CA) for both size selection and to limit the high particle loadings produced in this experiment. When scanned with the DMA, particle size distribution showed a peak at 300 nm.

3.2.4 Ambient measurements

PALMS with the sTOF analyzer was used to sample ambient air between May 26, 2017 and June 2, 2017. A 1/4" stainless steel tube sticking out of the building wall was used as the ambient inlet. PALMS sampled the ambient air in parallel with an OPS (TSI 3000; TSI, Shoreview, MN). The inlet was placed at the 13th floor level in the MIT EAPS building, facing the city of Cambridge and the MIT campus. Local sources were urban and industrial, possibly originating from several construction projects nearby. Some marine influence is also expected. Meteorological data is available from the weather station on the building roof. Overall, 172,007 single particle spectra were acquired, 94,790 positive and 77,217 negative.

3.3 Results and Discussion

3.3.1 Comparison of sTOF and reflectron-TOF

The sTOF was found to have a higher resolution than the reflectron-TOF. Chemical effects can complicate a definite quantification of the resolution improvement, however. Figure C-13 shows a comparison of peak widths quantified as full width at half height in raw mass spectra as a function of the mass-to-charge ratio. Black carbon particles (impure, with substantial non-combusted fraction) and elemental sulfur particles (pure particles produced by photooxidation of COS) were used to plot this figure because of repeating chains of peaks that are easy to locate and assign. Black

carbon impurities are usually seen in positive spectra at low (<100) masses, which accounts for the higher resolution of the positive mode than the negative in this region (some peaks close together in low resolution spectra may not be correctly assigned by the peak-finding algorithm used here, which is different from the standard PALMS peak finding method). Nevertheless, a resolution improvement is seen with the sTOF. For example, for m/z = 228 in positive mode, the resolution is 300. For the reflectronTOF, it is 200. Better resolution is seen with pure elemental sulfur particles. When sampled with the sTOF, unit mass resolution can be seen for masses as high as m/z = 288. For m/z = 224 in positive mode, the resolution is 600. The case of elemental sulfur might be the best-case resolution that could be achieved with the prototype laboratory set-up. This is lower than the resolutions reported by Murphy (2017) for the first prototype experiment (2,000 for lead), which is probably directly attributable to the long drift length between the source region and the sTOF entrance.

Figure C-14 shows a more visual comparison of sTOF and reflectron-TOF resolutions using example spectra. Panels C-14A, C-14C and C-14E show lead example spectra. Lead is present as a trace component on many atmospheric particles previously observed with PALMS and its accurate quantification is of interest both because it is toxic and because it has been shown to lead to an inadvertent climate modification (Murphy et al., 2007; Cziczo et al., 2009). Both the sTOF and the reflectron-TOF spectra of lead in Figure C-14A are ambient atmospheric spectra particularly rich in lead, and it is clear that while the reflectron-TOF does not resolve the individual isotopes, the sTOF resolves them easily. Figure C-14C illustrates an interesting case of radiogenic lead: both spectra are of monazite-Ce laboratory sample and in this case, both ^{208}Pb and ^{206}Pb isotopes are decay products of thorium and uranium-238, respectively. Because ^{207}Pb is not present, the concentration of non-radiogenic lead (as well as uranium-235 which decays to lead-207) in this sample is probably low. Those features cannot be resolved precisely with the reflectron-TOF. Spectra in Figure C-14E are of laboratory fly ash samples (Miami F) and in addition to lead, thallium can be clearly identified in the sTOF spectra. Thallium is a rare element that its presence was suspected but not definitively confirmed in fly ash spectra until

now. A few particles with matching thallium and lead signatures were also found the the ambient sample set. Panels C-14B, C-14D and C-14F show other elements with fine isotopic structure: zirconium, tin and barium. The advantage in increased sTOF resolution is also apparent here, particularly for small isotopes of barium, which are not apparent in the reflectron-TOF spectra. Panel C-14G shows the rare earth region of monazite-Ce, where small contributions from different isotopes of neodymium and samarium can be clearly seen in the sTOF spectrum, but not in the reflectron-TOF spectrum.

3.3.2 Isotopic ratio measurements

Improved resolution of the sTOF shows promise for quantification of isotopic ratios. Developing a method to do so would be advantageous for two reasons: (1) most isotopic ratios are quite invariant and therefore it provides a useful check on the mass spectrometer biases or biases in laser extraction of ions and (2) when isotopic ratios can vary (as in the case of radiogenic lead), accurate quantification can aid in source apportionment. The laser desorption/ionization used in PALMS is very different from inductively coupled plasma ionization instruments that are usually used for high resolution isotopic analysis. It is possible that isotopic fractionation occurs during laser extraction, as it has been reported for various other ionization methods (both laser and non-laser based) (Lyon et al., 1994; Isselhardt et al., 2011). There are likely other effects that may or may not obscure any systematic ionization biases: for example, saturation of ion signals on the MCP for ions with the greatest abundance can occur even though a logarithmic amplifier is used to increase the dynamic range. Additionally, precise isotopic composition usually requires extensive sample preparation to isolate the element of interest from potential isobaric interferences (other chemical constituents that have the same m/z). For example, while ^{87}Sr is a useful radiogenic tracer, in practice it has to be chemically separated from ^{87}Rb (Deniel and Pin, 2001). Extensive sample preparation is not suitable to a fast in-situ analysis technique such as PALMS.

Figure C-15 reports measured isotopic ratios of 10 different elements (calcium,

lithium, tin, rubidium, magnesium, titanium, zirconium, barium, lead, iron and sulfur) quantified for 29 aerosol samples. In all cases, except for lead, the reported ratios are those of less abundant isotopes to the most abundant isotope (i.e. for calcium, $^{44}Ca/^{40}Ca$, $^{42}Ca/^{40}Ca$,$^{48}Ca/^{40}Ca$ and $^{43}Ca/^{40}Ca$). For lead, the ratios calculated are $^{207}Pb/^{206}Pb$ and $^{208}Pb/^{206}Pb$ for consistency with literature. Not every sample is used for every ratio, as sometimes the relevant elements are not present or fall below the detection limit. The method of extracting the ratios from ensembles of single particle mass spectra is standardized as follows: relative peak areas of isotopes of interest are first averaged for every three particle spectra. Then, a least-squares linear regression is calculated. Best-fit line slope is reported as the isotopic ratio and one sigma standard deviation is reported as the error bar. The measured isotopic ratios are compared to expected natural ratios in Figure C-15. Absent interferences and errors, the correspondence should be close to the 1:1 line through the centers of the plots.

Panels C-15A, C-15B and C-15C show the accuracy of isotopic ratio quantifications with respect to three different variables represented by color scales: excimer laser power, area of the principal peak (i.e. the most abundant isotope in all of these, except for lead, where it is defined as ^{206}Pb) and m/z of the principal peak. Some broad conclusions can be observed from Figure C-15: isotopic ratios larger than 0.1 can be quantified more accurately than isotopic ratios lower than 0.1. Isotopic ratios between 0.01 and 0.1 can be accurate in some cases, but ratios below 0.01 are probably too small to be quantified accurately. There does not seem to be a strong correlation with the laser power used for ionization (Figure C-15A). There does appear to be some correlation between the area of the principal peak and the ratio quantification accuracy, with trace materials (lead, barium, tin) showing better correlations than those that tend to be most abundant in the spectra (calcium, iron) (Figure C-15B). This is likely a consequence of principal peak saturation. The m/z of the principal peak shows some correlation, but this is probably a consequence of the fact that trace elements are heavier (Figure C-15C).

Some materials tend to be frequent outliers in these plots. For example, Welsh

C fly ash for barium, which as discussed later, is likely an isobaric interference and monazite-Ce in the case of lead, which is radiogenic (Figure C-14C).

Tin

Somewhat unexpectedly, tin provided the best accuracy for quantification of isotopic ratios (Figure C-16A). All particles used to quantify the isotopic ratios of tin were derived from ambient measurements (about 100-200 total particles). The particle chemical composition was either organic with a pronounced tin contribution or metallic also containing iron, zinc and lead. Tin is a trace element and the masses of its isotopes might not have any appreciable isobaric interferences for the particles observed here.

Zirconium

Zirconium isotopic ratios were quantified using a natural sample of zircon sand. Zirconium isotopes have similar masses to tin and as Figure C-16C suggests, quantification of isotopic ratios with a similar accuracy might be possible. Figure C-16C shows an effect of laser power: particles ionized with the highest laser power show decreased accuracy. This is expected, as with high laser fluence, resolution-limiting space charge effects can occur.

Barium

Barium isotopes were quantified using four fly ash samples (fly ash tends to be rich in barium) and two dust samples (Arizona Test Dust and a natural soil dust sample from Germany). Different chemical compositions of those particles illustrate isobaric effects. While three fly ash species (Joppa C, Clifty F and Miami F) tend to reproduce natural ratios well, Welsh C fly ash shows high discrepancies (Figure C-16B) for the $^{137}Ba/^{138}Ba$ ratio. Because those ratios are overestimated, there is a likely isobaric interference for m/z = 137. The chemical identity of this interference has not been confirmed.

When barium isotopic ratios are quantified for dusts, a surprising precision and reproducibility can be demonstrated (Figure C-16D), but they are very consistently underestimated. This also may be an isobaric effect, but in this case it would affect m/z = 138. As before, the chemical identity of the interference is still under question. However, in this specific case, the reproducibility suggests that it might be possible to correct for this interference.

Elemental sulfur

Isobaric interferences from non-sulfur chemical constituents are small or nonexistent in elemental sulfur spectra because of the pure particle composition. Interferences from other sulfur ions, such as doubly charged species, are still possible, but they were not detected in the mass spectra. Figure C-17 shows quantification accuracy for positive and negative sulfur isotopic ratios calculated here. Sulfur has three isotopes, ^{32}S, ^{33}S, ^{34}S and ^{36}S and in addition, ratios of multiple element clusters were also quantified (i.e. $^{65}S_2/^{64}S_2$,$^{98}S_3/^{96}S_3$, etc.). Natural abundances of those were approximated with the on-line Isotope Distribution Calculator from Scientific Instrument Services (SIS). As shown in Figure C-18, positive and negative sulfur spectra show clusters of sulfur atoms until S_8 (longer chains are present in the positive polarity). In order for the low fragmentation to be possible, low ionization laser powers were used with those particles (~0.1 V on the joulemeter).

Figure C-17 shows shows that particle size does not systematically affect isotopic fractionation. An effect of particle size-dependent isotopic fractionation was reported for laser ablation coupled to ICP-MS, where it was hypothesized to be related to incomplete ablation of large aerosol particles (Jackson and Günther, 2003). Because of the low laser power used in the PALMS experiments, particle desorption is probably incomplete for all sizes. Ratios reported in Figure C-17 definitely show saturation effects for S_2 in positive spectra and possibly for S in both polarities. Ratios for S_5, S_6, S_7 and S_8 can generally be quantified accurately; however, a lot of variability is present for lower-mass clusters and small (< 0.1) ratios.

3.4 Future work

The analysis presented here is very preliminary, but it does represent the first analytical use of the new sTOF mass analyzer and shows some promise for deriving isotopic ratios from PALMS spectra of single particles. Future work will be focused on understanding the effects of saturation on isotopic ratio quantifications (spectra of analytical standards of $CaSO_4$ particles with known weight percent of calcium were acquired to study this in more detail). Additionally, identification of isobaric interferences, such as the ones that can be inferred from Figure C-16 is the first step to correcting them. It is surprising that impure tin-rich ambient particles show much more accuracy and precision in isotopic ratios than compositionally pure elemental sulfur particles and understanding the underlying causes is the first step in deriving useful isotopic ratios from PALMS spectra.

Isotopic ratios of lead calculated as a part of this experiment show significant variability (see Figure C-15), but this kind of variability is expected for lead as it is strongly affected by radioactivity of thorium and uranium. Precise measurement of lead isotopic fractionation allows tracing of material to specific ores (Townley and Godwin, 2001; Sangster et al., 2000; Carignan et al., 2005). A lot of work is still needed to make PALMS lead isotopic ratios quantitative, but lead is potentially a good candidate for future studies: it is a trace element and therefore its signal does not saturate, lead isotopes are very clearly resolved by the sTOF and its mass is high enough that there are not many isobaric interferences to be expected. One source of interference from calcium-rich particles is Ca_4O_3 at $m/z = 208$.

For future sTOF integration with PALMS, shorter drift length between the ion source and the mass analyzer is needed for an even further improved resolution.

3.5 Conclusion

The new sTOF mass analyzer (Murphy, 2017) was integrated into the existing laboratory PALMS instrument and used for chemical characterization of laboratory-

generated aerosol particles as well as measurements of ambient particles over Cambridge, MA. The resolution of the sTOF in this configuration was found to be 2-3 times better than the reflectron-TOF and it can be further improved with better mass analyzer integration into the current system (Murphy, 2017).

To take advantage of the increased resolution, the ability of PALMS coupled to sTOF to quantify isotopic ratios was explored. While some quantification was possible, accuracy is still very variable and subject to effects of saturation, isobaric interferences, and laser power variations. Further work is needed to disentangle those effects. Quantification of isotopic ratios of tin in ambient particles, probably originating from construction, was found to be most accurate. This is best explained by trace amounts of tin, which means that it does not saturate and its m/z, which seems to be more invariant to isobaric interferences than other (especially lighter) masses. Analysis of isotopic ratios of zircon revealed that quantification becomes less accurate at high laser powers (>0.3 V), possibly due to space-charge effects. Isotopic ratios of barium showed significant isobaric inferences, especially for Welsh C fly ash. Elemental sulfur particles were also analyzed. Their purity allowed for exclusion of isobaric interferences, but isotopic ratios still showed effects of saturation. Accurate quantification is possible only for higher-order clusters of sulfur atoms (S_5, S_6, S_7 and S_8).

3.6 Acknowledgments

We thank Daniel M. Murphy for providing the prototype sTOF mass analyzer and Jeehyun Yang and Shuhei Ono for the COS photooxidation experiment.

Chapter 4

Quantifying and improving the performance of the Laser Ablation Aerosol Particle Time of Flight Mass Spectrometer (LAAPToF) instrument

Single particle mass spectrometer (SPMS) instruments have been used for in-situ chemical characterization of atmospheric aerosols, both in the field and laboratory, for over two decades. SPMSs typically combine precise optical particle sizing with laser desorption and ionization followed by time of flight mass spectrometry. Among the advantages of SPMSs over other aerosol chemistry measurement techniques are their single particle resolution and high sensitivity to trace chemical species. The AeroMegt Laser Ablation Aerosol Particle Time of Flight Mass Spectrometer (LAAPToF) is a commercially available member of this instrument class, aiming for a compact size and simplicity for the end user. This paper quantifies the performance of LAAPToF with an emphasis on optical counting efficiency. Recommendations for improving detection compared to the base LAAPToF hardware are described. Our results show that changes to the optical detection scheme can lead to over two orders of magnitude improvement in optical counting efficiency in the size range 500-2000 nm vacuum

aerodynamic diameter. We also present mass spectral performance for characterizing atmospherically-relevant particles in a comparison to a current SPMS design, the Particle Analysis by Laser Mass Spectrometry (PALMS).

4.1 Introduction

Aerosols of both natural and anthropogenic origin have an effect on climate, atmospheric chemistry and human health (Boucher et al., 2013; George and Abbatt, 2010; Miller et al., 2007). Aerosol concentration, size distributions and chemical composition need to be measured in order to better understand those effects. Chemical composition measurements that differentiate internal and external mixtures and volatile and refractory components have been especially challenging. Historically, chemical composition of aerosol particles relied on bulk collection of material for subsequent off-line analysis. Mass spectra of individual aerosol particles can also allow for differentiation between internally and externally mixed components, in contrast to bulk collection. Bulk techniques also suffer from poor temporal resolution and can be affected by sampling artifacts such as chemical reactions of the collected sample or losses due to evaporation (Sullivan and Prather, 2005). Since the mid-1990s, mass spectrometric techniques have been instrumental in determining the chemical composition of atmospheric aerosols in-situ and with high temporal resolution. Such instruments are also able to probe small aerosol loadings ($\sim 10^{-15}$ g) with high sensitivity to trace elements as well as both refractory and volatile components (Murphy and Schein, 1998; Jimenez et al., 2009; Cziczo et al., 2013).

Commonly used mass spectrometric techniques differ primarily in the method of vaporization and ionization of aerosol particles. One class of instruments, such as the Aerodyne aerosol mass spectrometer (AMS), uses thermal vaporization via aerosol impaction on a resistively heated surface followed by electron impact ionization (DeCarlo et al., 2006; Jayne et al., 2000). Another, including PALMS, Aerosol Time-of-Flight Mass Spectrometer (ATOFMS) and LAAPToF, uses laser ablation and ionization (Cziczo et al., 2006; Phares et al., 2002; Pratt et al., 2009; Zelenyuk

and Imre, 2005). This paper focuses on the latter class of instruments, collectively termed Single Particle Mass Spectrometers (SPMSs). SPMS instruments have been covered in detail in several previous review papers (Coe and Allan, 2006; Johnston, 2000; Murphy, 2007).

Most current SPMS instruments use an aerodynamic inlet to introduce aerosol particles into a differentially pumped low-pressure ($\sim 10^{-5}$ Torr) region and to collimate the particles into a low-diverging particle beam of around 100 μm diameter (Cziczo et al., 2006; Pratt et al., 2009; Zelenyuk and Imre, 2005). Particles are then detected via light scattering from a continuous wave (CW) laser. Using two continuous wave laser beams allows accurate determination of vacuum aerodynamic diameter of particles by measuring the particle transit time between them (Cziczo et al., 2006; Gard et al., 1997). The scattering events trigger the ablation/ionization laser(s). The particles undergo ablation and ionization, either simultaneously or as a two-step process (Morrical et al., 1998; Zelenyuk et al., 1999). Chemical composition is typically analyzed via time of flight mass spectrometry (Cziczo et al., 2006; Murphy, 2007; Zelenyuk et al., 2009).

One important design constraint of SPMS instruments is the choice of the ablation/ionization laser. Pulsed UV lasers such as a 193 nm excimer or a 266 nm frequency-quadrupled Neodymium: Yttrium-Aluminum-Garnett (Nd:YAG) laser are commonly used because they can ionize most atmospherically-relevant components (Thomson et al., 1997). When the ablation/ionization laser is triggered by a scattering event, an excimer laser can fire quickly with a delay on the order of a few hundred nanoseconds. A Nd:YAG laser requires more than 100 μs to produce a pulse, during which time the transiting particle has typically moved $\sim$10 cm. Nd:YAG-based instruments therefore require a trigger delay and a different spacing of internal components: the ablation/ionization region has to be physically removed from the optical detection region (Gard et al., 1997; Pratt et al., 2009; Su et al., 2004). Conversely, excimer-based instruments can have a more compact construction: the ablation/ionization laser beam can be positioned very close to the particle detection laser beam.

The majority of modern SPMS instruments are custom-built. Exceptions are the

now-discontinued TSI Aerosol Time of Flight Mass Spectrometer (ATOFMS 3800 series) (Dall'Osto and Harrison, 2006; Drewnick et al., 2008), Single Particle Aerosol Mass Spectrometer (SPAMS) manufactured by the Hexin Company in China (Chen et al., 2016) and the topic of this paper, the AeroMegt LAAPToF. Among the current SPMS designs are PALMS (Cziczo et al., 2006; Thomson et al., 2000), ATOFMS (Gard et al., 1997; Pratt et al., 2009), the Aircraft-based Laser Ablation Aerosol Mass Spectrometer (ALABAMA) (Brands et al., 2011) and the mini-Single Particle Laser Ablation Time of Flight Mass Spectrometer (mini-SPLAT) (Zelenyuk and Imre, 2005; Zelenyuk et al., 2009, 2015). All but LAAPToF rely on a large-area elliptical reflector to collect light scattered from a CW laser and transmit it into a photomultiplier tube (PMT) detector for particle detection. The LAAPToF instrument takes a different approach, using a fiber optic assembly, the details of which are described in the following sections, to extract scattered light. Generally, the optical counting efficiency of an SPMS is limited at smaller sizes by the low sensitivity of light collection to weak scatter signals and at the upper end to the inlet transmission efficiency of super-micron particles. Within this range, both optical detection and physical transmission efficiency are largely determined by the size of the CW laser spot compared to the width of the particle beam produced by the aerodynamic focusing lens.

ATOFMS and ALABAMA both use a 266 nm Nd:YAG ablation/ionization laser, necessitating the use of a trigger delay and a physical separation of the optical detection and the ion source region (Brands et al., 2011; Gard et al., 1997; Pratt et al., 2009; Su et al., 2004). On the other hand, PALMS instrument uses a 193 nm excimer laser, allowing the instrument to be more compact due to the small trigger delay. Despite using a 193 nm excimer laser for ionization, the optical detection stages and the ion source region are physically separated in the SPLAT instrument, allowing for greater flexibility in design of the optical stages (Zelenyuk and Imre, 2005; Zelenyuk et al., 2009, 2015) which is not possible for the compact source region on PALMS (Cziczo et al., 2006). The LAAPToF instrument design attempts to combine the high ionization rate of the PALMS design with a modern bipolar mass spectrometer. As discussed in subsequent sections, this comes at the price of optical counting efficiency

as space for large-area elliptical reflectors is not permitted in this design.

Aspects of the LAAPToF instrument performance were recently assessed by two other groups (Gemayel et al., 2016; Marsden et al., 2016). In one case, the performance of the base commercial LAAPToF version is described (Gemayel et al., 2016). The other study reports on development of an improved particle detection scheme using a high-powered collimated laser (Marsden et al., 2016). This study also demonstrates modifications to the base LAAPToF hardware; however, it concentrates on improving the light detection efficiency. The improvements described in this paper and in Marsden et al. (2016) are complementary and they result in similar instrument performance.

This paper aims to (1) assess the performance of LAAPToF by comparison to established SPMS designs, (2) discuss modifications that can be made to the existing hardware to increase the optical counting efficiency and (3) provide an initial comparison of LAAPToF mass spectra to those acquired by PALMS.

4.2 Experimental Methods

4.2.1 Inlet and pumping scheme

LAAPTOF has been previously described, but an overview of the specific version of the instrument investigated here is given in this and following sections (Gemayel et al., 2016; Marsden et al., 2016). A LAAPToF schematic is depicted in Figure C-19. It consists of four differentially-pumped regions with a total length of 47 cm. The instrument functions at low pressure using a turbomolecular pump with four pumping stages (SplitFlow 270, Pfeiffer Vacuum, Asslar, Germany), backed by a 1.7 m^3/h membrane pump (MD 1 VARIO-SP, Vacuubrand, Essex, CT).

The aerodynamic focusing lens is used to introduce particles into the vacuum region and collimate them into a beam. Two lenses have been used. The initial design uses the Aerodyne standard lens (Aerodyne Research, Inc., Billerica, MA), described previously by Zhang et al. (2002, 2004), with approximately unity transmission in the

range 90-700 nm. Alternately, an Aerodyne PM2.5 lens (Aerodyne Research, Inc., Billerica, MA), described by Peck et al. (2016) and Xu et al. (2017) with approximate 50% transmission in the range 100-3000 nm, was also used in this work. In both cases, a critical orifice, consisting of a steel plate with a bore of 100 μm diameter (Structure Probe, Inc., West Chester, PA), restricts the flow to the instrument to 0.1 standard liter per minute (slpm) and thereby reduces the pressure in front of the aerodynamic focusing lens. Pressure between the critical orifice and the lens is measured with a compact Pirani gauge (TPR 280, Pfeiffer Vacuum, Asslar, Germany).

4.2.2 Optical detection of particles

The original optical detection stages of LAAPToF have undergone significant changes as a part of this work. The original LAAPToF design used 405 nm laser diodes of unknown specifications mounted on a threaded copper tube that was directly attached to the top of the instrument and coupled to the vacuum through plain glass windows. The laser beams then passed through a fixed lens that focused them to a spot of $\sim$50 μm diameter at the particle beam location in the flight tube. The alignment of the diode lasers was achieved by manual tilt, i.e., without use of standard optical mounts, restricting the accuracy and repeatability of alignment with the particle beam. Below the particle beam, a ring of 12 optical fibers collected the scattered light at $\sim$15° with respect to direct forward scattering. The optical fibers exited the vacuum and were coupled to PMTs (H10722-110, Hamamatsu, Hamamatsu, Japan), where two PMTs were used to read the signals from six fibers each.

The modifications performed to LAAPToF were (1) adding a laser with better beam quality, (2) using optical mounts for directing the beam into the chamber for easier and more reproducible alignment, and (3) increasing the amount of scattered light collected using light guides. The modifications to the optical path are shown in Figure C-19. Not shown is the laser, a 100 mW, 405 nm diode with a heat sink, fan, and USB-interfaced controller (OBIS, Coherent, Santa Clara, CA). The OBIS beam is collimated to $\sim$1 mm at the laser exit with $<$ 1 mrad full angle divergence. The OBIS laser couples to the vacuum chamber through a series of mirrors mounted on optical

kinematic mounts as shown in Figure C-19: the beam exits the laser, couples onto mirror 1 (M_1), which is mounted on a micrometer stage providing movement in the y-direction. The beam is then split by a 50:50 beam splitter (BS_1) (Thorlabs, Newton, NJ) into two beams that couple into the scattering ports via antireflective-coated glass windows to reduce reflection losses. The beams are focused at the particle beam with 120 mm plano-convex lenses (Thorlabs, Newton, NJ) to a diameter of 100 μm. BS_1 and M_2 are mounted on kinematic mounts, providing control over spot position inside the chamber and enhancing the rigidity of the optical path.

Optical counting efficiency measurements are reported as percentage of particles detected at a PMT compared to the number of particles transmitted to the inlet, as measured by an optical particle sizer (OPS) (OPS 3330, TSI, Shoreview, MN) or a condensation particle counter (CPC) (Brechtel, Hayward, CA). Particles used for the optical counting efficiency tests were Polystyrene Latex Spheres (PSL) (Polysciences, Inc. Warrington, PA) of known size that were wet-generated with an atomizer (Aerosol Generator 3076, TSI, Shoreview, MN) and dried with a custom built diffusion dryer. Monodisperse number concentrations on the order of 100 cm^{-3} were used to investigate the optical counting efficiency, which is comparable to ambient concentrations of 200 nm - 2.5 μm particles (Stanier et al., 2004). For other optical counting efficiency tests the atomizer, followed by the diffusion dryer, was used to generate polydisperse ammonium sulfate aerosol. For both PSL and ammonium sulfate tests, the dry aerosol was size-selected using a differential mobility analyzer (DMA) (Brechtel, Hayward, CA).

4.2.3 Ionization and analysis

The LAAPToF instrument differs in geometry of particle ionization from the previously discussed SPMSs. As shown in Figure C-19, the ablation/ionization laser beam counter-propagates with respect to the particle beam. Such an orientation has been used previously where the laser was "free fired" to strike particles that happened to be within the ionization region (Carson et al., 1997b; Phares et al., 2002; Reents et al., 1995).

LAAPToF uses an ArF 193 nm excimer laser (EX5, GAM Laser, Inc., Orlando, FL), producing 6-8 ns pulses at a frequency of up to 250 Hz with maximum energy of 12 mJ. Because of its geometry, it does not use a trigger delay; the excimer laser is fired immediately after the detection PMT detects scattered light. The excimer laser couples into the flight tube through a lens (L_5) and an uncoated fused silica window. Because the particle beam ultimately impacts the rear window, it must be cleaned or changed periodically. The window lifetime is dependent on typical concentrations and types of particles sampled with the instrument. The results reported in this paper used excimer powers between 1 and 5 mJ, comparable to those used with PALMS, enabling a comparison of the reference spectra discussed in the next sections. The excimer laser is focused into the ionization region but no further beam shaping is performed to maintain a homogeneous profile. The laser irradiance inside the ionization region is therefore unknown and cannot be easily estimated because of the non-Gaussian character of the beam profile. The alignment of the excimer laser is achieved empirically by adjusting the L_5 lens position to maximize the ionization rate of particles.

The mass spectrometer is a commercial bipolar time-of-flight mass analyzer, designed by ToFWerk (Thun, Switzerland), with two reflectrons in a "B-ToF" configuration (Gemayel et al., 2016). The ion source region is situated in the space between two metal plates, ~6 mm across. This dimension restricts the size of the beam dump that can be used with the light guides. The metal plates closest to the ion source region (shown as gray shaded areas in Figure C-19 for reference) are grounded, creating a "field-free" ion source region for a delayed ion extraction (Vera et al., 2005).

4.3 Results and discussion

4.3.1 Optical counting efficiency

In the original LAAPToF design, the 12 member optical fiber ring collected only a minor fraction of the solid angle of light scattered from each aerosol particle. In

order to be able to detect smaller particles, the amount of scattered light ultimately detected by the PMTs needed to be enhanced. This was achieved by implementing a light guide to maximize the scattered light collected. The usage of a glass light guide, as shown in Figure C-19, allows extraction of the maximum possible solid angle (35°, not accounting for the beam dump) of scattered light from the existing scattering port. The glass light guides used here have a central 3 mm diameter beam dump machined out of anodized aluminum to block the direct laser beam. The glass light guide is a custom built optic (Rocky Mountain Instrument Co, Lafayette, CO), machined out of N-BK7 glass with a diameter of 17.8 mm and a length of about 76 mm. Its geometry is such that a scattered light ray undergoes exactly one internal reflection inside the light guide. A ray trace of the light guides implemented here is shown in Figure C-19. Two lenses, a biconvex lens with a focal length of f = 25.4 mm (Thorlabs, Newton, NJ; L_3 in Figure C-19) and a plano-convex lens with f = 40.0 mm (Thorlabs, Newton, NJ, L_4) focus the light exiting the light guide onto the 8 mm diameter active surface area of the PMT. The light guides are housed inside a threaded tube to minimize light from external sources. A black-anodized aluminum positioning ring is epoxied (TS10, Thorlabs, Newton, NJ) to the light guide and, together with an o-ring, provides the vacuum seal to the chamber.

The difference in performance between the base optical detection system and the new laser and light guide combination are shown in Figure C-20. The optical counting efficiency for both the timing (Figure C-20A) and detection ports (Figure C-20B) are given for the two configurations using different test particles and sizes. In all cases, the OBIS laser, not the original diodes, was used. When the original instrument configuration with directly-coupled diodes was tested no particles were detected at the number concentrations used in the experiments. Furthermore, there were spontaneous overheating failures with the original diodes that could not be overcome. The base case data presented here are therefore expected to be superior to the original design using diode lasers. For both the timing and detection signals, an improvement in efficiency between two and three orders of magnitude resulted from switching from optical fibers to light guides. With the light guides, LAAPToF can detect particles

larger than 500 nm with better than 1% efficiency at the detection laser and ~10% at the upstream timing laser. The instrument reliably detects particles larger than 250 nm at near-ambient concentrations. This is an improvement over the recent commercial LAAPToF report, which characterizes the lower detection limit as 350 nm (Gemayel et al., 2016).

The geometry of the LAAPToF instrument results in challenging alignment of the optical components. The laser foci have to be incident above the light guide beam dumps in such a way as to minimize the stray light. Small changes to this alignment can result in large changes to optical counting efficiency. This is illustrated in Figure C-20 with PSL calibration points, which were obtained over the course of several different optical alignments. The PSL measurements show more scatter than the ammonium sulfate measurements, which were obtained all at once right after a successful alignment. Decreasing the amount of stray light inside the instrument should decrease the alignment sensitivity, while improving the overall optical counting efficiency.

As Table B.2 illustrates, the LAAPToF optical system does not tend to perform as well as the standard elliptical reflector designs common to other SPMS instruments. Direct comparisons between different instruments are complicated by different laser powers and spot sizes. A comparison of the theoretical performance between the various optical detection devices is shown in Figure C-21. The amount of light collected per spherical particle is presented for different light collection geometries based on numerically integrating the Mie scattering curve for different effective apertures. The ATOFMS curve was constructed following the treatment in Moffet and Prather (2005). The curve for LAAPToF with light guides was constructed following the treatment in Hodkinson and Greenfield (1965) for forward scattering, parallel illumination, along the axis and based on the physical dimensions of the light guides implemented for this work. The curve for the original LAAPToF design was constructed in the same manner except the fibers were treated as a continuous ring, instead of discrete points, for simplicity (i.e., this overestimates the solid angle of light collection by a factor of ~2-3). The figure therefore represents a theoretical limit that can be achieved with

the light guides and an upper limit for the fiber design due to the assumed simplified geometry.

The change in optical counting efficiency as a function of laser power is presented in Figure C-22. Note that the x-axis shows total laser power, half of which is incident to each scattering region, as the beam is split before entering the instrument (see Figure C-19). As the total laser power is varied from 40 mW to 100 mW (i.e. 20 mW to 50 mW in each scattering region), the amount of light scattered by 950 nm PSL particles changes slightly. Optical counting efficiency drops significantly below 60 mW. The stray light background, defined as the DC level registered by the PMT with the laser beam on without particles, increases continuously as the beam power is increased. 60 mW was therefore chosen as the nominal laser power level that minimized stray light but maintained particle scatter. From 500 to 950 nm PSL the use of 60 mW resulted in a factor of 2 to 10 improvement in optical counting efficiency compared to 100 mW.

A trend of increasing optical counting efficiency with increasing spot size of the detection laser is apparent in Table B.2. This is because a larger laser beam cuts through a larger fraction of the particle beam. Increasing the detection beam spot size for LAAPToF did not follow this trend, however, due to the resulting increase in the amount of stray light. The SPLAT II design uses both a large spot size and high laser power because stray light has been minimized by baffling and black anodization of the optical region (Zelenyuk and Imre, 2005). This represents a possible modification that could yield further improved detection efficiency in LAAPToF. Table B.2 also illustrates another issue with the LAAPToF design that may also lend to future modification: the total length of the instrument (i.e., the beam spacing). While LAAPToF is similar to SPLAT II, the latter has a much larger detection beam spot size to compensate for particle beam divergence. Hence, another possible future modification to improve LAAPToF performance is to shorten the instrument to decrease particle beam divergence.

4.3.2 Mass spectrometer performance

In order to test the mass spectral performance of LAAPToF atmospherically-relevant aerosol types were sampled and compared with spectra obtained by other SPMSs. Figure C-23 shows single-particle spectra taken with LAAPToF and PALMS for (A) Potassium rich feldspar (K-Feldspar), (B) elemental carbon, (C) Snomax, a desiccated and ground bacterium and (D) an Argentinian soil dust. The aerosol particles were sampled at the Karlsruhe Institute of Technology Aerosol Interactions and Dynamics in the Atmosphere (AIDA) facility during the Fifth Ice Nucleation Workshop (FIN-01). K-Feldspar and soil dust samples were dry-dispersed, the elemental carbon was produced by a CAST burner and the Snomax was wet-generated with an atomizer and dried with a diffusion dryer.

Mentioned previously, the LAAPToF excimer beam counter-propagates relative to the particle beam. This orientation runs the risk of ionizing multiple particles coincident in the ion source region when the laser is fired. Counter-propagation also results in an increases in the volume in which particles can be ionized, leading to lower certainty of the source of ions. Even when only a single particle is ablated and ionized the latter effect reduces the reproducibility of the measured flight times of the ions due to different initial ion formation locations. This effect was quantified with elemental carbon particles where the arrival time of the carbon cluster ions ($^{12}C_n^+$, where n = integer) peaks could be determined from the ToF in the mass spectrometer. A 0.3-0.6% offset in the ToF was observed within 100 sample sets. This will primarily affect the mass calibration, resulting in an instrument that needs to be calibrated more frequently and a greater need for mass calibration adjustments in data processing.

PALMS and LAAPToF both use a 193 nm excimer laser for ablation/ionization and the extracted ions are therefore expected to be similar. PALMS excimer power density at the focus is $\sim 9 \times 10^8$ W/cm^2. Because the LAAPToF excimer beam profile is non-Gaussian, the spot size after the lens cannot be reliably calculated resulting in an uncertain laser power density at the focus. In Figure C-23, the LAAPToF mass scales were offset to match the PALMS scales. The LAAPToF spectra show saturation

of peaks for the most abundant ions (e.g. Al^+, K^+, Na^+), an effect not observed for PALMS spectra due use of a logarithmic amplifier which extends the dynamic range of the instrument (Thomson et al., 2000). Spectra of soot and Snomax show a high abundance of the elemental carbon ion ($^{12}C_n^+$) for LAAPToF but not for PALMS. More fragmentation of organics, leading to a very high $^{12}C_n^+$ ion signal, suggests a higher effective power density for LAAPToF than for PALMS. LAAPToF spectra also show a higher relative PO^+ ion signal for Snomax. In general, LAAPToF peaks exhibit broadening with increasing mass. This can be observed most clearly in the negative soot spectrum in Figure C-23B. The origin of this broadening is most likely the large ion source area due to the excimer laser counter-propagation.

4.4 Conclusion

The performance of LAAPToF, one of the few currently available commercial SPMS instruments, has been evaluated. The optical particle detection stages were redesigned to detect more scattered light, resulting in an improvement of 2-3 orders of magnitude in optical counting efficiency of incident particles. We suggest that particle detection could be further improved by reducing the stray light inside the instrument using a better beam dump and/or by anodization of the instrument components to attenuate internal reflections. The modifications described here allow for sizing and acquisition of mass spectra for 1-10% of particles larger than ~500 nm vacuum aerodynamic diameter.

LAAPToF has fundamental detection limitations due to its geometry. The collected scattered light is limited by the size of the ports that housed the original fiber optics and, due to space limitations, can not achieve the performance of the elliptical reflectors used on most SPMSs. When compared to an existing SPMSs, LAAPToF spectra exhibit more variability in ion ToF and peak width. This is in part due to counter-propagation of the excimer beam, but a more well-defined beam (i.e., with the addition of beam shaping optics) should increase the particle ionization rate and make spectra more reproducible without affecting the mass scale uncertainty associ-

ated with the counter-propagating geometry. Software/data processing improvements and frequent mass calibrations are required to minimize this issue.

With only the modifications described in this paper, which are easy to implement and do not require a large-scale redesign, the LAAPToF instrument is ambient-capable for particles larger than 250 nm. This should enable it to successfully characterize PM1.0 and PM2.5 in locations where such particles are abundant, for example urban areas.

4.5 Acknowledgements

The authors gratefully acknowledge funding from NSF grant #AGS-1339264 and DOE grant #DE-SC0014487. M. A. Z. acknowledges the support of NASA Earth and Space Science Fellowship. The authors would like to thank the KIT AIDA facility staff for hosting the FIN01 workshop and Leah Williams for helpful comments on this manuscript.

This chapter is under review at Atmospheric Measurement Techniques: Zawadowicz, M. A., Lance, S., Jayne, J. T., Croteau, P., Worsnop, D. R., Mahrt, F., Leisner, T., Cziczo, D. J.: Quantifying and improving the performance of the Laser Ablation Aerosol Particle Time of Flight Mass Spectrometer (LAAPToF) instrument, Atmos. Meas. Tech. Discuss., https://doi.org/10.5194/amt-2017-1, in review, 2017.

Chapter 5

Improved identification of primary biological aerosol particles using single particle mass spectrometry

Measurements of primary biological aerosol particles, especially at altitudes relevant to cloud formation, are scarce. Single particle mass spectrometry (SPMS) has been used to probe aerosol chemical composition from ground and aircraft for over 20 years. Here we develop a method for identifying bioaerosols using SPMS. We show that identification of bioaerosol using SPMS is complicated because phosphorus-bearing mineral dust and phosphorus-rich combustion by-products such as fly ash produce mass spectra with peaks similar to those typically used as markers for bioaerosol. We have developed a methodology to differentiate and identify bioaerosol using machine learning statistical techniques applied to mass spectra of known particle types. This improved method provides far fewer false positives compared to approaches reported in the literature. The new method was then applied to two sets of ambient data collected at Storm Peak Laboratory and a forested site in Central Valley, California to show that 0.04-2% of particles in the 200 - 3000 nm aerodynamic diameter range were identified as bioaerosol. In addition, 36% - 56% of particles identified as biological also contained spectral features consistent with mineral dust, suggesting internal dust/biological mixtures.

5.1 Introduction

Biological atmospheric aerosol (or bioaerosol) has recently garnered interest because certain species of bacteria and plant material might impact climate via the nucleation of ice in clouds (Hiranuma et al., 2015; Möhler et al., 2008). However, many field-based measurements of ice nuclei and ice residuals do not indicate that bioaerosol is a major class of ice active particles (Cziczo et al., 2013; DeMott et al., 2003; Ebert et al., 2011). While modeling efforts suggest that biological material is not significant in ice cloud formation on a global scale, uncertainties continue to exist because field measurements of ice nucleating particles are currently sparse (Hoose et al., 2010; Sesartic et al., 2012).

In this paper, "bioaerosol" is defined as primary biological aerosol particles (PBAP) (i.e. airborne whole and fragmentary bacteria, pollen and spores) and particles that contain fragments of PBAP as a part of an internal mixture. Measurement techniques specific to bioaerosol include collection of aerosol on filters followed by analysis with microscopy techniques, either electron microscopy (EM) or optical microscopy coupled with fluorescent staining of the samples (Amato et al., 2005; Bauer et al., 2002, 2008; Bowers et al., 2009, 2011; Griffin et al., 2001; Matthias-Maser and Jaenicke, 1994; Pósfai et al., 2003; Sattler et al., 2001; Wiedinmyer et al., 2009; Xia et al., 2013). Aerosol samples collected in the atmosphere have been cultured for identification of the microbial strains present (Amato et al., 2005, 2007; Fahlgren et al., 2010; Fang et al., 2007; Griffin et al., 2001, 2006; Prospero et al., 2005).

In-situ techniques specific to biological samples are typically based on fluorescence of biological material following UV excitation. Examples include the wide-band integrated bioaerosol sensor (WIBS) which is available commercially (Kaye et al., 2000, 2005). WIBS has been successfully deployed in several locations (Gabey et al., 2010; Toprak and Schnaiter, 2013). Using fluorescence to detect biological aerosol can have interferences, however. For example, polycyclic aromatic compounds or humic acids can have similar fluorescent properties (Gabey et al., 2010; Pan et al., 1999). Cigarette smoke has similar fluorescent properties to bacteria (Hill et al., 1999). In an

attempt to address interferences, WIBS collects fluorescence information using several channels with different wavelengths while also measuring the size and shape of the particles. Table B.3 summarizes some recent measurements of bioaerosol. More information can be found in recent reviews focused on bioaerosols in the atmosphere, such as Després et al. (2012).

Measurements of bioaerosol in the free and upper troposphere, where they could be relevant to cloud formation, remain scarce. Four of the recent studies reported in Table B.3 used an aircraft to access altitudes higher than 4,000 m (DeLeon-Rodriguez et al., 2013; Pósfai et al., 2003; Twohy et al., 2016; Ziemba et al., 2016). Two of these used the WIBS sensor to report vertical profiles of fluorescent particles (Twohy et al., 2016; Ziemba et al., 2016). In the remaining two cases, aerosols were collected on filters and analyzed off-line. There can exist significant uncertainty in these measurements. A recent aircraft-based study by DeLeon-Rodriguez et al. (2013) reports analysis of high altitude (8-15 km) samples taken before, after and during two major tropical hurricanes. The abundances of microbes, mostly bacteria, were reported between 3.6 $\times 10^4$ and 3.0 $\times 10^5$ particles m^{-3} in the 0.25 - 1 μm size range. The methods and conclusions of this study were re-evaluated by Smith et al. (2013), who argued that in some instances the reported concentration of bioaerosol were not possible because they exceeded the total aerosol by several factors. The samples were also taken over periods of hours, possibly including sampling in clouds when the high-speed impaction of droplets and ice can dislodge particles from the inlet (Cziczo and Froyd, 2014; Froyd et al., 2010; Murphy et al., 2004).

Although difficult, measurements of bioaerosol in the upper troposphere are necessary in order to constrain their influence on atmospheric properties and cloud formation processes. All of the techniques discussed above, except for WIBS, are off-line and require expertise in sample processing and decontamination. WIBS is a possible in situ detection technique for bioaerosols, but it is relatively new and, as a result, has a short deployment history. There has been considerable interest in using aerosol mass spectrometry techniques to measure bioaerosol. Single particle mass spectrometry (SPMS) has been successfully used since the mid-1990s to characterize chemical

composition of atmospheric aerosol particles in situ and in real time (Murphy, 2007). The ability of SPMS to simultaneously characterize volatile and refractory aerosol components makes it an attractive tool for investigating the mechanisms of cloud formation (Cziczo et al., 2013; Friedman et al., 2013). The general principle behind SPMS, and in particular the instrument discussed in this paper, the Particle Analysis by Laser Mass Spectrometry (PALMS), is the use of a pulsed UV laser for the ablation and ionization of single aerosol particles. Ions are then accelerated into a time-of-flight mass spectrometer. Laser ablation/ionization used with SPMS produces ion fragments and clusters and is susceptible to matrix effects such that quantitative results are possible only with careful calibration and consistent composition (Cziczo et al., 2001).

Biological aerosols have been studied with SPMS, in particular the Aerosol Time of Flight Mass Spectrometer (ATOFMS) (Cahill et al., 2015; Creamean et al., 2013; Fergenson et al., 2004; Pratt et al., 2009). A property of SPMS bioaerosol spectra that has been exploited for their detection is the presence of phosphate (PO^-, PO_2^-, PO_3^-) and organic nitrogen ions (CN^-, CNO^-) (Cahill et al., 2015; Fergenson et al., 2004). Those ions have also previously been shown to be present in non-biological particles with the same instrument, however, such as vehicular exhaust (Sodeman et al., 2005) and soil dust (Silva et al., 2000). Particles that contain phosphates, organic nitrates and silicates have historically been classified as mixtures of bioaerosol and dust (Creamean et al., 2013). This work examines the prevalence of these ions in the context of spectra collected with PALMS.

Phosphorus was chosen as the focus of this paper because of its abundance in spectra of bioaerosol, but also because it does not undergo gas-phase partitioning in the atmosphere (Mahowald et al., 2008). Therefore, the presence of phosphorus on a particle can often constrain its source, and only the classes of particles that are most likely to contain phosphorus are examined here. Emission estimates qualitatively agree that mineral dust, combustion products, and biological particles constitute the principal phosphate emission sources. The global phosphorus budget has been modeled by Mahowald et al. (2008), indicating that 82% of the total burden is emitted in

the form of mineral dust. Bioaerosol accounts for 12% and anthropogenic combustion sources, including fossil fuels, biofuels and biomass burning, account for 5% (Mahowald et al., 2008). Recently, Wang et al. (2014) provided a higher estimate of phosphorus emissions from anthropogenic combustion sources, 31%. In this estimate, mineral dust was responsible for 27%, bioaerosol 17% and natural combustion sources 20% of total phosphorus emissions (Wang et al., 2014).

In this work, calcium phosphate-rich minerals (apatite and monazite) and fly ash are chosen to represent dust and industrial combustion particle classes, respectively. In atmospheric particles, the composition can be mixed, containing some phosphate from inorganic sources, such as calcium phosphate, and some phosphate from microbes. For instance, soils can contain minerals, live microbes, and biogenic matter at all stages of decomposition. Therefore, classifying soil-derived particles with a binary biological/non-biological classifier has uncertainties. These uncertainties are quantified here for soils using soil samples collected in various locations.

In this work, the presence of phosphorus in a mass spectrum is evaluated as proxy for bioaerosol. All biological cells contain phosphorus because it is a component of nucleic acids and cell membranes. Distinguishing the specific mass spectral phosphate signature of biological cells from other non-biological phosphorus is the topic of the analysis in this paper. The goal of this paper is to develop a method that can differentiate PALMS bioaerosol spectra from spectra of dust and combustion by-products.

5.2 Experimental Methods

The objective of this work is to describe and validate a new SPMS-based data analysis technique that allows for the selective measurement of bioaerosol. A dataset of bioaerosol, phosphate-rich mineral and coal fly ash single particle spectra—the three largest sources of phosphorus in atmospheric aerosols—was used to derive a classification algorithm for biological and non-biological phosphate-containing material. This classifier was then applied to an ambient data set collected at the Storm Peak

Laboratory during the Fifth Ice Nucleation workshop—phase 3 (FIN03).

5.2.1 PALMS

The NOAA PALMS instrument has been discussed in detail elsewhere (Cziczo et al., 2006; Thomson et al., 2000). Currently, there are two copies of the PALMS instrument, both of which were used in this work. The laboratory PALMS is a prototype for the flight PALMS, which is more compact and can be deployed unattended at field sites and on aircraft (Thomson et al., 2000). Briefly, PALMS uses an aerodynamic lens to sample aerosols and impart them with a size-dependent velocity (Zhang et al., 2002, 2004). Aerodynamic particle diameter is measured by timing the particles between two continuous-wave laser beams (532 nm Nd:YAG in laboratory PALMS and 405 nm diode in flight PALMS). The particles are ablated and ionized in one step by a 193 nm excimer laser. A unipolar reflectron time of flight mass spectrometer is then used to acquire mass spectra. PALMS acquires spectra in either positive or negative polarity, but not simultaneously. For field datasets presented in this paper, sampling polarity was switched every 5 minutes for FIN03 and every 30 minutes for CARES.

Due to the high laser fluence used for desorption and ionization ($\sim 10^9$ W/cm^2), PALMS spectra show both atomic ions and ion clusters, which complicate spectral interpretation. SPMS is considered a semi-quantitative technique because the ion signal depends on the abundance and ionization potential of the substance, rather than solely its abundance (Murphy, 2007). Additionally, the ion signals can depend on the overall chemical composition of the particle, known as matrix effects (Murphy, 2007). The lower particle size threshold for PALMS is $\sim$200 nm diameter and is set by the amount of detectable scattered light. The upper size threshold is set by transmission in the aerodynamic lens at ~ 3 μm diameter (Cziczo et al., 2006). In PALMS, Particles toward the larger end of this size range are transmitted into the laser beam more efficiently than smaller particles. The 193 nm excimer laser can ionize all atmospherically-relevant particles within this size range with little detection bias (Murphy, 2007). The ionization region is identical in the laboratory and flight PALMS instruments. Raw PALMS spectra are processed using a custom IDL

software. Mass peak intensities used in this paper refer to integrated peak areas normalized by the total ion current.

5.2.2 Aerosol standards

Table B.4 shows numbers of negative spectra for all analyses in this paper. A portion of the data from each of the bioaerosol and non-biological phosphate samples was used as "training data" to build the classification algorithm. The remaining test data were classified using the trained algorithm.

Training dataset

A collection of phosphorus-containing samples of biological and inorganic origin were used to train the classification algorithm used in this work. Some of the samples were analyzed with the laboratory PALMS at the Aerosol Interaction and Dynamics in the Atmosphere (AIDA) facility at Karlsruhe Institute of Technology (KIT) during the Fifth International Ice Nucleation Workshop—phase 1 (FIN01) with the remainder sampled at MIT.

Biological aerosol sampled at AIDA included two aerosolized cultures of *Pseudomonas syringae* bacteria, Snomax (Snomax International, Denver, CO) (irradiated, desiccated and ground *Pseudomonas syringae*) and hazelnut pollen wash water. The Snomax and *P. syringae* cultures were suspended in water and aerosolized with a Collison-type atomizer. The growth medium for *P. syringae* cultures was Pseudomonas Agar Base (CM0559, Oxoid Microbiology Products, Hampshire, UK).

Biological aerosol sampled at MIT included giant ragweed (*Ambrosia trifida*) pollen, oak (*Quercus rubra*) pollen, European white birch (*Betula pendula*) pollen, *Fusarium solani* spores and yeast. Samples of dried pollens and *F. solani* spores were purchased from Greer (Lenoir, NC). Information supplied by the manufacturer indicates that *F. solani* fungus was grown on enriched trypticase growth medium and killed with acetone prior to harvesting the spores. Ragweed and oak pollen originated from wild plants, while the birch pollen originated from a cultivated plant. Pollen

was collected, mechanically sieved and dried. The yeast used in this experiment was commercial active dry yeast (Star Market brand). The yeast powder was sampled by PALMS from a vial subjected to slight manual agitation. Pollen grains were too large (18.9 - 37.9 μm according to manufacturer's specification) to sample with PALMS. They were suspended in ultrapure water (18.2 MΩ·cm, Millipore, Bedford, MA) and the suspensions were sonicated in ultrasonic bath for $\sim$30 minutes to break up the grains. Large material was allowed to settle to the bottom and a few drops of the clear solution from the top of the suspensions were further dissolved in ultrapure water, and the resulting solutions were aerosolized with a disposable medical nebulizer (Briggs Healthcare, Waukegan, IL). A diffusion dryer was used to remove condensed phase water prior to sampling with PALMS. *F. solani* spores were sampled in two different ways: (1) dry and unprocessed, in the same way as the yeast and (2) fragmented in ultrasonic bath and wet-generated, in the same way as pollen samples. Examination of PALMS spectra revealed no changes in chemistry resulting from different processing methods.

Samples of fly ash from four coal-fired U.S. power plants were used as proxy for combustion aerosol: J. Robert Welsh Power Plant (Mount Pleasant, TX), Joppa Power Station (Joppa, IL), Clifty Creek Power Plant (Madison, IN) and Miami Fort Generating Station (Miami Fort, OH). The samples were obtained from a commercial fly ash supplier, Fly Ash Direct (Cincinnati, OH). Fly ash was dry-generated with the shaker.

Apatite and Monazite-Ce mineral samples were generated from $\sim$3" pieces of rock. The rocks were ground and the samples aerosolized with the shaker. Both apatite and monazite were sampled and processed at MIT. The apatite rock was contributed by Adam Sarafian (Woods Hole Oceanographic Institution, Woods Hole, MA).

Two samples of German soil were used as an example of agricultural soil that was known to be fertilized with inorganic phosphate. These were also sampled at the AIDA facility during FIN01. Note that while all other soil samples are used as test aerosols for a completed classifier, those two in particular are used in the training set to account for the presence of inorganic fertilizer.

Samples of apatite and J. Robert Welsh Power Plant fly ash were also subjected to processing with nitric acid to approximate atmospheric aging. Powdered sample was aerosolized from the shaker to fill a 9 L glass mixing volume. A hot plate below the volume was used to heat the air inside to 31°C measured in the center of the volume with a thermocouple. PALMS sampled at a flow rate of 0.44 slpm (STP: 0°C, 1 atm) from the 9 L volume. This constituted unprocessed aerosol. 80% HNO_3 was then placed with a Pasteur pipette at the heated bottom of the mixing volume. Two experiments were conducted: for experiments using 0.1 mL of nitric acid, the entire volume of HNO_3 evaporated, producing an estimated partial pressure of about 0.005 atm in a static situation. In 1 mL experiments some liquid HNO_3 remained at the bottom of the volume with an estimated partial pressure of HNO_3 of 0.04 atm. The aerosol and gas-phase HNO_3 were allowed to interact for 2 minutes at which point PALMS began sampling from the volume.

Test dataset

Samples of natural soil dust were collected from various locations listed in Table B.5. Five sampled were investigated at the AIDA facility during FIN01 (Bächli soil, Argentina soil, Ethiopian soil, Moroccan soil and Chinese soil) with the remaining analysis at MIT (Storm Peak and Saudi Arabian soil).

Internally mixed biological/mineral particles were also analyzed at MIT. Illite NX (Clay Mineral Society) without bioaerosol was sampled dry, using a shaker (Garimella et al., 2014), and wet-generated, using a medical nebulizer containing ultrapure water. A second disposable medical nebulizer was then used to aerosolize a suspension of illite NX and *F. solani* spore fragments. This wet generated aerosol was also dried with a diffusion dryer prior to PALMS sampling.

5.2.3 Statistical analysis

A support vector machine (SVM), a supervised machine learning algorithm (Cortes and Vapnik, 1995), was used as the statistical analysis method for analysis of these

data. In this case a non-linear binary classifier was constructed, using non-linear kernel functions (Ben-Hur et al., 2001; Cortes and Vapnik, 1995). A Gaussian radial basis function kernel was empirically determined to provide the best performance in this case. For this work, the SVM algorithm was implemented in MATLAB 2016a (MathWorks, Natick, MA) using the Statistics and Machine Learning toolbox.

5.2.4 Field data

The method was employed on two ambient data sets, one acquired at the Desert Research Institute's (DRI's) Storm Peak Laboratory located in Steamboat Springs, CO and the other acquired in Cool, CA site during Carbonaceous Aerosol and Radiative Effects Study (CARES). Storm Peak Laboratory is located on Mt. Werner at 3220 m elevation at 106.74 W, 40.45 N. This high altitude site is often in free tropospheric air, mainly during overnight hours, with minimal local sources (Borys and Wetzel, 1997). Ambient air was sampled using the Storm Peak facility inlet with the flight PALMS instrument in September, 2015. Measurements were made during Fifth International Ice Nucleation Workshop—phase 3 (FIN03). The measurements were carried out between September 14, 2015 and September 27, 2015.

The CARES study was carried out in the Summer, 2010 and included deployment of instruments at two different ground sites, one urban (Sacramento, CA) and another in the Sierra Nevada foothills area rich in biogenic emissions (Cool, CA site) (Zaveri et al., 2012). Thermally-driven winds tend to transport the urban plume into the Sierra Nevada foothills and sometimes back again into the Sacramento area (Zaveri et al., 2012). The laboratory PALMS instrument was deployed at the Cool, CA site at 450 m elevation at 121.02 W, 38.87 N in a trailer throughout the campaign. It sampled ambient air between June 4, 2010 and June 24, 2010.

5.3 Results

Figure C-24 shows the spectra of biological species: *P. syringae* bacteria, Snomax and hazelnut pollen wash water particles. These particles contain both organic and

inorganic compounds. Because they are easy to ionize, the inorganic ions sodium and potassium stand out in the positive spectra despite their minor fraction by mass. Sulfates, phosphates and nitrates are present, and visible in their associations with potassium. Negative spectra are dominated by CN^-, CNO^-, phosphate (PO_2^- and PO_3^-) and sulfate (HSO_4^-). Higher mass associations of potassium and sulfates, phosphates and nitrates occur ($K_3H_2SO_3^-$, $K_2H_3NO_4^-$, $K_3H_2PO_2^-$ and $K_3H_3SO_3^-$). Chlorine is present on some particles. Chlorine is a known contaminant from the Agar growth medium since spectra of aerosolized Agar devoid of bacteria contain large amounts of chlorine (not shown here).

Figure C-25 shows spectra of apatite. In positive polarity, apatite spectra are dominated by calcium, its oxides, and in associations with phosphate ($CaPO^+$, $CaPO_2^+$, $CaPO_3^+$, $Ca_2PO_3^+$ and $Ca_2PO_4^+$) and fluorine (CaF^+, Ca_2OF^+ and Ca_3OF^+). Negative spectra are dominated by phosphates (PO^-, PO_2^- and PO_3^-) and fluorine is often present. Lab-generated apatite spectra analyzed in this study contain little organic. This may be a result of post-processing of the apatite sample, in particular the use of ethanol as a grinding lubricant. In contrast, ethanol was not used in grinding the monazite sample here and its spectra exhibit peaks associated with organic matter (C_2H^-).

Figure C-26 shows spectra of coal fly ash from the J. Robert Welsh Power Plant. The positive spectra contain sodium, aluminum, calcium, iron, strontium, barium and lead. As in apatite, calcium/oxygen, calcium/phosphate and calcium/fluorine fragments are present. Fly ash particles also contain sulfate ($H_3SO_3^+$). The negative spectra contain phosphates (PO_2^-, PO_3^-), sulfates (HSO_4^-) and silicate fragments, such as $(SiO_2)_2^-$, $(SiO_2)_2O^-$, $(SiO_2)_2Si^-$ and $(SiO_2)_3^-$.

The results of HNO_3 processing experiments are also shown in Figures C-25 and C-26. Processing with nitric acid had an effect on both apatite and fly ash: the calcium/fluorine positive markers (CaF^+, Ca_2OF^+ and Ca_3OF^+) and the negative fluorine marker (F^-) are either reduced in intensity or completely absent after processing. Additionally, CN^- and CNO^- appear and/or intensify after processing.

A classifier was designed to use the ratios of phosphate (PO_2^-, PO_3^-) and organic

nitrogen (CN^-, CNO^-) spectral peaks. Those spectral peaks were used for several reasons: (1) they are clearly visible in all biological spectra that were acquired as a part of this study (Figure C-24), (2) they were used to distinguish bioaerosol from other species in previous studies (Creamean et al., 2013; Pratt et al., 2009) and (3) sources of phosphorus on aerosol particles are well-defined and documented in the literature (Mahowald et al., 2008). The only requirement for this analysis was that each spectrum used in the training set contains both phosphate and organic nitrogen (otherwise the ratios used here become undefined). This was ensured by selecting spectra, where $PO_2^- > 0.001$ and $CNO^- > 0.001$. Nearly all biological spectra in the training set satisfied this criterion (Table B.4). Figure C-27A shows normalized histograms of the PO_3^-/PO_2^- ratio for the laboratory aerosol. The aerosols that contain only inorganic phosphorus, such as apatite, monazite and fly ash cluster at PO_3^-/PO_2^- less than 4 and often less than 2. The bioaerosols cluster at PO_3^-/PO_2^- greater than 2 and often greater than 4. Ragweed pollen is an exception, with a wide cluster in PO_3^-/PO_2^- from 1 to 5. Processing of apatite with nitric acid tends to shift the PO_3^-/PO_2^- ratio to larger values, decreasing the disparity from the bioaerosols. Ragweed pollen is an exception, with a wide cluster in PO_3^-/PO_2^- from 1 to 5. Soil dusts are shown in Figure C-27, even though they are not used as training aerosol; their histogram shows a broad distribution with a tail extending into $PO_3^-/PO_2^- > 2$ region, indicating a mixed inorganic/biological composition. In comparison, fertilized soil dusts show a similar distribution to apatite ($PO_3^-/PO_2^- < 4$) due to presence of inorganic fertilizer, which is calcium phosphate.

The SVM algorithm was used here to optimize boundaries between clusters. To do this, the algorithm needs a training dataset, where the classes are known a priori. In this paper, the training dataset is defined in Table B.4. Once an optimized boundary is drawn, some of the training data can still fall on the incorrect side of the boundary, when the clusters are not perfectly separable. Accuracy here is defined as percentage of correctly classified particles in the training set once the optimized boundary is found. A simple 1D classifier can be made based only on the ratio of phosphate peaks PO_3^-/PO_2^- greater or less than 3. The accuracy of this simple filter is 70

- 80% for the materials considered here, with ragweed pollen and fly ash as the greatest sources of confusion between the bioaerosol and non-biological classes. A higher accuracy for differentiation of the bioaerosol and non-biological classes can be achieved if the ratio of organic nitrogen peaks is also taken into account. Figure C-27B shows normalized histograms of CN^-/CNO^- ratios for the test aerosol. In contrast to PO_3^-/PO_2^- ratios, CN^-/CNO^- ratios do not, by themselves, exhibit a clear difference between the classes. A superior separation is achieved when data are plotted in a CN^-/CNO^- vs. PO_3^-/PO_2^- space, as shown in Figure C-28. In this case, two clusters appear. The soil dust class was left out from the training set because it is not known a priori if and how much biological material it contains (classification of soil dusts with the SVM algorithm is discussed later). The boundary between the classes in CN^-/CNO^- vs. PO_3^-/PO_2^- space is non-linear, as shown in Figure C-28. The accuracy in this 2D classification is 97%. As before, ragweed pollen is the cause of most errors; if it is removed from training dataset, the accuracy increases to 99%. Processed mineral dust had a smaller impact on the accuracy: removing it from the training dataset increased the accuracy to 97.5%.

For every observation, a distance from the SVM boundary can be calculated (otherwise known as score). Those distances can then be converted to probability of correct identification. An optimized function to convert scores to probabilities was found by 10-fold cross-validation (Platt, 1999). Because in this experiment the classes are not perfectly separable, the conversion function is a sigmoid. Posterior probabilities near 0 and 1 indicate high-confidence identification. An uncertainty boundary was defined between 0.2 and 0.8. This boundary is shown in Figure C-28. Points that lie in this boundary are marked as low confidence assignments. Those correspond to shaded areas in Figures C-29 and C-30.

Once trained with the training set, the SVM algorithm was used to analyze the FIN03 and CARES field datasets collected at Cool, CA and Storm Peak. As a first step, "phosphorus-containing" particles were identified in both datasets. The criterion for phosphorus-containing used for this work is the presence of both PO_2^- and PO_3^- ions at fractional peak area (area of peak of interest/total spectral signal area) greater

than 0.01. This threshold was set by examination of the ambient mass spectra to determine when the phosphate peaks are distinct. Ambient particles commonly have numerous small peaks at masses below ~200 due to a diversity of organic components. The height of this background is ~0.01 and data below this level are considered uncertain. Phosphorus-containing ambient spectra were then classified by the SVM algorithm as bioaerosol or inorganic phosphorus if the CNO^- ion was also present at fractional peak area greater than 0.001. If CNO^- fractional area was less than 0.001, the spectrum was also classified as inorganic phosphorus.

During the FIN03 campaign, phosphorus-containing particles represented from 0.2 to 0.5% by number of the total detected particles in negative ion mode depending on the sampling day and a 0.4% average for the entire dataset. As shown in Figure C-29A when the binary classifier described in this work was applied to the phosphorus-containing particles, bioaerosol represented a 29% subset by number (i.e., 0.1% of total analyzed particles). During the CARES campaign, phosphorus-containing particles were 1.1% to 4.2% by number of the total particles detected in negative ion mode, with 2.4% average for the dataset (Figure C-30A). Bioaerosol particles represented 63% subset by number (i.e., 1.2% of total analyzed particles). This range (0.1% - 1.2%) is within, and towards the lower end, of previous estimates with biological-specific techniques (Table B.3). This lower end estimate may, in part, be due to PALMS sampling particles in the 200-500 nm diameter range as well as larger sizes. Previous estimates tend to show increased bioaerosol in the super-micrometer range and data are often unavailable for the numerous particles smaller than 500 nm diameter.

The origin of the non-biological phosphate particles is likely phosphate-bearing mineral dust or fly ash. The CARES site experienced influences of aged marine, urban and local biogenic sources. Within the urban plumes, a likely source of inorganic phosphate is industrial combustion aerosol. At Storm Peak a likely source is mining of phosphate rock and nearby monazite deposits. Figure C-29B shows HYSPLIT back trajectories for the ten days of the FIN03 campaign; the air masses sampled cross deposits of either phosphate rock (apatite) or rare earth elements (monazite or carbonatite). As examples, on 09/27 the back trajectory intersects the vicinity of

an active rare earth element (REE) mine in Mountain Pass, CA and on 09/18 and 09/20 the airmass intersected active phosphate mines in Idaho. Although negative spectra of apatite and monazite cannot be definitively differentiated from fly ash or soil dust spectra, positive spectra acquired during FIN03 additionally suggest that monazite-type material was present. In Figure C-25, panels G and H show non-biological phosphate-rich ambient spectra from FIN03. Figure C-25 panels E and F (monazite) contains similar features and matching rare earth elements.

In total, 56% and 36% of phosphate-containing particles analyzed in FIN03 and CARES respectively categorized as biological also contained silicate features. Considered in more detail in the next section, a subset of these may represent internal mixtures of biological and mineral components.

5.4 Discussion

The method of identification of bioaerosol described here is based on ratios of phosphate and organic nitrogen peaks. This work is specific to PALMS but can be considered a starting point from which identification and differentiation can be made with similar instruments. Previous work with PALMS shows this ratio approach can be used to identify differences in chemistry, for example among mineral dusts (Gallavardin et al., 2008). In this case the classes are bioaerosol and non-biological phosphorus; Figure C-27A shows that phosphorus ionizes differently in these classes. In apatite and monazite, phosphorus occurs as calcium phosphate. In biological particles, phosphorus occurs mostly in phospholipid bilayers and nucleic acids. In these experiments, the PO_3^-/PO_2^- ratio of those two forms is different (Figure C-27A). The agricultural soils considered here cluster with the minerals and fly ash and we assume the phosphorus is due to the use of inorganic fertilizer, which is derived from calcium phosphate (Koppelaar and Weikard, 2013). Fly ash aerosol clusters similarly to apatite and monazite but with a wider distribution; this is likely because the chemical from of phosphorus in fly ash is different than in the minerals. Phosphorus present in coal is volatilized and then condenses into different forms during the combustion process (Wang et al.,

2014).

During the FIN03 campaign at Storm Peak, 0.2-0.5% of particles by number detected in negative polarity contained measureable phosphorus (Figure C-29A). On most days, the majority of phosphorus-rich particles were inorganic. Particles with positive spectra showing the characteristics of monazite coupled to back trajectories over source areas suggests the origin of the inorganic phosphate particles. Although apatite/monazite particles make up a small portion of ambient particles at Storm Peak they are potentially interesting not only due to their possible confusion with biological phosphate but also as a tracer for industrial mining and processing activities. Currently, such activities are taking place in Idaho and until very recently at Mountain Pass, CA (U.S. Geological Survey, 2016b,a). Smaller exploration activities are also taking place at the Bear Lodge, WY and the REE-rich areas in Colorado, Idaho and Montana are of interest (U.S. Geological Survey, 2016a).

During the CARES campaign more particles contained phosphorus (1.1% - 4.2%) and a higher percentage of phosphate-rich particles were identified as biological (63% vs. 29% in FIN03). Because the site contains strong local biogenic and urban influences, the sources of biological particles are probably local. As shown in Figure C-30B, aged marine particles were also present on many days; however, only 4% of particles identified as biological also contained markers associated with sea salts.

5.4.1 Comparison with existing literature

Previous studies have attempted to identify bioaerosol with SPMS based on the presence of phosphate and organic nitrate components. Creamean et al. (2013) and Pratt et al. (2009) suggested a "Boolean criterion" where the existence of CN^-, CNO^- and PO_3^- in a particle resulted in its classification as biological. If silicate components were additionally present, the particle was classified as an internal mixture of mineral dust and biological components (Creamean et al., 2013, 2014). Such "Boolean" criteria for particle identification, can be helpful in distinguishing aerosol types when the signatures are unique to one particle type.

The selectivity of this simple three-component filter (presence or absence of CN^-,

CNO^- and PO_3^-) for biological particles was investigated for PALMS using the test aerosol database with results shown in Figure C-31. Note that previous literature does not provide information on the thresholds used to determine presence or absence of ions in analysis of ATOFMS spectra. Furthermore, because of hardware differences, detection limits of PALMS and ATOFMS are known to be different (Murphy, 2007). This analysis focuses on PALMS and the threshold for "presence" was chosen as 0.001, which was observed to be the detection limit for CN^-, CNO^- and PO_3^- in the laboratory aerosol database used here. The simple filter successfully picks biological material. However, it also has a high rate of false positives. For the material that contains inorganic phosphorus (i.e., samples known to be devoid of biological material) the three-component filter selects 56% of fly ash, 56% of agricultural dust and 32% of apatite and monazite. Soil dust is identified as biological 78% of the time.

The effect of misidentification of inorganic phosphate as biological can be considered in the context of the atmospheric abundance of the three major phosphate bearing aerosols: mineral dust, fly ash and bioaerosol (estimates given in Table B.6). Because the emissions estimates vary, the highest fraction of bioaerosol is the case of the highest estimate of bioaerosol coupled to the lowest estimate of fly ash and mineral dust (Table B.6 and Figure C-32A). Conversely, the lowest fraction of bioaerosol is the case of the lowest estimate of bioaerosol coupled to the highest estimate of fly ash and mineral dust (Table B.6 and Figure C-32B).

The misidentification rates noted above are then propagated onto the high and low estimates. As an example, the fraction of aerosol phosphate due to fly ash (1% in the high and 5% in the low bioaerosol estimate) is multiplied by 0.56 to indicate the fraction of fly ash that would be misidentified as biological phosphate with the simple three-component filter. This misidentification effect is repeated for the mineral dust emission rate and misidentification fraction. For simplicity, we considered the mineral dust fraction to be desert soils, termed aridsols and entisols, which are predominantly present in dust-productive regions, such as the Sahara or the dust bowl (Yang et al., 2013). According to Yang and Post (2011), the organic phosphate content of those soils is 5-15% but this is a second order effect when compared to misclassification.

In the high bioaerosol scenario 17% of the phosphate aerosol is biological (Figure C-32A) but when misidentification is considered 81% of particles are identified as such (Figure C-32C). In the low bioaerosol scenario 2% of the phosphate aerosol is biological (Figure C-32B) but when misidentification is considered 77% of the particles are identified as such (Figure C-32D). This illustrates that simplistic identification can lead to large misclassification errors of aerosol sources.

Misidentification can also lead to misattribution. Pratt et al. (2009) analyzed ice residuals sampled in an orographic cloud and suggested a biological source using the simple three-component filter applied to spectra containing calcium, sodium, organic carbon, organic nitrogen and phosphate. The processed apatite spectrum in Figure C-25, devoid of biological material, contains all of these markers. Similar to the Storm Peak dataset, the Pratt et al. (2009) wave cloud occurred in west-central Wyoming which is near the Idaho phosphate rock deposits (Figure C-29) and four U.S. states with active mining of phosphate rock for use as inorganic fertilizer in agriculture (U.S. Geological Survey, 2016b).

As noted above, the Pratt et al. (2009) and Creamean et al. (2013, 2014) studies were performed with a different SPMS, the ATOFMS (Gard et al., 1997; Pratt et al., 2009). Because the ATOFMS uses a desorption/ionization laser of a different wavelength (266 nm) the SVM algorithm used here may not directly translate to that instrument (Murphy, 2007). Instead, the calculation above assumes only that the misidentification rates between the simple three-component filter and the SVM algorithm applies.

5.4.2 Soil dust and internal dust/biological mixtures

Soil dust is an important but complicated category of phosphate-containing atmospheric particles. Modeling studies, such as Mahowald et al. (2008), treat all phosphorus in soil dust aerosol as inorganic. However, the phosphorus in soil investigated here took both organic and inorganic forms. Walker and Syers (1976) proposed a conceptual model of transformations of phosphorus depending on the age of the soil. At the beginning of its development, all soil phosphorus is bound in its primary min-

eral form, matching that of the parent material, which is primarily apatite (Walker and Syers, 1976; Yang and Post, 2011). As the soil ages, the primary phosphorus is released. Some of it enters the organic reservoir and is utilized by vegetation, some is adsorbed onto the surface of secondary soil minerals (non-occluded phosphorus) and then gradually encapsulated by secondary minerals (Fe and Al oxides) into an occluded form. The total phosphorus content of the soil decreases as the soil ages, due to leaching. The organic fraction can encompass microorganisms, their metabolic by-products and other biological matter at various stages of decomposition. Soil microorganisms are the key players in converting organic phosphorus back into the mineral form (Brookes et al., 1984). Yang and Post (2011) estimated organic and inorganic phosphorus content of various soils based on available data. Spodosols (moist forest soils) have the highest fraction of organic phosphorus (~45%) and aridsols (sandy desert soils) have the lowest (~5%) (Yang and Post, 2011). Yang et al. (2013) compiled a global map of soil phosphorus distribution and its forms and found that 20%, on average, of total phosphorus is organic. Wang et al. (2010) arrive at 34% of soil phosphorus as organic globally.

The biological PALMS filter was applied to several soil dust samples (Table B.5). As would be expected, soils collected in areas with less vegetation exhibit smaller biological contributions. We note that organic phosphorus content is not necessarily a direct indicator of microbes since it also encompasses decomposed biogenic and organic matter. At this time, we are not able to delineate between primary biological, biogenic or simply complex organic (such as humic acids) material.

In the FIN03 field dataset, 56% of particles identified as biological also contained silicate markers normally associated with mineral dust. In the CARES dataset the percentage of such particles was 36%. This represents an upper limit of particles that are an internal mixture of dust and biological material. As stated in the last paragraph, this biological material probably does not consist of whole cells sitting on mineral particles; such internally mixed mineral dust particle with surface whole or fragments of biological material are not supported by EM (Peter Buseck, personal communication). It currently remains unclear if such internally mixed particles would

be counted as biological with an optical microscope after fluorescent staining.

Internal mixtures of biological and mineral components were generated in the laboratory in order to investigate this; an exemplary spectrum of such particle is shown in Figure C-33. The spectrum contains alumino-silicate markers consistent with mineral dust together with phosphate markers that, in this case, come from the biological material. In spectra of pure illite, no phosphate markers are present. Using the classifier developed in this paper on the laboratory-generated internally mixed particles correctly identifies the phosphate signatures to be biological.

5.4.3 Uncertainty in bioaerosol identification in PALMS spectra

Phosphorus peak ratios in biological particles cluster differently than in inorganic phosphorus particles with ragweed pollen an exception (Figure C-27A). No satisfactory explanation for this observation has been found although contamination with phosphate fertilizer cannot be ruled out. The accuracy of the biological filter using PO_3^-/PO_2^- and CN^-/CNO^- ratios is 97% with ragweed alone the source of most of the error. This unexplained behavior is a cause for concern, as the list of biological samples used as a training set is extensive, but not exhaustive and other exceptions could exist.

The basic classifier presented in this paper is binary: all phosphate- and organic nitrogen-containing particles are classified either as biological or inorganic. However, spectra whose PO_3^-/PO_2^- and CN^-/CNO^- ratios are very close to the SVM boundary have more uncertain assignments than those whose PO_3^-/PO_2^- and CN^-/CNO^- ratios fall far away from the boundary. In order to provide an additional measure of classification uncertainty, a probability bound was defined as shown in Figure C-28. According to this definition, 96% of particles in the training dataset were classified with high-confidence (Figure C-28). In the FIN03 and CARES field datasets, 79% of phosphate-containing particles were classified with high confidence. The low-confidence assignments are shown on Figures C-29A and C-30A with shaded areas.

The low-confidence assignments in field datasets can be related to chemical processing of particles (either at the source like in soils or during transport) or to internal mixing of biological and inorganic phosphate.

Because soil dusts are a special category, where lines between biological and inorganic phosphorus sources can be blurry because of ongoing chemical transformations, they have higher classification uncertainties than other types of phosphate-containing aerosols. In the field data, dust/biological mixtures (defined as particles classified as biological with silicate features) are overrepresented in the low-confidence assignments. Dust/biological mixtures constitute 26% (CARES) - 46% (FIN03) of high-confidence assignments and 64% (CARES) - 68% (FIN03) of low-confidence assignments. Moreover, only 75% of phosphate-containing soil dust particles were classified with high confidence. However, in simple two-component internal mixtures of dust and biological fragments (Figure C-33) phosphate features can be identified as biological with high confidence (98%).

Because the field studies were performed during different time periods, it was difficult to control for a constant excimer laser fluence. However, laser fluence was similar for all laboratory samples acquired (3-5 mJ pulse energy). This is a possible source of uncertainty, as fragmentation patterns can differ depending on pulse energy.

5.5 Conclusion

This paper examines criteria that can be used with SPMS instruments to identify bioaerosol. We propose a new technique of bioaerosol detection and validate it using a database of phosphorus-bearing spectra. A simple binary classification scheme was optimized using a SVM algorithm, with 97% accuracy. Ambient data collected during FIN03 and CARES campaigns are then analyzed with this binary classifier. Particles with phosphorus were up to 0.5% for FIN03 and 4.2% for CARES by number of all ambient particles in the 200 - 3000 nm size range. On average, 29% (FIN03) and 63% (CARES) of these particles were identified as biological.

Our work expands on previous SPMS sampling that used a more simple Boolean

three marker criterion (CN^-, CNO^- and PO_3^-) to classify particles as primary biological or not (Creamean et al., 2013, 2014). We show that the presence of these markers is necessary but not sufficient. We show a false positive rate of the Boolean filter between 64% and 75% for a realistic atmospheric mixture of soil dust, fly ash and primary biological particles.

The trained SVM algorithm was also used to measure the biological content of soil dusts. Different soil dust samples can have different content of biological material with a range from 2 - 32% observed here. Consistent with the literature, samples taken from areas with vegetation exhibit a higher biological content.

5.6 Acknowledgements

The authors gratefully acknowledge funding from NASA grant NNX13AO15G, NSF grant AGS-1461347, NSF grant AGS-1339264, and DOE grant DE-SC0014487. M. A. Z. acknowledges the support of NASA Earth and Space Science Fellowship. The authors would like to thank Ottmar Moehler and the KIT AIDA facility staff for hosting the FIN01 workshop and Gannet Hallar, Ian McCubbin and DRI Storm Peak Laboratory for hosting the FIN03 workshop. The authors thank the entire CARES, FIN01 and FIN03 teams for support and Peter Buseck for useful discussions.

This chapter has been previously published: Zawadowicz, M. A., Froyd, K. D., Murphy, D. M., Cziczo, D. J.: Improved identification of primary biological aerosol particles using single-particle mass spectrometry, Atmos. Chem. Phys., 17, 7193-7212, 2017.

doi: 10.5194/acp-17-7193-2017.

5.7 Appendix: Machine Learning Approach Details

5.7.1 Algorithm description

Support vector machines (SVMs) are family of algorithms that enable binary classification of data. The training dataset is given as $(\mathbf{x}_i, y_i)$, where $\mathbf{x}_i$ is the ith vector

of inputs with M components and y_i is a label associated with $\mathbf{x}_i$. In the case described in this paper, the input vectors are points in two-dimensional CN^-/CNO^- vs. PO_3^-/PO_2^- space (i.e. every point on Figure C-28 is an input vector $\mathbf{x}$) and their labels are either "biological" or "inorganic". A discriminant function can be defined (Ben-Hur et al., 2008):

$$f(\mathbf{x}) = \mathbf{w} \cdot \mathbf{x} + b \tag{5.1}$$

Geometrically, $\mathbf{w} \cdot \mathbf{x} - b = 0$ describes a hyperplane, where $\mathbf{w}$ is its normal vector and b specifies the offset of the hyperplane from the origin. This is shown schematically in Figure C-34. Thus defined hyperplane separates the data into two classes, one where $f(\mathbf{x}) > 0$ and one where $f(\mathbf{x}) < 0$. The value of $f(\mathbf{x})$ for any $\mathbf{x}$ is known as the score.

Because there are many hyperplanes that can be drawn to separate the two hypothetical classes shown in Figure C-34, the algorithm computes the optimized separating hyperplane. In order to do this, it maximizes the margin, defined as the distance of the closest input vector to the decision boundary (Ben-Hur et al., 2008). Those closest input vectors are known as support vectors and they are indicated by filled symbols in Figure C-34. For the support vectors, the discriminant function is defined as $f(\mathbf{x}) = \pm 1$ and parameter b is chosen such that the hyperplane lies halfway between the closest positive and the closest negative support vector (Ben-Hur et al., 2008). The margin is then defined as $1/||\mathbf{w}||$ and in order to maximize the margin, the following optimization problem is solved (Ben-Hur et al., 2008):

$$\begin{aligned} &\underset{\mathbf{w},b}{\text{minimize}} \quad \frac{1}{2}||\mathbf{w}||^2 \\ &\text{subject to} \quad y_i(\mathbf{w} \cdot \mathbf{x_i} + b) \geq 1, \; i = 1, \ldots, n. \end{aligned}$$

Where n denotes the total number of input vectors in the training set. This quadratic optimization problem can be solved using standard computational tools.

The above description in the simplest case of the SVM algorithm also known as the hard margin SVM and it applies only to perfectly separable data. The modern

version of the algorithm, described by Cortes and Vapnik (1995) is the soft margin SVM, which allows for non-perfectly separable data. In the soft margin version of the algorithm, the optimization problem changes to (Ben-Hur et al., 2008; Cortes and Vapnik, 1995):

$$\begin{aligned} \underset{\mathbf{w},b}{\text{minimize}} \quad & \frac{1}{2}||\mathbf{w}||^2 + C\sum_{i=1}^{n}\xi_i \\ \text{subject to} \quad & y_i(\mathbf{w}\cdot\mathbf{x_i}+b) \geq 1-\xi_i,\ i=1,\xi_i \geq 0. \end{aligned} \tag{5.2}$$

Here non-negative slack variables, $\xi_i \geq 0$ are introduced to allow some input vectors to be inside the margin or misclassified. Because it is still advantageous to minimize the number of such errors, a term $C\sum_{i=1}^{n}\xi_i$ is also minimized. Variable C assigns a "penalty" to errors and it determines a trade-off between increasing the margin size and minimizing the misclassifications (Ben-Hur et al., 2008; Cortes and Vapnik, 1995).

The above described versions of the algorithm only work for linear cluster boundaries. For real data, however, a non-linear decision boundary might offer the best performance. A non-linear classifier can be defined using the "kernel trick" as first described by Boser et al. (1992). When two-dimensional data cannot be separated using a linear boundary, it can still be projected into a higher dimensional space ("feature space"), where an optimum separating hyperplane exists. Kernel functions are used in order to make this problem computationally manageable.

Using the method of Lagrange multipliers, the optimization problem 5.2 can be rewritten in terms of variables α_i as follows (Ben-Hur et al., 2008; Cortes and Vapnik, 1995; Boyd and Vandenberghe, 2004)

$$\begin{aligned} \underset{\alpha}{\text{maximize}} \quad & \sum_{i=1}^{n}\alpha_i - \frac{1}{2}\sum_{i=1}^{n}\sum_{j=1}^{n} y_i y_j \alpha_i \alpha_j (\mathbf{x}_i \cdot \mathbf{x}_j) \\ \text{subject to} \quad & \sum_{i=1}^{n} y_i \alpha_i = 0, 0 \leq \alpha_i \leq C. \end{aligned} \tag{5.3}$$

This is the so-called "dual" representation of the problem, which makes it very clear that in this algorithm, the input vectors $\mathbf{x}$ appear only inside the inner prod-

uct (Ben-Hur et al., 2008; Cortes and Vapnik, 1995; Boyd and Vandenberghe, 2004). Vector $\mathbf{w}$ satisfies $\mathbf{w} = \sum_{i=1}^{n} y_i \alpha_i \mathbf{x}_i$. Also, $\alpha_i > 0$ for the support vectors and $\alpha_i = 0$ only when $\mathbf{x}_i$ lies on the correct side of the boundary (Ben-Hur et al., 2008; Cortes and Vapnik, 1995)

The discriminant function 5.1 in dual representation becomes

$$f(\mathbf{x}) = \sum_{i=1}^{n} y_i \alpha_i (\mathbf{x}_i \cdot \mathbf{x}) + b \tag{5.4}$$

Note that similarly to 5.3 it also depends on the input vectors only through their inner products. This ensures that the kernel trick can be applied.

Let function ϕ be the mapping function of the input data into the feature space. We can replace the inner products of input vectors in equations 5.3 and 5.4 with the inner products of their transformations into the feature space as follows:

$$\begin{aligned} \underset{\alpha}{\text{maximize}} \quad & \sum_{i=1}^{n} \alpha_i - \frac{1}{2} \sum_{i=1}^{n} \sum_{j=1}^{n} y_i y_j \alpha_i \alpha_j (\phi(\mathbf{x}_i) \cdot \phi(\mathbf{x}_j)) \\ \text{subject to} \quad & \sum_{i=1}^{n} y_i \alpha_i = 0, 0 \leq \alpha_i \leq C. \end{aligned}$$

and

$$f(\mathbf{x}) = \sum_{i=1}^{n} y_i \alpha_i (\phi(\mathbf{x}_i) \cdot \phi(\mathbf{x})) + b$$

We can now define a kernel function that satisfies (Ben-Hur et al., 2008; Hofmann et al., 2008; Boser et al., 1992):

$$k(\mathbf{x}, \mathbf{x}') = \phi(\mathbf{x}) \cdot \phi(\mathbf{x}')$$

The optimization problem and the discriminant function now simplify to

$$\begin{aligned} \underset{\alpha}{\text{maximize}} \quad & \sum_{i=1}^{n} \alpha_i - \frac{1}{2} \sum_{i=1}^{n} \sum_{j=1}^{n} y_i y_j \alpha_i \alpha_j k(\mathbf{x}_i, \mathbf{x}_j) \\ \text{subject to} \quad & \sum_{i=1}^{n} y_i \alpha_i = 0, 0 \leq \alpha_i \leq C. \end{aligned}$$

and

$$f(\mathbf{x}) = \sum_{i=1}^{n} y_i \alpha_i k(\mathbf{x}_i, \mathbf{x}) + b$$

Note that using the kernel function is computationally simpler because explicit transformations into the feature space do not need to be carried out.

Some examples of commonly used kernel functions include the polynomial kernel: $k_{d,\kappa}(\mathbf{x}, \mathbf{x}') = (\mathbf{x} \cdot \mathbf{x}' + \kappa)^d$ and the Gaussian kernel: $k_\sigma(\mathbf{x}, \mathbf{x}') = \exp(-\frac{1}{\sigma}||\mathbf{x} - \mathbf{x}'||^2)$ (Ben-Hur et al., 2008).

The problem described in this paper, using support vector machines to compute a binary classifier of biological and non-biological PALMS spectra, uses the modern "soft-margin" version of the SVM algorithm and a Gaussian kernel. The algorithm outputs scores ($f(\mathbf{x})$ values) for every training vector provided (and subsequently for the "unknown" data to be classified). Geometrically, score translates to the distance from the decision boundary and therefore it is proportional to classification uncertainty, but it is not an explicit probability of correct classification. In order to simplify the interpretation of scores as uncertainties, Platt scaling is performed on the score values (Platt, 1999). This involves fitting the scores with the following function:

$$P(y = 1|x) = \frac{1}{1 + \exp(Af(\mathbf{x}) + B)}$$

Where A and B are the fitting constants. To avoid overfitting, 10-fold cross-validation is applied.

5.7.2 Some further work on machine learning applied to PALMS data

Constructing a binary classifier that separates biological and non-biological particle spectra in terms of ratios of their phosphate and organic nitrogen peaks is a simple but illustrative application of machine learning. The four peaks considered in this work (CN^-, CNO^-, PO_3^- and PO_2^-) were used in order to keep consistent with previous

literature approaches. When this is not a concern, all peaks in a spectrum could be used to build more complex classifiers with larger predictive power.

As an extension of this work, an ensemble of predictive models was used to extend the classification into a larger input space. In this case, the input vectors $\mathbf{x}_i$ consist of normalized stick mass spectra with m/z values from 1 to 220 and the aerodynamic size information (i.e. every $\mathbf{x}_i$ is 221-dimensional). Positive and negative spectra are considered separately. The classification models used in this case are not support vector machines, but decision trees, which are statistical decision models that classifiy based on a series of comparisons relating variables of input vector $\mathbf{x}_i$ to a learned threshold value (Breiman, 2001). A tree is a hierarchy of nodes, which connect to other nodes via branches: at each node, one or more variables of $\mathbf{x}_i$ are compared to threshold values which determine which branch is followed and this branch in turn leads to a different node. After a series of nodes, a class is assigned to $\mathbf{x}_i$. While decision trees can be constructed manually by an operator by defining a set of thresholds and outcomes, in the machine learning version, the thresholds and tree structures are learned automatically from the training data.

In order to create a more robust classifier, an ensemble of decision trees is grown, each tree independent of the others. In this case, a total of 1000 trees were grown, each using an independent random sample drawn from the training data. On average, each tree was built with 63% of the data. The remaining 47% of the training sample not used to grow the tree can be used to asses its classification error (this is the "out-of-bag" sample). In order to classify an input $\mathbf{x}_i$, each tree assigns a label to $\mathbf{x}_i$ and then, all trees "vote" on the final classification. Each vote is weighed equally and the final classification is the majority choice.

The training dataset used with this algorithm consisted of positive and negative mass spectra of atmospherically-relevant lab-generated aerosol sampled at the Karlsruhe Institute of Technology. The Aerosol Interactions and Dynamics in the Atmosphere (AIDA) facility was used during the Fifth Ice Nucleation workshop—part 1 (FIN01). The aerosol types are fully described in Table B.7.

Not all mass peaks are equally important to the classification. In addition, in-

correct mass assignments at high masses can introduce noise. The algorithm reduces dimensionality by comparing the performance of decision trees before an after removing information about each element of $\mathbf{x}_i$. In this way, the variables can be ranked in terms of their significance to the classification. Table B.8 shows the top 20 highest ranked positive and negative variables. Next, the algorithm was re-trained using only the most highly ranked variables to reduce the dimensionality and improve the speed of calculation. The final dimensionality was determined by adding variables in order of their ranking and observing if performance of the classifier increases. After two e-foldings in classification error, no further variables were added to the model. In addition, in the final model, lead isotopes (^{204}Pb, ^{206}Pb, ^{207}Pb, ^{208}Pb) were combined because they tend to suffer from incorrect mass assignments. This is caused by loss of resolution for high m/z values (see discussion in Chapter 3).

A convenient way to visualize the results of such a classification are confusion matrices. A confusion matrix shows misclassification tendencies by pair-wise matching model prediction with true aerosol labels. In Figure C-35, confusion matrices for positive and negative polarity classifiers have been normalized along each column to show the fraction of mislabelled aerosol particles for the out-of-bag samples. From the figure, the overall classification accuracy for both positive and negative classes is good, usually within 70% - 100%. Figure C-35 splits the aerosols by chemically similar classes. Within those classes, fertile soils (Argentina, China, Ethiopian, Moroccan and German soils) show the most classification errors (71% - 88%). This is expected due to the heterogeneity and chemical complexity of fertile soils. Pure dusts (ATD, illite and feldspars) can be separated very well from each other ($>$ 90%), but errors up to can occur when Feldspar coated with sulfuric acid or SOA is considered ($>$ 75%). This is also expected because coatings were thin. Additionally, feldspar coated with sulfuric acid is often mistaken for soot (75% accuracy) in negative polarity only, which is probably contamination of one aerosol type with another. The biological class (Agar growth medium, bacteria, cellulose, hazelnut pollen and Snomax) can be separated from each other and from other classes with very high accuracy (usually $>$ 90%, except for cellulose which was known to have some dust contamination).

This shows that a more complex classifier for bioaerosol could be written when more mass spectral peaks are considered. Of particular interest would be extending the bioaerosol classification to positive polarity and trying to separate different types of bioaerosol from one another. The list of aerosols sampled at AIDA does not include all possible interferences, however, as bioaerosol in positive polarity can often look similar to very processed atmospheric dust, biomass burning or sea salt. High degree of processing was not considered here and there are also no lab examples of biomass burning or sea salt.

5.7.3 Future work: Ambient aerosol and other SPMS instruments

The ensemble classifier performs well on AIDA laboratory data, as evident in Figure C-35. However, extending the ensemble classification to ambient aerosol is a difficult task. In general, the predictive power of this classifier is limited by how exhaustive the training dataset is. The AIDA dataset leaves out several important ambient aerosol classes, such as biomass burning or sea salt. Unfortunately, some of those natural particles are difficult to approximate exactly in a lab experiment, as they undergo various degrees of processing in the atmosphere. As seen in Table B.8, some of the best predictors can be organic, sulfate or nitrate ions, all of which will be heavily influenced by atmospheric processing. Features need to be pre-selected with this in mind if the classifier is to be generalizable. Additionally, particles that are internal mixtures of two distinct types might be more difficult to handle.

It is possible that for the best classification of ambient aerosol particles, supervised and unsupervised techniques need to be used in tandem. That is, unsupervised clustering techniques can be first used on ambient data to define natural cluster patterns and the resulting clusters can then be matched to reference laboratory particle types using supervised learning methods. This would help to avoid unintentional biasing of analysis of ambient datasets by attempting to compare them with a possibly limited, pre-determined set of laboratory data. Such an approach can be considered as future

work.

Overall, machine learning techniques offer significant promise for analysis of single particle mass spectra from any instrument. However, for laser ionization techniques, fragmentation patterns can be sensitively dependent on the fluence and wavelength of the ionization laser used. Because lasers in used in different SPMS instruments are often different, the classifiers described here are not expected to be the same for other instruments, such as SPLAT or ATOFMS. While the machine learning classifiers cannot be translated from one instrument to another, the techniques discussed here for derivations of the classifiers are applicable to any instrument that measures physical and chemical properties of particles. This also extends to instruments other than laser ionization mass spectrometers: AMS spectra could be feasibly analyzed with those techniques, as well.

We thank Costa Christopoulos for writing the ensemble classifier. Selected content from this Appendix is in preparation for publication in Atmospheric Measurement Techniques.

Chapter 6

Measurement and modeling of the vertical and seasonal abundance of bioaerosol

Measuring the composition of atmospheric aerosol is important for understanding radiative balance, cloud formation and chemical reactions in the atmosphere. As one example, certain species of bacteria have been found to be efficient ice nucleating particles (INPs) in laboratory studies, and it has therefore been suggested that biologically derived aerosol particles, or "bioaerosol", might play a role in atmospheric ice formation and precipitation. Observation and modeling of bioaerosol have been limited by sparse data on spatial and temporal variability. Here we apply a new methodology to measurements of single particles over four airborne sampling campaigns to derive seasonally-resolved vertical profiles of bioaerosol. The measurements are in general agreement with a global aerosol model and can be used to show that bioaerosols are at least ten times less abundant than mineral dust in the free and upper troposphere. In contrast, previous studies that report higher concentrations of bioaerosol are likely to have misidentified phosphorus-containing mineral dust as bioaerosol.

6.1 Introduction

The effects of aerosols, clouds and their mutual interactions on the climate system are more uncertain than those of greenhouse gases (Boucher et al., 2013). Aerosols can influence the Earth's radiative budget both directly, by scattering and absorbing incoming solar radiation, and indirectly, by nucleating clouds. Clouds can then scatter solar radiation and trap terrestrial heat with a balance that depends on their specific properties (Boucher et al., 2013). Water droplets and ice crystals nucleate on pre-existing particles termed cloud condensation nuclei (CCN) and ice nucleating particles (INPs), respectively. Bioaerosol particles can act as efficient CCN and, because certain bacteria have been shown to be efficient INPs in laboratory studies (Möhler et al., 2008), it has been proposed that bioaerosol could play a role in atmospheric ice nucleation (Möhler et al., 2007) although most in situ studies do not find evidence of it (Cziczo et al., 2013; Ebert et al., 2011). In order to model the importance of this effect, measurements of bioaerosol in the atmosphere at cloud-forming altitudes are necessary. Current emissions inventories are sparse, and most observations are carried out at ground level, which is difficult to translate to the free troposphere, i.e., above the planetary boundary layer.

Bioaerosol originates from a myriad of sources, including, but not limited to, microbes, fungal spores, pollen, and small fragments of vegetation (Després et al., 2012). Prior to the development of portable field sensors, measurements of atmospheric bioaerosol used off-line methods on collected aerosol, such as cultivation, fluorescent labeling, optical and electron microscopy (EM) and DNA amplification (Després et al., 2012; Burrows et al., 2009). Historical data from cultivation and fluorescent labeling/microscopy yields estimates of total bioaerosol concentrations in near-surface air between 1×10^4 m^{-3} and 7×10^5 m^{-3}, depending on the ecosystem (Burrows et al., 2009). Recent flow cytometry measurements at a remote mountain site reported bacterial concentrations between 1×10^3 m^{-3} and 1×10^5 m^{-3}, depending on the season (22% of all particles greater than 0.5 μm, on average) (Bowers et al., 2012). Other measurements, using a combination of scanning electron microscopy and optical mi-

croscopy, found 6×10^5 m^{-3} bioaerosol in the remote atmosphere (20% of all particles greater than 0.2 μm) (Matthias-Maser et al., 2000) and 3×10^6 m^{-3} in a semi-rural location (24% of all particles greater than 0.2 μm) (Jaenicke, 2005), averaged over the course of one year. In the marine atmosphere, transmission electron microscopy measurements reported concentrations, $\sim 1 \times 10^6$ m^{-3} bacteria (Pósfai et al., 2003) (1% of all particles greater than 0.2 μm, converted to absolute concentration using accumulation mode total aerosol measurements at a nearby location (Brechtel et al., 1998)).

In situ and real-time detection is now possible with commercial monitors that probe atmospheric aerosol that fluoresces when excitepd with UV radiation (Kaye et al., 2005). One such sensor was recently used on aircraft in the southeastern U.S. to report between 1×10^4 m^{-3} and 3×10^5 m^{-3} fluorescent particles in vertical profiles from surface level to upper troposphere (5-10% of total particles in the 0.6 - 5 μm range) (Ziemba et al., 2016). A similar technique was used to derive vertical profiles of fluorescent particles over the U.S. Great Plains (Twohy et al., 2016). Concentrations up to 1×10^3 m^{-3} of fluorescent particles in the 0.8 - 12 μm range were found in the mid- to upper troposphere (Twohy et al., 2016).

Ground- and aircraft-deployable instruments that determine the composition of single aerosol particles using mass spectrometry have existed since the mid-1990's and have generated an extensive record of atmospheric aerosol composition (Murphy, 2007). If bioaerosol can be properly distinguished, these data offer an opportunity to extend our knowledge of bioaerosol abundance and also link historic measurements and modern instrumentation specifically designed for their detection. Recently, bioaerosol particles have been distinguished using the presence and relative magnitude of phosphate and organic ion peaks in mass spectra (Zawadowicz et al., 2017). Using this technique, we derive vertical profiles—from the boundary layer to the free troposphere—from four airborne measurement campaigns. These datasets span the continental United States and two seasons: the New England Air Quality Study (NEAQS, June-August, 2004), Mid-latitude Airborne Cirrus Properties Experiment (MACPEX, March-April, 2011), Deep Convective Clouds and Chemistry (DC3,

May-June, 2012) and Studies of Emissions and Atmospheric Composition, Clouds and Climate Coupling by Regional Surveys (SEAC^{4}RS, August-September, 2013). We compare our vertical profiles to a global microphysics model (GLOMAP-mode), which includes bioaerosol emissions (Spracklen and Heald, 2014). Additionally, we conducted a direct comparison of the mass spectrometer and Wideband Integrated Bioaerosol Sensor (WIBS), a fluorescence technique, during the Fifth Ice Nucleation Workshop—phase 3 (FIN03), which took place at Storm Peak Laboratory, a high-altitude site atop Mt. Werner in Colorado (elevation: 3220 m M.S.L) during September, 2015.

6.2 Experimental Methods

The Particle Analysis by Laser Mass Spectrometry (PALMS) instrument was used for mass spectrometry and has been described previously (Murphy, 2007). The instrument can be deployed on the ground or on aircraft. The method to differentiate bioaerosol from phosphate-bearing mineral dust species has also been previously described (Zawadowicz et al., 2017). Briefly, it relies on a binary classifier derived by analysis of a large library of single particle mass spectra of biological, mineral and anthropogenic origin and application of a support vector machine classifier (Zawadowicz et al., 2017). The commercial fluorescence sensor used for this study was the Wideband Integrated Bioaerosol Sensor (WIBS-4A, DMT, Boulder, CO). We use the modal version of the Global Model of Aerosol Processes (GLOMAP-mode) with bacteria and fungal spore emissions included (Spracklen and Heald, 2014).

6.2.1 Particle Analysis by Laser Mass Spectrometry (PALMS)

The NOAA PALMS instrument has been discussed in detail elsewhere (Cziczo et al., 2006; Thomson et al., 2000). Briefly, PALMS uses an aerodynamic lens inlet to sample aerosols and impart them with a size-dependent velocity distribution (Zhang et al., 2002, 2004). Aerodynamic particle diameter is measured by timing the particle time of flight between two continuous-wave laser beams (532 nm Nd:YAG in laboratory

PALMS and 405 nm diode in flight PALMS). The particles are ablated and ionized in one step by a 193 nm excimer laser. A unipolar reflectron time of flight mass spectrometer is then used to acquire mass spectra. Due to the laser fluence used for desorption and ionization ($\sim 10^9$ W/cm^2), PALMS spectra show both atomic ions and ion clusters. SPMS is considered a semi-quantitative technique because the ion signal depends on the ionization potential of the substance and its abundance (Murphy, 2007). Additionally, the ionization potentials can depend on the overall chemical composition of the particle (matrix effects) (Murphy, 2007). The lower particle size threshold for PALMS is set by the amount of detectable scattered light at ~200 nm and the upper size threshold is set by the aerodynamic lens at ~3 μm (Cziczo et al., 2006). The 193 nm excimer laser can ionize all atmospherically-relevant particles within this size range with no known detection bias (Murphy, 2007). Currently, there are two builds of the PALMS instrument, and both of these have been used for this work. The laboratory PALMS is a working prototype for the flight PALMS, which is more compact and can be flown on WB-57 or DC-8 aircraft (Thomson et al., 2000).

6.2.2 Wideband Integrated Bioaerosol Sensor (WIBS)

WIBS (Droplet Measurement Technologies, Boulder, CO) is a commercial sensor that measures the optical size and fluorescence of individual particles which are used as a proxy for bioaerosol. Briefly, particles scatter light during transit of a 635 nm laser beam, which triggers the sequential firing of xenon flash lamps filtered to emit at 280 nm and 370 nm. The resulting emissions are imaged onto PMTs filtered to detect fluorescent light in two bands: 310 - 400 nm (the FL1 detector) and 420 - 650 nm (the FL2 detector). For data collected in 2015 at the Storm Peak Laboratory, the WIBS was run at an increased gain such that it was able to count, size and retrieve fluorescent information for particles between 0.4 and 10 μm. The counting efficiency in this size window was assessed by comparison with a co-located Laser Aerosol Spectrometer (LAS, manufactured by TSI Incorporated, Shoreview, MN) and the agreement between the two instruments was within 10% . The excitation and emission wavelengths were chosen to target fluorescence expected from tryptophan, an amino acid

and NADH, a by-product of bacterial metabolism (Gabey et al., 2010; Kaye et al., 2000, 2005). The FL1 detector detects fluoresence resulting from the 280 nm excitation and is saturated by the 370 nm flash while the FL2 detector detects fluorescence resulting from both flashes. Thus, each fluorescent particle can have signal in any of three "channels" and we use the associated categorization scheme described in Perring et al. (2015), along with laboratory results of known bioaerosol (Hernandez et al., 2016) to interpret fluorescent aerosol concentrations. What follows is a more detailed discussion of this interpretation.

Hernandez et al. (2016) report, for example, that bacteria generally have signal in the FL1 detector following 280 nm excitation (denoted channel A in Perring et al. (2015)) and do not have signal in either of the other channels. Similarly, fungal spores all tend to have signal in channel A and sometimes have signal detected by the FL2 detector following 280 nm excitation (channel B) and 370 nm excitation (channel C). Using the Perring et al. (2015) categorization this would be denoted as a mixture of types A, AB and ABC. Pollen tends to always have signal in channel C and sometimes has signal in channels A and B; in other words pollen appears as a mixture of types C, BC and ABC. Type B particles (i.e. particles for which the only fluorescent signal is seen by FL2 following 280 nm excitation) are very rarely found in tests of known bioaerosol and are, instead, frequently observed in ambient data during periods of biomass burning influence. Thus, for the present study, we derive our implied bioaerosol concentrations from the WIBS as the sum of all observed particles of types A, AB, ABC, BC or C and we exclude particles exhibiting type B fluorescence. Very few type AC particles are observed in the lab or in ambient data, however they are also excluded from reported bioaerosol concentrations in this study.

In typical applications size is also used as an identifying factor to further reduce the likelihood of non-biological fluorescent interferences. The theory behind this is that, if there are non-biological interferences in the accumulation mode, they can affect derived bioaerosol concentrations substantially even if only a tiny fraction of the accumulation mode number contributes. Therefore submicron fluorescent particles are often excluded from analysis. Here, in order to maximize the size range of

overlap between the PALMS and the WIBS, we have not excluded particles based on size though we note that there are potential interferences in the accumulation mode that are spectrally similar to known bioaerosol and which may impact our reported concentrations at the smaller sizes.

6.2.3 Field data

Four flight data sets included the New England Air Quality Study (NEAQS), consisting of 17 research flights on WP-3D aircraft in the summer of 2004 (Peltier et al., 2007). The flights were concentrated around New England and they were the lowest in altitude compared to the others used in this work. The 2012 Deep Convective Clouds and Chemistry (DC3) campaign was aimed at understanding the effect of convective storms on the upper troposphere (Barth et al., 2015). PALMS was flown on the NASA DC-8 aircraft and the flights were concentrated around Colorado, Kansas and Oklahoma. During the 2013 Studies of Emissions and Atmospheric Composition, Clouds and Climate Coupling by Regional Surveys (SEAC^{4}RS) field mission, PALMS was also deployed on the DC-8, and the flights included Western and Central U.S. (Toon et al., 2016). The 2011 The Mid-latitude Airborne Cirrus Properties Experiment (MACPEX) campaign was based in Houston, TX and it was focused on cirrus cloud properties (Cziczo et al., 2013). PALMS was deployed on the WB-57 aircraft. Flights focused on central U.S. and they reached higher altitudes than the other three campaigns used in this work.

The ground dataset used to compare WIBS and PALMS was acquired as a part of the Fifth Ice Nucleation Workshop—phase 3 (FIN-3). The flight PALMS instrument was used to sample ambient air at Storm Peak Laboratory in September, 2015. WIBS was used to sample the ambient air using the same inlet.

6.2.4 Data Analysis

The PALMS spectra considered here are negative-polarity only, as successful classification of bioaerosol can only be performed in negative mode, where phosphorus-

containing ions have the higher signal. Definitions and methods for classification of single particle spectra of bioaerosol and inorganic phosphorus-rich particles were described previously (Zawadowicz et al., 2017). Briefly, a library of single particle phosphorus-rich PALMS spectra of known composition was constructed, including biological, mineral and combustion aerosols. Those spectra were plotted in a CN^-/CNO^- vs. PO_3^-/PO_2^- space, according to relative abundances of phosphate and organic nitrate ions. A two-dimensional boundary for a binary classifier was calculated using support vector machines, a machine learning algorithm. This trained classifier can now be used on unknown data which contains phosphate and organic nitrate ions.

Criteria for classification of PALMS spectra as mineral dust in the negative mode have also been described previously (Cziczo et al., 2013). Classification relies on the presence of alumino-silicate oxide signatures, such as $AlSiO_x^-$, SiO_x^-, AlO_x^- and Si^-, and to a lesser extent, FeO_x^- and CrO_x^-. Because negative silicate ions have a lower ionization potential than sulfate or nitrate ions, they can fall below the detection threshold in spectra. Numbers reported in this paper should be considered a lower bound for mineral particles.

6.2.5 Modeling

The aerosol microphysics model used in this study is the modal version of the Global Model of Aerosol Processes (GLOMAP-mode) with incorporated fungal spore and bacteria emissions, as described previously (Spracklen and Heald, 2014; Hoose et al., 2010). Fungal spore emissions are driven by leaf area index (LAI) and water vapor concentrations (Heald and Spracklen, 2009) and bacteria emissions are implemented following Hoose et al. (2010).

6.3 Results

Flight tracks of the four field campaigns considered are shown in Figure C-36. The datasets were filtered for three types of particles; example spectra are shown in Fig-

ure C-37: bioaerosol (panel A), inorganic phosphorous-bearing mineral dust (panel C) and silicate mineral dust (panel E). Note that inorganic phosphorous particles have many of the same chemical features and similar size distributions (panels B and D) to bioaerosol and may have been previously confused with bioaerosol (Zawadowicz et al., 2017). Internal mixing (i.e., where silicate mineral features also exist on a bioaerosol particle) is not uncommon and might represent particles derived from fertile soils (Zawadowicz et al., 2017).

In these data, bioaerosols comprised 0.03-0.87% of particles in the 0.3 - 4 μm diameter size range. The relative abundance falls with altitude, and by cirrus cloud altitudes (>4 km) bioaerosol is <0.07% (Figure C-36). Silicate mineral dust particles, known to be effective INPs at these conditions (Atkinson et al., 2013), comprise 0.05 - 7% of particles at cirrus cloud altitudes. At intermediate altitudes (2 km - 4 km), bioaerosol particles comprise on average 0.15% with silicates $\sim$17 times more abundant. Vertical profiles of inorganic phosphorous-rich particles align with those of mineral dust, which likely reflects similar surface sources such as saltation or agricultural fertilizer use (Koppelaar and Weikard, 2013). Depending on the campaign and season, 30% - 82% of all bioaerosol particles also had silicate features (i.e., 0.01 - 0.56% of particles overall). Bioaerosol concentrations decrease with altitude faster than either inorganic phosphate-rich or mineral dust particles. Because the size distributions of all three particle types are similar (Figure C-37), mechanisms other than gravitational settling may influence the preferential removal of bioaerosol.

Concentrations of bioaerosol calculated here should be interpreted with the instrumental size range ($\sim$0.3 - 4 μm) in mind. Other instruments are sensitive to different size ranges. WIBS, for example, reports diameters between 0.5 μm and 16 μm (Gabey et al., 2010), and there is no technical upper limit with microscopy. Bioaerosol can be relatively large. For example, some pollen grains range from 10 μm to greater than 100 μm in diameter (Emberlin, 2008) although the atmospheric lifetime of $\sim$100 μm particles is short due to both gravitational settling and wet-depositional processes (Seinfeld and Pandis, 2006); this also highlights the difference between a surface and free tropospheric abundance. In the FIN03 study, WIBS provided loadings in the size

range of overlap with the PALMS (0.4 - 4 μm) of all particles for which fluorescence signals matched measurements of test bioaerosol. We note that positive interferences are likely worse at smaller sizes where accumulation-mode aerosol number increases dramatically which is why previous studies have often discussed only supermicron fluorescent particle loadings. The field measurements may therefore represent fragments of original pollen grains, spores or bacteria. Figure C-38 shows a comparison as a percentage of total particles detected. The percentages reported by the fluorescence sensor are similar, but on average 1.8 times higher than those reported by the mass spectrometer, over the 0.5 - 4 μm size range common to both instruments. In an intermediate size range, 1.5 - 3 μm, the agreement is within 10%. The overall bioaerosol abundance reported by both instruments, <1% of total particles in the 0.5 - 4 μm size range, is consistent with EM results (Pósfai et al., 2003).

The paucity of bioaerosol measurements translates into uncertainties in the emission inventories that are used to assess global effects in models. Contemporary microscopy and cultivation measurements of bacteria have been summarized by ecosystem type (Burrows et al., 2009); bacterial fluxes derived from those measurements (Burrows et al., 2009) were then used in multiple modeling studies aimed at assessing the importance of bioaerosol in climate (Hoose et al., 2010; Sesartic et al., 2012; Spracklen and Heald, 2014). However, much of these data are derived from isolated studies carried out at ground level, and application to seasonal cycles and vertical profiles are not straightforward (Burrows et al., 2009). For example, Figure C-39A shows a direct comparison of the bacteria concentrations for a forest ecosystem (Burrows et al., 2009), with mass spectrometry and fluorescence data collected at the Storm Peak Laboratory, revealing an order of magnitude discrepancy for this location.

The vertical profiles derived here are compared with the results of an aerosol microphysics model, which includes parameterizations of bacteria and fungal spore emissions (Figure C-39B). The model results capture the decline in bioaerosol concentrations with altitude, however they overestimate lower atmosphere (<4 km) concentrations by an order of magnitude, particularly in the summer. The discrepancy near the surface may reflect a lack of detail in the bacteria emission scheme and/or

boundary layer mixing and removal. In particular, the aseasonal bacteria emissions in the model appear to overestimate summertime sources, consistent with the comparisons in Figure C-39A. At cirrus altitudes (>4 km), the model result are within a factor of 3.5 (on average, for all flights).

6.4 Discussion

Two issues should be considered when discussing the importance of bioaerosol in the atmosphere: (1) the total abundance of all bioaerosol and (2) the distribution and abundance of the highly ice active species compared to other bioaerosol. While *Pseudomonas syringae* and *Pseudomonas fluorescens* can induce ice nucleation at temperatures as warm as -5°C, the majority of biological material (pollen, fungal spores) has similar, or somewhat better, ice nucleation properties to mineral dust (Murray et al., 2012). The technique described here can be used to constrain only (1); it does not provide bioaerosol speciation necessary to constrain (2). Point measurements of ice active *Pseudomonas* species have been made before. For example, Maki and Willoughby (1978) isolated a number of bacterial cultures from leaf litter, rain water and snow, finding that 14% of isolates were ice active at temperatures warmer than -10°C. Those were almost exclusively strains of *P. syringae* and *P. fluorescens*. Lindemann et al. (1982) isolated bacteria from air over agricultural areas and found that, on average, 1% of isolates were ice active at temperatures warmer than -10°C. Those isolates were also dominated by *P. syringae*. Constantinidou et al. (1990) isolated airborne bacteria from air over a soybean field and found that 5.5% were highly ice nucleation active. This evidence suggests that highly ice active species account for ~10% of total bacteria concentrations emitted into the atmosphere. This study did not differentiate between bacteria and other types of aerosol, and highly ice-active species would probably account for <10% of concentrations reported here.

The bioaerosol measurements reported here show good agreement with GLOMAP model results for altitudes higher than 3 km. The GLOMAP model uses the same parametrizations of bacteria and spore emissions as two prominent modeling stud-

ies on this subject, Hoose et al. (2010) and Sesartic et al. (2012). In particular, this study reports that concentrations of mineral dust are, in general, an order of magnitude higher than those of bioaerosols, in agreement with simulations reported in Sesartic et al. (2012) for a realistic emissions scenario. Both of those modeling studies examined cases where 1% - 10% of bioaerosols were allowed to be highly ice active, which is realistic considering the abundance of *Pseudomonas* species. In those cases, Hoose et al. (2010) reports that bioaerosol contribution to global rates of heterogeneous ice nucleation is up to 0.03%. The rates were dominated by mineral dust and soot (Hoose et al., 2010). In the Sesartic et al. (2012) simulations, when 1% of bacteria were allowed to act as IN, global immersion freezing rates are still dominated by mineral dust, but some influence of bacteria can be seen at the equator and high northern latitudes, where there is a lot of vegetation (Sesartic et al., 2012). Allowing 10% of bacteria act as IN made them dominate the global immersion freezing rates (Sesartic et al., 2012). However, the concentrations of ice active bacteria in this simulation were still an order of magnitude less abundant than mineral dust and the overall effect on ice water path (IWP) and liquid water path (LWP) was small (Sesartic et al., 2012).

Previous modeling studies also include extreme test cases, where the concentrations of ice active bacteria are allowed to become comparable to mineral dust. In the simulation where bacteria emissions rates were increased 100-fold and 100% of the bacteria were allowed to act as IN, Sesartic et al. (2012) reported a significant reduction (7%) in LWP and a net change of 1 W/m^2 in radiative forcing by clouds. Those effects are very strong, but they would require total bioaerosol concentrations to be three orders of magnitude larger than those reported here, accounting for the fact that only $\sim$10% of bioaerosols are probably highly ice active.

The method of bioaerosol identification used here allows measurement of primary biological particles and, in some cases, internal mixtures and fragments using PALMS, which can be deployed both on the ground and aircraft. There is however, information that it cannot provide, such as speciation of bioaerosol, which can be very important for predicting microphysical properties of those particles (Murray et al., 2012). While

some work on speciation of bioaerosol is being done with WIBS (Hernandez et al., 2016), the only certain way to determine whether or not a given bioaerosol particle belongs to one of the highly ice active species is by DNA sequencing. Usually, this involves collecting bioaerosols on filters and subsequent amplification of the DNA by polymerase chain reaction (PCR) (Xia et al., 2015; Bowers et al., 2012). PCR involves extensive laboratory treatment and cannot be done *in situ* (Vial et al., 2017). Recently, techniques for sensitive DNA detection that are faster than PCR and require less sample pre-treatment have emerged using either nanoparticle labels or on-chip sensors (Sato et al., 2010; Vial et al., 2017; Hoffmann et al., 2008; Stagni et al., 2006; Nam et al., 2004). Those could eventually show some promise for atmospheric DNA detection. Additionally, measuring distributions and concentrations of bioaerosols that act as IN will be important in further constraining bioaerosol. This could include aircraft measurements of ice residual chemistry in cirrus and mixed phase clouds along with cloud chamber experiments on ambient aerosol populations.

6.5 Conclusion

In this study, we apply a new bioaerosol identification technique (Zawadowicz et al., 2017) to airborne mass spectrometry data to derive vertical profiles of bioaerosol. Our measurements show an agreement with an aerosol microphysics model within a few factors in the upper troposphere and within an order of magnitude near the surface. We also compare mass spectrometry measurements with a commercial fluorescence sensor, showing an agreement to within a factor of two in the 0.5 - 4 μm size range. The agreement between two different measurement techniques and a model is an important step in constraining global abundances of this poorly understood and potentially important source of atmospheric aerosol and representing it accurately in models. This offers the potential to use past data sets over different seasons, locations and the depth of the troposphere to build long-term trends in bioaerosol to both constrain and compare to models.

6.6 Acknowledgements

We thank the DRI SPL staff and the FIN03 team for their logistical support and scientific discussions of the fieldwork at SPL and the aircraft crews, support staff and scientists of the DC3, SEAC4RS, NEAQS and MACPEX studies for assistance with data acquisition. We acknowledge funding from NSF and DOE, which allowed our participation in CARES and FIN03 (grants AGS-1461347 and DE-SC0014487, respectively). We acknowledge NASA for funding data analysis (grant NNX13AO15G) and DC3, SEAC4RS and MACPEX. We thank NOAA for funding the NEAQS studies. M.A.Z. acknowledges the support of NASA Earth and Space Science Fellowship. D.J.C. acknowledges the support of Victor P. Starr Career Development Chair. C.L.H. acknowledges NSF funding (ATM-1564495). AEP was supported by the NOAA Health of the Atmosphere Program and the NOAA Atmospheric Composition and Climate Program.

This chapter is in preparation for submission to Nature Geoscience as M. A. Zawadowicz, K. D. Froyd, A. E. Perring, D. M. Murphy, D. V. Spracklen, C. L. Heald, P. R. Buseck, D. J. Cziczo: Measurement and Modeling of the Vertical and Seasonal Abundance of Bioaerosol.

Chapter 7

Conclusion

The results presented in this work outline some possible future directions for laser desorption/ionization mass spectrometry of single aerosol particles and how they can be used to improve our understanding of atmospheric aerosols. From the individual chapters, the following conclusions can be drawn:

(1) Further work on understanding laser ionization is needed. Coupling a femtosecond laser to the PALMS instrument did not prove to produce spectra that were appreciably less fragmented and it did not make the ionization more consistent. The conclusions were somewhat surprising in that a very short ~100 fs pulses produced spectra that were similar to the traditional 193 nm excimer that produces pulses on the order of nanoseconds. This shows that laser ionization of aerosol particles in vacuum is still very poorly understood.

(2) Use of a new generation compact high resolution mass analyzer shows significant promise. The use of the new sTOF mass analyzer improved the resolution over the traditional reflectron-TOF 2-3 times, even with extra drift tube that could be eliminated. Initial measurements of isotopic ratios illustrate some effects that inhibit quantification, such as saturation and isobaric interferences. More analysis of this system and the spectra obtained will allow better understanding of single particle mass spectra produced by laser desorption/ionization. Characterization of the new mass analyzer shows promise for future miniaturization of PALMS, as the sTOF mass analyzer is significantly smaller and lighter than the reflectron-TOF.

(3) The new commercial laser desorption/ionization mass spectrometer LAAPToF is now better suited to ambient particle measurements, but significant improvements could be made. The optical design of the LAAPToF instrument was significantly improved by introduction light guides. However, the instrument is still difficult to align and use because of the total length of the vacuum region and resulting divergence of the particle beam. The LAAPToF instrument should be significantly shorter for better particle detection.

(4) Use of novel statistical analysis techniques and extensive laboratory characterization can help identify new particle types. The bioaerosol identification method required development of extensive laboratory-based particle library and use of appropriate data analysis methods. Leveraging similar methods for other difficult to identify particle types shows some promise, but potential interferences should be considered in all cases. In particular, some modern machine learning techniques are especially well-suited to problems in clustering and classification of single particle mass spectra.

7.1 Future Work

7.1.1 Near-term future work

Development of the biological particle identification criteria opens the possibility of better quantification of bioaerosol in the atmosphere in future SPMS measurements, which can improve their representation in models and constrain their effect on mixed cloud formation, which has been hypothesized, but not definitely confirmed in *in situ* studies. Future ice residual measurements, both from aircraft and using cloud chambers, can now unambiguously identify biological ice residuals. In the future, some more laboratory studies on more complex mixtures of biological and non-biological material could be undertaken. For example, representing complex soil particles or similarly complex marine biological particles would be useful to represent some of the natural variability of this material.

Identification of bioaerosol is only one example of using the information in single

particle mass spectra to make new aerosol measurements. There is a lot of potential in using machine learning clustering and classification methods to identify patterns in single particle mass spectra that may correspond to real chemical variability. Such analysis should always be paired with analysis of laboratory standards, as some variability in single particle mass spectra is simply due to laser power or particle matrix differences. However, novel data processing techniques coupled with laboratory studies of atmospherically representative particles can offer new insights into aerosol chemistry. In particular, using decision tree classification schemes on known populations of atmospherically-relevant aerosol has already shown promise for identification of many major classes of mineral dust aerosols, along with coated mineral dust and bioaerosols (Chapter 5).

The work in this thesis demonstrates potential for taking higher resolution single particle mass spectra. Currently, the resolution of the sTOF is sufficient to resolve isotopes of, for example, sulfur and carbon (see Figure C-18). However, the ability of this technique to measure small changes to isotopic ratios is not necessarily limited by the resolution. Small variations tend to be very difficult to tell apart from fluctuations inherent in laser ionization and isobaric interferences with other species. Those two effects should be examined in order to determine whether isotopic analysis can be performed. While isobaric interferences are unavoidable in a sample that cannot be chemically processed prior to analysis, methods to make laser ionization more consistent from particle to particle could be explored, such as laser homogenization (Wenzel and Prather, 2004) and two-step ionization (Zelenyuk et al., 1999).

Lead would be a good first candidate for further exploration of isotopic ratios. Because lead is radiogenic, the differences in isotopic compositions of different ores tend to be large and therefore easier to measure. Also isobaric interferences tend to be less prominent at high masses, as there are not many fragments heavier than $m/z = 200$. In order to figure out how sensitive measurements of lead isotopic ratios can be, standards would have to be developed and measurements would have to be compared with standard techniques, such as ICP-MS.

The other instrument considered in this work, LAAPToF, currently suffers from

particle undercounting due to improper spatial layout of the components. The instrument should be overall shorter in order to prevent particle beam divergence and it should employ elliptical light collection, similarly to other the SPMS designs. This would necessitate moving particle counting optics away from the source region and using a timing circuit for the excimer. Even with a decrease of ionization efficiency due to the delayed excimer firing, ensuring compact construction and better beam positioning (using position sensitive detectors, for example) would overcome most of the problems of the current design of poor particle transmission and difficult alignment.

7.1.2 Long-term future work

Improved *in situ* measurements of single aerosol particles are needed in order to represent indirect effects in global climate models more accurately, constrain anthropogenic influences on aerosol populations and better describe heterogeneous atmospheric chemistry (Boucher et al., 2013; National Academies of Sciences Engineering and Medicine, 2016). However, obtaining targeted single particle mass spectrometry measurements with high spatial and temporal resolution is challenging, because the instruments are limited by their size to only a few airborne platforms (WB-57 and DC-8 aircraft for PALMS). Currently, there are no laser desorption/ionization single particle mass spectrometers capable of deployment on small manned and unmanned aircraft, such as NASA Global Hawk or NASA ER-2, which can provide targeted high-resolution aerosol chemistry measurements in upper troposphere and stratosphere. Additionally, aerosol measurements in the parts of the atmosphere that are very vital to climate (Arctic), as well as those that are currently under-studied (Southern Hemisphere) are needed.

Research outlined in this thesis opens some possibilities of miniaturization of existing single particle laser desorption/ionization mass spectrometers. In particular, the new PALMS sTOF analyzer can be used to provide a lighter and more compact time-of-flight mass spectrometer, with the added benefit of higher resolution. A redesign of PALMS source region would allow for coupling of the sTOF much closer to the ion source, ensuring further improvement in spectral resolution. The com-

pact design also allows use of two sTOF mass analyzers to provide bipolar spectra, although this would require introducing a separate light scattering optic inside the source region. Modernizing other components of the instrument (such as vacuum system or the excimer laser) would also provide an improvement in size, weight and power consumption.

In order to decrease the size and weight of PALMS by several factors, the technology is already available. The sTOF mass analyzer is already 2-3 times smaller and lighter than the reflectron-TOF. Additionally, turbomolecular vacuum pumps are now available as integrated units which save on the space currently devoted to the vacuum system. A system that uses the sTOF mass analyzer, along with compactly packaged excimer laser, an integrated multistage vacuum system and compact arrangement of all the other components could become 2-3 times smaller than the current flight-deployable PALMS. Such a system would be already deployable on a wider variety of platforms, such as smaller aircraft and perhaps even larger UAVs, such as NASA Global Hawk.

The sector-based mass analyzer offers even more potential for miniaturization, as the sectors can be made smaller (with a loss of resolution) or more smaller sectors can be deployed in different geometries, such as the cloverleaf design described by Sakurai et al. (1985).

A component that is by far the most difficult to miniaturize is the excimer laser. The laser relies on a physical gas-filled cavity as a lasing medium and not much can be done to package it more compactly. To a certain extent, retaining only the essential components, such as the chamber and high voltage electronics could help, however, those lasers will never be as small as their solid state equivalents. For a very miniature system, a frequency-quadrupled Nd:YAG laser might be advantageous, although those systems suffer from long trigger delays that cause reduced particle hit rates and undercounting of difficult to ionize particles, such as sulfuric acid (Murphy, 2007). The first limitation can be possibly mitigated by faster electronics in the future.

When designing future single-particle aerosol mass spectrometers, ease of inter-

pretation of mass spectra as well as potential for quantification should be considered. Figure C-40 shows a continuum, where soft ionization falls on one end of the spectrum and hard ionization falls on the other end. In soft ionization, molecules are ionized but left intact, such as in electrospray and MALDI ionization schemes. Hard ionization, on the other hand, breaks up all molecules down to atomic components. The ionization used in PALMS falls somewhere in the middle, but closer to the hard ionization end of the spectrum. PALMS mass spectra show some functional groups and even occasionally molecular ions (PAHs and oxalic acid can be left unionized at lower laser powers), but in general they break up organics into smaller fragments and sometimes atomic ions. Using different excimer laser powers allows for tuning the fragmentation patterns along the continuum to some extent. For atmospheric studies, all types of ionization can be beneficial. For example, soft ionization allows better identification of organics in secondary organic aerosol. On the other hand, for the isotopic ratio analysis with the sTOF, hard ionization would be beneficial because it would decrease the possibility of isobaric interferences by unknown ionized fragments. More control over ionization type by adjusting the excimer laser parameters would be highly desirable. To that end, homogenizing the excimer laser beam and/or employing two-step ionization schemes, as described in Zelenyuk et al. (1999) could be explored further.

Appendix A

Appendix: Additional Data

A.1 Tuning the SVM classifier

The most important parameter for robust performance of a support vector machine classifier is the choice of the kernel function. Here, the performance of a simple linear classifier was compared to two types of non-linear classifiers: those using polynomial kernels and those using Gaussian kernels.

Recall that the polynomial kernel has the form (Ben-Hur et al., 2008):

$$k_{d,\kappa}(\mathbf{x}, \mathbf{x}') = (\mathbf{x} \cdot \mathbf{x}' + \kappa)^d \tag{A.1}$$

Here, two values of d were used, $d = 2$ for a quadratic kernel and $d = 3$ for a cubic kernel.

The Gaussian kernel, on the other hand, has the form (Ben-Hur et al., 2008):

$$k_\sigma(\mathbf{x}, \mathbf{x}') = \exp(-\frac{1}{\sigma}||\mathbf{x} - \mathbf{x}'||^2) \tag{A.2}$$

Here, the tunable parameter is known as $\gamma = \frac{1}{\sigma}$, which describes the "scale" of the kernel, or the resolution: the smaller the γ parameter, the more fine features the classifier will be able to resolve. As a starting point, three different Gaussian kernels were compared: a fine resolution kernel, where $\gamma = 0.35$, a medium resolution kernel, where $\gamma = 1.4$ and a coarse resolution kernel, where $\gamma = 5.6$.

Two standard performance metrics were used to asses the classifier performance: five-fold validation accuracy metric and the receiver operating characteristic (ROC) curve. In five-fold validation, the algorithm randomly partitions the training data into five different subsets. Four of those subsets are used to calculate the classifier and the remaining subset is used to test its accuracy. This process is repeated five times and the final accuracy estimate is the average of the five tests. The ROC curve is a plot of true positive rate of the classifier vs. false positive rate at various threshold settings. The area under the ROC curve (AUC) is often used for comparisons of binary classifiers and it can be interpreted as the probability that the classifier will assign a higher score to a randomly chosen positive example than to a randomly chosen negative example (Jin Huang and Ling, 2005).

Figure C-41 shows boundaries drawn by the six different SVM algorithms using the biological/non-biological training data from Chapter 5. The linear, quadratic and cubic versions of the SVM algorithm struggle to define clear boundaries between the two classes. From a simple visual examination, it is clear that fine and medium resolution Gaussian kernels offer a superior performance. Additionally, the effect of the γ parameter in terms of fine features that can be captured by the boundaries is clear in this example.

The superior performance of the Gaussian kernels can also be seen from the ROC curves of all six classifiers shown in Figure C-42. A classifier that minimizes false positives and maximizes true positives is desirable, and therefore, the ROC curve of a well-performing classifier should reach the upper-left corner of the ROC space. This is especially true of the fine and medium resolution Gaussian kernels. The cubic polynomial kernel offers a marked increase in performance over the quadratic polynomial kernel, which might indicate that higher-order polynomial kernels might perform even better. However, the polynomial kernels also took 2-3 as long to train compared to the Gaussian kernels and this was not explored any further.

Figure C-43A shows a summary of AUC values for the six classifiers and Figure C-43B shows the summary of the five-fold validation accuracy values. This further corroborates the conclusion that fine and medium resolution Gaussian kernels perform

the best out of the six classifiers examined.

From Figure C-43B, the coarse resolution Gaussian classifier shows a reduction in accuracy compared to the kernels with finer resolution. This can be also seen in Figure C-41. In Figure C-43C, the five-fold validation accuracy was plotted for classifiers with many different γ values between 0 and 10, in order to capture the turning point in the loss of classifier accuracy. The classifier has >97% accuracy for all γ values less than 2. The vertical line in Figure C-43C shows the γ that was ultimately used in the biological/non-biological classifier described in Chapter 5 ($\gamma = 1.4$).

An additional adjustable parameter for the SVM classification is the C constant defined in Chapter 5 Appendix (equation 5.2). The performance of the Gaussian kernel SVM classifier was found to be very insensitive to this parameter, however. Values between 1 and 1,000 were tried with no loss of in five-fold validation accuracy or AUC.

The classifier is reproducible. When repeated 10-fold validation tests are are performed, the variation in resulting reported accuracy is only 0.4%.

A.2 Tuning the sTOF operating voltages

Overall, the resolution of the sTOF was found to be remarkably insensitive to tuning of the operating voltages. In general, setting any of the voltages to values larger than $\pm 10\%$ of the optimized conditions defined in Table B.9 resulted in a loss of signal strength rather than the loss of resolution. This behavior is different than the reflectron-TOF, whose resolution is sensitive to the reflectron and source region voltage settings.

In order to test this systematically, single particle mass spectra of different types of laboratory-generated aerosols were acquired at different operating voltages for both the sTOF and the source region. Results are shown in Figures C-44 and C-45. The peak widths at half maximum are used as a proxy for spectral resolution. Those are quantified using a peak-picking algorithm implemented using Matlab's peak analysis

routines.

Three different conditions for the sTOF voltages were explored: a balanced condition where the same magnitude voltage (600 V) was applied to inner and outer sectors, an unbalanced condition, where 570 V was applied to the outer sectors and -670 V was applied to the inner sectors (in positive mode), and an even more unbalanced condition, where 500 V was applied to the outer sectors and -730 V was applied to the inner sectors (in positive mode). Theoretically, the unbalanced conditions are more favorable because they produce additional focusing of the ion beam in the y-direction (Murphy, 2017). However, while this improves the ion transmission to the detector, it would not necessarily change the resolution. The three different sector voltage combinations were tested in both positive and negative modes with three different aerosol species: soot, ATD and apatite. The results are reported in Figures C-44A and C-44B. Those results show no systematic differences in the sTOF voltage conditions for the different chemical species. Three different voltages were also applied to the Einzel lens at the entrance of the sTOF: -2,000 V, -2,300 V and -1,700 V (positive mode). This test was performed in positive and negative modes for soot particles only. The results are shown in Figures C-44C and C-44D, but there also no obvious differences in resolution.

Source region voltages were also tuned for soot particles in both positive and negative modes. In Figures C-45A and C-45B, three different backing voltages were tested: 4,000 V, 4,100 V and 3,900 V (positive mode). The resolutions did not show any change, however, the signal strength in the 4,100 V conditions was lower, which produces the larger error bars seen in Figure C-45B. Similarly, three voltages were used for the mirror (the ion extraction plate, which is also an optical component): 1,000 V, 1,100 V and 900 V (positive mode). Similarly, there was no change in resolution (Figures C-45C and C-45D), but the 1,100 V condition produced spectra with lower overall signal resulting in larger error bars in Figure C-45D. Four different voltage conditions were tested for the Einzel lens following the source region: -3,300 V, -3,100 V, -3,000 V and -2,800 V (positive mode). As seen in Figures C-45E and C-45F, there is, again, no effect on resolution.

The insensitivity of sTOF resolution to the operating voltage conditions is, overall, an advantage. The voltages do not need to be controlled as precisely and there is less potential for drifts in resolution over time. The starting position of ions inside the source region also does not affect the resolution (it does tend to affect signal strength, however). This was tested by translating the excimer beam around the source region in both x- and y-directions and visually compering the resulting spectra.

To significantly affect the resolution, spatial arrangement of the sTOF components would have to be changed. For example, the distance from the source region to the mass analyzer could be changed, sectors could be re-arranged or more sectors could be added.

Appendix B

Tables

Table B.1: Laboratory samples used for sTOF characterization.

Sample	Source	Generation method	Reference
$CaSO_4$	Sigma Aldrich	Wet-generated from $CaSO_4/NH_4NO_3$ solution (atomizer)	N/A
$CaSO_4$	Stephane Gallavardin	Dry dispersed	Gallavardin et al. (2008)
$CaSO_4$	Stephane Gallavardin	Dry dispersed	Gallavardin et al. (2008)
Apatite	Adam Sarafian, WHOI	Dry dispersed	Zawadowicz et al. (2017)
Dolomite	Stephane Gallavardin	Dry dispersed	Gallavardin et al. (2008)
Portland cement	Stephane Gallavardin	Dry dispersed	Gallavardin et al. (2008)
Petalite	Stephane Gallavardin	Dry dispersed	Gallavardin et al. (2008)
Mica	Stephane Gallavardin	Dry dispersed	Gallavardin et al. (2008)
Illite NX	Clay Mineral Society	Dry dispersed	Garimella et al. (2014)
Illite NX	KIT	Dry dispersed	Hiranuma et al. (2015)
Arizona Test Dust	Powder Technology, Inc.	Dry dispersed	N/A
K-Feldspar	KIT	Dry dispersed	Peckhaus et al. (2016)
Mojave Mars simulant dust		Dry dispersed	Peters et al. (2008)
Na-Montmorillonite	Clay Mineral Society	Dry dispersed	Garimella et al. (2014)
Welsh C fly ash	Fly Ash Direct	Dry dispersed	Zawadowicz et al. (2017)
Joppa C fly ash	Fly Ash Direct	Dry dispersed	Zawadowicz et al. (2017)
Clifty F fly ash	Fly Ash Direct	Dry dispersed	Zawadowicz et al. (2017)
Miami F fly ash	Fly Ash Direct	Dry dispersed	Zawadowicz et al. (2017)
Synthetic sea water	Sigma Aldrich	Wet-generated (bubbler)	N/A
Kaolinite	Clay Mineral Society	Dry dispersed	Garimella et al. (2014)
Zircon sand	Stephane Gallavardin	Dry dispersed	Gallavardin et al. (2008)
German soil dust	KIT	Dry dispersed	Steinke et al. (2016)
Monazite-Ce	Natural sample sourced from the Petaca Mining District, NM	Dry dispersed	Zawadowicz et al. (2017)
Mongolian soil dust	KIT	Dry dispersed	Steinke et al. (2016)
Argentina soil dust	KIT	Dry dispersed	Steinke et al. (2016)
Volcanic ash		Dry dispersed	N/A
Magnetite	Stephane Gallavardin	Dry dispersed	Gallavardin et al. (2008)
Elemental sulfur	Generated in a laboratory photochemical experiment, see text	See text for details	N/A

Table B.2: Comparison of optical design choices and performance metrics of three existing SPMSs and the improved LAAPToF.

	SPLAT II/ miniSPLAT	ALABAMA	ATOFMS/ A-ATOFMS	PALMS	LAAPToF
Optical counting efficiency	100% for 125 nm - 600 nm PSL 1.5% for 70 nm PSL	80% for 300 nm - 500 nm PSL 0.3% for 200 nm PSL	30% for 220 nm - 2 μm PSL 0.4% 120 nm PSL	10% for 300 nm - 1 μm PSL 0.1% for 150 nm PSL	1-10% for 1 μm - 2.5 μm PSL 0.1% for 250 nm PSL
Detection beam spot size (μm)	330	190	1000	100 x 25 (elliptical)	100
Beam spacing (cm)	10.5	7	6	3.4	11.7
Detection beam power (mW)	300	50	50	50	30
Detection beam wavelength (nm)	532	532	532	532	405
Detection method	Elliptical reflector/PMT	Elliptical reflector/PMT	Elliptical reflector/PMT	Elliptical reflector/PMT	Light guide/PMT
References	Zelenyuk and Imre (2005); Zelenyuk et al. (2015)	Brands et al. (2011)	Gard et al. (1997); Pratt et al. (2009)	Cziczo et al. (2006)	This work

Table B.3: Measurements of biological aerosol in the atmosphere (NR - not reported, FBAP - fluorescent particles, attributed to bioaerosol). *Comment in response to DeLeon-Rodriguez et al. (2013) by Smith et al. (2013).

Site	Elevation (m)	Technique	Concentration of bioaerosol detected (particles m^{-3})	% of total particles (size range)	Type of bioaerosol	Ref.
Ground sites						
Jungfroujoch	3,450	Fluorescent microscopy	3.4×10^4(free troposphere) 7.5×10^4(over surface)	NR	Bacteria	Xia et al. (2013)
Storm Peak Lab	3,220	Fluorescent microscopy	9.6×10^5 - 6.6×10^6	NR	Bacteria (51%) Fungi (45%) Plant material (4%)	Wiedinmyer et al. (2009)
Storm Peak Lab	3,220	Flow cytometry	3.9×10^5(spring) 4.0×10^4(summer) 1.5×10^5(fall) 2.7×10^4(winter)	22% (0.5 - 20 μm)	Bacteria	Bowers et al. (2012)
Mt. Rax (Alps)	1,644	Fluorescent microscopy	1.1×10^4(bacteria) 3.5×10^2(fungi)	NR	Bacteria and fungi	Bauer et al. (2002)
Various locations in Colorado	1,485-2,973	Fluorescent microscopy	1.0×10^5 - 2.6×10^6	NR	Bacteria	Bowers et al. (2011)
Vienna	150-550	Fluorescent microscopy	3.6×10^3 - 2.9×10^4	NR	Fungi	Bauer et al. (2008)
U.S. Virgin Islands	NR	Fluorescent microscopy	3.6×10^4 - 5.7×10^5	NR	Bacteria and possible viruses	Griffin et al. (2001)
Various sites in the U.K.	50-130	Fluorescent microscopy	5.3×10^3 - 1.7×10^4(spring) 8.3×10^3 - 1.5×10^4(summer) 6.0×10^3 - 1.4×10^4(fall) 2.9×10^3 - 1.0×10^4(winter)	NR	Bacteria	Harrison et al. (2005)
Danum Valley, Malaysian Borneo	150-1,000	WIBS	2.0×10^5(above forest canopy) 1.5×10^6(below forest canopy)	NR	FBAP	Gabey et al. (2010)
Karlsruhe, Germany	112	WIBS	2.9×10^4(spring) 4.6×10^4(summer) 2.9×10^4(fall) 1.9×10^4(winter)	4-11% (0.5 - 16 μm)	FBAP	Toprak and Schnaiter (2013)
Aircraft campaigns						
Cape Grim	30-5,400	TEM	NR	1% (>0.2 μm)	Bacteria	Pósfai et al. (2003)
Flights around the Gulf of Mexico, California and Florida	3,000-10,000	Fluorescent microscopy	3.6×10^4 - 3.0×10^5	3.6-276% (0.25 - 1 μm)*	Mostly bacteria	DeLeon-Rodriguez et al. (2013)
Flights over southeastern U.S. (SEAC^{4}RS)	Vertical profiles up to 12,000	WIBS	3.4×10^5(average, <0.5 km) 7.0×10^4(average, 3 km) 1.8×10^4(average, 6 km)	5-10% (0.6 - 5 μm)	FBAP	Ziemba et al. (2016)
Flights over Colorado, Wyoming, Nebraska and South Dakota	Vertical profiles up to 10,000	WIBS	1.0×10^4 - 1.0×10^5(<2.5 km) 0 - 3.0×10^3(>2.5 km)	NR	FBAP	Twohy et al. (2016)

Table B.4: Summary of particle statistics for samples used to both train and test the classifier.

Category	**Total negative spectra**	**Used for training the classifier**
Bare apatite	338	135
Processed apatite (~0.1 mL)	994	359
Processed apatite (~1 mL)	987	203
Fertilized soil dusts	1953	1774
Fly ash	3986	3536
Processed fly ash (~0.1 mL)	824	312
Monazite	415	371
P. syringae	1429	1429
Snomax	497	497
F. solani (whole)	1053	1010
F. solani (fragmented)	1129	1127
Yeast	778	757
Birch pollen	1136	1137
Hazelnut pollen	183	183
Oak pollen	1193	1191
Ragweed pollen	1207	1187
Bächli soil dust	501	Not used
Moroccan soil dust	460	Not used
Ethiopian soil dust	502	Not used
Storm Peak Lab dust	464	Not used
Argentinian soil dust	507	Not used
Chinese soil dust	1002	Not used
Saudi Arabian soil dust	3131	Not used
Illite NX (dry-generated)	1002	Not used
Illite NX (wet-generated)	1030	Not used
Illite NX/*F. solani* mixed	1396	Not used
FIN03 ambient sampling	26019	Not used
CARES ambient sampling	19011	Not used

Table B.5: Soil dust samples used in this work. The last column shows the results of analysis with the SVM classifier developed here as a percentage of negative spectra acquired.

Sample	**Site description**	**Approx. collection coordinates**	**% biological**
Bachli	Outflow sediment of a glacier in a feldspar-rich granitic environment. No vegetation.	46.6 N, 8.3 E	6.0
Morocco	Rock desert with vegetation. Close proximity to a road.	33.2 N, 2.0 W	20.4
Ethiopia	Collected in Lake Shala National Park from a region between two lakes. Area vegetated by shrubs and acacia treees.	7.5 N, 38.7 E	32.1
Storm Peak Lab	Collected near Storm Peak Lab. Grass and shrubs present.	40.5 N, 106.7 W	31.3
Argentina	La Pampa province. Top soil collected from arable land with sandy loam Steinke et al. (2016).	37 S, 64 W	21.3
China/Inner Mongolia	Xilingele steppe. Top soil collected from a pasture with loam Steinke et al. (2016).	44 N, 117 E	2.0
Saudi Arabia	Various samples from several locations. Arid, sandy soils.	24.6 N - 26.3 N, 46.1 E - 49.6 E	14.5

Table B.6: Literature estimates of emission rates of primary biological particles, dust and fly ash.

Particle	**Emissions (Tg yr^{-1})**	
	low estimate	*high estimate*
Dust	1490 Zender (2003)	7800 Jacobson and Streets (2009)
Primary biological	186 Mahowald et al. (2008)	298 Jacobson and Streets (2009)
Fly ash	14.9 Garimella (2016)	390 Garimella (2016)

Table B.7: Aerosol reference samples used to develop the ensemble classifier. Majority were sampled at KIT, Aerosol Interactions and Dynamics in the Atmosphere (AIDA) facility.

Aerosol type	Description and/or supplier	Generation method	Location of sampling	Reference
Argentina	Soil dust collected in La Pampa province, Argentina	Dry-dispersed	KIT	Steinke et al. (2016)
China	Soil collected from Xilingele steppe, China/Inner Mongolia	Dry-dispersed	KIT	Steinke et al. (2016)
Ethiopian	Soil collected in Lake Shala National Park, Ethiopia (collection coordinates: 7.5 N, 38.7 E)	Dry-dispersed	KIT	N/A
German	Arable soil collected near Karlsruhe, Germany	Dry-dispersed	KIT	Steinke et al. (2016)
Moroccan	Soil collected in a rock desert in Morocco (collection coordinates: 33.2 N, 2.0 W)	Dry-dispersed	KIT	N/A
Paulinenaue	Arable soil collected in Northern Germany (Brandenburg)	Dry-dispersed	KIT	Steinke et al. (2016)
ATD	Arizona Test Dust, Powder Technology, Inc. (Arden Hills, MN)	Dry-dispersed	MIT	N/A
Illite	Illite NX (Arginotec, Germany)	Dry-dispersed	KIT	Hiranuma et al. (2015)
Fly ash	Four samples of fly ash from U.S. power plants: J. Robert Welsh Power Plant (Mount Pleasant, TX), Joppa Power Station (Joppa, IL), Clifty Creek Power Plant (Madison, IN) and Miami Fort Generating Station (Miami Fort, OH) (Fly Ash Direct, Cincinnati, OH)	Dry-dispersed	MIT	Garimella (2016); Zawadowicz et al. (2017)
Na-Feldspar	Sodium and calcium-rich feldspar, samples provided by Institute of Applied Geosciences, Technical University of Darmstadt (Germany) and University of Leeds (UK)	Dry-dispersed	KIT	Peckhaus et al. (2016)

K-Feldspar	Potassium-rich feldspar, samples provided by Institute of Applied Geosciences, Technical Universityof Darmstadt (Germany) and University of Leeds (UK)	Dry-dispersed	KIT	Peckhaus et al. (2016)
Agar	Agar growth medium for bacteria, Pseudomonas Agar Base (CM0559, Oxoid Microbiology Products, Hampshire, UK)	Wet-generated	KIT	N/A
Bacteria	Two different cultures of *Pseudomonas syringae*	Cultures grown on the agar growth medium (as above), suspended in nanopure water and wet-generated	KIT	Zawadowicz et al. (2017)
Cellulose	Microcrystalline and fibrous cellulose (Sigma Aldrich, St. Louis, MO)	Wet-generated	KIT	Hiranuma et al. (2015)
Hazenut	Natural hazelnut pollen (GREER, Lenoir, NC) wash water	Wet-generated	KIT	Zawadowicz et al. (2017)
Snomax	Snomax (Snomax International, Denver, CO) irradiated, dessicated and ground *Pseudomonas syringae*	Wet-generated	KIT	Zawadowicz et al. (2017)
PSL	Polystyrene latex spheres (Polysciences, Inc. Warrington, PA), various sizes	Wet-generated	MIT	N/A
Soot	CAST soot	miniCAST flame soot generator	KIT	Henning et al. (2012)
SOA	Secondary organic aerosol	Ozonolysis of α-pinene	KIT	Saathoff et al. (2003)
K-Feldspar cSA	Potassium-rich feldspar (as above) coated with sulfuric acid (SA)	Small amounts of sulfuric acid were incrementally added to the chamber filled with K-feldspar to achieve thin coatings, as judged from PALMS spectra	KIT	Saathoff et al. (2003)
K-Feldspar cSOA	Potassium-rich feldspar (as above) coated with secondary organic aerosol (SOA)	Small amounts of α-pinene were incrementally added to the chamber filled with K-feldspar to achieve thin coatings, as judged from PALMS spectra	KIT	Saathoff et al. (2003)

Table B.8: Top 20 spectral features with greatest predictive power used for dimensionality reduction of the ensemble classifier (see text for details).

Negative		**Positive**	
ion	**label**	**ion**	**label**
35	$^{35}Cl^-$	23	Na^+
25	C_2H^-	59	Co^+/CaF^+ $/C_2H_2OOH^+$
24	C_2^-	39	$^{39}K^+$
57	C_2OOH^-	12	C^+
59	$C_2H_2OOH^-$ $/AlO_2^-$	24	C_2^+
43	HCN^-/AlO^-	41	$^{41}K^+/C_3H_5^+$
1	H^-	204-208	Pb region (^{204}Pb, ^{206}Pb, ^{207}Pb and ^{208}Pb)
26	$CN^-/C_2H_2^-$	27	$Al^+/C_2H_3^+$
46	NO_2^-	44	$SiO^+/COO^+/^{44}Ca^+$ $/AlOH^+$
16	O^-	57	$^{57}Fe^+/CaOH^+$ $/C_3H_4OH^+$
17	OH^-	N/A	aerodynamic diameter
61	$SiO_2H^-/^{29}SiO_2^-$ $/C_5H^-/CHO_3^-$	83	$H_3SO_3^+/C_4H_2OOH^+$
63	PO_2^-	87	$^{87}Rb^+/CaPO^+$
19	F^-/H_3O^-	13	CH^+
76	SiO_3^-	66	$^{66}Zn^+$
77	$SiO_3H^-/^{29}SiO_3^-$	28	Si^+/CO^+
79	PO_3^-	85	$^{85}Rb^+$
60	$SiO_2^-/C_5^-/CO_3^-$ $/AlO_2H^-$	72	FeO^+/CaO_2^+
45	$COOH^-$	54	$^{54}Fe^+$
N/A	aerodynamic diameter	82	ZnO^+

Table B.9: Tuned sTOF voltages used for majority of the sTOF experiments. Positive polarity, reverse for negative.

Component	**Voltage**
Source Region	
Backing plate	4,000 V
Mirror	1,000 V
Einzel lens	-3,000 V
Mass analyzer	
Outer sectors	570 V
Inner sectors	-670 V
Einzel lens	-2,000 V

Appendix C

Figures

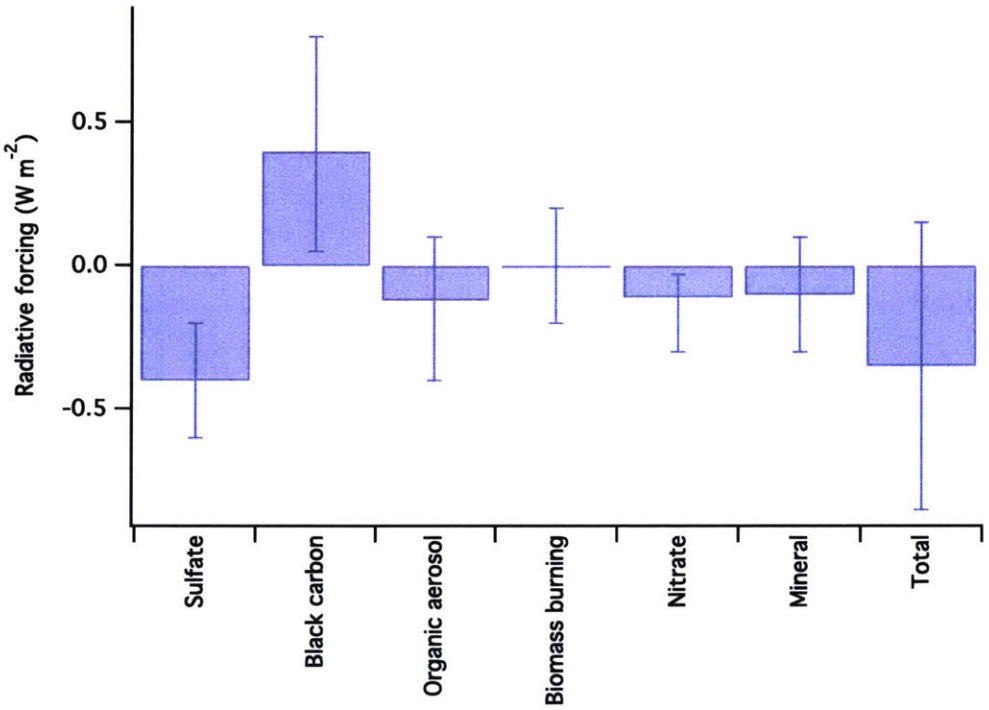

Figure C-1: Contributions of different aerosol types to direct radiative forcing of aerosols. Data are best estimates of 2013 IPCC report and error bars are best estimates of uncertainties (Boucher et al., 2013).

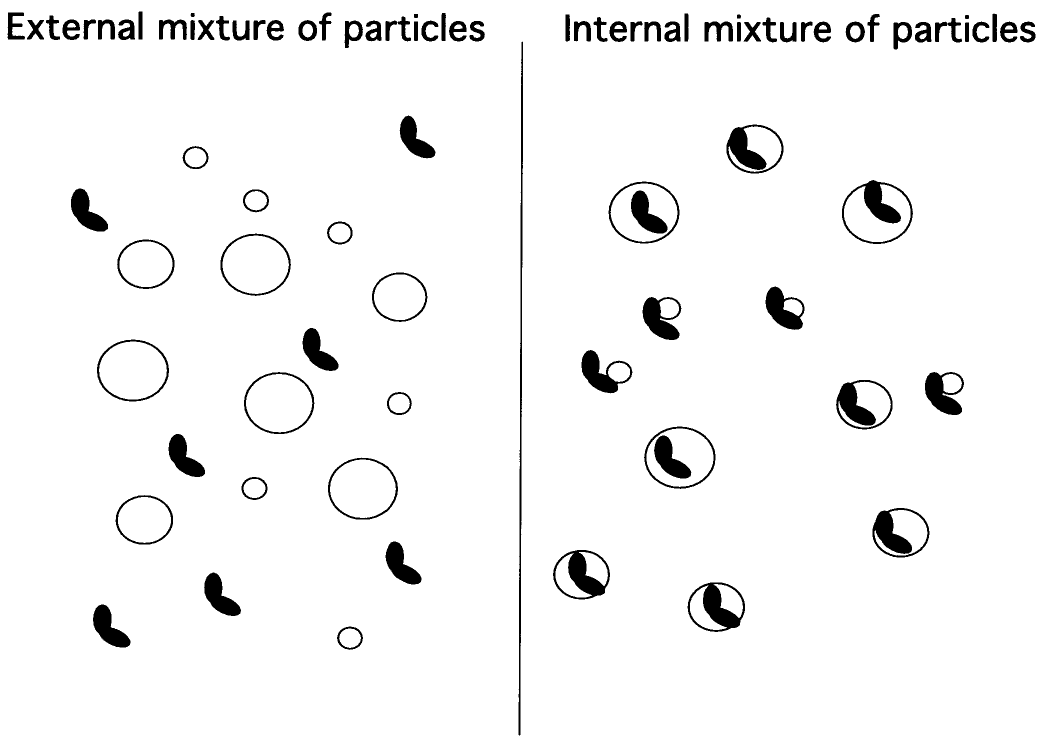

Figure C-2: Internal and external mixtures of aerosols. A schematic representation.

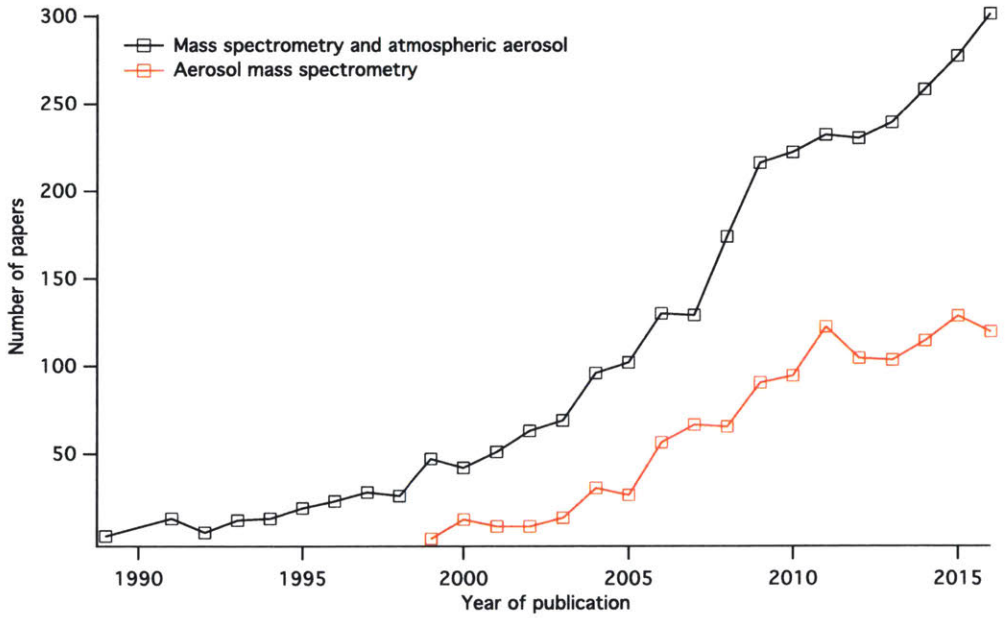

Figure C-3: Numbers of aerosol mass spectrometry papers published in recent years. Paper numbers are obtained by searching keywords "mass spectrometry" and "atmospheric aerosol" and "aerosol mass spectrometry" in the Web of Science database.

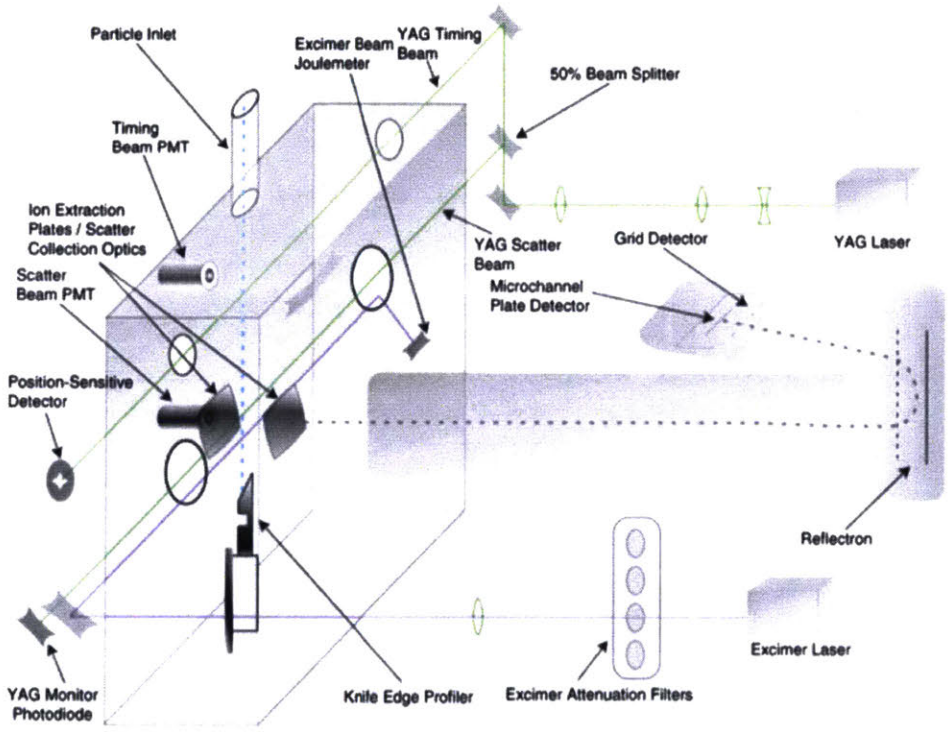

Figure C-4: Schematic of the PALMS instrument. Adapted from Cziczo et al. (2006).

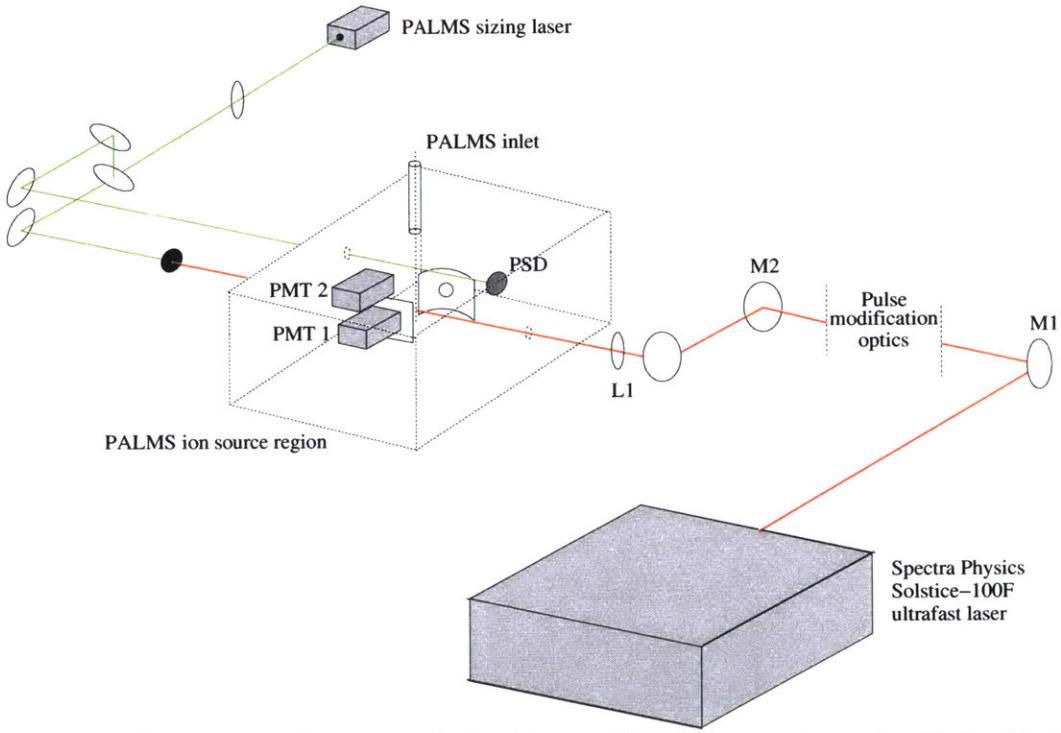

Figure C-5: Schematic diagram of the femto-PALMS experiment. Note that the traditional PALMS excimer laser would occupy the volume to the upper right in the figure. For these experiments it has been replaced with a femtosecond laser (Spectra Physics Solstice-100F) with the beam directed into the PALMS ion source region using two mirrors (M1 and M2) and a lens (L1).

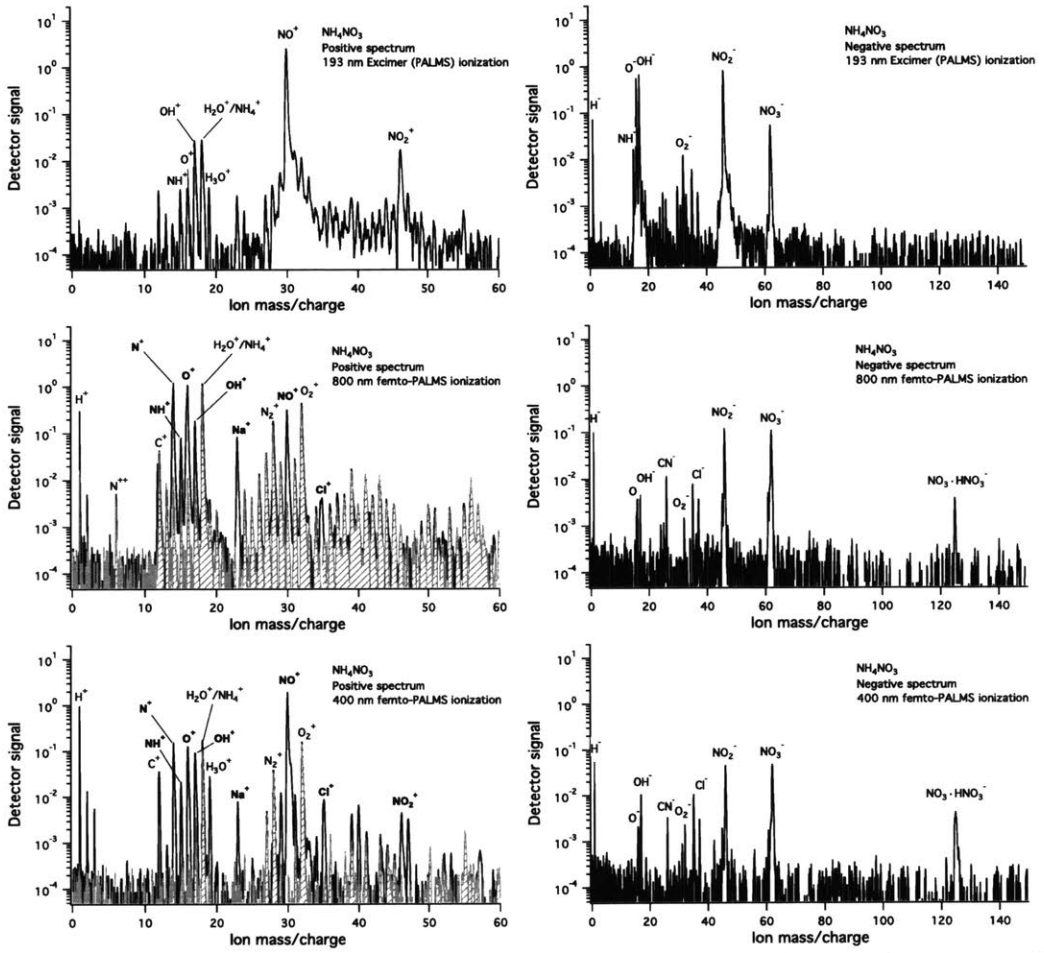

Figure C-6: Representative positive and negative spectra of NH_4NO_3 acquired with PALMS using a 193 nm excimer laser (top panel), with femto-PALMS using a 800 nm femtosecond laser (middle panel) and with femto-PALMS using a frequency doubled femtosecond laser at 400 nm (bottom panel). Hatched areas for positive femto-PALMS spectra represent background peaks not associated with NH_4NO_3 particles. Peaks associated only with NH_4NO_3 particles are labeled in bold type.

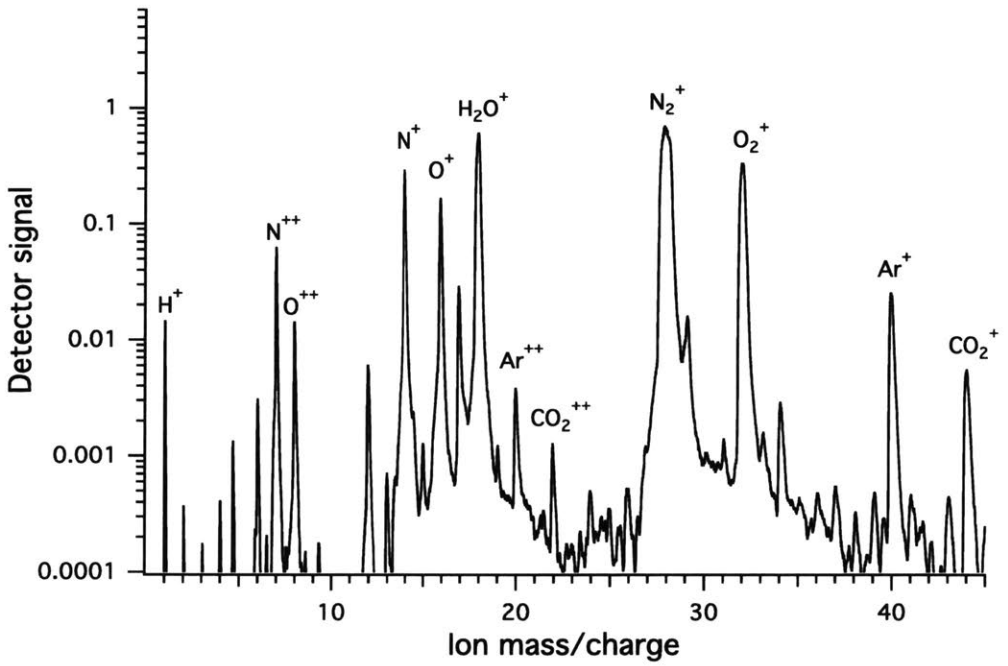

Figure C-7: Spectrum of the air background created by the femtosecond laser. Note the presence of atomic singly and doubly charged ions.

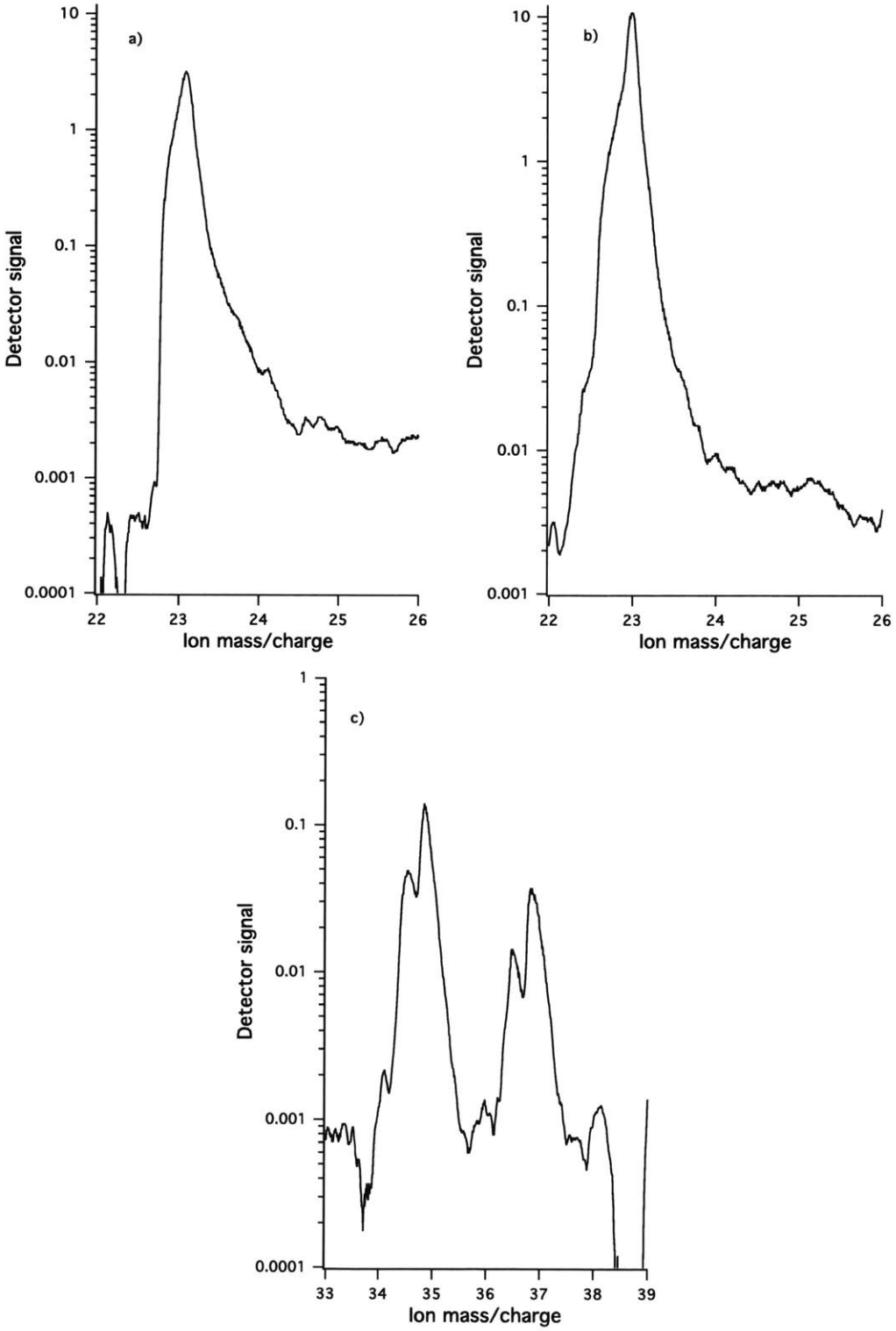

Figure C-8: Peak shapes characteristic of PALMS and femto-PALMS. Panel a) Na^+ peak characteristic of traditional PALMS. Panel b) Na^+ peak characteristic of femto-PALMS. Panel c) $^{35}Cl^+$ and $^{37}Cl^+$ peaks characteristic of femto-PALMS. Note the split peak shape discussed in the main text.

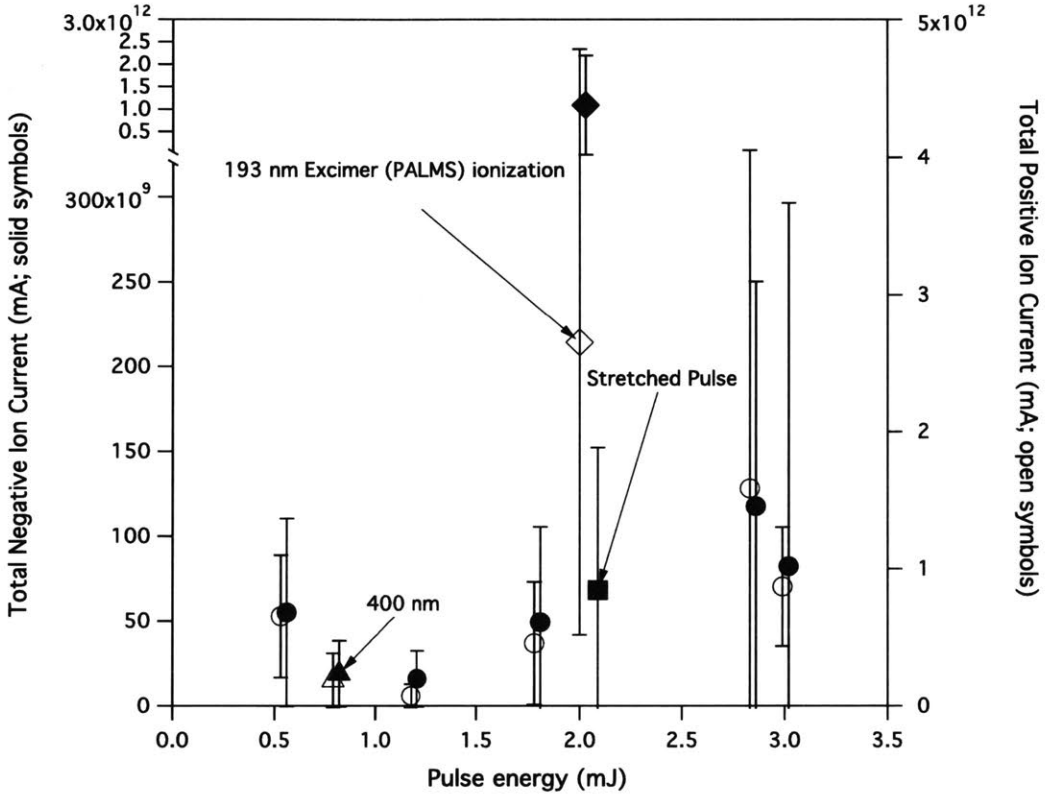

Figure C-9: Average total ion current (mA) generated per spectrum of NH_4NO_3 as a function of laser power. Solid circles represent negative polarity data (left axis) while open circles represent positive polarity data (right axis). Ion current data for a negative polarity experiment where the pulse length was stretched from 100 to 104 fs are shown with a solid square. Ion current data for experiments where frequency doubling to 400 nm was utilized are shown with triangles. Ion current data for traditional PALMS with a 193 nm excimer laser are shown for comparison with diamonds. Negative polarity data are offset in power (+ 0.03 W) to avoid overlap of error bars

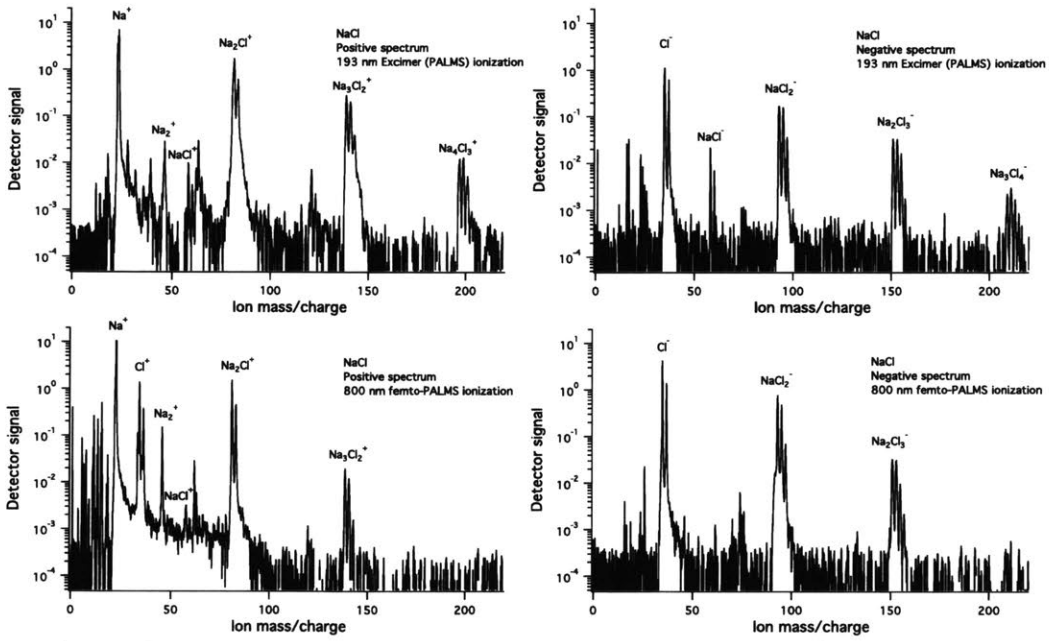

Figure C-10: Representative positive and negative spectra of NaCl acquired with PALMS (top panel) and with femto-PALMS (bottom panel).

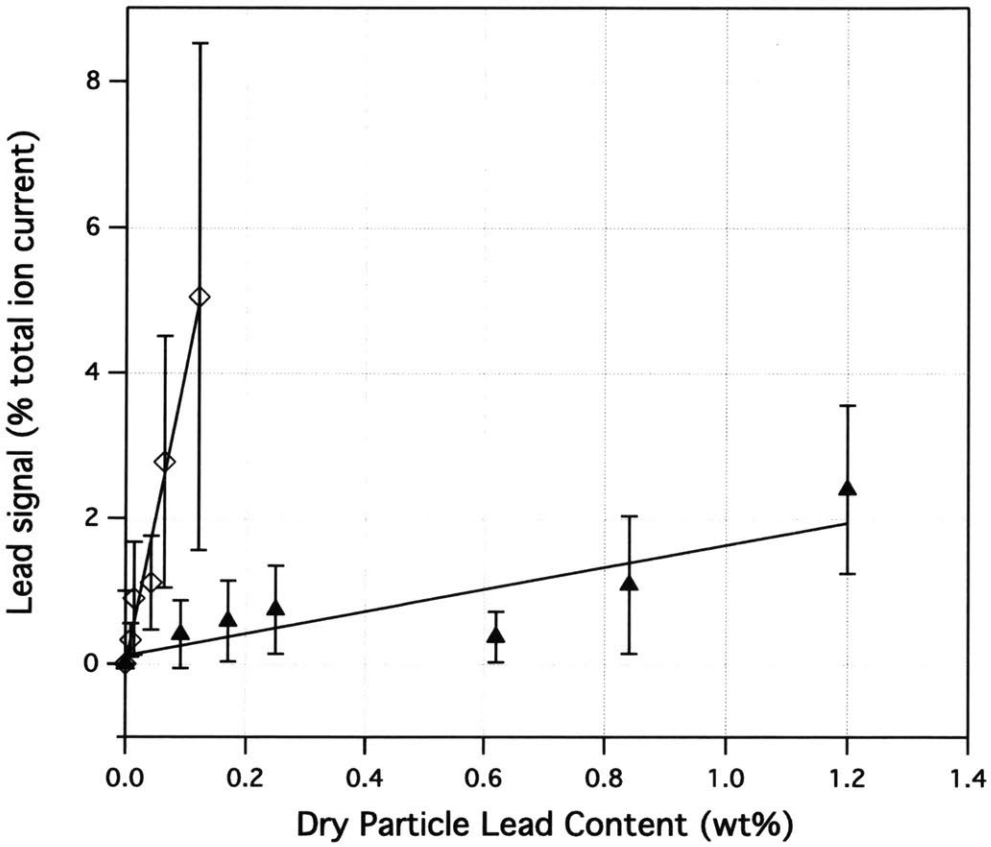

Figure C-11: Sensitivity of the signal of the lead isotope at mass 208 (in percentage of total ion current generated) to the dry particle mass content (in weight percent) where NH_4NO_3 was used as the matrix. Solid triangles represent data acquired with femto-PALMS and traditional PALMS data are open diamonds. PALMS data are reproduced from Murphy et al. (2007) Error bars indicate the range of signals in the single particle data.

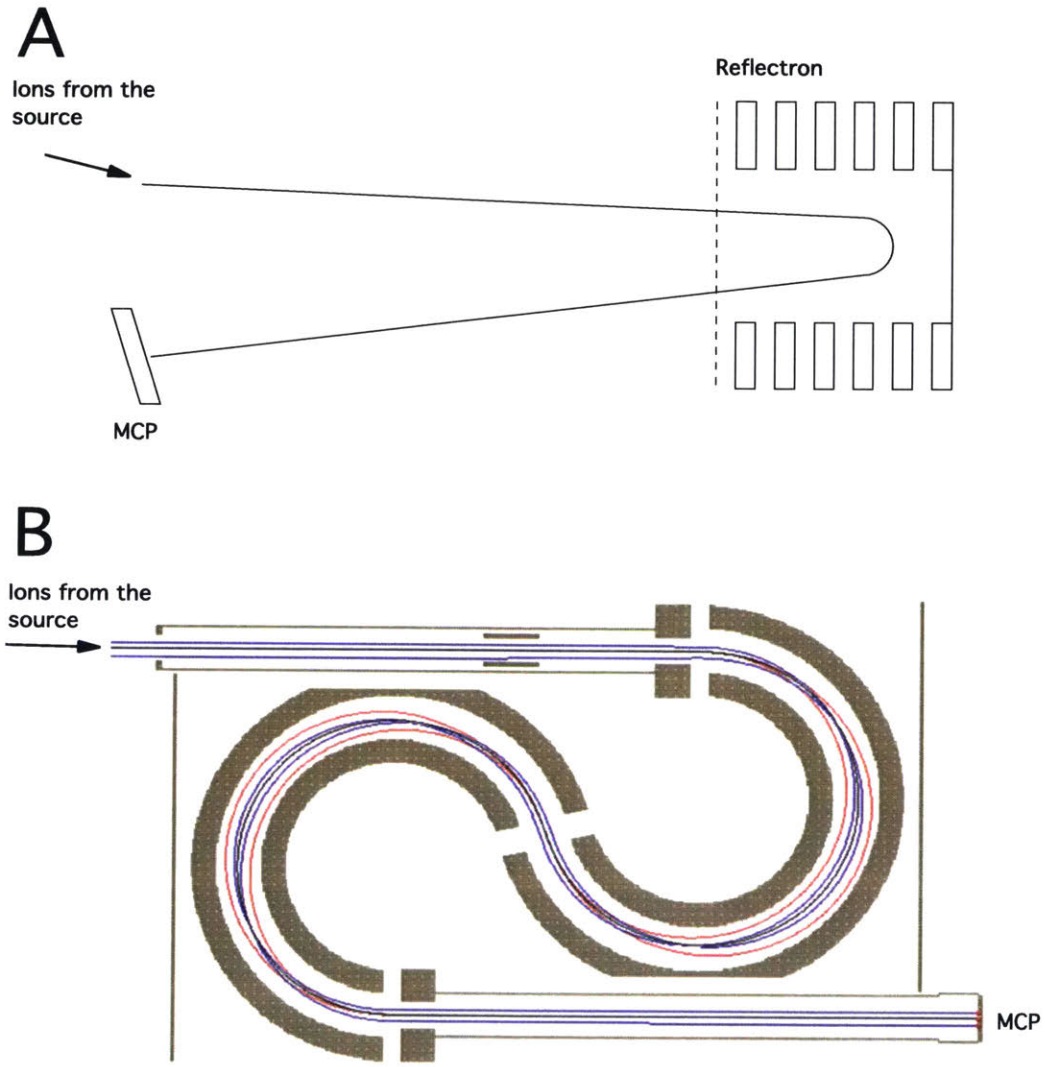

Figure C-12: Schematics of the traditional reflectron-TOF and the new sTOF analyzer. A. Reflectron-TOF. B. sTOF Simion simulation adapted from Murphy (2017). Note the ion paths though the sectors: the red ions have $\pm 10\%$ energy of the blue ions.

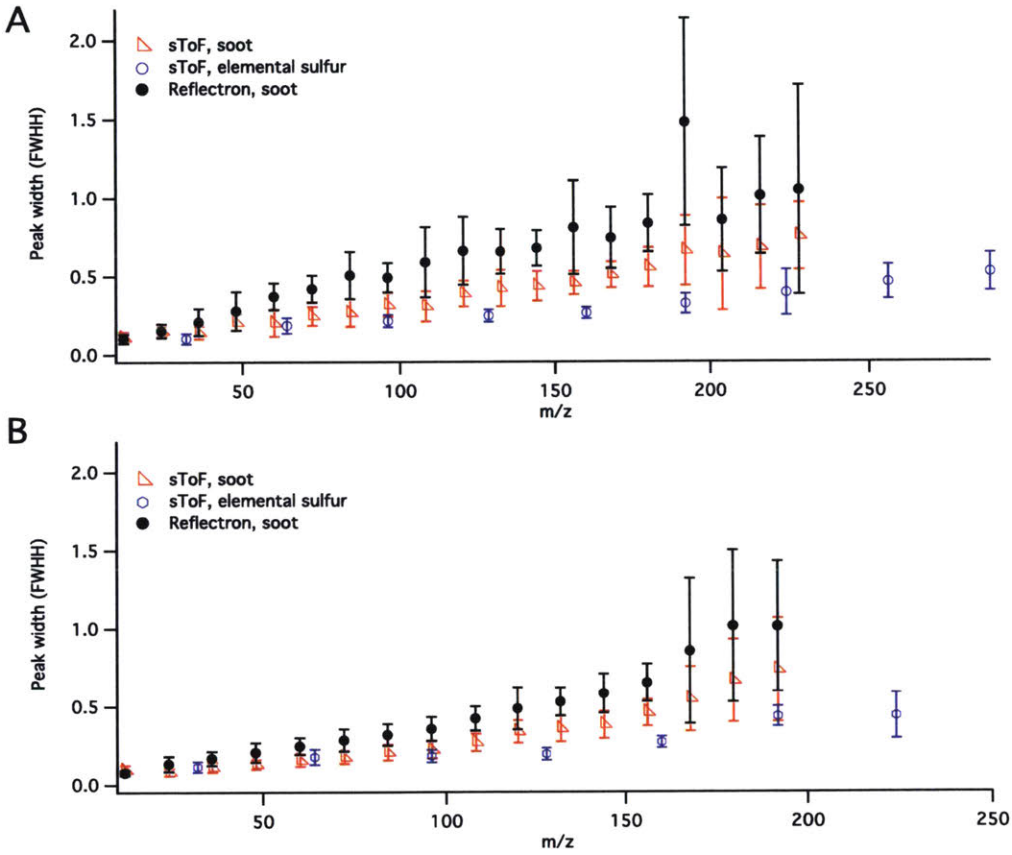

Figure C-13: Quantitative comparison of sTOF and reflectron-TOF resolution for soot and elemental sulfur samples. A. Positive polarity. B. Negative polarity.

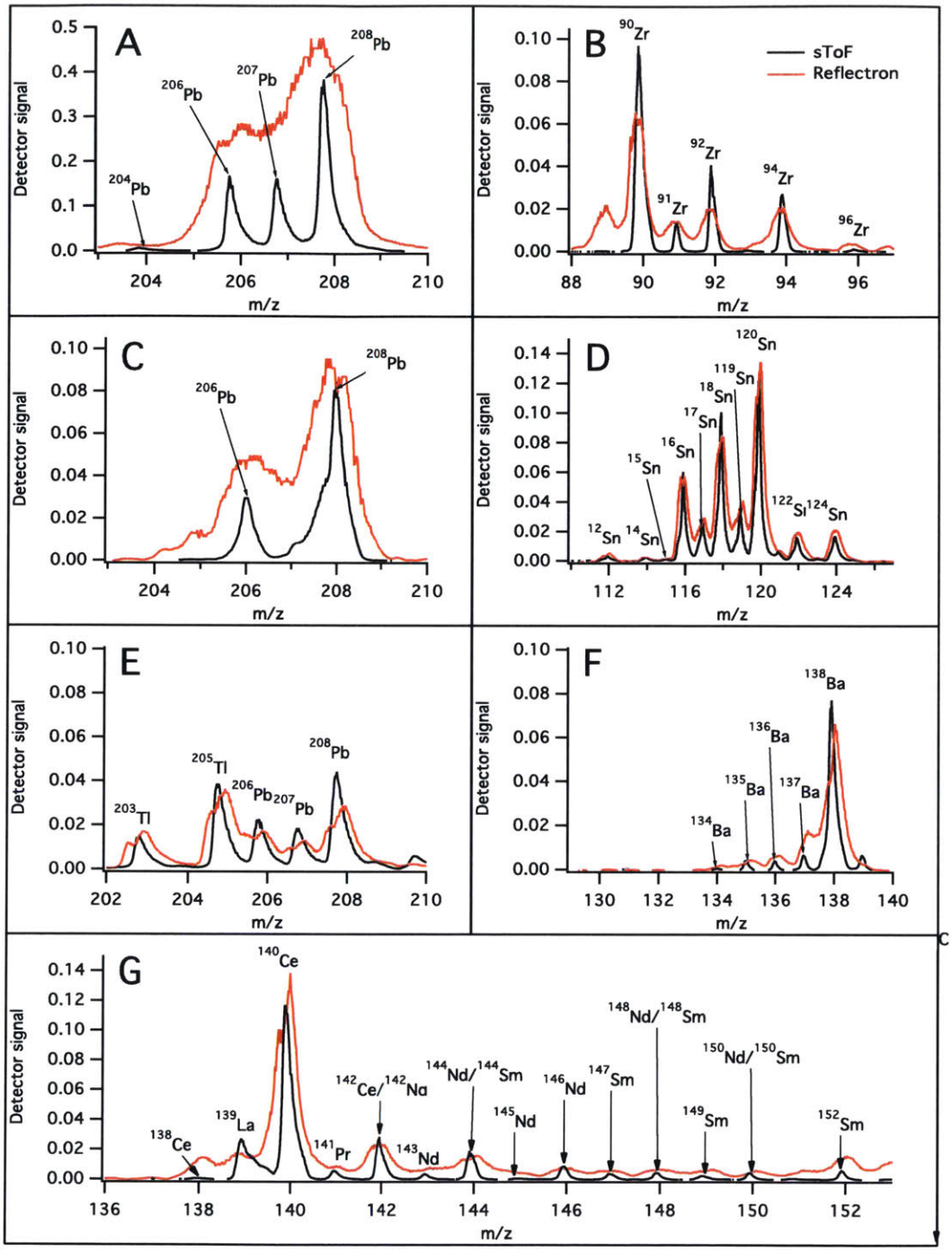

Figure C-14: Qualitative comparison of sTOF and reflectron-TOF resolution for various elements. A. Ambient lead-rich particles, sampled from the MIT EAPS building inlet for sTOF and from the Storm Peak Lab for the reflectron-TOF. B. Zirconium, zircon sand sample. C. Radiogenic lead, monazite-Ce sample. Note no ^{207}Pb peak. D. Ambient tin-rich particles, sampled from the MIT EAPS building inlet for sTOF and from the Storm Peak Lab for the reflectron-TOF. E. Lead and thallium, Miami F fly ash sample. F. Barium, Welsh C fly ash sample. G. Rare Earth Elements, monazite-Ce sample.

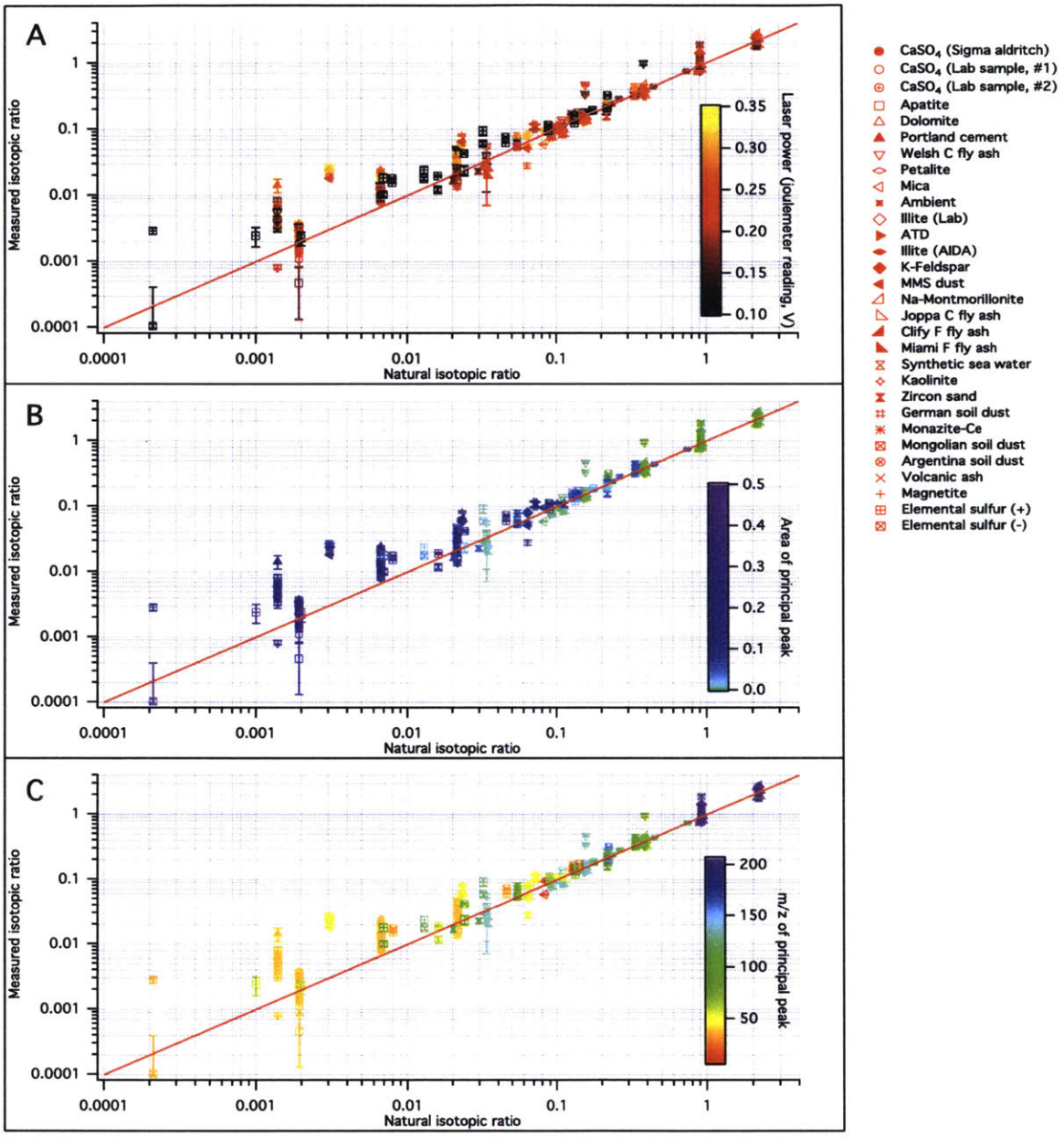

Figure C-15: Summary figure comparing measured isotopic ratios for 10 elements (calcium, lithium, tin, rubidium, magnesium, titanium, zirconium, barium, lead, iron and sulfur) quantified for 29 aerosol samples (denoted in different markers) to expected natural isotopic ratios. A. The color bar represent ionization laser energy expressed as the joulemeter reading. B. The color bar represents the relative peak area for the principal peak (the most abundant isotope in most cases, see text for details). C. The color bar represents the m/z for the principal peak.

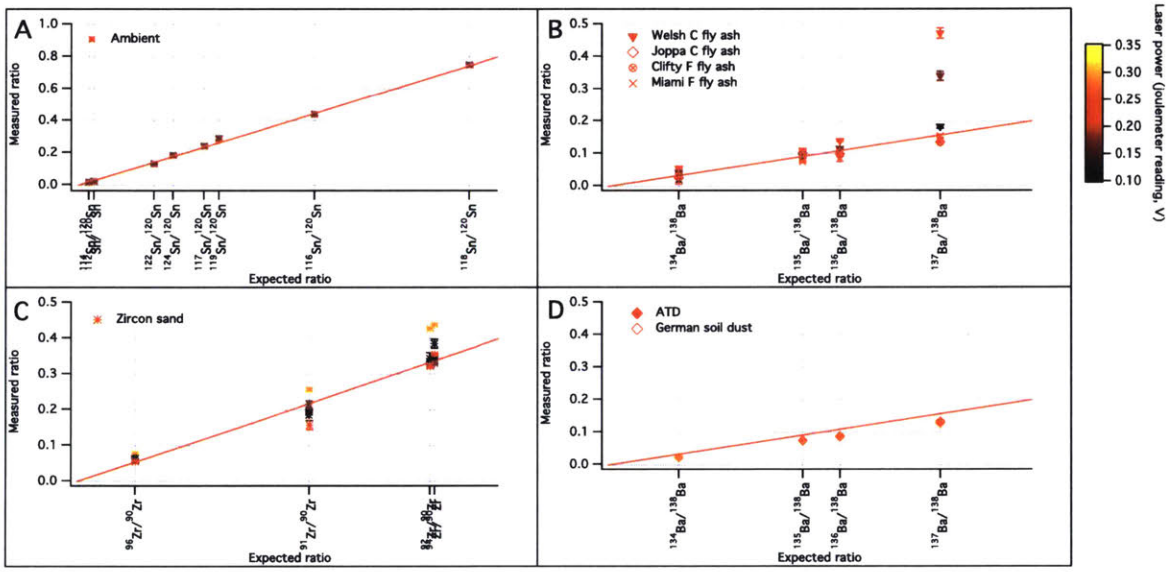

Figure C-16: Comparisons of measured isotopic ratios for three elements to expected natural isotopic ratios. A. Ambient tin. B. Barium in fly ash samples. C. Zirconium in zircon sand. D. Barium in dusts.

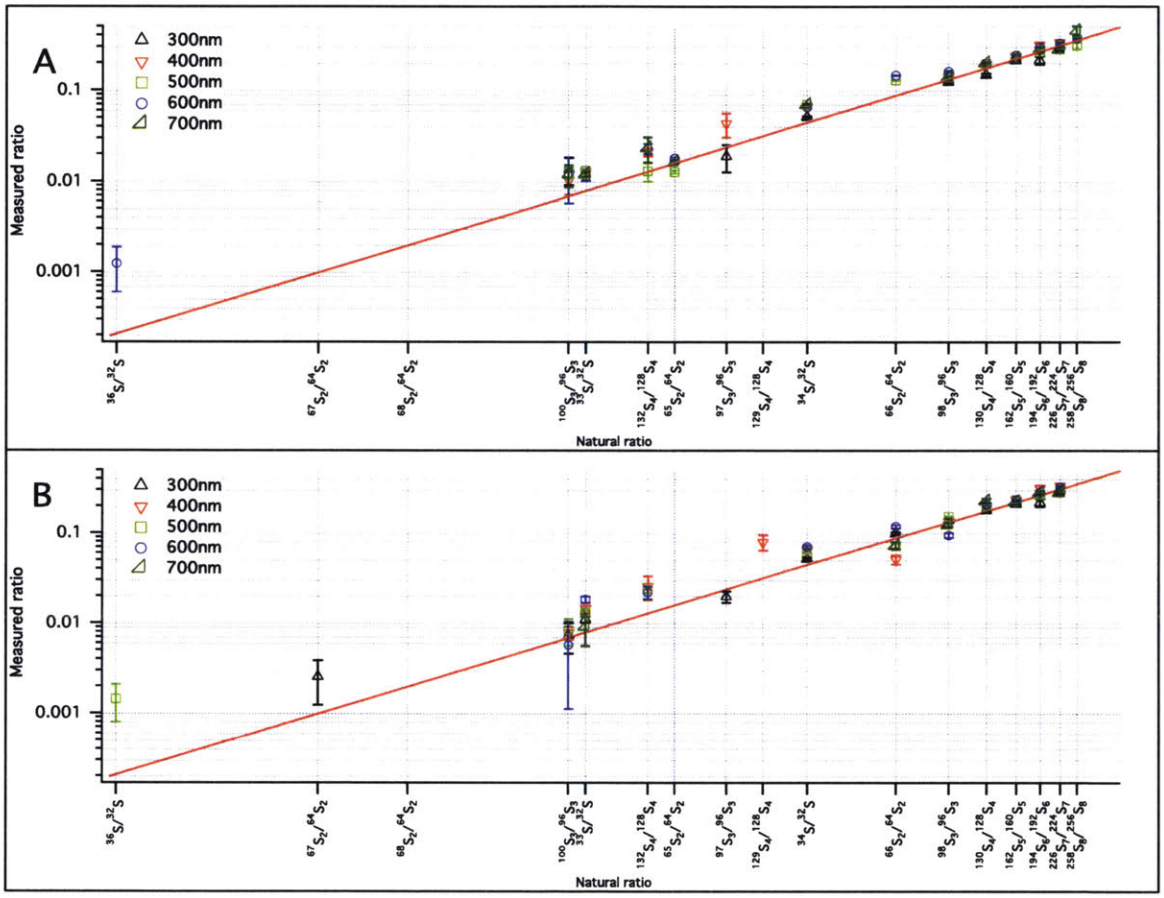

Figure C-17: Comparisons of measured isotopic ratios for elemental sulfur particles produced by photooxidation of COS to expected natural isotopic ratios. Effects of particle size is explored. A. Positive polarity. B. Negative polarity.

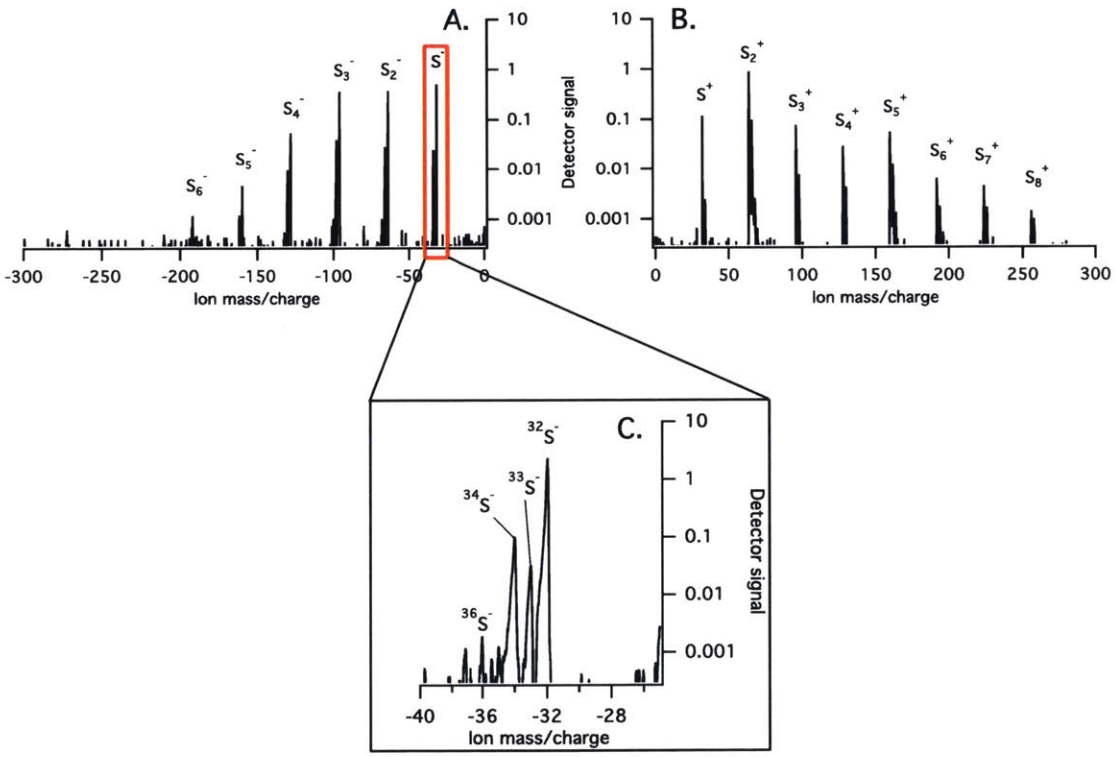

Figure C-18: Example spectra of elemental sulfur. A. Negative polarity. B. Positive polarity. C. Detail of S isotopes in the negative mode.

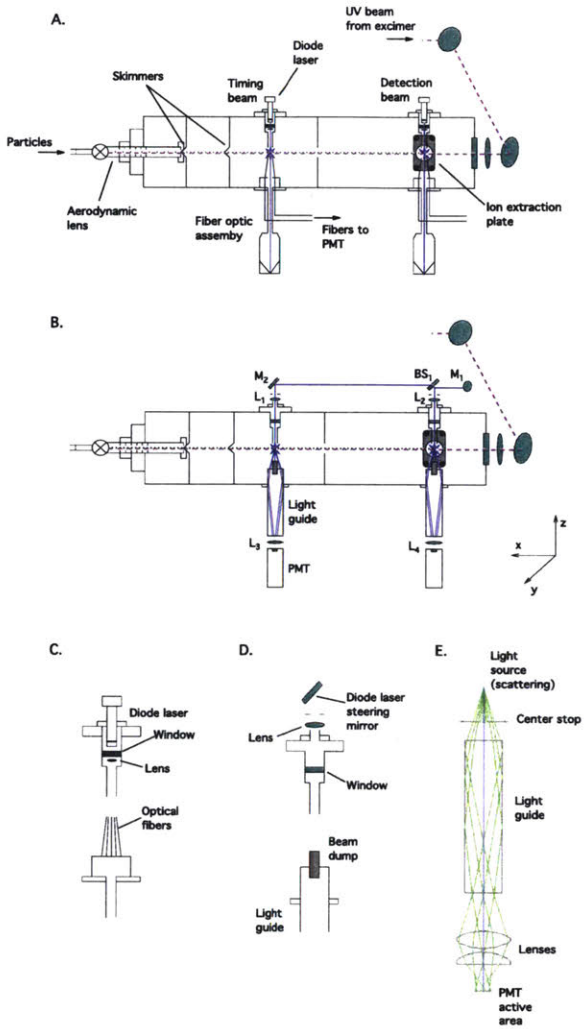

Figure C-19: A. Base LAAPToF configuration with light scattered by particles collected with fiber optics. Note that the mass spectrometer axes come in and out of the page in this orientation (the ion extraction plate is shown for clarity). B. LAAPToF with enhanced light collection using light guides. Note that a signal at the detection beam is required to trigger the desorption and ionization laser. An additional signal at the timing beam is required for a determination of particle vacuum aerodynamic diameter. Optics are labelled in the schematic. M_1 - diode laser steering mirror, BS_1 - beam splitter, M_2 - steering mirror for the timing beam, L_1 and L_2 - focusing lenses for the diode laser, L_3 and L_4 - focusing lenses for scattered light. C. Detail of the fiber ring used to collect the scattered light in the base instrument configuration. D. Detail of the scattering regions with the light guide. E. Ray trace of the light guide described in this paper together with detail of lenses used to focus the scattered light onto the PMT. Ray trace prepared with the OSLO software (Lambda Research Corporation, Littleton, MA).

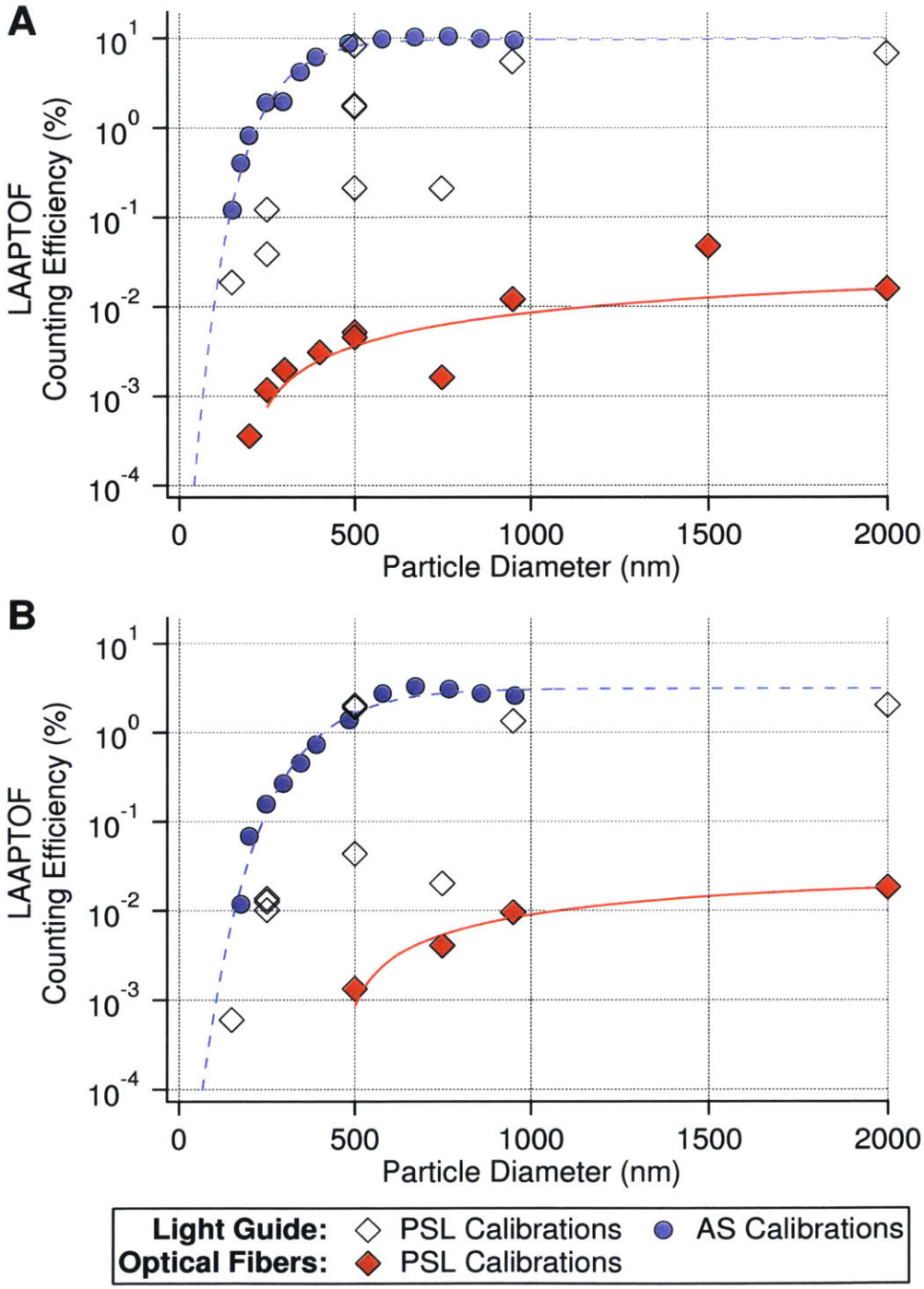

Figure C-20: Optical counting efficiency versus particle size using the original fiber optics and the light guide modification described in this work. Size selected PSLs and ammonium sulfate (AS) particles were used. The scatter in PSL measurements illustrates the sensitivity of the system to laser focus alignment above the light guide beam dump. A. Optical counting efficiency at the timing beam. B. Optical counting efficiency at the detection beam.

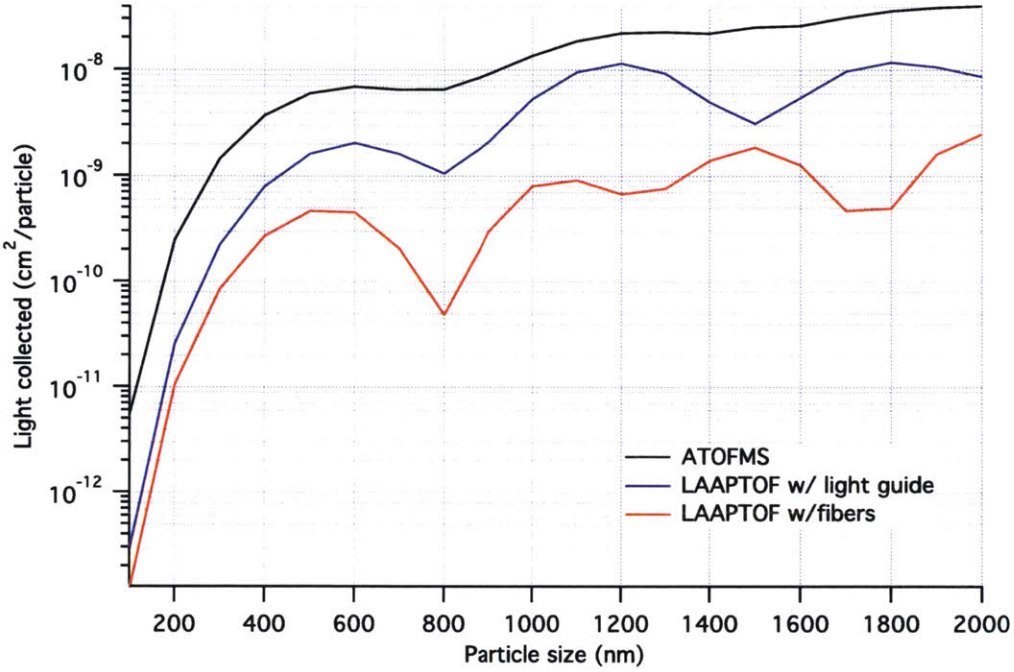

Figure C-21: Modeled scattered light collection for ATOFMS and two detector configurations of LAAPToF (Hodkinson and Greenfield, 1965; Moffet and Prather, 2005). Fibers denote the standard LAAPToF geometry and light guides are the improvement described in this work. The resonances are a consequence of Mie theory.

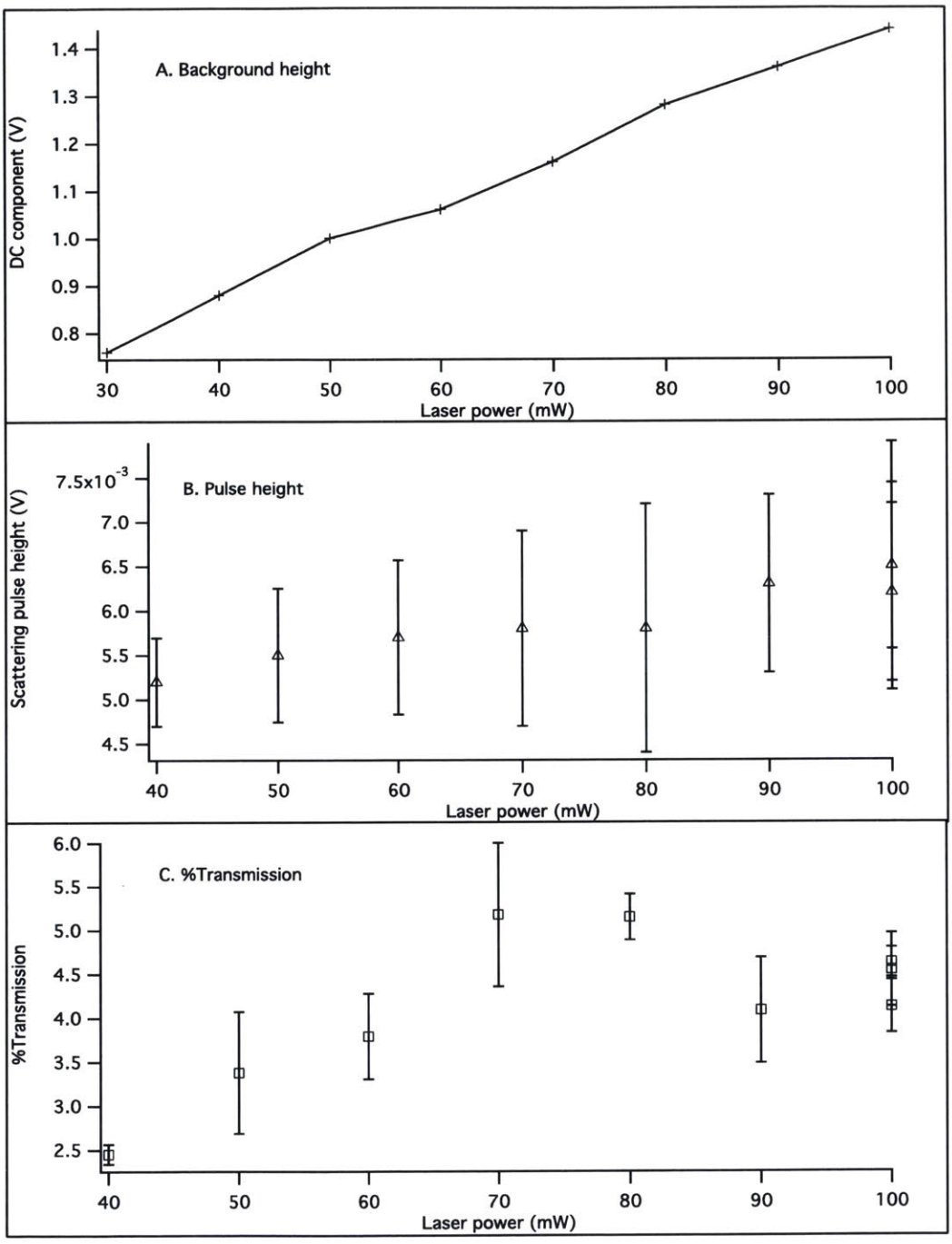

Figure C-22: A: Stray light background (i.e., direct current (DC) measurement of the PMT) at the timing beam as a function of total OBIS laser power. B: Height of light scattering pulses for 950 nm PSL particles at the timing beam as a function of total OBIS laser power. C: Optical counting efficiency for 950 nm PSL particles at the timing beam as a function of total OBIS laser power.

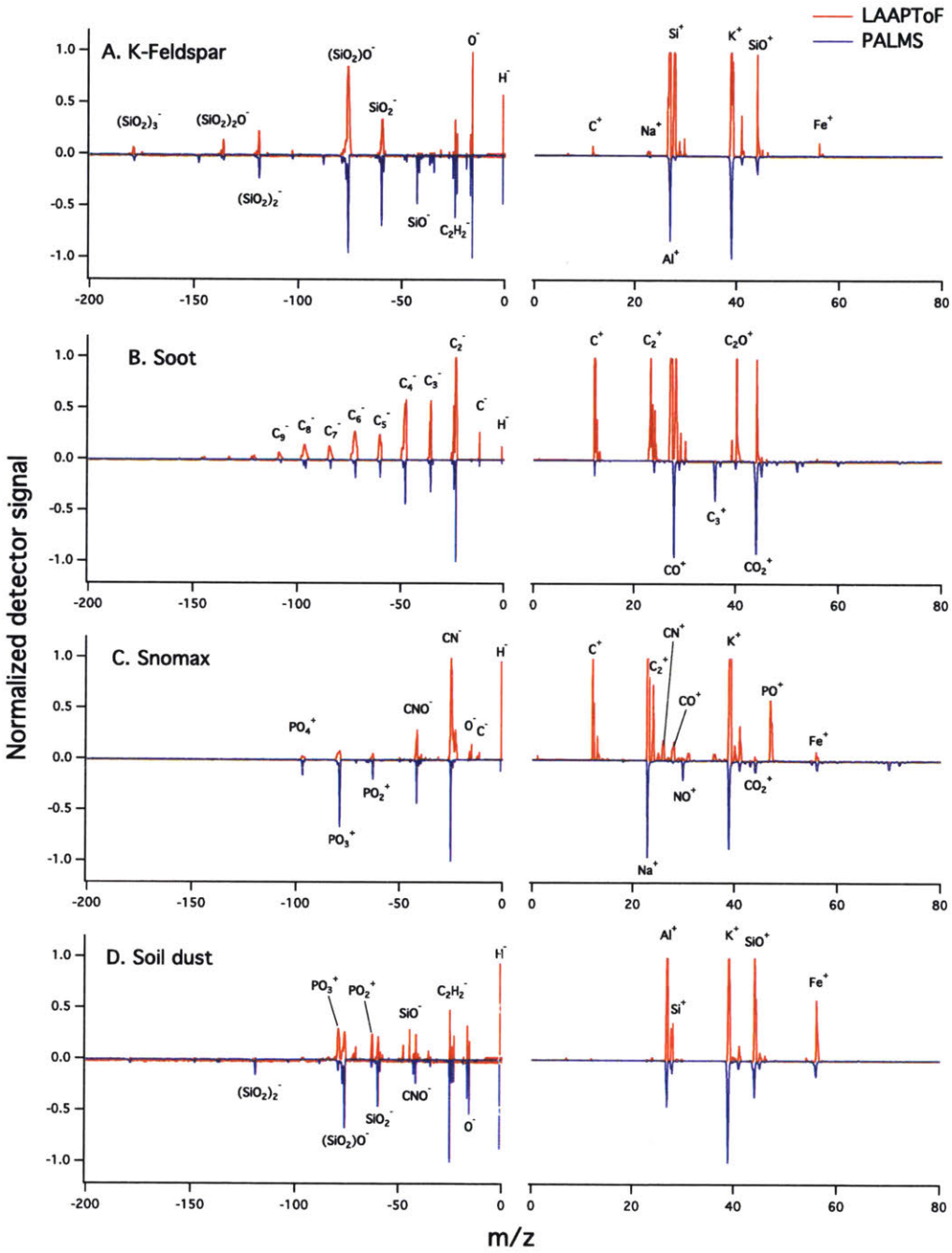

Figure C-23: LAAPToF to PALMS spectral comparison. The signal of the largest peak in each spectrum is normalized for comparison.

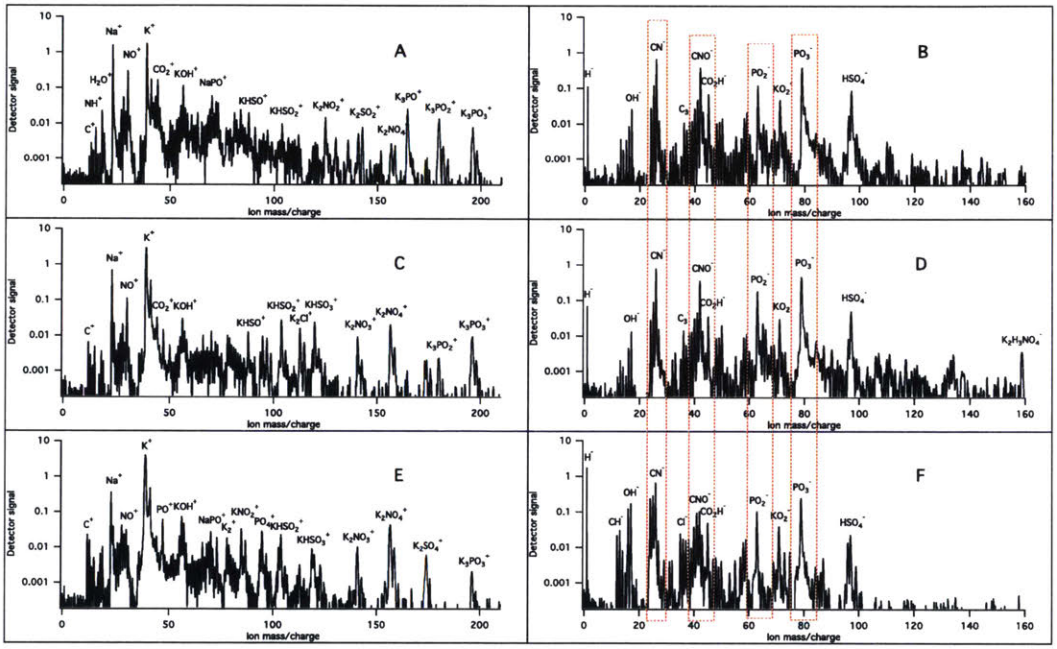

Figure C-24: Representative PALMS spectra of bioaerosol. A and B: Snomax. C and D: P. syringae. E and F: Hazelnut wash water. Right and left columns are positive and negative polarity, respectively. Red dotted lines are features indicated in the literature as markers for biological material.

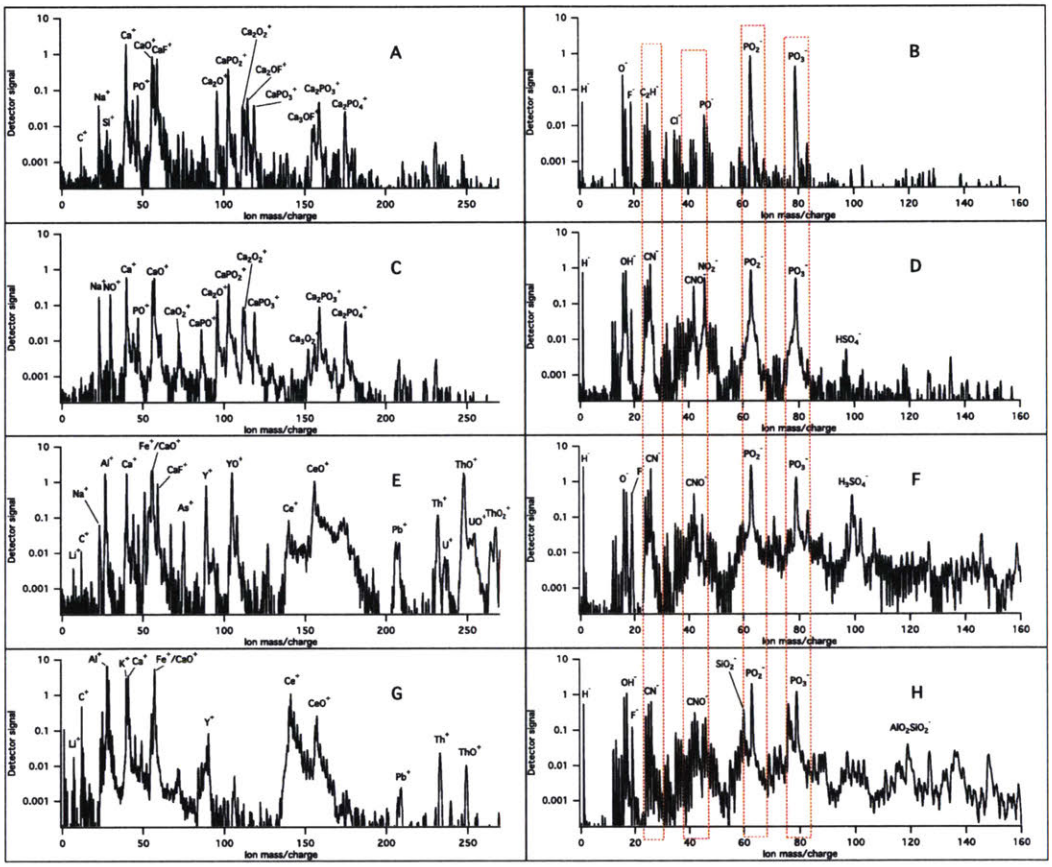

Figure C-25: Representative PALMS spectra of phosphorus-rich minerals and ambient aerosol. A and B: Unprocessed apatite. C and D: Apatite processed with HNO_3 (see text for details). E and F: Monazite-Ce. G and H: Ambient particles sampled at Storm Peak matching monazite chemistry. Right and left columns are positive and negative polarity, respectively. Red dotted lines are features indicated in the literature as markers for biological material.

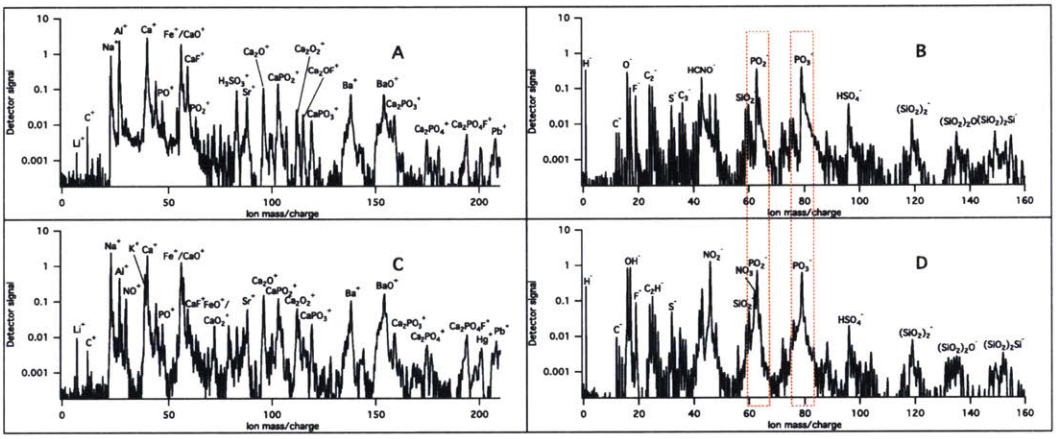

Figure C-26: Representative PALMS spectra of coal fly ash from the J. Robert Welsh power plant. A and B: Unprocessed fly ash. C and D: Fly ash processed with HNO_3 (see text for details). Right and left columns are positive and negative polarity, respectively. Red dotted lines are features indicated in the literature as markers for biological material.

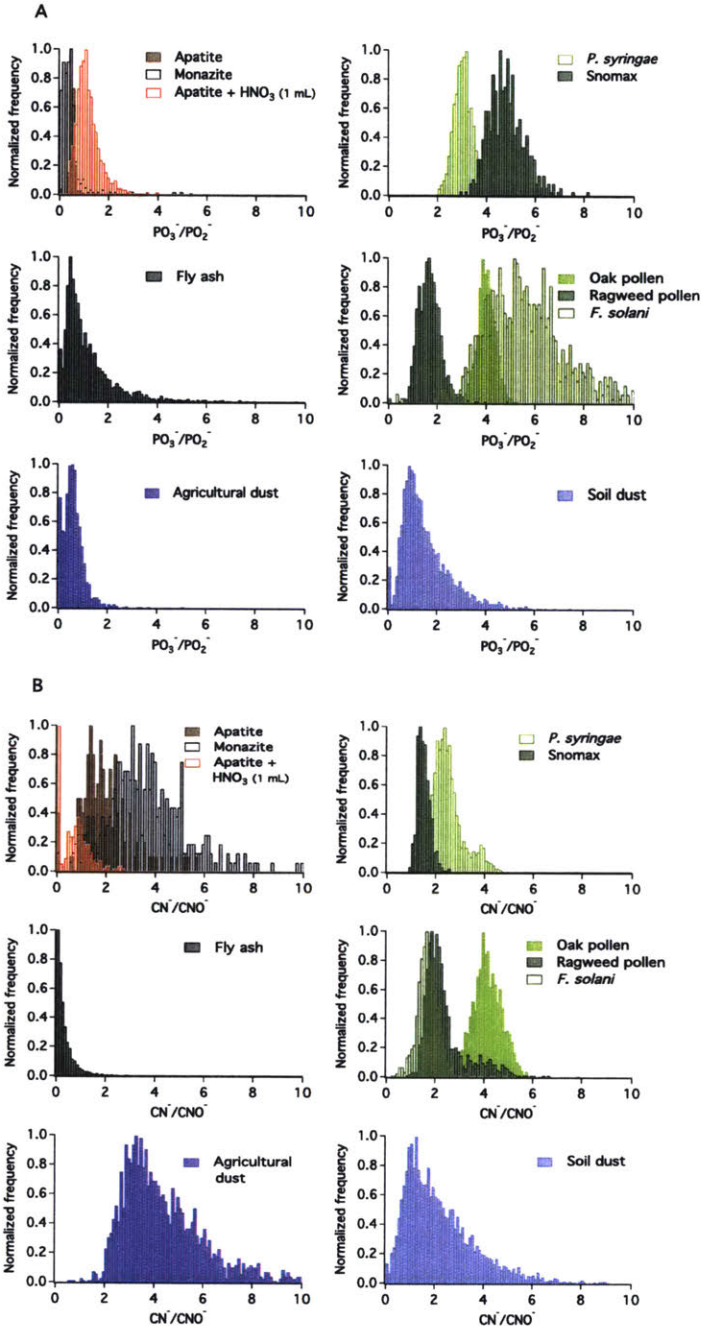

Figure C-27: A: Normalized histograms of the PO_3^-/PO_2^- ratio for the laboratory aerosol. B: Normalized histograms of the CN^-/CNO^- ratio for the same laboratory aerosol as in A. Delineation between the clusters at a PO_3^-/PO_2^- ratio of 3 results in a 70-80% classification accuracy depending on the types of particles considered. Note that soil dusts were not used as part of the training dataset and that not all training aerosols are shown here for clarity.

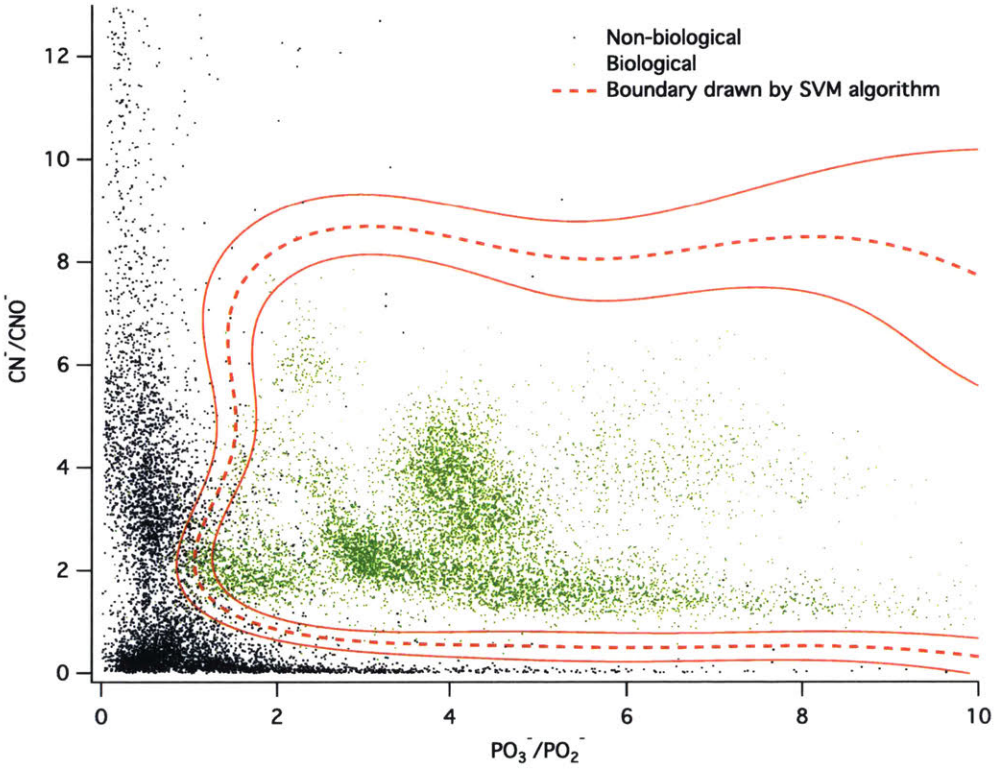

Figure C-28: Inorganic and biological particle clusters in CN^-/CNO^- vs. PO_3^-/PO_2^- space. The SVM algorithm delineates between the clusters with the red dashed line with an overall 97% classification accuracy. Solid red lines indicate the uncertainty boundary (see text for further details).

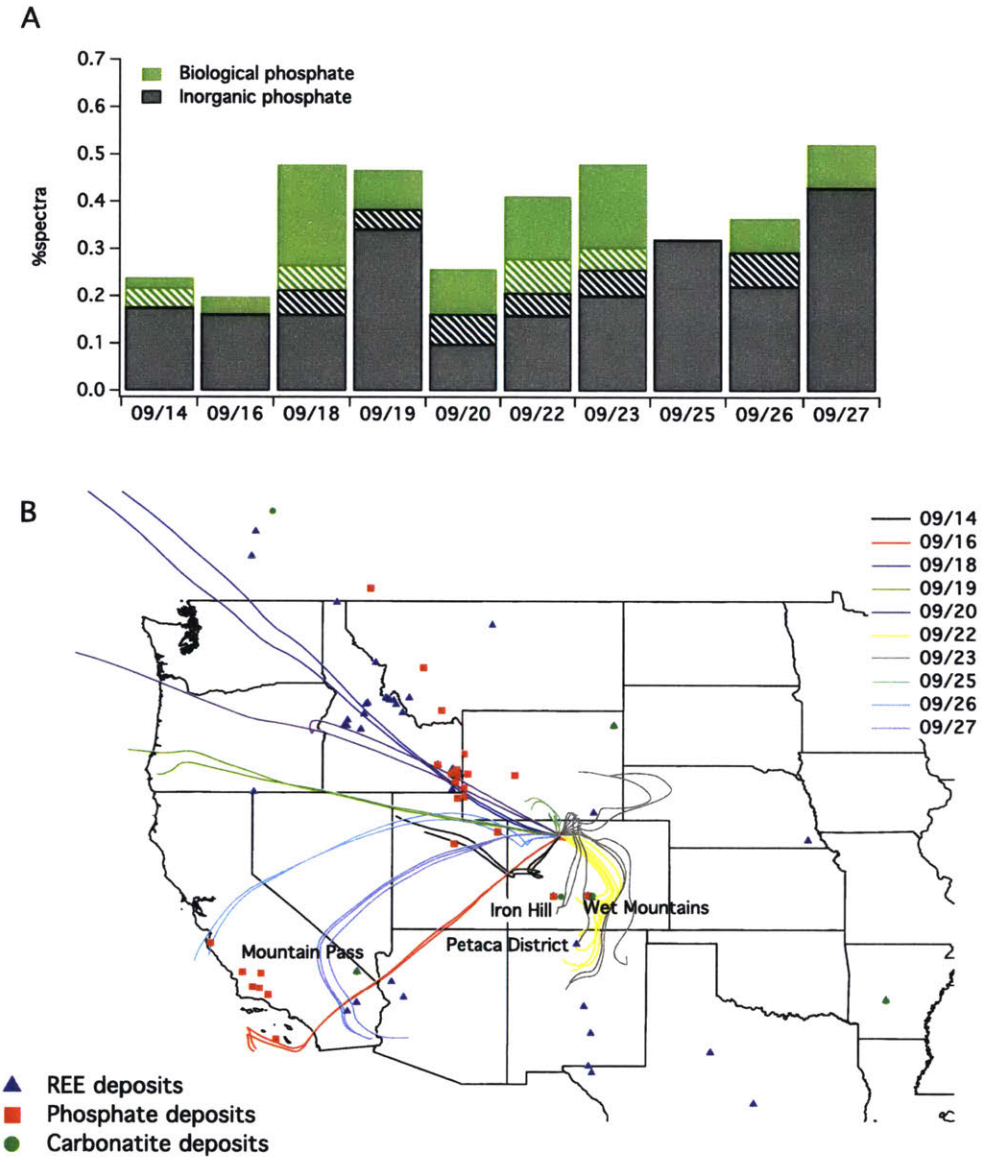

Figure C-29: A: The percentage of ambient aerosol particles from FIN03 dataset categorized as biological and inorganic (phosphate-bearing mineral dust or fly ash) phosphate using the criteria developed in this work. Hatched regions indicate uncertain assignments per the boundaries in Figure C-28. Note that at this location and time of year inorganic phosphate dominates biological. B: HYSPLIT back trajectories plotted for ten measurement days at Storm Peak Laboratory. Locations of REE, phosphate and carobonatite deposits, sourced from U.S. Geological Survey, are co-plotted (Berger et al., 2009; Chernoff and Orris, 2002; Orris and Grauch, 2002).

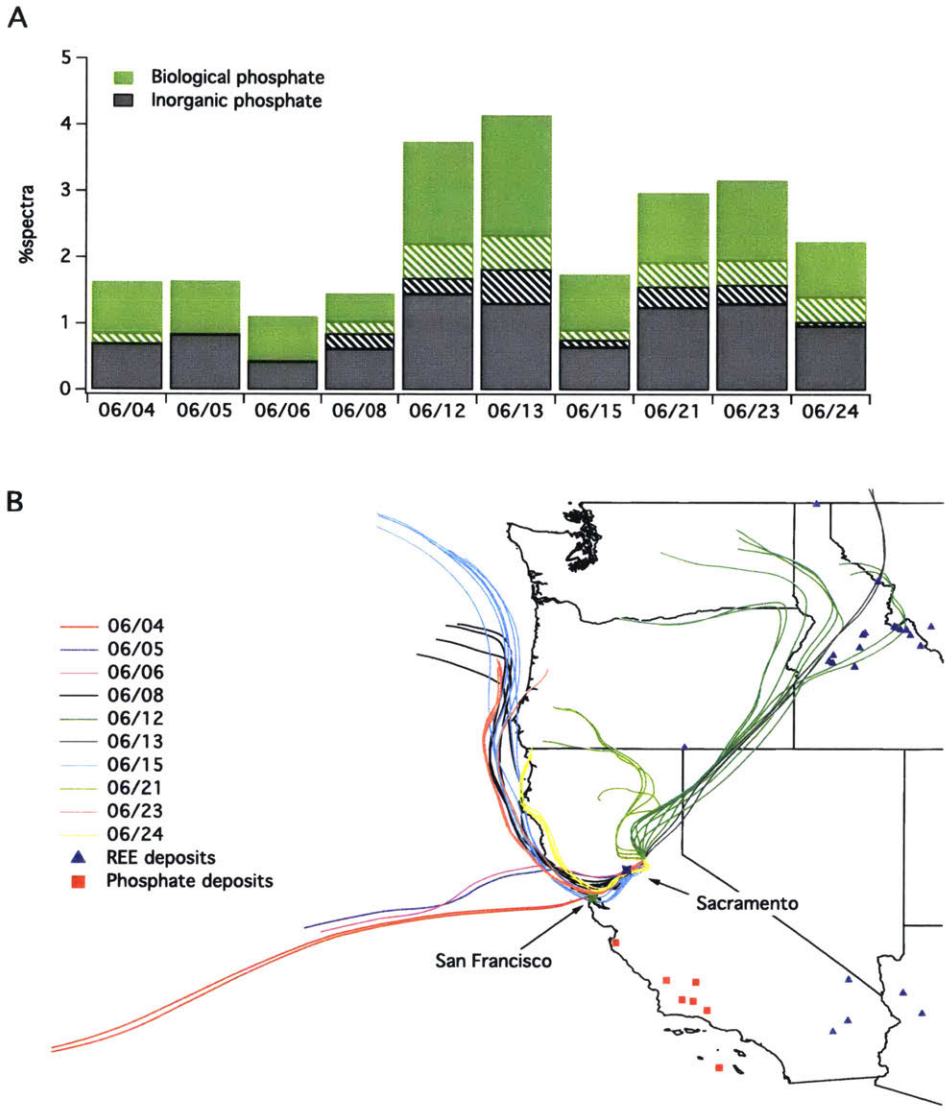

Figure C-30: A: The percentage of ambient aerosol particles from CARES dataset categorized as biological and inorganic (phosphate-bearing mineral dust or fly ash) phosphate using the criteria developed in this work. Hatched regions indicate uncertain assignments per the boundaries in Figure C-28. B: HYSPLIT back trajectories plotted for ten measurement days at the Cool, CA site. Locations of REE, phosphate and carobonatite deposits, sourced from U.S. Geological Survey, are co-plotted (Berger et al., 2009; Chernoff and Orris, 2002; Orris and Grauch, 2002) along with locations of major urban centers.

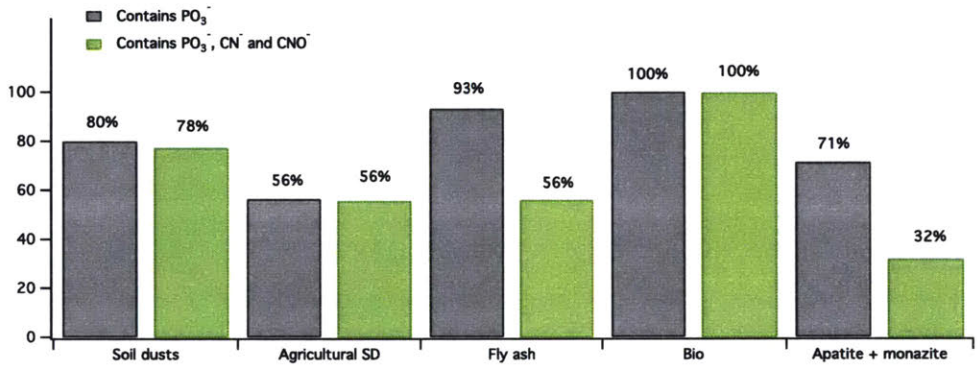

Figure C-31: Percentage of particles that include PO_3^-, CN^- and CNO^- markers in five classes of atmospherically-relevant aerosol spectra acquired with PALMS in this work. Note that the green bars indicate the percentage of particles of each type identified as biological using literature criteria. In the case of bioaerosol the identification is correct. In all other aerosol classes the green bar denotes a typical level of misidentification.

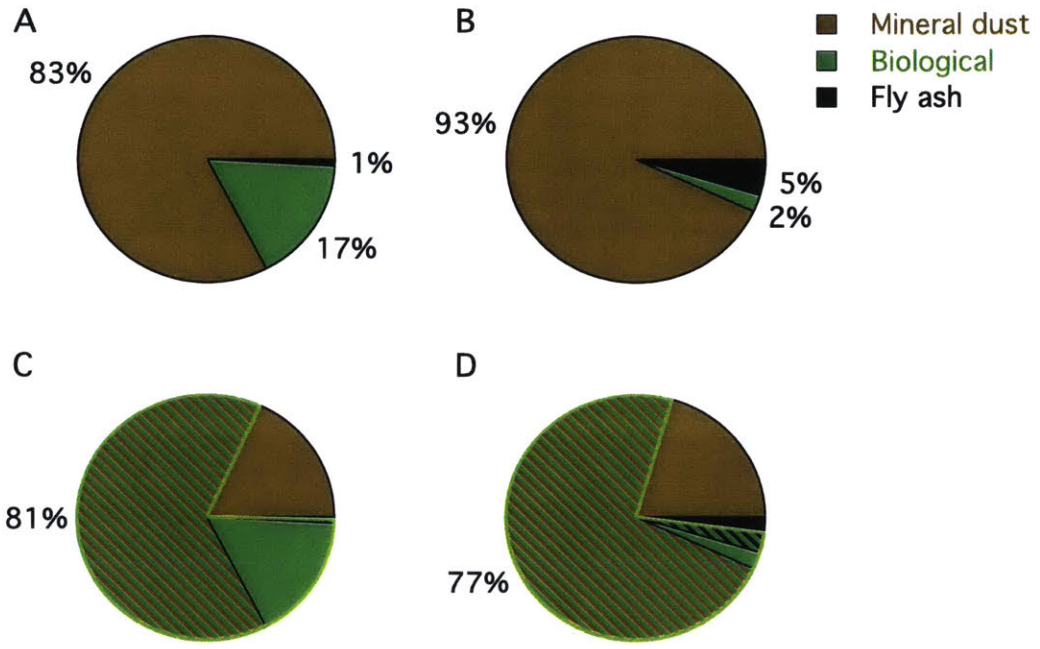

Figure C-32: Abundance of bioaerosol, mineral dust and fly ash in the atmosphere constructed using emissions estimates in Table B.6 A: Highest estimate for bioaerosol coupled to lowest estimates for dust and fly ash. B: Lowest estimate of bioaerosol in the atmosphere coupled to highest estimates for dust and fly ash. C and D: Effect of misidentification of phosphate- and organic nitrogen-containing aerosol as biological using the emissions in A and B, respectively. The hatched regions correspond to the misidentified fractions of mineral dust and fly ash. In these estimates the correct emissions (solid green region) in A and B (17 and 2%, respectively) are overestimated (hatched green region of misidentified aerosol plus solid green region) in C and D (as 81 and 77%, respectively).

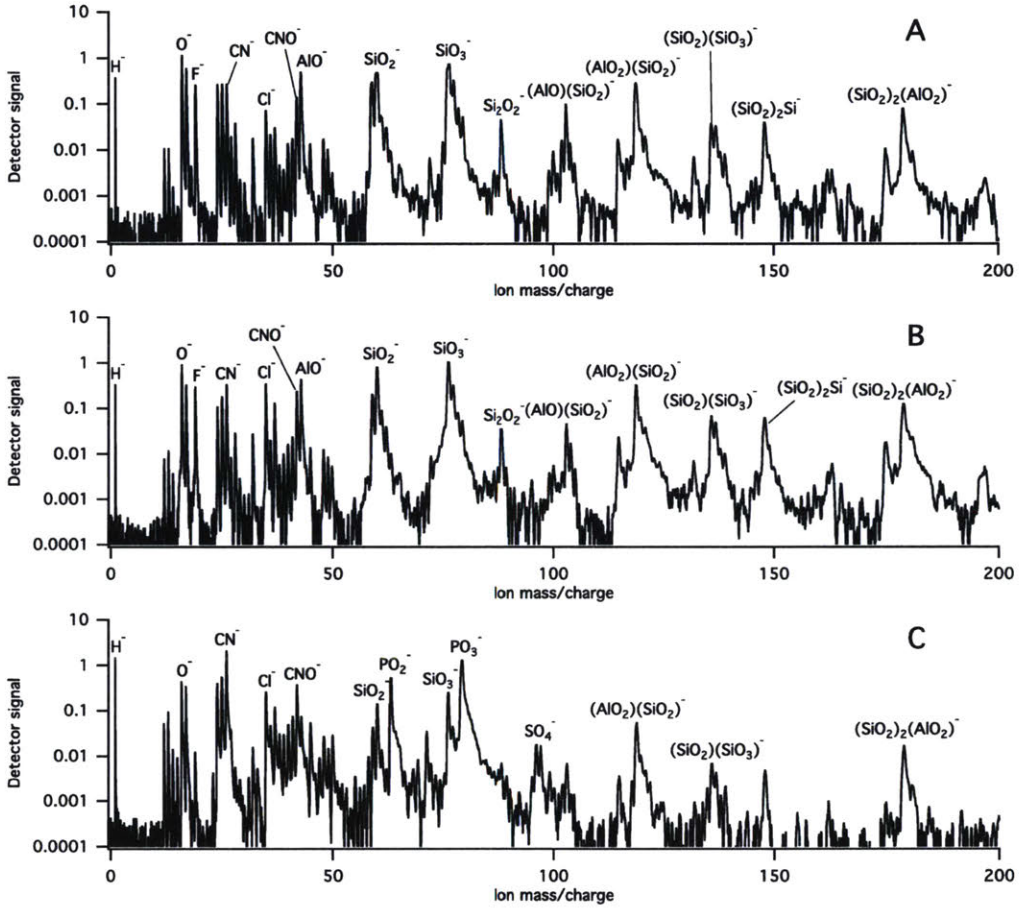

Figure C-33: Exemplary PALMS negative polarity spectra of A: dry-dispersed illite NX, B: wet-dispersed illite NX from a distilled, deionized water slurry and C: similarly wet-dispersed illite NX but from a water slurry that also contained F. solani spores. Note that phosphate features are absent in A and B but present in C due to addition of biological material to the mineral dust.

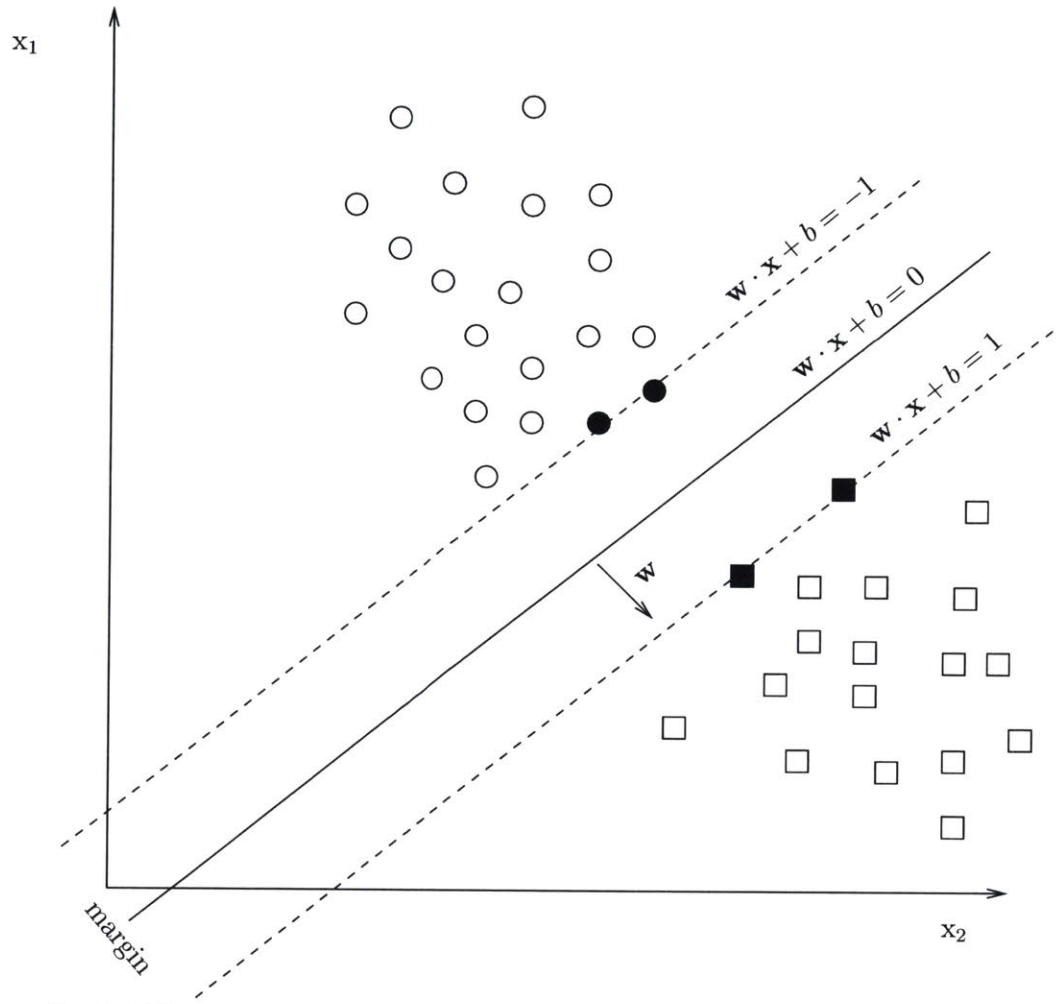

Figure C-34: Schematic representation of two data clusters (circles and squares) and a decision boundary hyperplane separating them. The SVM algorithm optimizes the boundary so that the margin is maximized. Vector **w** is normal to the separating hyperplane. The filled symbols are the support vectors.

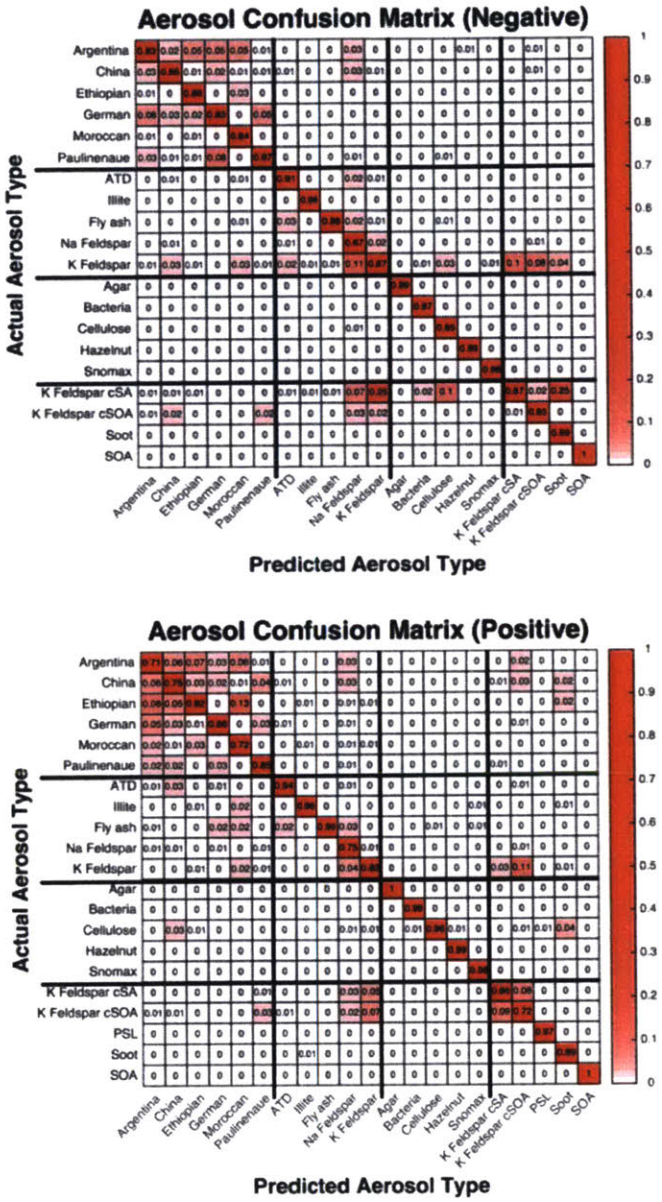

Figure C-35: Confusion matrices (see text for explanation) for various laboratory aerosol types sampled at AIDA during FIN-1. The classifier used is an ensemble of decision trees.

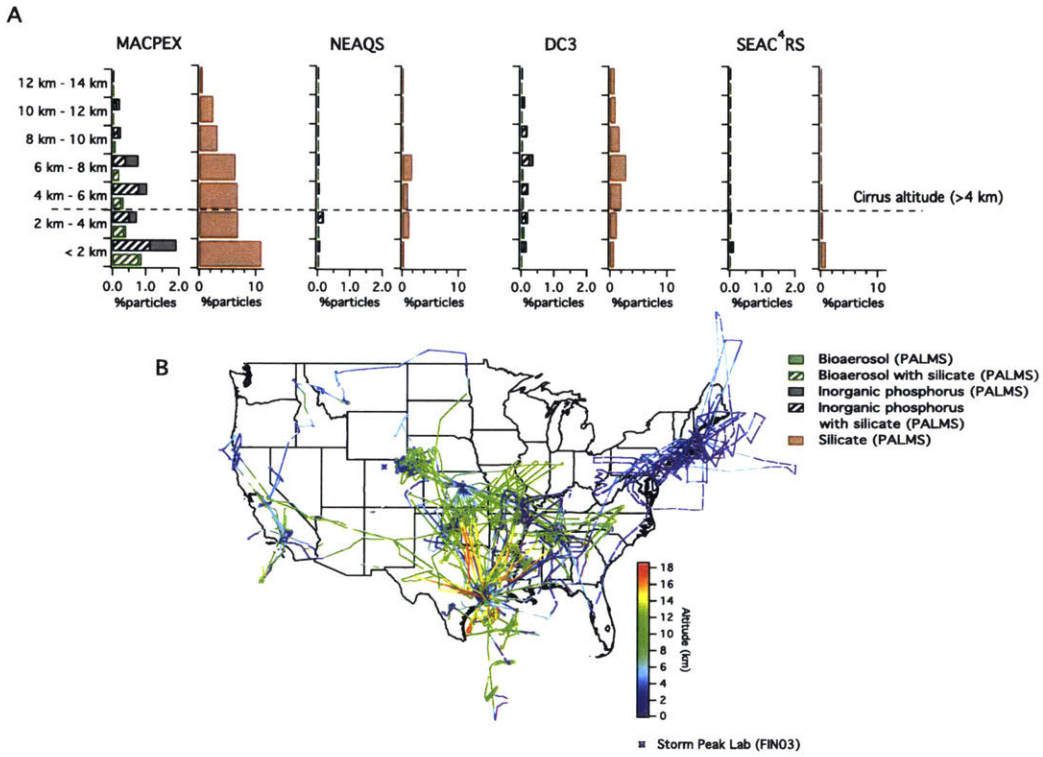

Figure C-36: Flight tracks and altitude-resolved percentages of particles categorized as bioaerosol, inorganic phosphate-rich and mineral dust during the DC3, SEAC4RS, NEAQS and MACPEX aircraft studies. Note the higher abundance of all three particle types near ground level, which decreases with altitude; the DC3 campaign, which targeted convective conditions, is an exception. Also note that the x-axis scale for mineral dust profiles is 5x the x-axis scale of bioaerosol and inorganic phosphate-rich profiles.

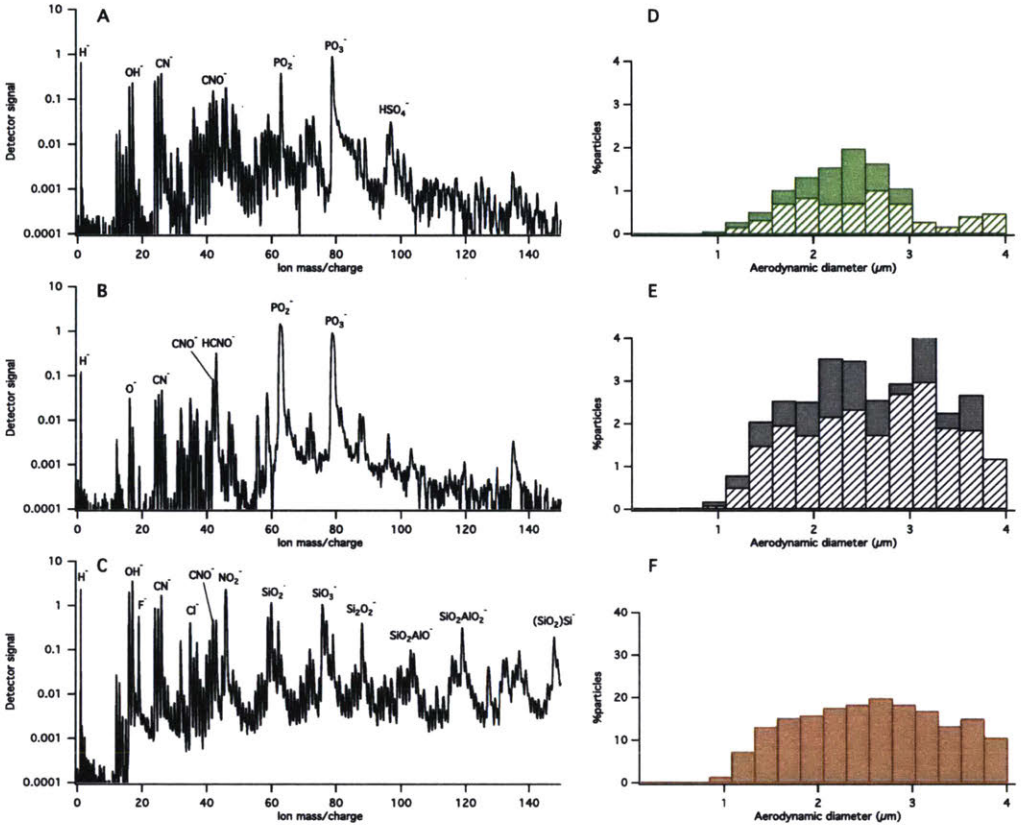

Figure C-37: Representative spectra and size distributions of three types of particles discussed in this study. A. Representative spectrum of bioaerosol (DC3 campaign). B. Size distribution of bioaerosol particles in DC3, SEAC4RS, NEAQS, MACPEX and FIN03 campaigns. Hatched pattern indicates the percentage of particles that also include silicate mineral markers in each size bin. C. Representative spectrum of an inorganic phosphate-rich particle (DC3 campaign). D. Size distribution of inorganic phosphate-rich particles in DC3, SEAC4RS, NEAQS, MACPEX and FIN03 campaigns. Hatched pattern indicates the percentage of particles that also include silicate mineral markers in each size bin. E. Representative spectrum of a mineral dust particle (DC3 campaign). F. Size distribution of mineral dust particles in DC3, SEAC4RS, NEAQS, MACPEX and FIN03 campaigns. Note that the y-axis scale for F is 10x the y-axis scales in B and D.

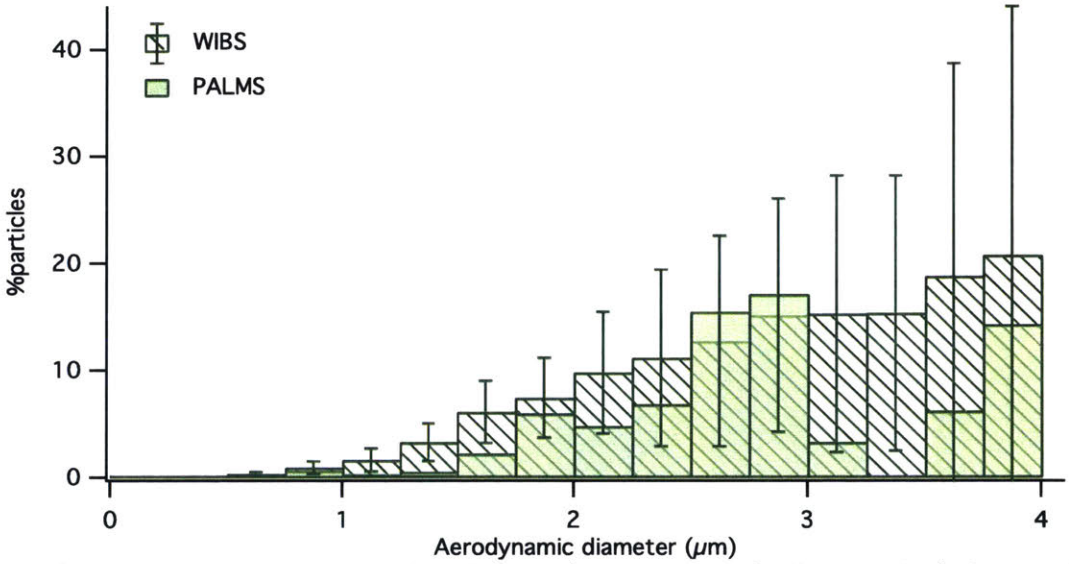

Figure C-38: FIN03 bioaerosol abundances (as percent of all particles) detected by the mass spectrometer and fluorescence sensor grouped into size bins. The error bars on WIBS data represent standard deviations of the hourly average fractions in each size bin over all of the ambient sampling during the campaign.

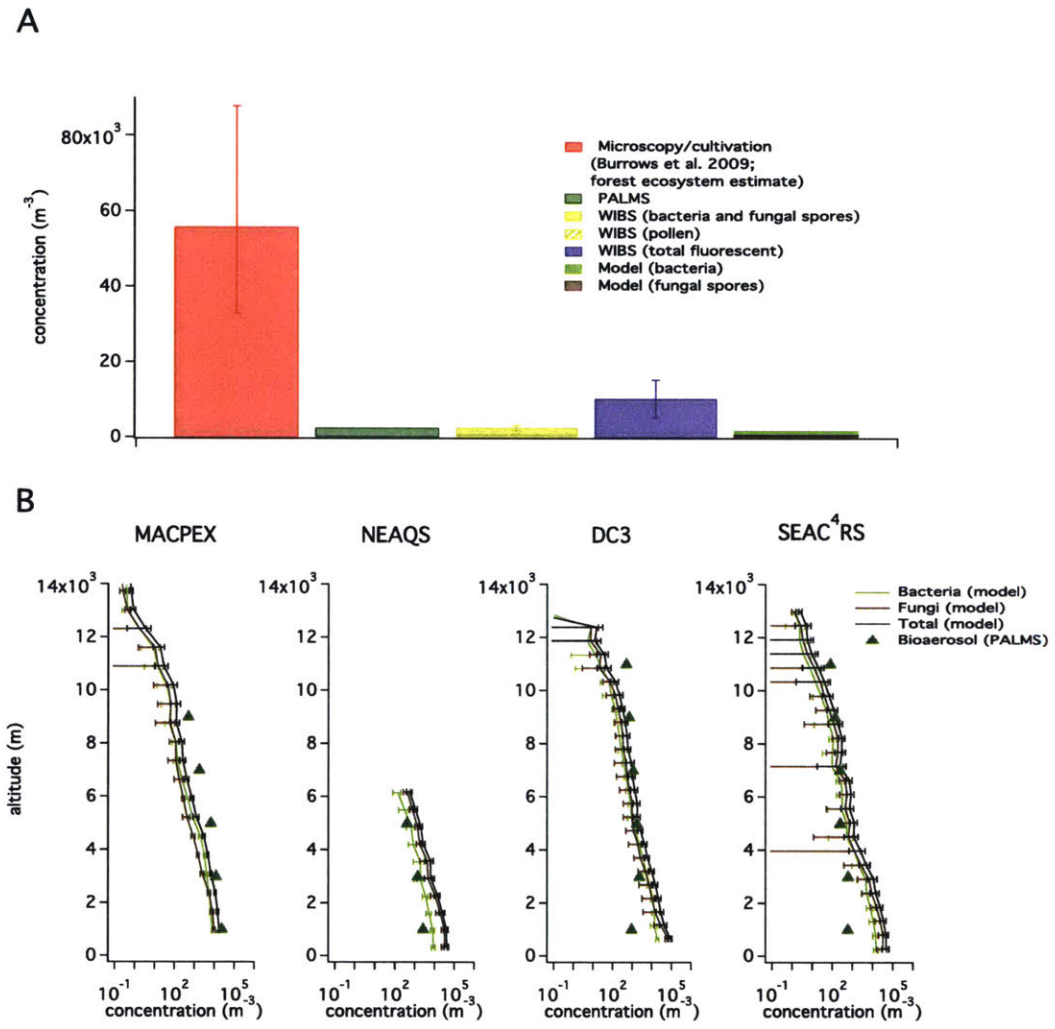

Figure C-39: Comparisons between bioaerosol concentration measurements reported in this paper, historical measurements used to derive bacteria fluxes used in previous modeling studies and results of a global aerosol microphysics model. A. A comparison of measurements performed at the Storm Peak Lab (mass spectrometry and fluorescence) with microscopy measurements reported in Burrows et al. (2009) for a forest ecosystem and aerosol model results. B. Vertical profiles corresponding to the four field campaigns considered in this study compared to the model results. Error bars correspond to standard deviations in the model estimates in each altitude bin. The standard deviations represent the variability in latitude and longitude.

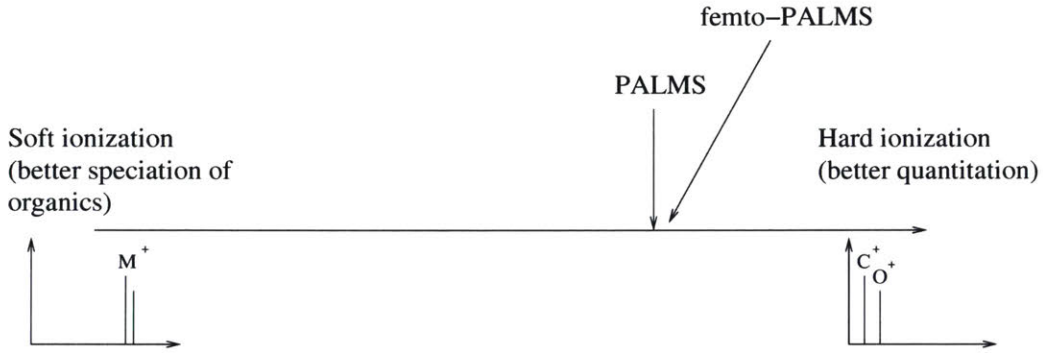

Figure C-40: Schematic representation of ionization strength experimental space. Soft ionization leaves molecules intact. Hard ionization produces atomic ions only. We assign femto-PALMS (Chapter 2) very close to traditional PALMS due to similarity of mass spectra produced.

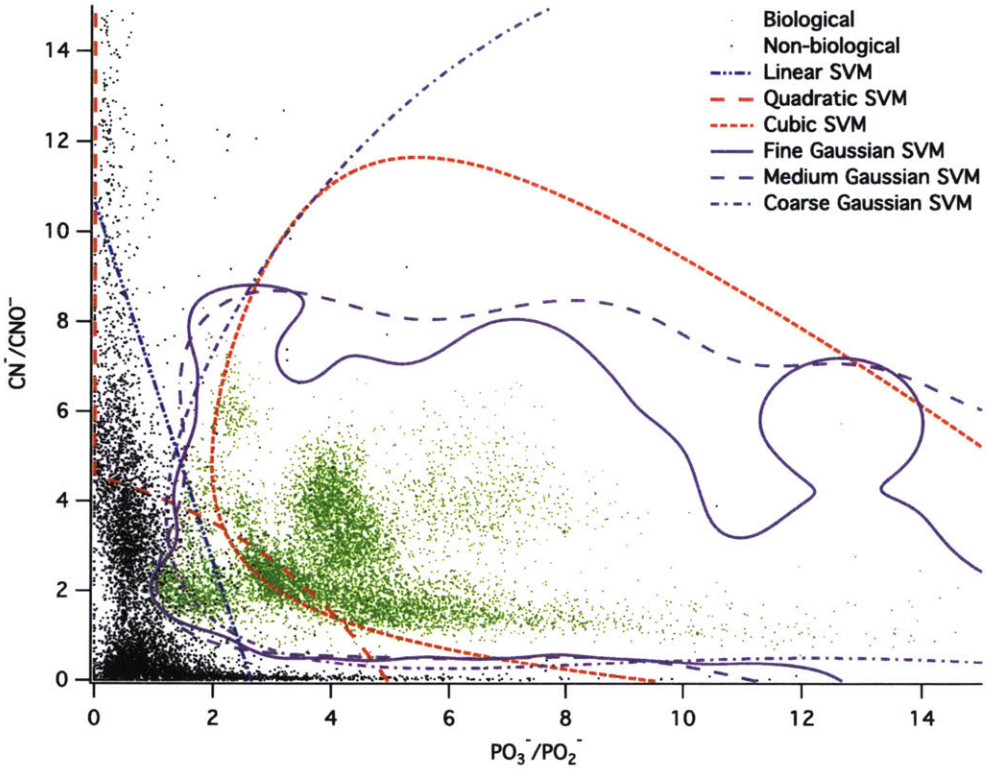

Figure C-41: Boundaries "drawn" by six types of SVM classifiers used on the biological/non-biological (Chapter 5) training data. Note that the Gaussian SVM classifiers separate the clusters most accurately.

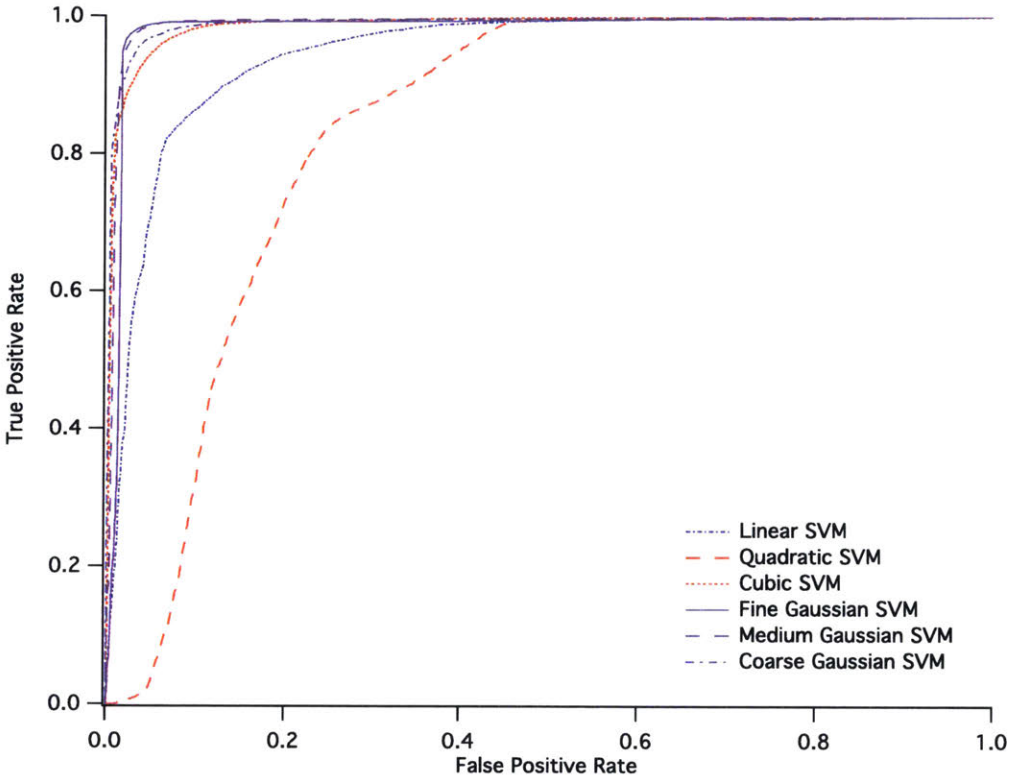

Figure C-42: Receiver Operating Characteristic (ROC) curves for the six types of SVM classifiers used on the biological/non-biological (Chapter 5) training data. Classifiers whose ROC curves reach the upper left corner are more successful in separating the classes.

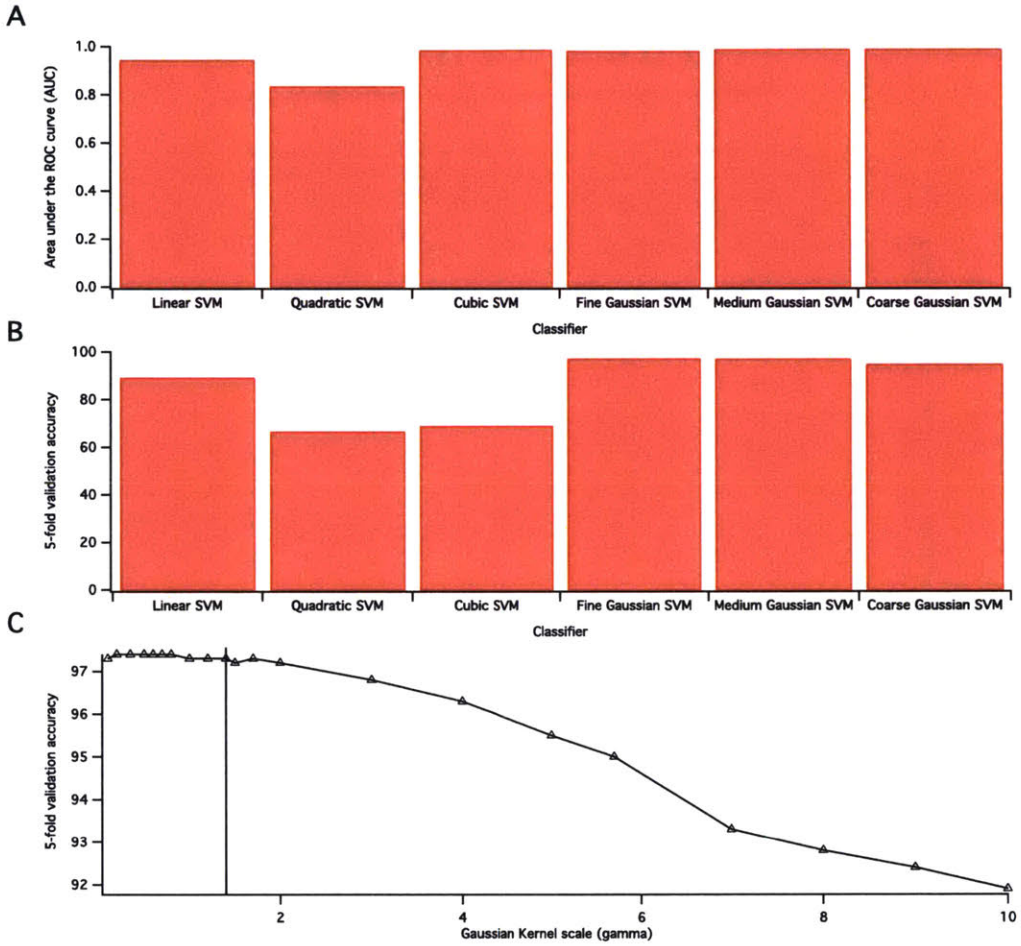

Figure C-43: A. Comparison of areas under the ROC curves (Figure C-42) for six types of SVM classifiers used on the biological/non-biological (Chapter 5) training data. B. Comparison of 5-fold validation accuracies for six types of SVM classifiers used on the biological/non-biological (Chapter 5) training data. C. 5-fold validation accuracy for the Gaussian SVM classifier plotted as a function of the kernel scale (γ) parameter (see text for details). The vertical line is the scale used in the final, optimized classifier.

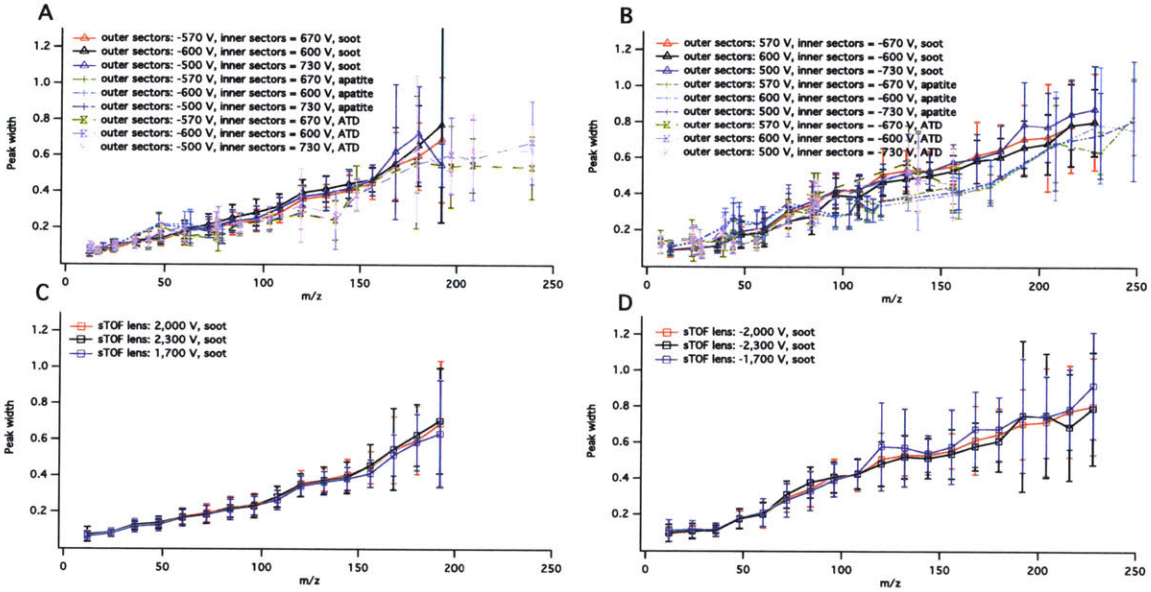

Figure C-44: Spectral peak width (FWHH) as a function of m/z for single particle mass spectra plotted for various sTOF voltage conditions and chemical species. A. Negative polarity, sector voltages. B. Positive polarity, sector voltages. C. Negative polarity, sTOF entrance Einzel lens. D. Positive polarity, sTOF entrance Einzel lens.

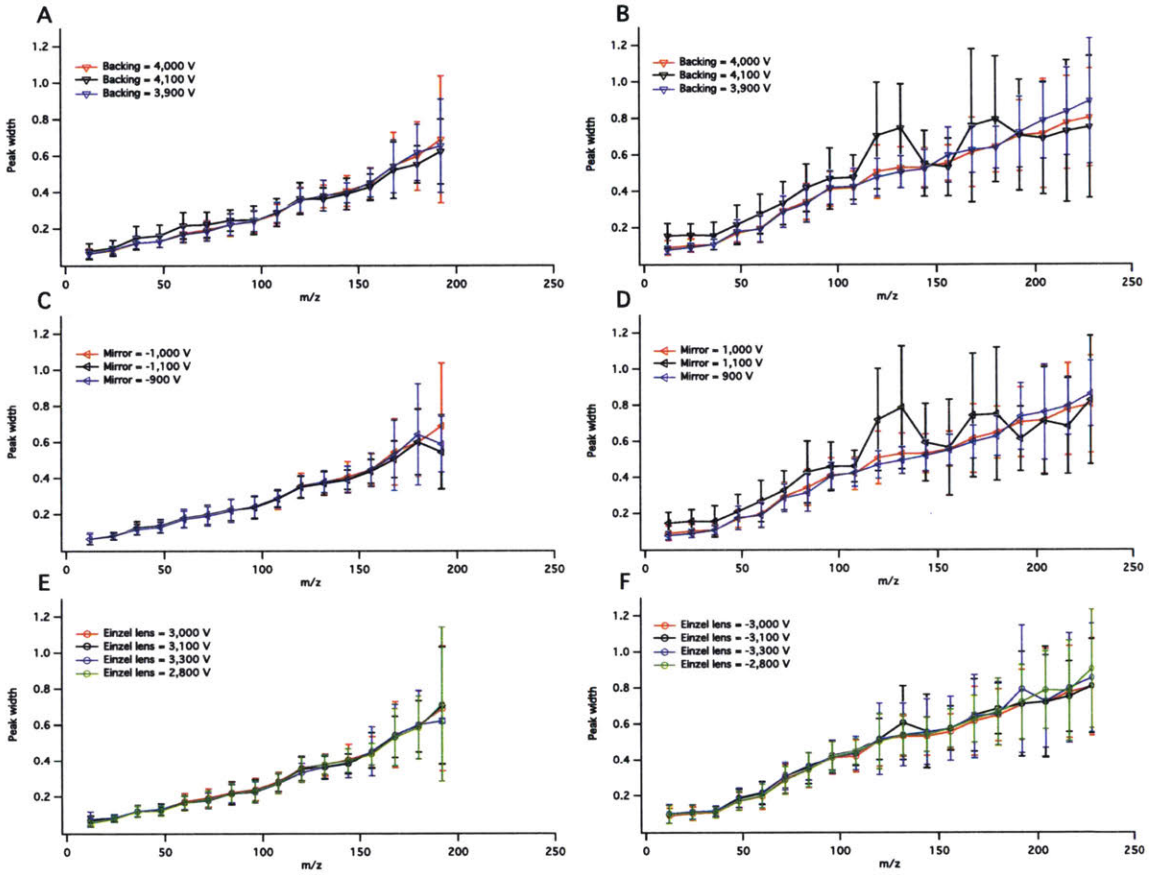

Figure C-45: Spectral peak width (FWHH) as a function of m/z for single particle mass spectra of soot plotted for various source region voltage conditions. A. Negative polarity, backing voltages. B. Positive polarity, backing voltages. C. Negative polarity, mirror voltages. D. Positive polarity, mirror voltages. E. Negative polarity, Einzel lens. F. Positive polarity, Einzel lens.

Bibliography

Abdelmonem, A., J. Lützenkirchen, and T. Leisner (2015). Probing ice-nucleation processes on the molecular level using second harmonic generation spectroscopy. *Atmospheric Measurement Techniques 8*(8), 3519–3526.

Adler, G., J. M. Flores, A. Abo Riziq, S. Borrmann, and Y. Rudich (2011). Chemical, physical, and optical evolution of biomass burning aerosols: a case study. *Atmospheric Chemistry and Physics 11*(4), 1491–1503.

Amato, P., M. Ménager, M. Sancelme, P. Laj, G. Mailhot, and A.-M. Delort (2005). Microbial population in cloud water at the Puy de Dôme: Implications for the chemistry of clouds. *Atmospheric Environment 39*(22), 4143–4153.

Amato, P., M. Parazols, M. Sancelme, P. Laj, G. Mailhot, and A.-M. Delort (2007). Microorganisms isolated from the water phase of tropospheric clouds at the Puy de Dôme: major groups and growth abilities at low temperatures. *FEMS Microbiology Ecology 59*(2), 242–254.

Atkinson, J. D., B. J. Murray, M. T. Woodhouse, T. F. Whale, K. J. Baustian, K. S. Carslaw, S. Dobbie, D. O'Sullivan, and T. L. Malkin (2013). The importance of feldspar for ice nucleation by mineral dust in mixed-phase clouds. *Nature 498*(7454), 355–358.

Ault, A. P., T. M. Peters, E. J. Sawvel, G. S. Casuccio, R. D. Willis, G. A. Norris, and V. H. Grassian (2012). Single-Particle SEM-EDX Analysis of Iron-Containing Coarse Particulate Matter in an Urban Environment: Sources and Distribution of Iron within Cleveland, Ohio. *Environmental Science & Technology 46*(8), 4331–4339.

Ban-Weiss, G. A., L. Cao, G. Bala, and K. Caldeira (2012). Dependence of climate forcing and response on the altitude of black carbon aerosols. *Climate Dynamics 38*(5-6), 897–911.

Barth, M. C., C. A. Cantrell, W. H. Brune, S. A. Rutledge, J. H. Crawford, H. Huntrieser, L. D. Carey, D. MacGorman, M. Weisman, K. E. Pickering, E. Bruning, B. Anderson, E. Apel, M. Biggerstaff, T. Campos, P. Campuzano-Jost, R. Cohen, J. Crounse, D. A. Day, G. Diskin, F. Flocke, A. Fried, C. Garland, B. Heikes, S. Honomichl, R. Hornbrook, L. G. Huey, J. L. Jimenez, T. Lang, M. Lichtenstern, T. Mikoviny, B. Nault, D. O'Sullivan, L. L. Pan, J. Peischl, I. Pollack, D. Richter,

D. Riemer, T. Ryerson, H. Schlager, J. St. Clair, J. Walega, P. Weibring, A. Weinheimer, P. Wennberg, A. Wisthaler, P. J. Wooldridge, and C. Ziegler (2015). The Deep Convective Clouds and Chemistry (DC3) Field Campaign. *Bulletin of the American Meteorological Society 96*(8), 1281–1309.

Bauer, H., A. Kasper-Giebl, M. Löflund, H. Giebl, R. Hitzenberger, F. Zibuschka, and H. Puxbaum (2002). The contribution of bacteria and fungal spores to the organic carbon content of cloud water, precipitation and aerosols. *Atmospheric Research 64*(1-4), 109–119.

Bauer, H., E. Schueller, G. Weinke, A. Berger, R. Hitzenberger, I. L. Marr, and H. Puxbaum (2008). Significant contributions of fungal spores to the organic carbon and to the aerosol mass balance of the urban atmospheric aerosol. *Atmospheric Environment 42*(22), 5542–5549.

Ben-Hur, A., D. Horn, H. T. Siegelmann, and V. Vapnik (2001). Support Vector Clustering. *Journal of Machine Learning Research 2*, 125–137.

Ben-Hur, A., C. S. Ong, S. Sonnenburg, B. Schölkopf, and G. Rätsch (2008, oct). Support Vector Machines and Kernels for Computational Biology. *PLoS Computational Biology 4*(10), e1000173.

Berger, V. I., D. A. Singer, and G. J. Orris (2009). Carbonatites of the world, explored deposits of Nb and REE; database and grade and tonnage models: U.S. Geological Survey Open-File Report 2009-1139, 17 p. and database. Technical report, U.S. Geological Survey.

Borys, R. D. and M. A. Wetzel (1997). Storm Peak Laboratory: A Research, Teaching, and Service Facility for the Atmospheric Sciences. *Bulletin of the American Meteorological Society 78*(10), 2115–2123.

Boser, B. E., I. M. Guyon, and V. N. Vapnik (1992). A training algorithm for optimal margin classifiers. In *Proceedings of the fifth annual workshop on Computational learning theory - COLT '92*, New York, New York, USA, pp. 144–152. ACM Press.

Boucher, O., D. Randall, P. Artaxo, C. Bretherton, G. Feingold, P. Forster, V.-M. Kerminen, Y. Kondo, H. Liao, U. Lohmann, P. Rasch, S. K. Satheesh, S. Sherwood, B. Stevens, and X. Y. Zhang (2013). Clouds and Aerosols. In: Climate Change 2013: The Physical Science Basis. Contribution of Working Group I to the Fifth Assesment Report of the Intergovernmental Panel on Climate Change. Cambridge, United Kingdom and New York, NY, USA: Cambridge University Press.

Bowers, R. M., C. L. Lauber, C. Wiedinmyer, M. Hamady, A. G. Hallar, R. Fall, R. Knight, and N. Fierer (2009). Characterization of Airborne Microbial Communities at a High-Elevation Site and Their Potential To Act as Atmospheric Ice Nuclei. *Applied and Environmental Microbiology 75*(15), 5121–5130.

Bowers, R. M., I. B. McCubbin, A. G. Hallar, and N. Fierer (2012). Seasonal variability in airborne bacterial communities at a high-elevation site. *Atmospheric Environment 50*, 41–49.

Bowers, R. M., S. McLetchie, R. Knight, and N. Fierer (2011). Spatial variability in airborne bacterial communities across land-use types and their relationship to the bacterial communities of potential source environments. *The ISME Journal 5*(4), 601–612.

Boyd, S. and L. Vandenberghe (2004). *Convex Optimization*. Cambridge University Press.

Brands, M., M. Kamphus, T. Böttger, J. Schneider, F. Drewnick, A. Roth, J. Curtius, C. Voigt, A. Borbon, M. Beekmann, A. Bourdon, T. Perrin, and S. Borrmann (2011). Characterization of a Newly Developed Aircraft-Based Laser Ablation Aerosol Mass Spectrometer (ALABAMA) and First Field Deployment in Urban Pollution Plumes over Paris During MEGAPOLI 2009. *Aerosol Science and Technology 45*(1), 46–64.

Brechtel, F. J., S. M. Kreidenweis, and H. B. Swan (1998). Air mass characteristics, aerosol particle number concentrations, and number size distributions at Macquarie Island during the First Aerosol Characterization Experiment (ACE 1). *Journal of Geophysical Research: Atmospheres 103*(D13), 16351–16367.

Breiman, L. (2001). Random Forests. *Machine Learning 45*(1), 5–32.

Brookes, P., D. Powlson, and D. Jenkinson (1984). Phosphorus in the soil microbial biomass. *Soil Biology and Biochemistry 16*(2), 169–175.

Burrows, S. M., T. Butler, P. Jöckel, H. Tost, A. Kerkweg, U. Pöschl, and M. G. Lawrence (2009). Bacteria in the global atmosphere – Part 2: Modeling of emissions and transport between different ecosystems. *Atmospheric Chemistry and Physics 9*(23), 9281–9297.

Burrows, S. M., W. Elbert, M. G. Lawrence, and U. Pöschl (2009). Bacteria in the global atmosphere – Part 1: Review and synthesis of literature data for different ecosystems. *Atmospheric Chemistry and Physics 9*(23), 9263–9280.

Cahill, J. F., T. K. Darlington, C. Fitzgerald, N. G. Schoepp, J. Beld, M. D. Burkart, and K. A. Prather (2015). Online Analysis of Single Cyanobacteria and Algae Cells under Nitrogen-Limited Conditions Using Aerosol Time-of-Flight Mass Spectrometry. *Analytical Chemistry 87*(16), 8039–8046.

Canagaratna, M., J. Jayne, J. Jimenez, J. Allan, M. Alfarra, Q. Zhang, T. Onasch, F. Drewnick, H. Coe, A. Middlebrook, A. Delia, L. Williams, A. Trimborn, M. Northway, P. DeCarlo, C. Kolb, P. Davidovits, and D. Worsnop (2007). Chemical and microphysical characterization of ambient aerosols with the aerodyne aerosol mass spectrometer. *Mass Spectrometry Reviews 26*(2), 185–222.

Canagaratna, M. R., J. L. Jimenez, J. H. Kroll, Q. Chen, S. H. Kessler, P. Massoli, L. Hildebrandt Ruiz, E. Fortner, L. R. Williams, K. R. Wilson, J. D. Surratt, N. M. Donahue, J. T. Jayne, and D. R. Worsnop (2015). Elemental ratio measurements of organic compounds using aerosol mass spectrometry: characterization, improved calibration, and implications. *Atmospheric Chemistry and Physics 15*(1), 253–272.

Capes, G., B. Johnson, G. McFiggans, P. I. Williams, J. Haywood, and H. Coe (2008). Aging of biomass burning aerosols over West Africa: Aircraft measurements of chemical composition, microphysical properties, and emission ratios. *Journal of Geophysical Research 113*, D00C15.

Carignan, J., G. Libourel, C. Cloquet, and L. Le Forestier (2005). Lead Isotopic Composition of Fly Ash and Flue Gas Residues from Municipal Solid Waste Combustors in France: Implications for Atmospheric Lead Source Tracing. *Environmental Science & Technology 39*(7), 2018–2024.

Carson, P. G., M. V. Johnston, and A. S. Wexler (1997a). Laser desorption/ionization of ultrafine aerosol particles. *Rapid Communications in Mass Spectrometry 11*(9), 993–996.

Carson, P. G., M. V. Johnston, and A. S. Wexler (1997b). Real-Time Monitoring of the Surface and Total Composition of Aerosol Particles. *Aerosol Science and Technology 26*(4), 291–300.

Chen, Y., J. Cao, R. Huang, F. Yang, Q. Wang, and Y. Wang (2016). Characterization, mixing state, and evolution of urban single particles in Xi'an (China) during wintertime haze days. *Science of The Total Environment 573*, 937–945.

Chernoff, C. B. and G. J. Orris (2002). Data set of world phosphate mines, deposits, and occurrences–Part A. Geologic Data; Part B. Location and Mineral Economic Data: U.S. Geological Survey Open-File Report 02-156. Technical report, U.S. Geological Survey.

Chow, J. C. (1995). Measurement Methods to Determine Compliance with Ambient Air Quality Standards for Suspended Particles. *Journal of the Air & Waste Management Association 45*(5), 320–382.

Cochran, R. E., O. Laskina, J. V. Trueblood, A. D. Estillore, H. S. Morris, T. Jayarathne, C. M. Sultana, C. Lee, P. Lin, J. Laskin, A. Laskin, J. A. Dowling, Z. Qin, C. D. Cappa, T. H. Bertram, A. V. Tivanski, E. A. Stone, K. A. Prather, and V. H. Grassian (2017). Molecular Diversity of Sea Spray Aerosol Particles: Impact of Ocean Biology on Particle Composition and Hygroscopicity. *Chem 2*(5), 655–667.

Coe, H. and J. D. Allan (2006). Mass Spectrometric Methods for Aerosol Composition Measurements. In D. E. Heard (Ed.), *Analytical Techniques for Atmospheric Measurement*, pp. 265–311. Blackwell Publishing.

Constantinidou, H. A., S. S. Hirano, L. S. Baker, and C. D. Upper (1990). Atmospheric Dispersal of Ice Nucleation-Active Bacteria: The Role of Rain. *Phytopathology 80*(10), 934.

Cooper, D. W. (1986). Particulate Contamination and Microelectronics Manufacturing: An Introduction. *Aerosol Science and Technology 5*(3), 287–299.

Cortes, C. and V. Vapnik (1995). Support-vector networks. *Machine Learning 20*(3), 273–297.

Creamean, J. M., C. Lee, T. C. Hill, A. P. Ault, P. J. DeMott, A. B. White, F. M. Ralph, and K. A. Prather (2014). Chemical properties of insoluble precipitation residue particles. *Journal of Aerosol Science 76*, 13–27.

Creamean, J. M., K. J. Suski, D. Rosenfeld, A. Cazorla, P. J. DeMott, R. C. Sullivan, A. B. White, F. M. Ralph, P. Minnis, J. M. Comstock, J. M. Tomlinson, and K. A. Prather (2013). Dust and Biological Aerosols from the Sahara and Asia Influence Precipitation in the Western U.S. *Science 339*(6127), 1572–1578.

Cubison, M. J., A. M. Ortega, P. L. Hayes, D. K. Farmer, D. Day, M. J. Lechner, W. H. Brune, E. Apel, G. S. Diskin, J. A. Fisher, H. E. Fuelberg, A. Hecobian, D. J. Knapp, T. Mikoviny, D. Riemer, G. W. Sachse, W. Sessions, R. J. Weber, A. J. Weinheimer, A. Wisthaler, and J. L. Jimenez (2011). Effects of aging on organic aerosol from open biomass burning smoke in aircraft and laboratory studies. *Atmospheric Chemistry and Physics 11*(23), 12049–12064.

Cziczo, D. J., P. J. DeMott, C. Brock, P. K. Hudson, B. Jesse, S. M. Kreidenweis, A. J. Prenni, J. Schreiner, D. S. Thomson, and D. M. Murphy (2003). A method for single particle mass spectrometry of ice nuclei. *Aerosol Science and Technology 37*, 460–470.

Cziczo, D. J. and K. D. Froyd (2014). Sampling the composition of cirrus ice residuals. *Atmospheric Research 142*, 15–31.

Cziczo, D. J., K. D. Froyd, S. J. Gallavardin, O. Moehler, S. Benz, H. Saathoff, and D. M. Murphy (2009). Deactivation of ice nuclei due to atmospherically relevant surface coatings. *Environmental Research Letters 4*(4), 044013.

Cziczo, D. J., K. D. Froyd, C. Hoose, E. J. Jensen, M. Diao, M. A. Zondlo, J. B. Smith, C. H. Twohy, and D. M. Murphy (2013). Clarifying the Dominant Sources and Mechanisms of Cirrus Cloud Formation. *Science 340*, 1320–1324.

Cziczo, D. J., D. M. Murphy, P. K. Hudson, and D. S. Thomson (2004). Single particle measurements of the chemical composition of cirrus ice residue during CRYSTAL-FACE. *Journal of Geophysical Research 109*, D04201.

Cziczo, D. J., O. Stetzer, A. Worringen, M. Ebert, S. Weinbruch, M. Kamphus, S. J. Gallavardin, J. Curtius, S. Borrmann, K. D. Froyd, S. Mertes, O. Möhler, and

U. Lohmann (2009). Inadvertent climate modification due to anthropogenic lead. *Nature Geoscience 2*(5), 333–336.

Cziczo, D. J., D. S. Thomson, and D. M. Murphy (2001). Ablation, Flux, and Atmospheric Implications of Meteors Inferred from Stratospheric Aerosol. *Science 291*(5509), 1772–1775.

Cziczo, D. J., D. S. Thomson, T. L. Thompson, P. J. DeMott, and D. M. Murphy (2006). Particle analysis by laser mass spectrometry (PALMS) studies of ice nuclei and other low number density particles. *International Journal of Mass Spectrometry 258*(1–3), 21–29.

Dall'Osto, M. and R. M. Harrison (2006). Chemical characterisation of single airborne particles in Athens (Greece) by ATOFMS. *Atmospheric Environment 40*(39), 7614–7631.

DeCarlo, P. F., J. R. Kimmel, A. Trimborn, M. J. Northway, J. T. Jayne, A. C. Aiken, M. Gonin, K. Fuhrer, T. Horvath, K. S. Docherty, D. R. Worsnop, and J. L. Jimenez (2006). Field-Deployable, High-Resolution, Time-of-Flight Aerosol Mass Spectrometer. *Analytical Chemistry 78*(24), 8281–8289.

DeLeon-Rodriguez, N., T. L. Lathem, L. M. Rodriguez-R, J. M. Barazesh, B. E. Anderson, A. J. Beyersdorf, L. D. Ziemba, M. Bergin, A. Nenes, and K. T. Konstantinidis (2013). Microbiome of the upper troposphere: Species composition and prevalence, effects of tropical storms, and atmospheric implications. *Proceedings of the National Academy of Sciences 110*(7), 2575–2580.

DeMott, P. J., D. J. Cziczo, A. J. Prenni, D. M. Murphy, S. M. Kreidenweis, D. S. Thomson, R. Borys, and D. C. Rogers (2003). Measurements of the concentration and composition of nuclei for cirrus formation. *Proceedings of the National Academy of Sciences 100*(25), 14655–14660.

Deniel, C. and C. Pin (2001). Single-stage method for the simultaneous isolation of lead and strontium from silicate samples for isotopic measurements. *Analytica Chimica Acta 426*(1), 95–103.

Després, V. R., J. Alex Huffman, S. M. Burrows, C. Hoose, A. S. Safatov, G. Buryak, J. Fröhlich-Nowoisky, W. Elbert, M. O. Andreae, U. Pöschl, and R. Jaenicke (2012). Primary biological aerosol particles in the atmosphere: a review. *Tellus B 64*, 1–58.

Dockery, D. W., C. A. Pope, X. Xu, J. D. Spengler, J. H. Ware, M. E. Fay, B. G. Ferris, and F. E. Speizer (1993). An Association between Air Pollution and Mortality in Six U.S. Cities. *New England Journal of Medicine 329*(24), 1753–1759.

Drewnick, F., M. Dall'Osto, and R. M. Harrison (2008). Characterization of aerosol particles from grass mowing by joint deployment of ToF-AMS and ATOFMS instruments. *Atmospheric Environment 42*(13), 3006–3017.

Drewnick, F., S. S. Hings, P. DeCarlo, J. T. Jayne, M. Gonin, K. Fuhrer, S. Weimer, J. L. Jimenez, K. L. Demerjian, S. Borrmann, and D. R. Worsnop (2005). A New Time-of-Flight Aerosol Mass Spectrometer (TOF-AMS)—Instrument Description and First Field Deployment. *Aerosol Science and Technology 39*(7), 637–658.

Ebert, M., A. Worringen, N. Benker, S. Mertes, E. Weingartner, and S. Weinbruch (2011). Chemical composition and mixing-state of ice residuals sampled within mixed phase clouds. *Atmospheric Chemistry and Physics 11*(6), 2805–2816.

Emberlin, J. (2008). Grass, Tree, and Weed Pollen. In *Allergy and Allergic Diseases*, pp. 942–962. Oxford, UK: Wiley-Blackwell.

Fahlgren, C., A. Hagstrom, D. Nilsson, and U. L. Zweifel (2010). Annual Variations in the Diversity, Viability, and Origin of Airborne Bacteria. *Applied and Environmental Microbiology 76*(9), 3015–3025.

Fang, Z., Z. Ouyang, H. Zheng, X. Wang, and L. Hu (2007). Culturable Airborne Bacteria in Outdoor Environments in Beijing, China. *Microbial Ecology 54*(3), 487–496.

Fergenson, D. P., M. E. Pitesky, H. J. Tobias, P. T. Steele, G. A. Czerwieniec, S. C. Russell, C. B. Lebrilla, J. M. Horn, K. R. Coffee, A. Srivastava, S. P. Pillai, M.-T. P. Shih, H. L. Hall, A. J. Ramponi, J. T. Chang, R. G. Langlois, P. L. Estacio, R. T. Hadley, M. Frank, and E. E. Gard (2004). Reagentless Detection and Classification of Individual Bioaerosol Particles in Seconds. *Analytical Chemistry 76*(2), 373–378.

Friedman, B., A. Zelenyuk, J. Beranek, G. Kulkarni, M. Pekour, A. Gannet Hallar, I. B. McCubbin, J. A. Thornton, and D. J. Cziczo (2013). Aerosol measurements at a high-elevation site: composition, size, and cloud condensation nuclei activity. *Atmospheric Chemistry and Physics 13*(23), 11839–11851.

Froyd, K. D., D. M. Murphy, P. Lawson, D. Baumgardner, and R. L. Herman (2010). Aerosols that form subvisible cirrus at the tropical tropopause. *Atmospheric Chemistry and Physics 10*(1), 209–218.

Froyd, K. D., S. M. Murphy, D. M. Murphy, J. A. de Gouw, N. C. Eddingsaas, and P. O. Wennberg (2010). Contribution of isoprene-derived organosulfates to free tropospheric aerosol mass. *Proceedings of the National Academy of Sciences 107*(50), 21360–21365.

Gabey, A. M., M. W. Gallagher, J. Whitehead, J. R. Dorsey, P. H. Kaye, and W. R. Stanley (2010). Measurements and comparison of primary biological aerosol above and below a tropical forest canopy using a dual channel fluorescence spectrometer. *Atmospheric Chemistry and Physics 10*(10), 4453–4466.

Gallavardin, S., U. Lohmann, and D. Cziczo (2008). Analysis and differentiation of mineral dust by single particle laser mass spectrometry. *International Journal of Mass Spectrometry 274*(1–3), 56–63.

Gao, R. S., J. P. Schwarz, K. K. Kelly, D. W. Fahey, L. A. Watts, T. L. Thompson, J. R. Spackman, J. G. Slowik, E. S. Cross, J.-H. Han, P. Davidovits, T. B. Onasch, and D. R. Worsnop (2007). A Novel Method for Estimating Light-Scattering Properties of Soot Aerosols Using a Modified Single-Particle Soot Photometer. *Aerosol Science and Technology 41*(2), 125–135.

Gard, E., J. E. Mayer, B. D. Morrical, T. Dienes, D. P. Fergenson, and K. A. Prather (1997). Real-Time Analysis of Individual Atmospheric Aerosol Particles: Design and Performance of a Portable ATOFMS. *Analytical Chemistry 69*(20), 4083–4091.

Garimella, S. (2016). *A vertically-integrated approach to climate science: from measurements and machine learning to models and policy.* Ph. D. thesis, Massachusetts Institute of Technology.

Garimella, S., Y.-W. Huang, J. S. Seewald, and D. J. Cziczo (2014). Cloud condensation nucleus activity comparison of dry- and wet-generated mineral dust aerosol: the significance of soluble material. *Atmospheric Chemistry and Physics 14*(12), 6003–6019.

Gemayel, R., S. Hellebust, B. Temime-Roussel, N. Hayeck, J. T. Van Elteren, H. Wortham, and S. Gligorovski (2016). The performance and the characterization of laser ablation aerosol particle time-of-flight mass spectrometry (LAAP-ToF-MS). *Atmospheric Measurement Techniques 9*(4), 1947–1959.

George, I. J. and J. P. D. Abbatt (2010). Heterogeneous oxidation of atmospheric aerosol particles by gas-phase radicals. *Nat Chem 2*(9), 713–722.

Ghan, S. J., X. Liu, R. C. Easter, R. Zaveri, P. J. Rasch, J.-H. Yoon, and B. Eaton (2012). Toward a Minimal Representation of Aerosols in Climate Models: Comparative Decomposition of Aerosol Direct, Semidirect, and Indirect Radiative Forcing. *Journal of Climate 25*(19), 6461–6476.

Griffin, D. W., V. H. Garrison, J. R. Herman, and E. A. Shinn (2001). African desert dust in the Caribbean atmosphere: Microbiology and public health. *Aerobiologia 17*(3), 203–213.

Griffin, D. W., D. L. Westphal, and M. A. Gray (2006). Airborne microorganisms in the African desert dust corridor over the mid-Atlantic ridge, Ocean Drilling Program, Leg 209. *Aerobiologia 22*(3), 211–226.

Gross, D. S., M. E. Gälli, P. J. Silva, and K. A. Prather (2000). Relative Sensitivity Factors for Alkali Metal and Ammonium Cations in Single-Particle Aerosol Time-of-Flight Mass Spectra. *Analytical Chemistry 72*(2), 416–422.

Hankin, S. M., D. M. Villeneuve, P. B. Corkum, and D. M. Rayner (2000). Nonlinear Ionization of Organic Molecules in High Intensity Laser Fields. *Phys. Rev. Lett. 84*(22), 5082–5085.

Harrison, R. M., A. M. Jones, P. D. E. Biggins, N. Pomeroy, C. S. Cox, S. P. Kidd, J. L. Hobman, N. L. Brown, and A. Beswick (2005). Climate factors influencing bacterial count in background air samples. *International Journal of Biometeorology 49*(3), 167–178.

Heald, C. L. and D. V. Spracklen (2009). Atmospheric budget of primary biological aerosol particles from fungal spores. *Geophysical Research Letters 36*(9), L09806.

Henning, S., M. Ziese, A. Kiselev, H. Saathoff, O. Möhler, T. F. Mentel, A. Buchholz, C. Spindler, V. Michaud, M. Monier, K. Sellegri, and F. Stratmann (2012). Hygroscopic growth and droplet activation of soot particles: uncoated, succinic or sulfuric acid coated. *Atmospheric Chemistry and Physics 12*(10), 4525–4537.

Hergenröder, R., O. Samek, and V. Hommes (2006). Femtosecond laser ablation elemental mass spectrometry. *Mass Spectrometry Reviews 25*(4), 551–572.

Hernandez, M., A. E. Perring, K. McCabe, G. Kok, G. Granger, and D. Baumgardner (2016). Chamber catalogues of optical and fluorescent signatures distinguish bioaerosol classes. *Atmospheric Measurement Techniques 9*(7), 3283–3292.

Hill, S. C., R. G. Pinnick, S. Niles, Y.-L. Pan, S. Holler, R. K. Chang, J. Bottiger, B. T. Chen, C.-S. Orr, and G. Feather (1999). Real-time measurement of fluorescence spectra from single airborne biological particles. *Field Analytical Chemistry & Technology 3*(4-5), 221–239.

Hiranuma, N., S. Augustin-Bauditz, H. Bingemer, C. Budke, J. Curtius, A. Danielczok, K. Diehl, K. Dreischmeier, M. Ebert, F. Frank, N. Hoffmann, K. Kandler, A. Kiselev, T. Koop, T. Leisner, O. Möhler, B. Nillius, A. Peckhaus, D. Rose, S. Weinbruch, H. Wex, Y. Boose, P. J. Demott, J. D. Hader, T. C. J. Hill, Z. A. Kanji, G. Kulkarni, E. J. T. Levin, C. S. McCluskey, M. Murakami, B. J. Murray, D. Niedermeier, M. D. Petters, D. O'Sullivan, A. Saito, G. P. Schill, T. Tajiri, M. A. Tolbert, A. Welti, T. F. Whale, T. P. Wright, and K. Yamashita (2015). A comprehensive laboratory study on the immersion freezing behavior of illite NX particles: A comparison of 17 ice nucleation measurement techniques. *Atmospheric Chemistry and Physics 15*(5), 2489–2518.

Hiranuma, N., O. Möhler, K. Yamashita, T. Tajiri, A. Saito, A. Kiselev, N. Hoffmann, C. Hoose, E. Jantsch, T. Koop, and M. Murakami (2015). Ice nucleation by cellulose and its potential contribution to ice formation in clouds. *Nature Geoscience 8*(4), 273–277.

Hodkinson, J. R. and J. R. Greenfield (1965). Response Calculations for Light-Scattering Aerosol Counters and Photometers. *Appl. Opt. 4*(11), 1463–1474.

Hoffmann, W., H. Muhberger, W. Hwang, H. Demattio, A. Guber, and V. Saile (2008, nov). Towards high sensitive label free DNA detection in lab-on-chip systems. In *2008 3rd International Conference on Sensing Technology*, pp. 615–619. IEEE.

Hofmann, T., B. Schölkopf, and A. J. Smola (2008, jun). Kernel methods in machine learning. *The Annals of Statistics 36*(3), 1171–1220.

Hoose, C., J. E. Kristjánsson, and S. M. Burrows (2010). How important is biological ice nucleation in clouds on a global scale? *Environmental Research Letters 5*(2), 024009.

Hoose, C. and O. Möhler (2012). Heterogeneous ice nucleation on atmospheric aerosols: a review of results from laboratory experiments. *Atmospheric Chemistry and Physics 12*(20), 9817–9854.

Hu, J., K. P. Johnston, and R. O. Williams (2004). Nanoparticle Engineering Processes for Enhancing the Dissolution Rates of Poorly Water Soluble Drugs. *Drug Development and Industrial Pharmacy 30*(3), 233–245.

Hudson, P. K., D. M. Murphy, D. J. Cziczo, D. S. Thomson, J. A. de Gouw, C. Warneke, J. Holloway, H.-J. Jost, and G. Hübler (2004). Biomass-burning particle measurements: Characteristic composition and chemical processing. *Journal of Geophysical Research: Atmospheres 109*(D23), D23S27.

Isselhardt, B. H., M. R. Savina, K. B. Knight, M. J. Pellin, I. D. Hutcheon, and S. G. Prussin (2011). Improving Precision in Resonance Ionization Mass Spectrometry: Influence of Laser Bandwidth in Uranium Isotope Ratio Measurements. *Analytical Chemistry 83*(7), 2469–2475.

Itakura, R., J. Watanabe, A. Hishikawa, and K. Yamanouchi (2001). Ionization and fragmentation dynamics of benzene in intense laser fields by tandem mass spectroscopy. *The Journal of Chemical Physics 114*, 5598–5606.

Jackson, S. E. and D. Günther (2003). The nature and sources of laser induced isotopic fractionation in laser ablation-multicollector-inductively coupled plasma-mass spectrometry. *Journal of Analytical Atomic Spectrometry 18*(3), 205–212.

Jacobson, M. Z. and D. G. Streets (2009). Influence of future anthropogenic emissions on climate, natural emissions, and air quality. *Journal of Geophysical Research 114*(D8), D08118.

Jaenicke, R. (2005). Abundance of Cellular Material and Proteins in the Atmosphere. *Science 308*(5718), 73–73.

Jayne, J. T., D. C. Leard, X. Zhang, P. Davidovits, K. A. Smith, C. E. Kolb, and D. R. Worsnop (2000). Development of an Aerosol Mass Spectrometer for Size and Composition Analysis of Submicron Particles. *Aerosol Science and Technology 33*(1-2), 49–70.

Jimenez, J. L., M. R. Canagaratna, N. M. Donahue, A. S. H. Prevot, Q. Zhang, J. H. Kroll, P. F. DeCarlo, J. D. Allan, H. Coe, N. L. Ng, A. C. Aiken, K. S. Docherty, I. M. Ulbrich, A. P. Grieshop, A. L. Robinson, J. Duplissy, J. D. Smith, K. R.

Wilson, V. A. Lanz, C. Hueglin, Y. L. Sun, J. Tian, A. Laaksonen, T. Raatikainen, J. Rautiainen, P. Vaattovaara, M. Ehn, M. Kulmala, J. M. Tomlinson, D. R. Collins, M. J. Cubison, J. Dunlea, J. A. Huffman, T. B. Onasch, M. R. Alfarra, P. I. Williams, K. Bower, Y. Kondo, J. Schneider, F. Drewnick, S. Borrmann, S. Weimer, K. Demerjian, D. Salcedo, L. Cottrell, R. Griffin, A. Takami, T. Miyoshi, S. Hatakeyama, A. Shimono, J. Y. Sun, Y. M. Zhang, K. Dzepina, J. R. Kimmel, D. Sueper, J. T. Jayne, S. C. Herndon, A. M. Trimborn, L. R. Williams, E. C. Wood, A. M. Middlebrook, C. E. Kolb, U. Baltensperger, and D. R. Worsnop (2009). Evolution of Organic Aerosols in the Atmosphere. *Science 326*(5959), 1525–1529.

Jimenez, J. L., J. T. Jayne, Q. Shi, C. E. Kolb, D. R. Worsnop, I. Yourshaw, J. H. Seinfeld, R. C. Flagan, X. Zhang, K. A. Smith, J. W. Morris, and P. Davidovits (2003). Ambient aerosol sampling using the Aerodyne Aerosol Mass Spectrometer. *Journal of Geophysical Research 108*(D7), 8425.

Jin Huang and C. Ling (2005, mar). Using AUC and accuracy in evaluating learning algorithms. *IEEE Transactions on Knowledge and Data Engineering 17*(3), 299–310.

Johnston, M. V. (2000). Sampling and analysis of individual particles by aerosol mass spectrometry. *Journal of Mass Spectrometry 35*(5), 585–595.

Kato, T., T. Kobayashi, Y. Matsuo, M. Kurata-Nishimura, R. Oyama, Y. Matsumura, H. Yamamoto, J. Kawai, and Y. Hayashizaki (2007). Comparison between femtosecond and nanosecond laser ablation of solution samples applied on a substrate. *Journal of Physics: Conference Series 59*, 372–375.

Kaye, P. H., J. E. Barton, E. Hirst, and J. M. Clark (2000). Simultaneous light scattering and intrinsic fluorescence measurement for the classification of airborne particles. *Applied Optics 39*(21), 3738.

Kaye, P. H., W. R. Stanley, E. Hirst, E. Foot, K. L. Baxter, and S. J. Barrington (2005). Single particle multichannel bio-aerosol fluorescence sensor. *Optics Express 13*(10), 3583.

Kok, J. F., E. J. R. Parteli, T. I. Michaels, and D. B. Karam (2012). The physics of wind-blown sand and dust. *Reports on Progress in Physics 75*(10), 106901.

Koppelaar, R. and H. Weikard (2013). Assessing phosphate rock depletion and phosphorus recycling options. *Global Environmental Change 23*(6), 1454–1466.

Kreisberg, N. M., S. V. Hering, B. J. Williams, D. R. Worton, and A. H. Goldstein (2009). Quantification of Hourly Speciated Organic Compounds in Atmospheric Aerosols, Measured by an In-Situ Thermal Desorption Aerosol Gas Chromatograph (TAG). *Aerosol Science and Technology 43*(1), 38–52.

Kroll, J. H. and J. H. Seinfeld (2008). Chemistry of secondary organic aerosol: Formation and evolution of low-volatility organics in the atmosphere. *Atmospheric Environment 42*(16), 3593–3624.

Kurata-Nishimura, M., F. Tokanai, Y. Matsuo, T. Kobayashi, J. Kawai, H. Kumagai, K. Midorikawa, I. Tanihata, and Y. Hayashizaki (2002). Simultaneous atomization and ionization of large organic molecules using femtosecond laser ablation. *Applied Surface Science 197-198*, 715–719.

Liao, J., K. D. Froyd, D. M. Murphy, F. N. Keutsch, G. Yu, P. O. Wennberg, J. M. St. Clair, J. D. Crounse, A. Wisthaler, T. Mikoviny, J. L. Jimenez, P. Campuzano-Jost, D. A. Day, W. Hu, T. B. Ryerson, I. B. Pollack, J. Peischl, B. E. Anderson, L. D. Ziemba, D. R. Blake, S. Meinardi, and G. Diskin (2015). Airborne measurements of organosulfates over the continental U.S. *Journal of Geophysical Research: Atmospheres 120*(7), 2990–3005.

Lindemann, J., H. A. Constantinidou, W. R. Barchet, and C. D. Upper (1982). Plants as Sources of Airborne Bacteria, Including Ice Nucleation-Active Bacteria. *Applied and Environmental Microbiology 44*(5), 1059–1063.

Liu, D., J. Whitehead, M. R. Alfarra, E. Reyes-Villegas, D. V. Spracklen, C. L. Reddington, S. Kong, P. I. Williams, Y.-C. Ting, S. Haslett, J. W. Taylor, M. J. Flynn, W. T. Morgan, G. McFiggans, H. Coe, and J. D. Allan (2017). Black-carbon absorption enhancement in the atmosphere determined by particle mixing state. *Nature Geoscience 10*(3), 184–188.

Liu, M., C. Wu, Z. Wu, H. Yang, Q. Gong, W. Huang, and T. Zhu (2010). Application of Femtosecond Laser Mass Spectrometry to the Analysis of Volatile Organic Compounds. *American Society for Mass Spectrometry 21*, 1122–1128.

Lohmann, U. and J. Feichter (2005). Global indirect aerosol effects: a review. *Atmospheric Chemistry and Physics 5*(3), 715–737.

Lohmann, U. and S. Ferrachat (2010). Impact of parametric uncertainties on the present-day climate and on the anthropogenic aerosol effect. *Atmospheric Chemistry and Physics 10*(23), 11373–11383.

Lopez-Hilfiker, F. D., C. Mohr, M. Ehn, F. Rubach, E. Kleist, J. Wildt, T. F. Mentel, A. Lutz, M. Hallquist, D. Worsnop, and J. A. Thornton (2014). A novel method for online analysis of gas and particle composition: description and evaluation of a Filter Inlet for Gases and AEROsols (FIGAERO). *Atmospheric Measurement Techniques 7*(4), 983–1001.

Lynch, D. K. (2002). Cirrus: History and Definition. In D. K. Lynch, K. Sassen, D. O. Starr, and G. Stephens (Eds.), *Cirrus*, pp. 3–10. Oxford University Press.

Lyon, I. C., J. M. Saxton, G. Turner, and R. Hinton (1994). Isotopic fractionation in secondary ionization mass spectrometry. *Rapid Communications in Mass Spectrometry 8*(10), 837–843.

Mahowald, N., T. D. Jickells, A. R. Baker, P. Artaxo, C. R. Benitez-Nelson, G. Bergametti, T. C. Bond, Y. Chen, D. D. Cohen, B. Herut, N. Kubilay, R. Losno, C. Luo, W. Maenhaut, K. A. McGee, G. S. Okin, R. L. Siefert, and S. Tsukuda (2008). Global distribution of atmospheric phosphorus sources, concentrations and deposition rates, and anthropogenic impacts. *Global Biogeochemical Cycles 22*(4), GB4026.

Maki, L. R. and K. J. Willoughby (1978, jul). Bacteria as Biogenic Sources of Freezing Nuclei. *Journal of Applied Meteorology 17*(7), 1049–1053.

Margetic, V., K. Niemax, and R. Hergenröder (2003). Application of Femtosecond Laser Ablation Time-of-Flight Mass Spectrometry to In-Depth Multilayer Analysis. *Analytical Chemistry 75*(14), 3435–3439.

Marsden, N., M. J. Flynn, J. W. Taylor, J. D. Allan, and H. Coe (2016). Evaluating the influence of laser wavelength and detection stage geometry on optical detection efficiency in a single-particle mass spectrometer. *Atmospheric Measurement Techniques 9*(12), 6051–6068.

Matthias-Maser, S. and R. Jaenicke (1994). Examination of atmospheric bioaerosol particles with radii > 0.2 μm. *Journal of Aerosol Science 25*(8), 1605–1613.

Matthias-Maser, S., V. Obolkin, T. Khodzer, and R. Jaenicke (2000). Seasonal variation of primary biological aerosol particles in the remote continental region of Lake Baikal/Siberia. *Atmospheric Environment 34*(22), 3805–3811.

McNeill, V. F. (2015). Aqueous Organic Chemistry in the Atmosphere: Sources and Chemical Processing of Organic Aerosols. *Environmental Science & Technology 49*(3), 1237–1244.

Middlebrook, A. M., D. S. Thomson, and D. M. Murphy (1997). On the Purity of Laboratory-Generated Sulfuric Acid Droplets and Ambient Particles Studied by Laser Mass Spectrometry. *Aerosol Science and Technology 27*(3), 293–307.

Miller, K. A., D. S. Siscovick, L. Sheppard, K. Shepherd, J. H. Sullivan, G. L. Anderson, and J. D. Kaufman (2007). Long-Term Exposure to Air Pollution and Incidence of Cardiovascular Events in Women. *New England Journal of Medicine 356*(5), 447–458.

Moffet, R. C. and K. A. Prather (2005). Extending ATOFMS Measurements To Include Refractive Index and Density. *Analytical Chemistry 77*(20), 6535–6541.

Möhler, O., P. J. DeMott, G. Vali, and Z. Levin (2007). Microbiology and atmospheric processes: the role of biological particles in cloud physics. *Biogeosciences 4*(6), 1059–1071.

Möhler, O., D. G. Georgakopoulos, C. E. Morris, S. Benz, V. Ebert, S. Hunsmann, H. Saathoff, M. Schnaiter, and R. Wagner (2008). Heterogeneous ice nucleation

activity of bacteria: new laboratory experiments at simulated cloud conditions. *Biogeosciences 5*(5), 1425–1435.

Morrical, B. D., D. P. Fergenson, and K. A. Prather (1998). Coupling Two-Step Laser Desorption/Ionization with Aerosol Time-of-Flight Mass Spectrometry for the Analysis of Individual Organic Particles. *Journal of American Society for Mass Spectrometry 9*, 1068–1073.

Murphy, D. M. (2007). The design of single particle laser mass spectrometers. *Mass Spectrometry Reviews 26*(2), 150–165.

Murphy, D. M. (2017). The sTOF, a Favorable Geometry for a Time-of-Flight Analyzer. *Journal of The American Society for Mass Spectrometry 28*(2), 242–246.

Murphy, D. M., D. J. Cziczo, P. K. Hudson, M. E. Schein, and D. S. Thomson (2004). Particle density inferred from simultaneous optical and aerodynamic diameters sorted by composition. *Journal of Aerosol Science 35*(1), 135–139.

Murphy, D. M., K. D. Froyd, J. P. Schwarz, and J. C. Wilson (2014). Observations of the chemical composition of stratospheric aerosol particles. *Quarterly Journal of the Royal Meteorological Society 140*(681), 1269–1278.

Murphy, D. M., P. K. Hudson, D. J. Cziczo, S. Gallavardin, K. D. Froyd, M. V. Johnston, A. M. Middlebrook, M. S. Reinard, D. S. Thomson, T. Thornberry, and A. S. Wexler (2007). Distribution of lead in single atmospheric particles. *Atmospheric Chemistry and Physics 7*(12), 3195–3210.

Murphy, D. M. and M. E. Schein (1998). Wind Tunnel Tests of a Shrouded Aircraft Inlet. *Aerosol Science and Technology 28*(1), 33–39.

Murphy, D. M. and D. S. Thomson (1995). Laser Ionization Mass Spectroscopy of Single Aerosol Particles. *Aerosol Science and Technology 22*(3), 237–249.

Murphy, D. M., D. S. Thomson, and M. J. Mahoney (1998). In situ measurements of organics, meteoritic material, mercury and other elements in aerosols at 5 to 19 kilometers. *Science 282*, 1664–1669.

Murphy, D. M., D. S. Thomson, A. M. Middlebrook, and M. E. Schein (1998). In situ single-particle characterization at Cape Grim. *Journal of Geophysical Research: Atmospheres 103*(D13), 16485–16491.

Murray, B. J., D. O'Sullivan, J. D. Atkinson, and M. E. Webb (2012). Ice nucleation by particles immersed in supercooled cloud droplets. *Chemical Society Reviews 41*(19), 6519.

Nabat, P., S. Somot, M. Mallet, A. Sanchez-Lorenzo, and M. Wild (2014). Contribution of anthropogenic sulfate aerosols to the changing Euro-Mediterranean climate since 1980. *Geophysical Research Letters 41*(15), 5605–5611.

Nakashima, N. and T. Yatsuhashi (2007). Intact Molecular Ion Formation of Some Organic Molecules by Femtosecond Lasers. In K. Yamanouchi, S. L. Chin, P. Agostini, and G. Ferrante (Eds.), *Progress in Ultrafast Intense Laser Science II Springer Series in Chemical Physics Volume 85*, pp. 25–41. Springer.

Nam, J.-M., S. I. Stoeva, and C. A. Mirkin (2004, may). Bio-bar-code-based DNA detection with PCR-like sensitivity. *Journal of the American Chemical Society 126*(19), 5932–3.

National Academies of Sciences Engineering and Medicine (2016). *The Future of Atmospheric Chemistry Research*. Washington, D.C.: National Academies Press.

Nikolajeff, F., S. Hård, and B. Curtis (1997). Diffractive microlenses replicated in fused silica for excimer laser-beam homogenizing. *Applied Optics 36*(32), 8481.

Noble, C. A. and K. A. Prather (2000). Real-time single particle mass spectrometry: A historical review of a quarter century of the chemical analysis of aerosols. *Mass Spectrometry Reviews 19*(4), 248–274.

Orris, G. J. and R. I. Grauch (2002). Rare earth element mines, deposits, and occurrences: U.S. Geological Survey, Open-File Report 02-189. Technical report, U.S. Geological Survey.

Pan, Y.-l., S. Holler, R. K. Chang, S. C. Hill, R. G. Pinnick, S. Niles, and J. R. Bottiger (1999). Single-shot fluorescence spectra of individual micrometer-sized bioaerosols illuminated by a 351- or a 266-nm ultraviolet laser. *Optics Letters 24*(2), 116.

Panchapakesan, B., D. L. DeVoe, M. R. Widmaier, R. Cavicchi, and S. Semancik (2001). Nanoparticle engineering and control of tin oxide microstructures for chemical microsensor applications. *Nanotechnology 12*(3), 336–349.

Peck, J., L. A. Gonzalez, L. R. Williams, W. Xu, P. L. Croteau, M. T. Timko, J. T. Jayne, D. R. Worsnop, R. C. Miake-Lye, and K. A. Smith (2016). Development of an aerosol mass spectrometer lens system for PM2.5. *Aerosol Science and Technology 50*(8), 781–789.

Peckhaus, A., A. Kiselev, T. Hiron, M. Ebert, and T. Leisner (2016). A comparative study of K-rich and Na/Ca-rich feldspar ice-nucleating particles in a nanoliter droplet freezing assay. *Atmospheric Chemistry and Physics 16*(18), 11477–11496.

Peltier, R. E., A. P. Sullivan, R. J. Weber, C. A. Brock, A. G. Wollny, J. S. Holloway, J. A. de Gouw, and C. Warneke (2007). Fine aerosol bulk composition measured on WP-3D research aircraft in vicinity of the Northeastern United States—results from NEAQS. *Atmospheric Chemistry and Physics 7*(12), 3231–3247.

Perring, A. E., J. P. Schwarz, D. Baumgardner, M. T. Hernandez, D. V. Spracklen, C. L. Heald, R. S. Gao, G. Kok, G. R. McMeeking, J. B. McQuaid, and D. W. Fahey (2015). Airborne observations of regional variation in fluorescent aerosol

across the United States. *Journal of Geophysical Research: Atmospheres 120*(3), 1153–1170.

Peters, G. H., W. Abbey, G. H. Bearman, G. S. Mungas, J. A. Smith, R. C. Anderson, S. Douglas, and L. W. Beegle (2008). Mojave Mars simulant—Characterization of a new geologic Mars analog. *Icarus 197*(2), 470–479.

Petersen, P. B. and R. J. Saykally (2006). Probing the Interfacial Structure of Aqueous Electrolytes with Femtosecond Second Harmonic Generation Spectroscopy. *The Journal of Physical Chemistry B 110*(29), 14060–14073.

Petters, M. D. and S. M. Kreidenweis (2007). A single parameter representation of hygroscopic growth and cloud condensation nucleus activity. *Atmospheric Chemistry and Physics 7*(8), 1961–1971.

Phares, D. J., K. P. Rhoads, and A. S. Wexler (2002). Performance of a Single Ultrafine Particle Mass Spectrometer. *Aerosol Science and Technology 36*(5), 583–592.

Platt, J. C. (1999). Probabilistic outputs for support vector machines and comparisons to regularized likelihood methods. In *Advances in Large Margin Classifiers*, pp. 61–74. MIT Press.

Pósfai, M., D. Axisa, É. Tompa, E. Freney, R. Bruintjes, and P. R. Buseck (2013). Interactions of mineral dust with pollution and clouds: An individual-particle TEM study of atmospheric aerosol from Saudi Arabia. *Atmospheric Research 122*, 347–361.

Pósfai, M. and P. R. Buseck (2010). Nature and Climate Effects of Individual Tropospheric Aerosol Particles. *Annual Review of Earth and Planetary Sciences 38*(1), 17–43.

Pósfai, M., J. Li, J. R. Anderson, and P. R. Buseck (2003). Aerosol bacteria over the Southern Ocean during ACE-1. *Atmospheric Research 66*(4), 231–240.

Pratt, K. A., P. J. DeMott, J. R. French, Z. Wang, D. L. Westphal, A. J. Heymsfield, C. H. Twohy, A. J. Prenni, and K. A. Prather (2009). In situ detection of biological particles in cloud ice-crystals. *Nature Geoscience 2*, 398–401.

Pratt, K. A., J. E. Mayer, J. C. Holecek, R. C. Moffet, R. O. Sanchez, T. P. Rebotier, H. Furutani, M. Gonin, K. Fuhrer, Y. Su, S. Guazzotti, and K. A. Prather (2009). Development and Characterization of an Aircraft Aerosol Time-of-Flight Mass Spectrometer. *Analytical Chemistry 81*(5), 1792–1800.

Prospero, J. M., E. Blades, G. Mathison, and R. Naidu (2005). Interhemispheric transport of viable fungi and bacteria from Africa to the Caribbean with soil dust. *Aerobiologia 21*(1), 1–19.

Ramanathan, V. and G. Carmichael (2008). Global and regional climate changes due to black carbon. *Nature Geoscience 1*(4), 221–227.

Ramanathan, V., P. J. Crutzen, J. T. Kiehl, and D. Rosenfeld (2001). Aerosols, Climate, and the Hydrological Cycle. *Science 294*(5549), 2119–2124.

Reents, W. D., S. W. Downey, A. B. Emerson, A. M. Mujsce, A. J. Muller, D. J. Siconolfi, J. D. Sinclair, and A. G. Swanson (1995). Single Particle Characterization by Time-of-Flight Mass Spectrometry. *Aerosol Science and Technology 23*(3), 263–270.

Reents, W. D. and Z. Ge (2000). Simultaneous Elemental Composition and Size Distributions of Submicron Particles in Real Time Using Laser Atomization Ionization Mass Spectrometry. *Aerosol Science and Technology 33*(1-2), 122–134.

Reents, W. D. and M. J. Schabel (2001). Measurement of Individual Particle Atomic Composition by Aerosol Mass Spectrometry. *Analytical Chemistry 73*(22), 5403–5414.

Reff, A., P. V. Bhave, H. Simon, T. G. Pace, G. A. Pouliot, J. D. Mobley, and M. Houyoux (2009). Emissions Inventory of PM 2.5 Trace Elements across the United States. *Environmental Science & Technology 43*(15), 5790–5796.

Reinard, M. S. and M. V. Johnston (2008). Ion formation mechanism in laser desorption ionization of individual nanoparticles. *Journal of the American Society for Mass Spectrometry 19*(3), 389–399.

Saathoff, H., K.-H. Naumann, M. Schnaiter, W. Schöck, O. Möhler, U. Schurath, E. Weingartner, M. Gysel, and U. Baltensperger (2003). Coating of soot and (NH4)2SO4 particles by ozonolysis products of α-pinene. *Journal of Aerosol Science 34*(10), 1297–1321.

Sakurai, T., T. Matsuo, and H. Matsuda (1985). Ion optics for time-of-flight mass spectrometers with multiple symmetry. *International Journal of Mass Spectrometry and Ion Processes 63*(2-3), 273–287.

Sangster, D. F., P. M. Outridge, and W. J. Davis (2000). Stable lead isotope characteristics of lead ore deposits of environmental significance. *Environmental Reviews 8*(2), 115–147.

Sato, K., A. Tachihara, B. Renberg, K. Mawatari, K. Sato, Y. Tanaka, J. Jarvius, M. Nilsson, and T. Kitamori (2010). Microbead-based rolling circle amplification in a microchip for sensitive DNA detection. *Lab on a Chip 10*(10), 1262.

Sattler, B., H. Puxbaum, and R. Psenner (2001). Bacterial growth in supercooled cloud droplets. *Geophysical Research Letters 28*(2), 239–242.

Schafer, K. J. and K. C. Kulander (1997). High Harmonic Generation from Ultrafast Pump Lasers. *Phys. Rev. Lett. 78*(4), 638–641.

Schreiner, J., U. Schild, C. Voigt, and K. Mauersberger (1999). Focusing of Aerosols into a Particle Beam at Pressures from 10 to 150 Torr. *Aerosol Science and Technology 31*(5), 373–382.

Schreiner, J., C. Voigt, K. Mauersberger, P. McMurry, and P. Ziemann (1998). Aerodynamic Lens System for Producing Particle Beams at Stratospheric Pressures. *Aerosol Science and Technology 29*(1), 50–56.

Schwarz, J. P., R. S. Gao, D. W. Fahey, D. S. Thomson, L. A. Watts, J. C. Wilson, J. M. Reeves, M. Darbeheshti, D. G. Baumgardner, G. L. Kok, S. H. Chung, M. Schulz, J. Hendricks, A. Lauer, B. Kärcher, J. G. Slowik, K. H. Rosenlof, T. L. Thompson, A. O. Langford, M. Loewenstein, and K. C. Aikin (2006). Single-particle measurements of midlatitude black carbon and light-scattering aerosols from the boundary layer to the lower stratosphere. *Journal of Geophysical Research 111*(D16), D16207.

Seinfeld, J. H. and S. N. Pandis (2006). *Atmospheric Chemistry and Physics: From Air Pollution to Climate Change* (2 ed.). New York, NY: John Wiley & Sons, Inc.

Sesartic, A., U. Lohmann, and T. Storelvmo (2012). Bacteria in the ECHAM5-HAM global climate model. *Atmospheric Chemistry and Physics 12*(18), 8645–8661.

Shim, S. and R. A. Mathies (2008). Femtosecond Raman-induced Kerr effect spectroscopy. *Journal of Raman Spectroscopy 39*(11), 1526–1530.

Silva, P. J., R. A. Carlin, and K. A. Prather (2000). Single particle analysis of suspended soil dust from Southern California. *Atmospheric Environment 34*(11), 1811–1820.

Silva, P. J. and K. A. Prather (2000). Interpretation of Mass Spectra from Organic Compounds in Aerosol Time-of-Flight Mass Spectrometry. *Analytical Chemistry 72*(15), 3553–3562.

Slowik, J. G., E. S. Cross, J.-H. Han, P. Davidovits, T. B. Onasch, J. T. Jayne, L. R. Williams, M. R. Canagaratna, D. R. Worsnop, R. K. Chakrabarty, H. Moosmüller, W. P. Arnott, J. P. Schwarz, R.-S. Gao, D. W. Fahey, G. L. Kok, and A. Petzold (2007). An Inter-Comparison of Instruments Measuring Black Carbon Content of Soot Particles. *Aerosol Science and Technology 41*(3), 295–314.

Smith, D. J., H. J. Timonen, D. A. Jaffe, D. W. Griffin, M. N. Birmele, K. D. Perry, P. D. Ward, and M. S. Roberts (2013). Intercontinental Dispersal of Bacteria and Archaea by Transpacific Winds. *Applied and Environmental Microbiology 79*(4), 1134–1139.

Sodeman, D. A., S. M. Toner, and K. A. Prather (2005). Determination of Single Particle Mass Spectral Signatures from Light-Duty Vehicle Emissions. *Environmental Science & Technology 39*(12), 4569–4580.

Solomon, S., D. Kinnison, R. R. Garcia, J. Bandoro, M. Mills, C. Wilka, R. R. Neely, A. Schmidt, J. E. Barnes, J.-P. Vernier, and M. Höpfner (2016). Monsoon circulations and tropical heterogeneous chlorine chemistry in the stratosphere. *Geophysical Research Letters 43*(24), 12,624–12,633.

Spencer, M. T. and K. A. Prather (2006). Using ATOFMS to Determine OC/EC Mass Fractions in Particles. *Aerosol Science and Technology 40*(8), 585–594.

Spracklen, D. V. and C. L. Heald (2014). The contribution of fungal spores and bacteria to regional and global aerosol number and ice nucleation immersion freezing rates. *Atmospheric Chemistry and Physics 14*(17), 9051–9059.

Stagni, C., D. Esposti, C. Guiducci, C. Paulus, M. Schienle, M. Augustyniak, G. Zuccheri, B. Samori, L. Benini, B. Ricco, and R. Thewes (2006). Fully Electronic CMOS DNA Detection Array Based on Capacitance Measurement with On-Chip Analog-to-Digital Conversion. In *2006 IEEE International Solid State Circuits Conference - Digest of Technical Papers*, pp. 69–78. IEEE.

Stanier, C. O., A. Y. Khlystov, and S. N. Pandis (2004). Ambient aerosol size distributions and number concentrations measured during the Pittsburgh Air Quality Study (PAQS). *Atmospheric Environment 38*(20), 3275–3284.

Steinke, I., R. Funk, J. Busse, A. Iturri, S. Kirchen, M. Leue, O. Möhler, T. Schwartz, M. Schnaiter, B. Sierau, E. Toprak, R. Ullrich, A. Ulrich, C. Hoose, and T. Leisner (2016). Ice nucleation activity of agricultural soil dust aerosols from Mongolia, Argentina, and Germany. *Journal of Geophysical Research: Atmospheres 121*(22), 13559–13576.

Su, Y., M. F. Sipin, H. Furutani, and K. A. Prather (2004). Development and Characterization of an Aerosol Time-of-Flight Mass Spectrometer with Increased Detection Efficiency. *Analytical Chemistry 76*(3), 712–719.

Sullivan, R. C. and K. A. Prather (2005). Recent Advances in Our Understanding of Atmospheric Chemistry and Climate Made Possible by On-Line Aerosol Analysis Instrumentation. *Analytical Chemistry 77*, 3861–3886.

Tegen, I. and I. Fung (1995). Contribution to the atmospheric mineral aerosol load from land surface modification. *Journal of Geophysical Research 100*(D9), 18707.

Tersoff, J. and D. R. Hamann (1985). Theory of the scanning tunneling microscope. *Phys. Rev. B 31*(2), 805–813.

Thomson, D. S., A. M. Middlebrook, and D. M. Murphy (1997). Thresholds for Laser-Induced Ion Formation from Aerosols in a Vacuum Using Ultraviolet and Vacuum-Ultraviolet Laser Wavelengths. *Aerosol Science and Technology 26*, 544–559.

Thomson, D. S. and D. M. Murphy (1993). Laser-induced ion formation thresholds of aerosol particles in a vacuum. *Appl. Opt. 32*(33), 6818–6826.

Thomson, D. S., M. E. Schein, and D. M. Murphy (2000). Particle analysis by laser mass spectrometry {WB}-57 instrument overview. *Aerosol Science and Technology 33*, 153–169.

Toon, O. B., H. Maring, J. Dibb, R. Ferrare, D. J. Jacob, E. J. Jensen, Z. J. Luo, G. G. Mace, L. L. Pan, L. Pfister, K. H. Rosenlof, J. Redemann, J. S. Reid, H. B. Singh, A. M. Thompson, R. Yokelson, P. Minnis, G. Chen, K. W. Jucks, and A. Pszenny (2016). Planning, implementation, and scientific goals of the Studies of Emissions and Atmospheric Composition, Clouds and Climate Coupling by Regional Surveys (SEAC 4 RS) field mission. *Journal of Geophysical Research: Atmospheres 121*(9), 4967–5009.

Toprak, E. and M. Schnaiter (2013). Fluorescent biological aerosol particles measured with the Waveband Integrated Bioaerosol Sensor WIBS-4: laboratory tests combined with a one year field study. *Atmospheric Chemistry and Physics 13*(1), 225–243.

Townley, B. K. and C. I. Godwin (2001). Isotope characterization of lead in galena from ore deposits of the Aysén Region, southern Chile. *Mineralium Deposita 36*(1), 45–57.

Twohy, C. H., G. R. McMeeking, P. J. DeMott, C. S. McCluskey, T. C. J. Hill, S. M. Burrows, G. R. Kulkarni, M. Tanarhte, D. N. Kafle, and D. W. Toohey (2016). Abundance of fluorescent biological aerosol particles at temperatures conducive to the formation of mixed-phase and cirrus clouds. *Atmospheric Chemistry and Physics 16*(13), 8205–8225.

U.S. Geological Survey (2016a). 2013 Minerals Yearbook. Rare Earths. Technical report, U.S. Geological Survey.

U.S. Geological Survey (2016b). Mineral commodity summaries 2016. Technical report, U.S. Geological Survey.

Usher, C. R., A. E. Michel, and V. H. Grassian (2003). Reactions on Mineral Dust. *Chemical Reviews 103*(12), 4883–4940.

Vera, C. C., A. Trimborn, K.-P. Hinz, and B. Spengler (2005). Initial velocity distributions of ions generated by in-flight laser desorption/ionization of individual polystyrene latex microparticles as studied by the delayed ion extraction method. *Rapid Communications in Mass Spectrometry 19*(2), 133–146.

Vial, S., Y. Berrahal, M. Prado, and J. Wenger (2017, feb). Single-Step DNA Detection Assay Monitoring Dual-Color Light Scattering from Individual Metal Nanoparticle Aggregates. *ACS Sensors 2*(2), 251–256.

Walker, T. and J. Syers (1976). The fate of phosphorus during pedogenesis. *Geoderma 15*(1), 1–19.

Wang, R., Y. Balkanski, O. Boucher, P. Ciais, J. Peñuelas, and S. Tao (2014). Significant contribution of combustion-related emissions to the atmospheric phosphorus budget. *Nature Geoscience 8*(1), 48–54.

Wang, S. and M. V. Johnston (2006). Airborne nanoparticle characterization with a digital ion trap–reflectron time of flight mass spectrometer. *International Journal of Mass Spectrometry 258*(1-3), 50–57.

Wang, X., F. E. Kruis, and P. H. McMurry (2005). Aerodynamic Focusing of Nanoparticles: I. Guidelines for Designing Aerodynamic Lenses for Nanoparticles. *Aerosol Science and Technology 39*(7), 611–623.

Wang, Y. P., R. M. Law, and B. Pak (2010). A global model of carbon, nitrogen and phosphorus cycles for the terrestrial biosphere. *Biogeosciences 7*(7), 2261–2282.

Wenzel, R. J. and K. A. Prather (2004). Improvements in ion signal reproducibility obtained using a homogeneous laser beam for on-line laser desorption/ionization of single particles. *Rapid Communications in Mass Spectrometry 18*(13), 1525–1533.

Wiedinmyer, C., R. M. Bowers, N. Fierer, E. Horanyi, M. Hannigan, A. G. Hallar, I. McCubbin, and K. Baustian (2009). The contribution of biological particles to observed particulate organic carbon at a remote high altitude site. *Atmospheric Environment 43*(28), 4278–4282.

Xia, X., J. Wang, J. Ji, J. Zhang, L. Chen, and R. Zhang (2015). Bacterial Communities in Marine Aerosols Revealed by 454 Pyrosequencing of the 16S rRNA Gene*. *Journal of the Atmospheric Sciences 72*(8), 2997–3008.

Xia, Y., F. Conen, and C. Alewell (2013). Total bacterial number concentration in free tropospheric air above the Alps. *Aerobiologia 29*(1), 153–159.

Xu, W., P. Croteau, L. Williams, M. Canagaratna, T. Onasch, E. Cross, X. Zhang, W. Robinson, D. Worsnop, and J. Jayne (2017). Laboratory characterization of an aerosol chemical speciation monitor with PM 2.5 measurement capability. *Aerosol Science and Technology 51*(1), 69–83.

Yang, X. and W. M. Post (2011). Phosphorus transformations as a function of pedogenesis: A synthesis of soil phosphorus data using Hedley fractionation method. *Biogeosciences 8*(10), 2907–2916.

Yang, X., W. M. Post, P. E. Thornton, and A. Jain (2013). The distribution of soil phosphorus for global biogeochemical modeling. *Biogeosciences 10*(4), 2525–2537.

Yu, P., D. M. Murphy, R. W. Portmann, O. B. Toon, K. D. Froyd, A. W. Rollins, R.-S. Gao, and K. H. Rosenlof (2016). Radiative forcing from anthropogenic sulfur and organic emissions reaching the stratosphere. *Geophysical Research Letters 43*(17), 9361–9367.

Zaveri, R. A., W. J. Shaw, D. J. Cziczo, B. Schmid, R. A. Ferrare, M. L. Alexander, M. Alexandrov, R. J. Alvarez, W. P. Arnott, D. B. Atkinson, S. Baidar, R. M. Banta, J. C. Barnard, J. Beranek, L. K. Berg, F. Brechtel, W. A. Brewer, J. F. Cahill, B. Cairns, C. D. Cappa, D. Chand, S. China, J. M. Comstock, M. K. Dubey, R. C. Easter, M. H. Erickson, J. D. Fast, C. Floerchinger, B. A. Flowers, E. Fortner, J. S. Gaffney, M. K. Gilles, K. Gorkowski, W. I. Gustafson, M. Gyawali, J. Hair, R. M. Hardesty, J. W. Harworth, S. Herndon, N. Hiranuma, C. Hostetler, J. M. Hubbe, J. T. Jayne, H. Jeong, B. T. Jobson, E. I. Kassianov, L. I. Kleinman, C. Kluzek, B. Knighton, K. R. Kolesar, C. Kuang, A. Kubátová, A. O. Langford, A. Laskin, N. Laulainen, R. D. Marchbanks, C. Mazzoleni, F. Mei, R. C. Moffet, D. Nelson, M. D. Obland, H. Oetjen, T. B. Onasch, I. Ortega, M. Ottaviani, M. Pekour, K. A. Prather, J. G. Radney, R. R. Rogers, S. P. Sandberg, A. Sedlacek, C. J. Senff, G. Senum, A. Setyan, J. E. Shilling, M. Shrivastava, C. Song, S. R. Springston, R. Subramanian, K. Suski, J. Tomlinson, R. Volkamer, H. W. Wallace, J. Wang, A. M. Weickmann, D. R. Worsnop, X.-Y. Yu, A. Zelenyuk, and Q. Zhang (2012). Overview of the 2010 Carbonaceous Aerosols and Radiative Effects Study (CARES). *Atmospheric Chemistry and Physics 12*(16), 7647–7687.

Zawadowicz, M., K. Froyd, D. Murphy, and D. Cziczo (2017). Improved identification of primary biological aerosol particles using single-particle mass spectrometry. *Atmospheric Chemistry and Physics 17*(11), 7193–7212.

Zawadowicz, M. A., S. R. Proud, S. S. Seppalainen, and D. J. Cziczo (2015). Hygroscopic and phase separation properties of ammonium sulfate/organics/water ternary solutions. *Atmospheric Chemistry and Physics 15*(15), 8975–8986.

Zelenyuk, A., J. Cabalo, T. Baer, and R. E. Miller (1999). Mass Spectrometry of Liquid Aniline Aerosol Particles by IR/UV Laser Irradiation. *Analytical Chemistry 71*(9), 1802–1808.

Zelenyuk, A. and D. Imre (2005). Single Particle Laser Ablation Time-of-Flight Mass Spectrometer: An Introduction to SPLAT. *Aerosol Science and Technology 39*(6), 554–568.

Zelenyuk, A., D. Imre, J. Wilson, Z. Zhang, J. Wang, and K. Mueller (2015). Airborne Single Particle Mass Spectrometers (SPLAT II & miniSPLAT) and New Software for Data Visualization and Analysis in a Geo-Spatial Context. *Journal of The American Society for Mass Spectrometry 26*(2), 257–270.

Zelenyuk, A., J. Yang, E. Choi, and D. Imre (2009). SPLAT II: An Aircraft Compatible, Ultra-Sensitive, High Precision Instrument for In-Situ Characterization of the Size and Composition of Fine and Ultrafine Particles. *Aerosol Science and Technology 43*(5), 411–424.

Zender, C. S. (2003). Mineral Dust Entrainment and Deposition (DEAD) model: Description and 1990s dust climatology. *Journal of Geophysical Research 108*(D14), 4416.

Zhang, Q., J. L. Jimenez, M. R. Canagaratna, I. M. Ulbrich, N. L. Ng, D. R. Worsnop, and Y. Sun (2011). Understanding atmospheric organic aerosols via factor analysis of aerosol mass spectrometry: a review. *Analytical and Bioanalytical Chemistry 401*(10), 3045–3067.

Zhang, X., K. A. Smith, D. R. Worsnop, J. Jimenez, J. T. Jayne, and C. E. Kolb (2002). A Numerical Characterization of Particle Beam Collimation by an Aerodynamic Lens-Nozzle System: Part I. An Individual Lens or Nozzle. *Aerosol Science and Technology 36*(5), 617–631.

Zhang, X., K. A. Smith, D. R. Worsnop, J. L. Jimenez, J. T. Jayne, C. E. Kolb, J. Morris, and P. Davidovits (2004). Numerical Characterization of Particle Beam Collimation: Part II Integrated Aerodynamic-Lens–Nozzle System. *Aerosol Science and Technology 38*(6), 619–638.

Zhou, L., K. Park, H. M. Milchberg, and M. R. Zachariah (2007). Understanding the Interaction of an Intense Laser Pulse with Nanoparticles: Application to the Quantification of Single Particle Mass Spectrometry. *Aerosol Science and Technology 41*(9), 818–827.

Ziemba, L. D., A. J. Beyersdorf, G. Chen, C. A. Corr, S. N. Crumeyrolle, G. Diskin, C. Hudgins, R. Martin, T. Mikoviny, R. Moore, M. Shook, K. L. Thornhill, E. L. Winstead, A. Wisthaler, and B. E. Anderson (2016). Airborne observations of bioaerosol over the Southeast United States using a Wideband Integrated Bioaerosol Sensor. *Journal of Geophysical Research: Atmospheres 121*(14), 8506–8524.